2007

Probing the energy transfer dynamics of photosynthetic reaction center complexes through hole-burning and single-complex spectroscopy

Kerry Joseph Riley
Iowa State University

Probing the energy transfer dynamics of photosynthetic reaction center complexes through hole-burning and single-complex spectroscopy

by

Kerry Joseph Riley

A dissertation submitted to the graduate faculty in partial fulfillment of the requirements for the degree of

DOCTOR OF PHILOSOPHY

Major: Physical Chemistry

Program of Study Committee:
Ryszard Jankowiak, Co-Major Professor
Edward Yeung, Co-Major Professor
Yeon Kyun Shin
Xueyu Song
Hans U. Stauffer

Iowa State University

Ames, Iowa

2007

TABLE OF CONTENTS

CHAPTER 1 – PHOTOSYNTHESIS OVERVIEW

1.1 The Photosynthetic Process – A Brief Introduction

Photosynthesis is the process by which light energy is used to drive reactions that generate sugars to supply energy for cellular processes. It is one of the most important fundamental biological reactions and occurs in both prokaryotic (e.g. bacteria) and eukaryotic (e.g. plants and algae) organisms. Photosynthesis is also remarkably intricate, requiring the coordination of many different steps and reactions in order to successfully transform absorbed solar energy into a biochemical usable form of energy. However, the net reaction for all photosynthetic organisms can be reduced to the following, deceptively general, equation developed by Van Niel [1]

$$H_2 - D + A \overset{h\nu}{\Rightarrow} A - H_2 + D$$

where H_2-D is the electron donor, e.g. H_20, H_2S. A is the electron acceptor, e.g. CO_2, and A-H_2 is the synthesized sugar. Amazingly, this simple net equation is responsible for creating the oxidizing atmosphere of Earth and the recycling of CO_2, both of which are necessary for the sustainment of our global ecosystem [1-3].

The intricate process needed to arrive at the above equation for photosynthesis can be broken down into four main phases: (1) light absorption and energy delivery by antenna systems, (2) primary electron transfer in reaction centers, (3) energy stabilization by secondary electron transfer, and (4) synthesis and transport of stable sugar products [2]. The first phase is a photophysical process, the second and third phases are photochemical processes, and the fourth phase is a biochemical process. This dissertation is primarily concerned with the first two phases, the photophysical and initial

photochemical processes in photosynthetic complexes. These phases are often referred to as the early events of photosynthesis as they occur on extremely fast timescales (10^{-15} to 10^{-3} s) [3, 5].

The first two phases involve light harvesting by antenna system pigment-protein complexes and excitation energy transfer (EET) to reaction center (RC) pigment-protein complexes for initial charge separation and electron transfer. Antenna system pigment complexes consist of chlorophyll-type molecules, e.g. chlorophyll *a* and *b*, bacteriochlorophylls, pheophytin *a* and *b*, and other kinds of pigment molecules, e.g. carotenoid α and β, xanthophylls, to capture solar radiation (see Figure (Fig.) 1 for chemical structures) [1, 3]. Since the $S_1 \leftarrow S_0$ transitions for these molecules range from ~ 450 nm to 900 nm, light is collected over a broad wavelength range from the solar spectrum (300-1100 nm) filtered by the Earth's atmosphere [1]. Energy that is collected by the antenna complexes is transferred downward, like a funnel, to lower lying, chlorophyll containing RC pigment complexes (see Fig. 2). When excitation energy is transferred to a RC, it forms an excited electronic state with a very high redox potential (usually ~ 0.4 to 1.1 V) [2, 4] and can therefore donate its electron to a lower energy molecule (usually a pheophytin), forming a primary charge separated state. Altogether, the light harvesting and initial charge separation events are extremely efficient, yielding nearly 100% quantum efficiency [2].

In the third phase, the primary charge-separated state created by the reaction center is stabilized by further electron transfer along a chain that is coupled to an engine which can store energy in a chemical form (i.e. adenine triphosphate (ATP) synthase).

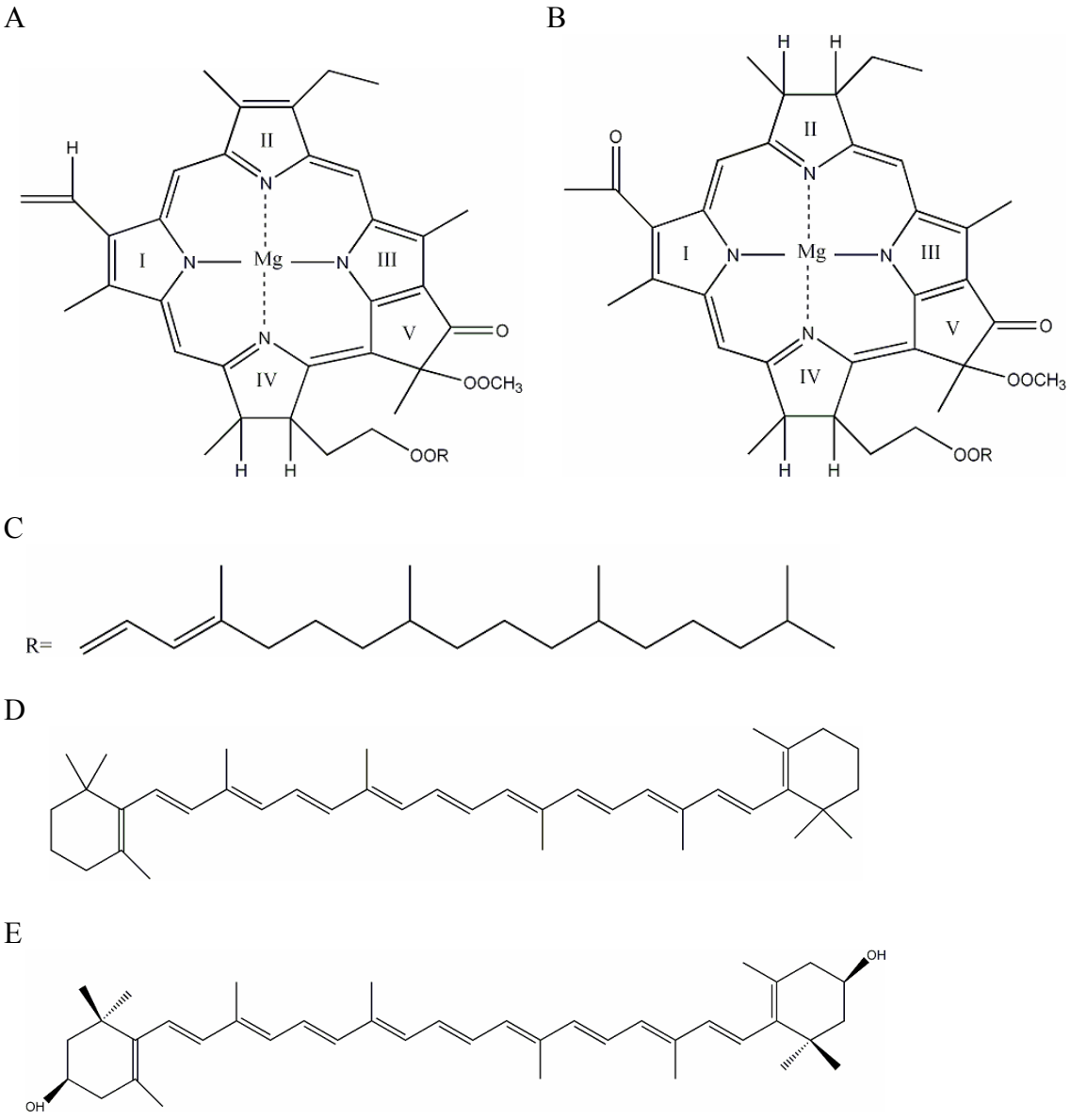

Figure 1. Chemical structures of (A) chlorophyll, (B) bacteriochlorophyll, (C) the phytyl tail, (D) beta-carotene, a carotenoid of photosystem II (PS II) which is responsible for quenching singlet states and preventing oxidation to the PS II RC, and (E) zeaxanthin, a xanthophyll which is an oxidized hydroxy derivative of beta-carotene, that is responsible for quenching reactive oxygen species in cyanobacterial and plant photosynthetic organisms. The phytl tail is abbreviated as R in structures (A) and (B). The Roman numbers I to V label the Chl and BChl rings according to the IUPAC nomenclature system. The structures of pheophytin and bacteriopheophytin are respectively identical to chlorophyll and bacteriochlorophyll, except that the central Mg atom is replaced with H atoms bonded to rings I and III.

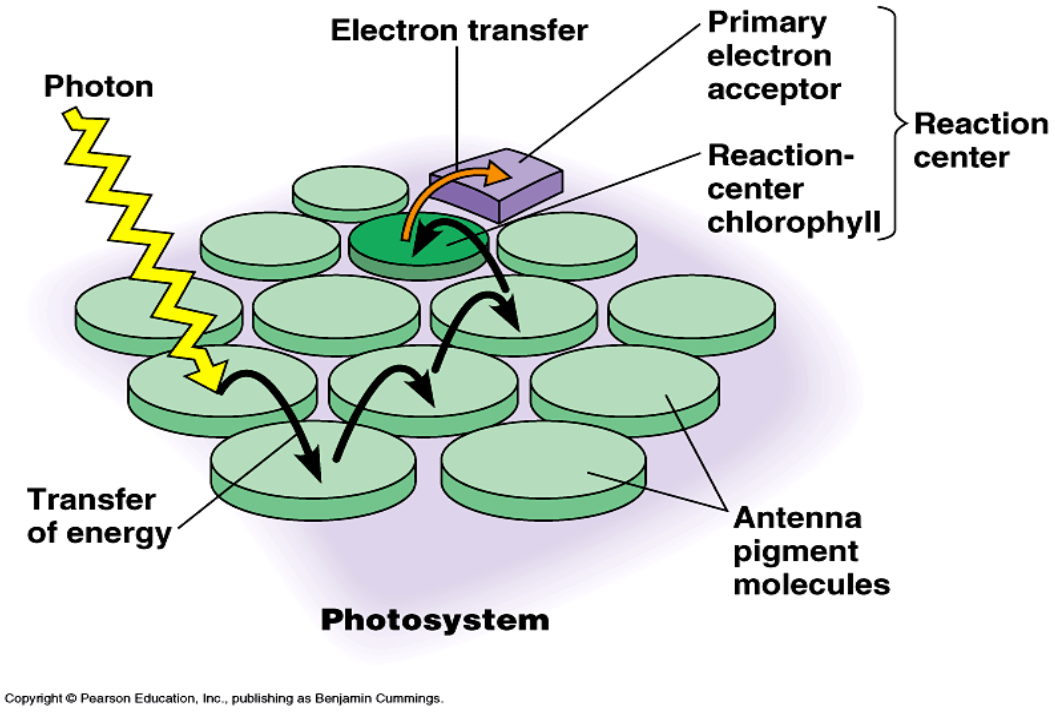

Figure 2. Schematic of light harvesting through antenna pigment molecules and transfer to the reaction center, to initiate primary electron transfer (i.e. charge separation) [6].

This electron transfer proceeds by either one of two distinct mechanisms: (i) non-cyclic phosphorylation or (ii) cyclic phosphorylation [phosphorylation in this sense means the light driven synthesis of ATP from adenine diphosphate (ADP) and phosphate (P_i)] [1, 6]. Non-cyclic phosphorylation is oxygenic and occurs in cyanobacteria and higher plants. Cyclic phosphorlyation is anoxygenic and occurs in green sulfur and purple bacteria [2]. However, cyanobacteria and plants can undergo cyclic phosphorylation when they are too low in energy to run non-cyclic phosphorylation. The differences between cyclic and non-cyclic phosphorylation are outlined in Figs 3-4. Basically, in cyclic phosphorylation, the electron lost from the reaction center returns to re-reduce it. In non-cyclic phosphorylation, the electrons are not recycled; electrons must be obtained from an outside source, i.e. H_20, to re-reduce the oxidized reaction center. Non-cyclic phosphorylation is also different from cyclic phosphorylation in that a reducing compound, nicotinamide adenine dinucleotide phosphate (NADPH), is produced along with ATP.

Consequently, the fourth phase uses the ATP and NADPH generated by the third phase in carbon fixation, which generates sugars that the organism can use for energy. These are commonly referred to as the dark reactions of photosynthesis, since they can take place in the absence of light via the fact that the ATP and NADPH has already been generated by light reactions of photosynthesis. In oxygenic organisms, the dark reactions are referred to as the Calvin, Basshan, and Besson cycle, or Calvin cycle [1, 4], after the researchers who determined the chemistry of these enzymatic reactions. The Calvin cycle is responsible for CO_2 fixation into carbohydrates in oxygenic organisms. For

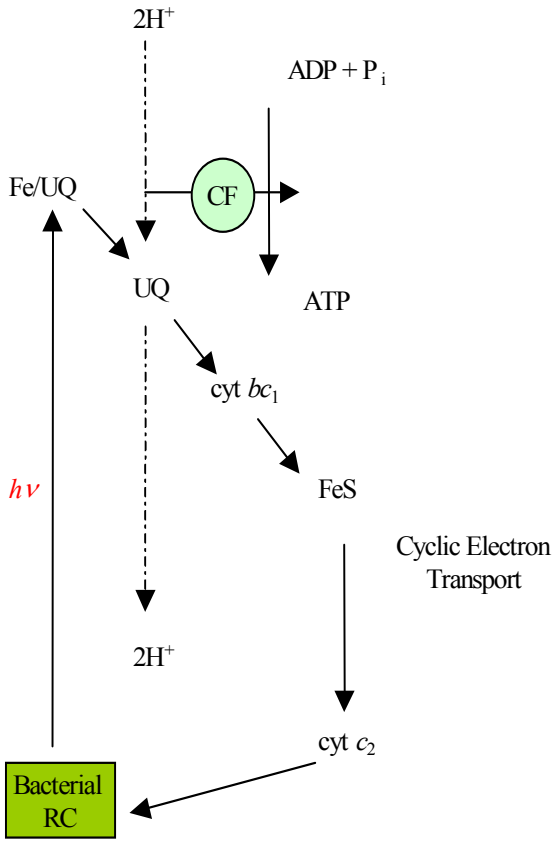

Figure 3. Schematic of cyclic phosphorylation in purple bacteria [5]. After the bacterial RC is excited by light ($h\nu$), primary electron transfer to an iron-ubiquinone complex (Fe/Uq) occurs. The electron leaves the RC through transfer to a ubiquinone (UQ). It then travels to cyctochromes bc_1 (cyt bc_1), to cytochromes c_2 (cyt c_2), and finally back to reduce the RC, completing the electron transfer cycle. Meanwhile, the electron transfer across the bacterial membrane through UQ creates a proton gradient, which drives ATP synthesis via the ATP synthase coupling factor (CF).

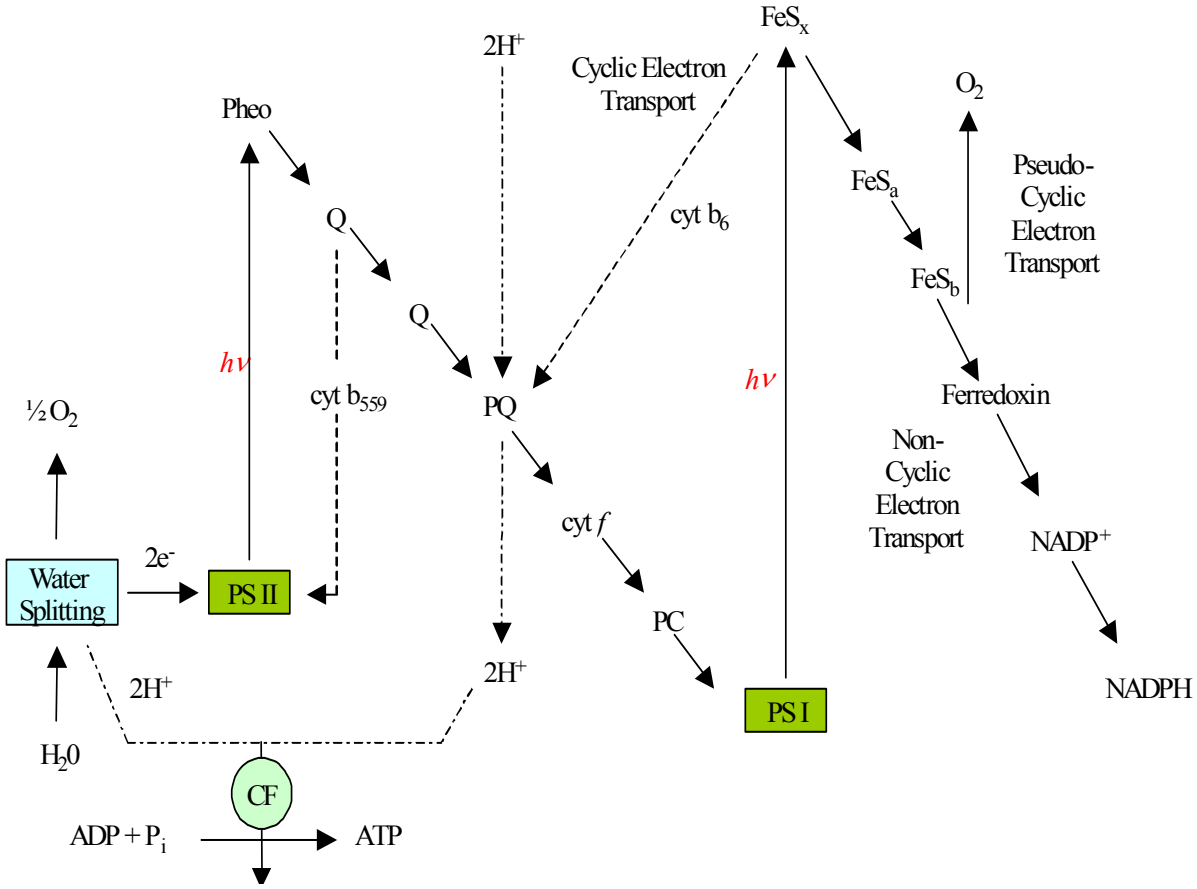

Figure 4. Schematic of non-cyclic phosphorylation in cyanobacteria and plants [1]. When the PS II RC is excited by ($h\nu$), primary electron transfer to pheophytin (Pheo) occurs, then is passed down to two quinones (Q), a plastiquinone (PQ), cytochrome *f* (cyt *f*), and to plastocyanin (PC). After excitation, the photosystem I (PS I) RC transfers an electron to a series of iron-sulfur complexes ($FeS_{x, a, b}$) and PS I is reduced by PC. Ferredoxin then reduces FeS_b, which is then reduced by NADP reductase ($NADP^+$), leading to the synthesis of NADPH and is used in the Calvin cycle. The PS II RC is reduced by H_2O (generating O_2) and cytochrome b_{559} (cyt b_{559}). Electron transfer across the thylakoid membrane creates a proton gradient, which drives ATP synthesis via the ATP synthase CF. If the organism is too low in NADPH to synthesize sugars, cyclic phosphorylation takes place. Then electron transfer from FeS_x to cytochrome b_6 (cyt b_6) takes place, ensuring that the PS I RC is reduced.

anoxygenic organisms, the Calvin cycle is present in purple bacteria, but in green sulphur bacteria, reverse tricarboxylic acid cycle (TCA) is used for carbon fixation [4].

As life has evolved from single celled prokaryotic bacteria to the complex multi-cellular biological structures of plants and animals, the morphology of photosynthesis has also changed. In prokaryotic organisms, of which there are three groups: cyanobacteria, photosynthetic bacteria, and Prochlorophyta, where the photosynthetic machinery is most simple. Cyanobacteria and Prochlorophyta [2, 4] evolve oxygen and contain chlorophyll *a* and *b* (which are present in plants). Photosynthetic bacteria are anoxygenic (they use carbon, nitrogen, and sulphur compounds as the reductant source) and consist of two subgroups: Rhodospirillineae and Chlorobiineae [2,4]. Rhodospirillineae, purple bacteria, can use carbon, sulphur, and nitrogen as electron donors and contain bacteriochlorophyll *a* and *b*. Chlorobiineae, green sulphur bacteria, use sulphur compounds as electron donors (only one species, *Chloroflexus aurantiacus*, uses CO_2 along with S^{2-} as reductants) and contain bacteriochlorophyll *a*, *c*, *d*, and *e*.

For all prokaryotes, the light driven reactions of photosynthesis take place in the cellular membrane, as there are no organelles. In eukaryotic organisms, such as plants and algae, the architecture of photosynthesis is much more advanced [1, 2, 4]. Unlike prokaryotes, all eukaryotes are oxygenic and contain chlorophyll *a* and *b*. Since eukaryotic cells are divided into subcellular organelle structures, photosynthesis takes place in organelles called chloroplasts. It has been speculated that chloroplasts evolved from the Prochlorophyta bacteria, *Prochloron* [4]. Chloroplasts are plastids, that is, they have a double membrane surrounding an internal membrane network. This internal membrane provides the chloroplasts with a large volume and surface area, for a very high

energy output. The internal membrane also has folds, known as the chloroplast envelope, which contains a liquid, the stroma, and stacks of inner membrane discs or thylakoids (see Fig. 5). Stacks of these thylakoids are called grana. All pigment protein complexes needed for the light dependent reactions of photosynthesis are located in the thylakoid membranes. The dark reactions of photosynthesis occur in the stroma (see Fig. 5B).

Understanding the complex, multiphasic process of photosynthesis has many important scientific implications. From a biological perspective, understanding photosynthesis and how it varies among different organisms is important from structural biological, biochemical, evolutionary, and genetic standpoints. From a more physical perspective, understanding the physics of photosynthesis, especially the early events of light-harvesting EET and electron transfer, is extremely important as a model for solar cell science and technology [8-10]. Information gleaned could have practical applications for third or fourth generation photovoltaic devices, in either creating solar cells that mimic photosynthesis [11, 12] or actually using photosynthetic complexes in bioengineered devices [13, 14].

1.2 Photosynthetic Complexes

While the exact photosynthetic process can vary greatly in different types of organisms, the early events of photosynthesis are very similar for all organisms. The basic schematic for all is, as stated before, energy collection by light harvesting complexes and transfer to the RC for charge separation. Light harvesting and RC complexes are pigment-protein structures where the chlorophyll or other pigments are coupled to a protein structure, giving these complexes unique structures and pigment arrangements. Together the light harvesting and RC complexes make up the

A

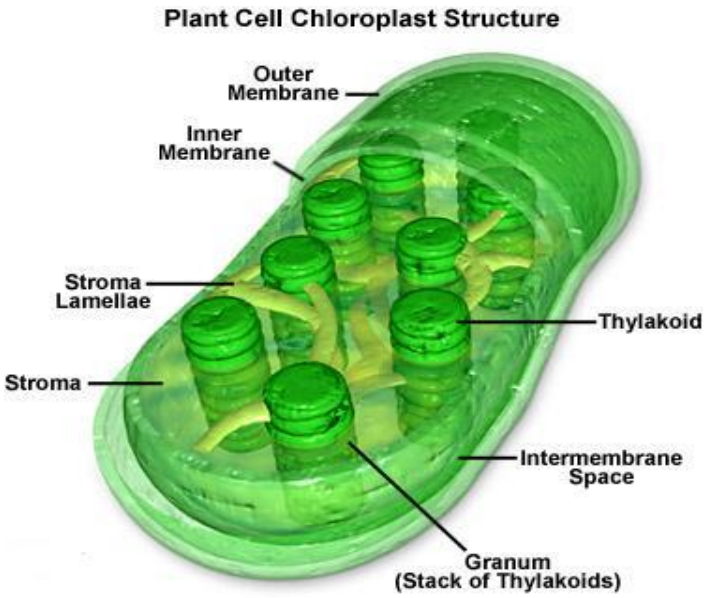

B

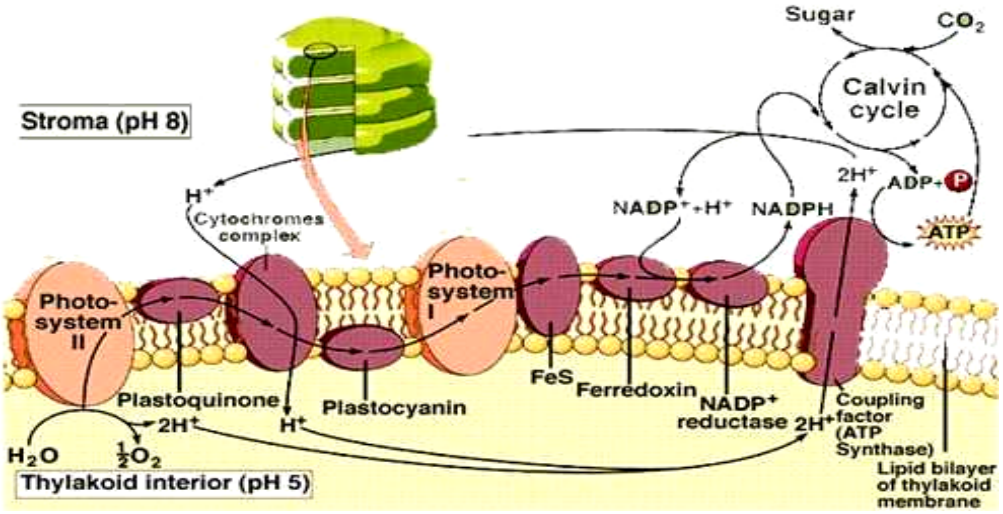

Figure 5. Structure and organization of the (A) chloroplast and thylakoid membrane (B) [7]. The chloroplast consists of an inner and outer membrane. In the chloroplast envelope, the thylakoid membrane is folded into columns (grana) as shown in (A). The fluid inside the chloroplast is the stroma, where the dark reactions or Calvin cycle takes place. All of the light driven reactions take place at the thylakoid membrane as shown in (B).

photosynthetic unit (PSU) [1, 15]. The PSU is the building block for photophysical and photochemical processes in photosynthesis for an organism. By definition, in one PSU, one absorbed photon can yield a charge separated state in a reaction center. In order to increase the surface area for absorption, hundreds of light harvesting complexes per reaction center makes up a PSU (see Fig. 6). Different organisms may have different light harvesting complexes and reaction center complexes, but they all conform to this basic architecture of the PSU.

Though different photosynthetic light harvesting and RC complexes serve the same function, they each have their own highly specific and unique properties. For example, the PS I RC of cyanobacteria and green plants, has states lower in energy than the primary electron donor and these states can act as long wavelength antennas or as energy traps for photoprotection [16, 17]. The PS II RC of cyanobacteria and green plants is the only RC complex with a primary electron donor high enough in redox potential to oxidize water (1.1 V) [18].

Light harvesting complexes show highly unique properties as well. The light harvesting 2 (LH2) complex of purple bacteria has two highly symmetric chlorophyll rings, where one ring is strongly coupled resulting in a manifold of excitonic states (B850) while the other ring (B800) has weak coupling between chlorophyll dimers resulting in localized excitonic states [19, 20]. The CP43 light harvesting complex of cyanobacteria and plants has two quasi-degenerate states at 682.9 nm (B state) and 683.3 nm (A state), where the B state serves most likely as the main energy transfer pathway to the RC due to high correlation with higher lying energy states while the A state functions as more of an energy sink, with an excited state lifetime approaching the radiative limit

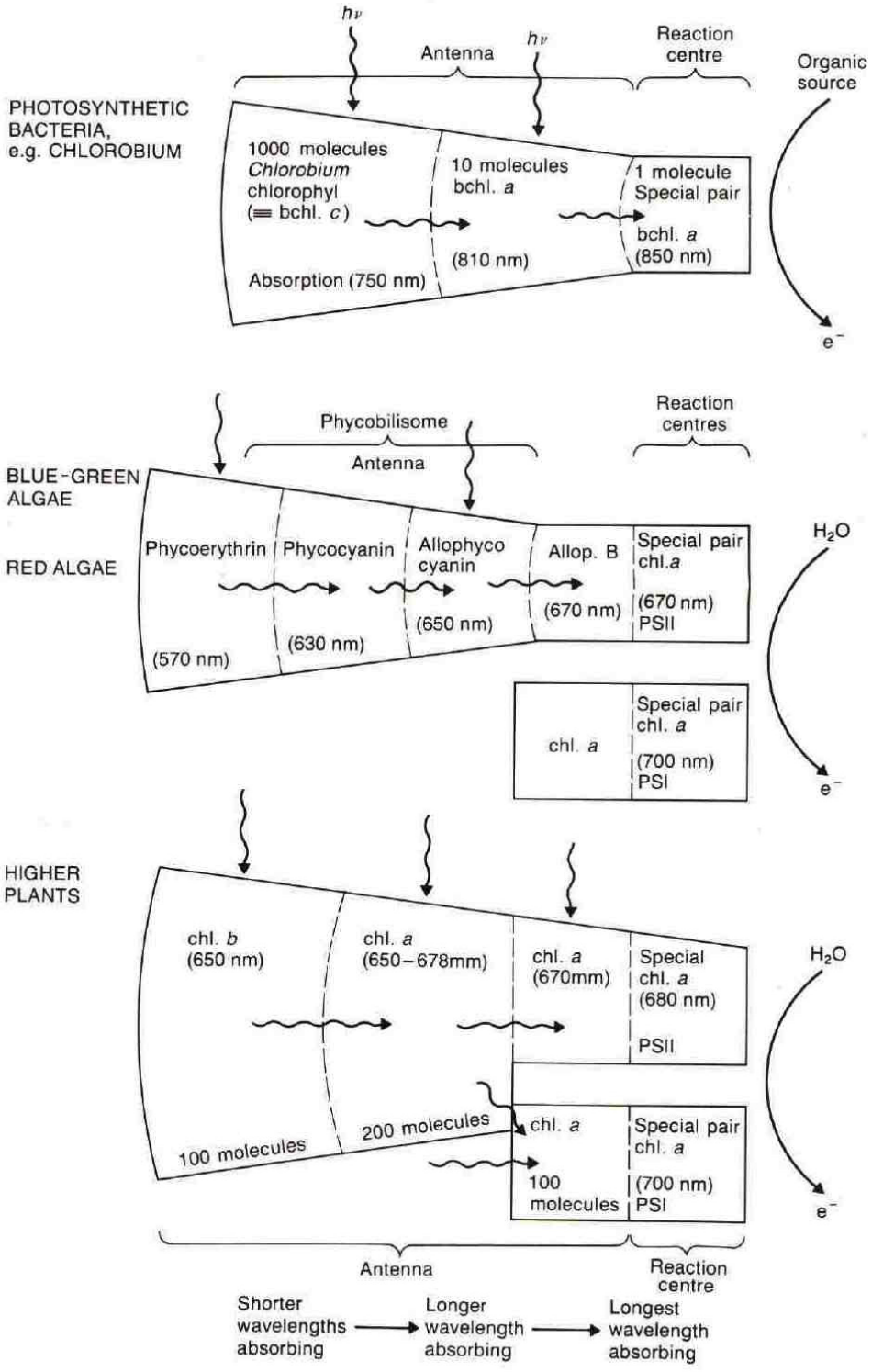

Figure 6. Schematic of the organization, electron, and energy transfer pathways of PSUs in different classes of photosynthetic organisms [1].

for a Chl transition (8 ± 1 ns) [21]. So while different light harvesting and RC complexes share the same basic purpose, each particular complex has their own specific niche and functionality for EET and/or electron transfer.

Since light harvesting complexes and reaction center complexes have distinct functional differences, and since the study of light harvesting and RC complexes has somewhat developed along independent paths, separate sections will be presented to discuss the highlights of important structural and spectroscopic research developments. Sections 1.2.1 and 1.2.2 will give an overview of historical and recent contributions from X-ray crystallography and ultrafast photon-echo, and hole-burning spectroscopy experiments for light harvesting and RC complexes, respectively. However, a more thorough treatment will be given to Section 1.2.2, especially regarding the PS I and PS II RCs, due to the fact that the research contained in this dissertation focuses on the EET and electron transfer properties of these RC complexes.

1.2.1 Light Harvesting Complexes

Light harvesting antenna complexes can be broadly separated into two classes: integral membrane antenna complexes and peripheral antenna complexes [2]. Integral membrane antennas are complexes in which the pigment-protein crosses the lipid bilayer. Peripheral antennas are complexes where the protein does not cross the lipid bilayer but coordinate with the pigment-protein complexes in the membrane. Peripheral antenna complexes function to transfer energy to the integral membrane complexes, where energy eventually travels to the reaction center. Peripheral antenna complexes include the phycobilisomes of cyanobacteria and red algae and the chlorosomes and Fenna-Matthews-Olsen (FMO) complex of green bacteria [2]. Due to the availability of a high

resolution X-ray structure of FMO [22], many experimental investigations have been performed on this complex [23-26].

Integral membrane antenna complexes are the most widely studied complexes because of their prime importance in shuttling energy to the RC and also their wide structural and functional diversity. Due to this diversity, they can be broken down into further categories [2]. Fused antenna complexes refer to pigment-protein complexes that cannot be biochemically separated from the RC. These include the PS I RC and the green sulfur bacterial RC antenna pigment-proteins. Core antenna complexes are pigment-proteins that coordinate with the RC complexes, but can be separated biochemically. These include the CP43/CP47 complexes of the PS II RC and the light harvesting 1 (LH1) complex of the purple bacterial RC. Accessory antenna complexes are strongly associated with the RC complexes. The accessory antenna complexes are extremely important because they are the complexes that directly couple the RC system to the major light harvesting antenna "pools". The amount of accessory complexes per RC plus core antennas is variable, usually depending on environmental conditions. Examples of accessory antenna complexes include light harvesting complex I (LHCI) and light harvesting complex II (LHCII) of the PS I and PS II RC, respectively, along with LH2 of the purple bacterial RC.

Purple bacterial LH2 and LH1 are among the most widely studied light harvesting antenna complexes mainly due to the 2.5 Å X-ray structure of LH2 from *Rds. Acidophila* by Cogdell et al. [27] available in 1995, and the 2.5 Å LH2 structure of *Rs. Molischianum* by Shulten et al. available in 1996 [28]. These structures show the cyclic nature of these pigment-protein complexes, 8 and 9 fold symmetric rings comprised of αβ-heterodimers

for *Rs. Molischianum* [27] and *Rds. Acidophila* [28], respectively. The structure of LH1 has been correlated to LH2 through electron density mapping by Ghosh et al. [29]; it is now thought that LH1 is a 16 fold symmetric ring that encloses the bacterial RC [30]. This structural data has stimulated much interest in the energy transfer properties of these complexes and the correlation with their cyclic structures. Theoretical investigations have modeled energy transfer in these rings through incoherent Förster hopping and exciton dynamics (see Chapter 2). Additional motivation for research on LH2 and LH1 is that the anoxygenic bacterial photosynthetic machinery is less complicated than the photosynthetic systems of oxygenic bacteria and plants, thus offering well-defined systems for studying EET and electron transfer processes. For those more interested, the spectral and energy transfer properties of LH2 and LH1 are summarized in references [19, 31, 32].

LHCII of PS II has had structural data available for many years, which has stimulated research into the properties of this complex. In 1994, Kühlbrandt et al. [33], through electron diffraction and electron microscopy experiments on two-dimensional crystals of LHCII at cryogenic temperatures, determined the structure of the trimeric form at 3.4 Å resolution (parallel to the crystal plane) and 4.4-4.9 Å (perpendicular to the crystal plane). Trimeric LHCII consists of three transmembrane α-helices and a short amphiphilic helix. Each monomer binds 12 Chls and 3 xanthophylls (Xan). The determination of this structure has been very important due to its high level of sequence homology with the minor light harvesting complexes of PS II complexes such as CP26/CP29 and LHCI of PS I [34]. Until recently [35], the structural determination did not provide a high enough resolution to correctly assign the positions of all the Chls and

Xans. While the exact structural model of LHCII has not been agreed upon, even with the recently obtained higher resolution structural data [35], LHCII has been found to have some very unique energy transfer properties [19, 34-37]. It has been found that the energy transfer time between the monomeric pigments in the trimer is much slower (tens of picoseconds) compared to energy equilibration in bacterial LH2 and LH1 (hundreds of femtoseconds) [19, 34, 37]. It was theorized in reference [37] that this slower transfer time allows for increased energy trapping in the PS II RC, in which energy transfer equilibrates on same timescale (tens of picoseconds) [34, 36, 37]. LHCII is also thought to serve as a structural model for LHCI [38, 39], due to homologous protein sequences, and, consequently, has stimulated experimental investigations of this complex [40, 41]. For more information on LHCI, and recent experimental investigations, the following references [34, 42, 43] are suggested.

Along with LHCII, CP43 and CP47 of PS II have also been widely studied. CP43 and CP47 are proximal core light antennas to the D_1 and D_2 proteins of PS II, which binds the RC cofactors. Since CP43 and CP47 are biochemically fused to the PS II RC, PS II RC complexes ("core" PS II complexes) can be prepared and studied to probe the coupling of CP43 and CP47 to the RC [44-46]. X-ray structural data has also been published on these complexes, with the most recent by Iwata et al. at 3.4 Å resolution in 2004 [47]. With no high-resolution structural data available, though, there is still some discrepancy over the exact Chl number, positions, and assignments in CP43/CP47 [47, 48]. Both CP43 and CP47, however, have three pair of α-helices and a shared sequence homology [49, 50]. Therefore, it is expected that CP43 and CP47 should bind a similar number of pigments. The recent data by Iwata et al. determines that CP43 and CP47 bind

14 and 16 Chls, respectively, and that for both CP43 and CP47, the Chls are arranged in layers on the stromal and luminal sides of the membrane except for one Chl equidistant between the membrane surfaces, forming stacks of Chls that span the membrane. Other earlier studies have suggested that CP43 and CP47 bind between 14-16 Chls [48, 50-52].

Many experimental investigations have been performed to determine the CP43/CP47-RC energy transfer kinetics. Frequency domain spectroscopic investigations (fluorescence line-narrowing [53] and hole-burning (HB) [48, 53, 54]) on isolated CP43/CP47 has shown the presence of a long lived energy trap (~ 50 ps) at 690 nm for CP47, which likely correlates to the lowest state of an excitonically coupled Chl dimer [53], while CP43 possesses two quasi-degenerate traps at ~ 683 nm that have dephasing times on the order of nanoseconds [48]. For comparison, ultrafast experiments for CP43/CP47 have shown energy transfer components of 200-400 fs and 2-3 ps [55]. Experiments on "core" PS II RC complexes also show similar results for frequency and time domain techniques, with HB experiments predicting CP43/CP47 to RC energy transfer times of 70-270 ps [44], and time-resolved fluorescence experiments predicting CP43/CP47 to RC energy transfer times of 1.5-10 ps [55]. Recent attention has also turned to the study of energy transfer in PS I-IsiA supercomplexes of cyanobacteria that form under iron stress conditions, where the IsiA complex is sequentially homologous to CP43 of PS II and is often referred to as CP43′ [56]. Preliminary experiments have shown that the spectral properties of CP43′ are very similar to CP43, but with a noticeable difference in that CP43′ possesses only one absorption band at ~ 682 nm and not two quasi-degenerate states like CP43 (see Chapter 5 for details).

1.2.2 Reaction Center Complexes

The RC, as stated before, is responsible for charge separation and initiating electron transfer and thus converting light energy into chemical energy. It is a complex with a definite stoichiometry that can be separated biochemically from the rest of the photosynthetic machinery [2]. However, the biochemical isolation and structural determination of reaction center complexes was a slow process with contributions from many research groups [2, 57-62]. The concept of the reaction center first developed out the flash experiments by Emerson and Arnold in the 1930s, in which they determined that only one molecule of O_2 was produced per ~ 2500 Chl molecules [52-54]. From this, Gaffron and Wahl theorized that not all chlorophylls have the same function and came with idea of the photosynthetic unit, differentiating between Chls that are responsible for light harvesting (antennas) and Chls involved in the photochemical processes of photosynthesis (reaction centers) [60-62]. Work by Duysens et al. in the 1950s on purple bacteria offered support for their RC model, along with later work Bessel Kok in 1957 on PS I and Horst Witt in 1967 on PS II.

1.2.2.a Bacterial Reaction Center

The purple bacterial RC complex is currently the most well understood RC due to the large amount of high resolution X-ray structural data available and also because of its straightforward spectral nature when compared to the RCs of oxygenic photosynthesis. In particular, the RC of *Rhodobacter (Rb.) Sphaeroides* is arguably the most widely studied and understood, serving as a basic model for RC energy and electron transfer. While *Rb. Sphaeroides* might be the best characterized, it was not the first purple bacterial RC to have its protein structure determined. The first high-resolution purple

bacterial X-ray structure was the four-subunit complex (LMHC) of *Rhodopseduomonas (Rps.) viridis* by Michel, Deisenhofer, and Huber [63-65]. Later, other groups determined the X-ray structure of the three-subunit complex (LMH) of *Rb. Sphaeroides* [66, 67].

Purple bacterial reaction centers can consist of either three or four protein subunits, depending upon the species [2]. The subunits are designated as light (L), medium (M), heavy (H), and/or cytochrome (C) [2, 69]. It should be noted, though, that these designations were made before the true molecular masses of the subunits could accurately be determined and do not indicate the true masses of the subunits (H is the lowest mass, L is the next heavier, and M is the heaviest mass). The reaction centers also contain a number of non-covalently bound cofactors, such as four bacteriochlorophyll molecules (BChl) – the bacteriochlorophyll special pair dimer (P_A, P_B) and the two accessory bacteriochlorophylls (B_A, B_B), two bacteriopheophytin molecules (BPh_A, BPh_B), two quinones (Q_A, Q_B), one metal atom (i.e. Fe 2^+), and usually one carotenoid [2]. The special pair BChls are interesting in that they are a strongly excitonically coupled dimer (~ 1350 cm^{-1} excitonic splitting at 4 K for *Rb. Sphaeroides* [70]), due to the small interplanar distance between these chlorins (see Fig. 8b), and also because they are the primary electron donor for electron transfer. The special pair BChls are referred to as P870 in *Rb. Sphaeroides* and P960 in *Rps. Viridis*. The above assignment is based on the maximum absorbance wavelength of their lowest excitonic bands, which for *Rb. Sphaeroides* and *Rps. Viridis* is at 870 and 960 nm, respectively.

In *Rb. Sphaeroides*, the L and M subunits are the core membrane structure, where both subunits consist of five transmembrane helices that are arranged in a pseudo-C2

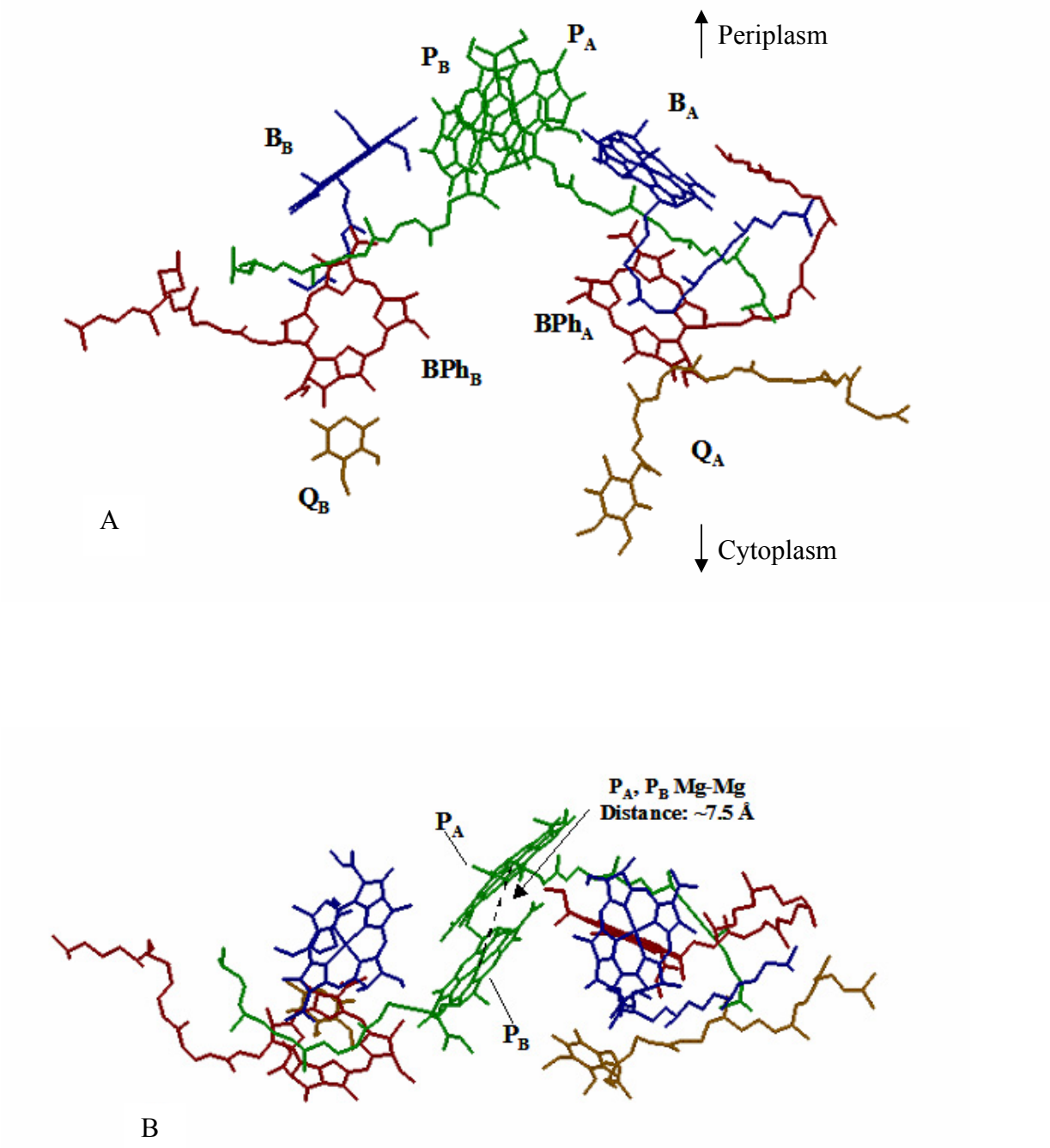

Figure 7. Bacterial RC structure at 2.55 Å resolution [68]. In (A), P_A, P_B are the special pair BChls, B_A, B_B are the accessory BChls, BPh_A, BPh_B are the bacteriopheophytins, and Q_A, Q_B are the quinones. The active branch where electron transfer occurs is labeled as A, while the inactive branch is labeled as B. The RC structure is located transversely across the membrane with the special pair oriented towards the periplasmic side and the quinones toward the cytoplasmic side. In (B), the short intermolecular distance between the special pair dimer Chls results in the large splitting of the excitonic states.

symmetry. The H subunit is oriented on the cytoplasmic side of the intracytoplasmic membrane. The C subunit is not present in all purple bacterial reaction centers and is not considered an integral membrane protein since it does not posses any transmembrane segments [2]. The C subunits main function is to bind four heme molecules that can accept an electron from cyt c_2 to reduce the oxidized reaction center. Additionally, the non-covalently bound cofactors are also arranged in a pseudo-C2 symmetry. The special pair bacteriochlorophylls (P_A, P_B) are oriented to the periplasmic side of the membrane and are surrounded by B_A and B_B. The two bacteriopheophytins (BPh_A, BPh_B) are each located behind the corresponding bacteriochlorophylls (B_A, B_B), towards the cytoplasmic side. Correspondingly, the quinones are located behind the bacteriopheophytins. Overall, this orientation of cofactors forms two electron transfer chains or pathways for charge separation in the RC (see Fig. 7A).

Upon optical excitation, P870 forms P870* in *Rb. Sphaeroides*, and initial electron transfer occurs within a few picoseconds [71], forming $P_A H_A^-$ through $P_A B_A^-$. After approximately 200 ps, further electron transfer forms $P_A Q_A^-$ and then eventually $P_A Q_B^-$. In wild-type RCs, electron transfer always occurs along the A branch and minimally along the B branch [65, 66]. It is theorized that A-side electron transfer occurs preferentially due to the relative free energy difference between the initial excited state P870* and $P_A B_A^-$, with electron transfer along this side conserving more energy for proton pumping [71]. This overall electron transfer reaction that forms the stable charge-separated state is shown in Fig. 3. Interestingly, the recombination rates of the electron transfer (back to the primary electron donor) are ~ 50 times slower than the forward transfer rates [2]. These advantageous kinetics help allow for charge separation to have

such a high quantum yield and to make the light driven reactions of photosynthesis so efficient.

Numerous spectroscopic studies have been performed on *Rb. Sphaeroides* and *Rps. Viridis* to investigate their energy and electron transfer properties. Both frequency and time domain spectroscopies have determined that the excited state lifetime of both P870* and P960*, which determines the primary charge separation process, to be ~ 3 ps and ~ 1 ps at room temperatures and cryogenic temperatures, respectively [74-76]. Spectral HB studies [77] have specifically shown that the special pair BChls of P870 and P960 have strong electron-phonon coupling which results in large homogeneous broadening of the band, with a special pair intramolecular phonon "marker" mode that contributes to the Marcus reorganization energy for initial electron transfer. However, this marker mode does not act as a phononic "trigger" for electron transfer, since the electron transfer rate increases as temperature decreases. Also, the lack of high energy satellite zero-phonon holes (ZPH) from this marker mode, which are vibronic replicas of the purely electronic ZPH, show that thermalization of the phonon modes for P* occurs on a ultrafast timescale of ~ 100 fs (for details, see Chapter 3).

1.2.2.b Photosystem I Reaction Center

In oxygenic photosynthetic systems, the PS I RC is the reaction center that is responsible for providing the electrons that reduce $NADP^+$ to NADPH, which is used in the Calvin cycle to synthesize sugars. The Calvin cycle is important from an ecological perspective because it is responsible for the recycling of atmospheric CO_2. The size of the PS I complex is very large when compared with other reaction center complexes, e.g. the complex coordinates ~ 90 Chl molecules and 12-16 β-carotene molecules in

monomeric form. Since most of these Chls and cofactors and part of the integral membrane antenna complex of PS I, they cannot be separated from the RC cofactors where charge separation occurs. PS I also occurs in a trimeric form in cyanobacteria, where the complex contains three RCs and ~ 270 antenna Chl molecules arranged in a C3-like symmetry.

The X-ray structure of trimeric cyanobacterial PS I from *Thermosynechococcus elongatus* is currently available at a resolution of 2.5 Å, determined by Fromme et al. [78]. Each monomer of the trimer is composed of 12 different protein subunits that bind 96 Chls, 22 carotenoids, three 4Fe4S clusters, 2 phylloquinones, and 4 lipids. The PSaA and PsaB subunits in the center of the monomer are the most important as they bind the RC Chls and cofactors along with the majority of the antenna pigments. The reaction center of PS I consists of six Chls (P700 special pair Chls, two A Chls, and two A_0 Chls), two phylloquinones (two A_1), and three iron sulfur (4Fe4S) centers, F_X, F_A, and F_B.

These cofactors are arranged in two symmetrical branches, like the bacterial RC, with pseudo-C2 symmetry. The P700 special pair are located most luminally compared to the other cofactors and are strongly coupled, like the bacterial RC, and form the primary electron donor P700* when optically excited. In fact, the P700 special pair is ~ 1-2 Å closer together than the bacterial special pair (6.3 Å vs. 7.5 Å); however, the coupling in P700 is not as strong due to less favorable orientation of the Chl transition dipole moments. The two symmetrical branches are labeled A and B, and contain the other A, A_0, and A_1 cofactors. The symmetry is then broken by the F_X iron sulfur center, which is located between the two branches. The $F_{A,B}$ clusters, which are not bound by PsaA or PsaB but rather PsaC, are located behind the F_X cluster. Fig. 8 shows the

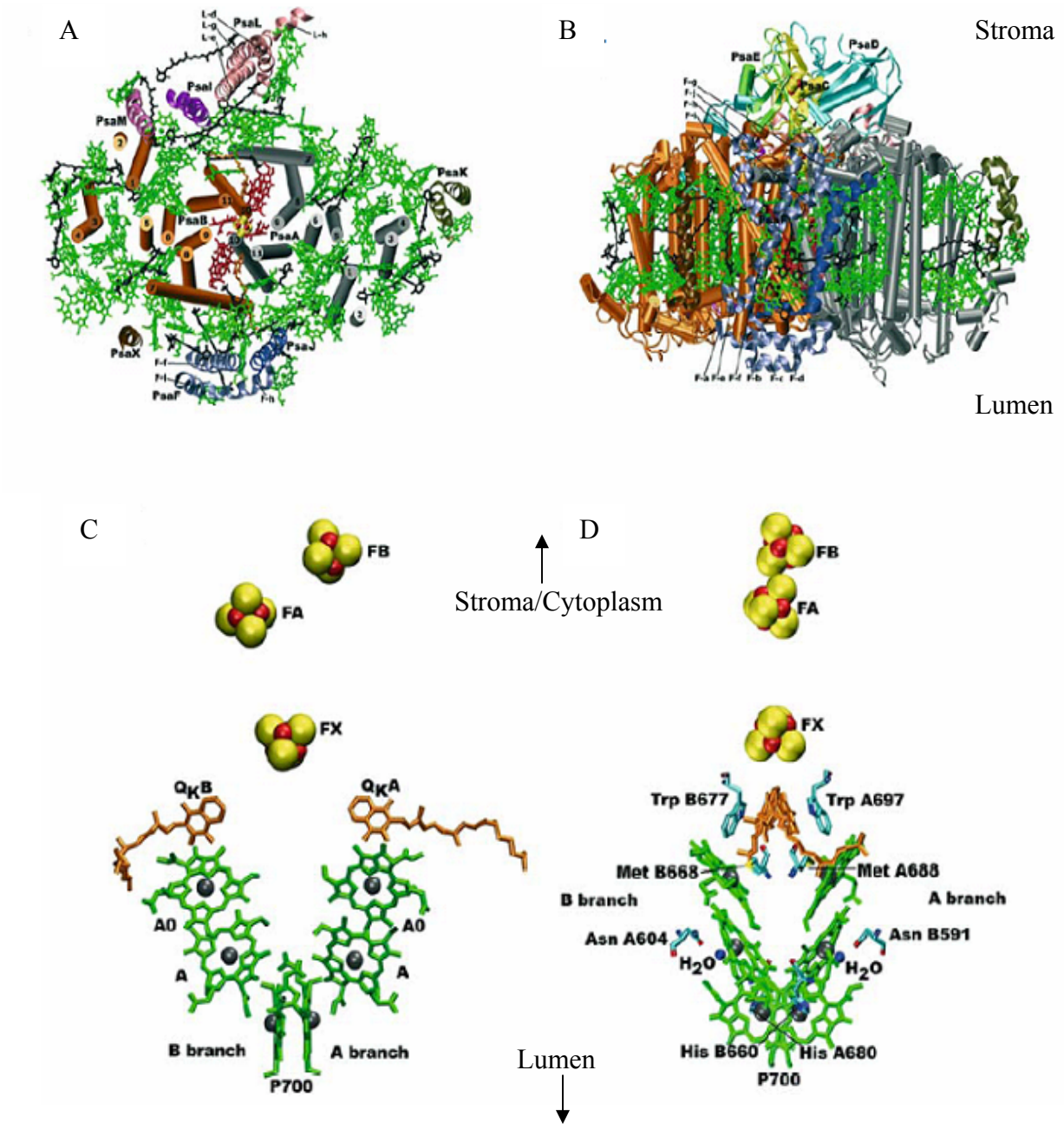

Figure 8. PS I X-ray structure at 3.0 Å resolution from Fromme et al. [91]. Frames (A) and (B) show the trimeric PS II structure which coordinates ~ 296 Chl molecules, from both (A) top (stromal) and (B) side (stromal-lumen) views. Frames (C) and (D) show the PS I RC structure from alternate angle views. P700 labels the primary electron donor Chls, A and A_0 labels the other Chls in the electron transfer chain and Q_K labels the quinone or A_1 cofactors. F_X, F_A, F_B are the iron-sulfur cofactors in the electron transfer chain that are responsible for creating a stable charge separated state.

the arrangement of various cofactors in the PS I reaction center.

The 90 antenna Chls surround the RC in each monomer in order to maximize the cross-sectional area available for light absorption. Except for two Chls, the minimum distance from any of the antenna Chls to the RC cofactors is ~ 20 Å. These two other Chls are ~ 14 Å from the RC cofactors and have been referred to as "linker" Chls, since it has been suggested that they function as 'connectors' for energy transport between the antenna and RC pigments [78, 79]. While cyanobacteria lack the LHCI complex present in PS I of green plants, there is high sequence homology between bacterial and plant PS I along with similar spectroscopic properties [80]. This indicates significant structural correlation between the two complexes. As a result, cyanobacterial PS I is often used as a structural model for plant PS I.

In cyanobacterial PS I, there is some discrepancy about the initial charge separation kinetics resulting from excitation of P700. For example, in references [81-83] it has been proposed that initial charge separation occurs in ~ 1 ps after P700 excitation; however, other researchers suggest that there is an additional slower phase of 6-10 ps due to energy equilibration among the RC cofactors [84, 85]. In primary charge separation, the A_0 Chl is thought to be the first electron acceptor that can be resolved spectroscopically, forming the $P700^+ A_0^-$ radical pair. The transfer times for the subsequent electron transfer reactions are more agreed upon, with the $P700^+ A_1^-$ radical pair forming in ~ 15-30 ps [82, 83, 85] and then $P700^+ Fe_X^-$ forming biphasically with time constants of ~ 25 and ~ 250 ns [86, 87]. Electron transfer is thought to be asymmetric in PS I, with transfer taking place on the A branch, as revealed recently by

experiments on PS I mutants [88]. A detailed illustration of these electron transfer steps is shown in Fig. 4.

Energy equilibration and transfer times in the antenna pigments of cyanobacterial PS I have reached a more unified agreement than the charge separation dynamics. Ultrafast spectroscopy experiments by a number of groups have indicated that these events occur on three different time scales: a ~ 400 fs component due to energy equilibration in "bulk" antenna Chls, a ~ 20-35 ps component resulting from energy transfer decay due to trapping by the RC, and a ~ 5 ps component due to energy equilibration between the bulk antenna Chls and "red" antenna Chls (antenna states that are lower in energy than the P700 primary donor state) [80, 89, 90]. The "red" states prevent a direct comparison of cyanobacterial light harvesting energy equilibration and transfer dynamics to those of green plants and algae, since the amount of the red states is species dependent. Overall, electron and energy transfer times for cyanobacterial PS I must be taken as "rule of thumb measurements" for other organisms because of the structural differences between PS I complexes.

The red antenna states in cyanobacterial PS I are thought to occur from strongly coupled Chl dimer or trimer molecules in the PS I antenna whose lowest excitonic state absorbs at longer wavelengths than P700 [16, 78]. The X-ray data indicates that there are many candidates that could be the origin of these red states, complicating their final assignments. Since the site energies for the Chl molecules cannot be precisely determined, different research groups have proposed different assignments of Chls that constitute the red antenna states [16, 78, 80, 91-93]. However, the number of red states for cyanobacteria is more agreed upon. It is generally thought that *Synechocystis* PCC

6803 and *Thermosynechococcus elongatus* possess two and three red states, respectively [78], with the most convincing evidence for these conclusions being supplied by Small and coworkers through high-resolution HB experiments [16, 94, 95]. Through coupling high pressure and electric field to HB measurements, they found that different linear-pressure shift rates, magnitude of permanent dipole moment change ($f\Delta\mu$), and electron-phonon coupling strengths for spectral holes burned between 700-725 nm identified three low energy states that absorb at 708 (C708), 715 (C715), and 719 nm (C719) in *Thermosynechococcus elongatus* [16]. In *Synechocystis* PCC 6803, Small and coworkers identified only two low energy red states that absorb at 708 (C708) and 714 nm (C714) [94, 95]. For green plants it has been suggested that there are two red states absorbing at 706 and 714 nm [94, 95]. Additionally, there is discrepancy over the function of these red state pigments. Some have argued that they increase the light absorption area of the antenna, especially for oceanic cyanobacteria where shorter wavelengths of light are filtered out [96, 97, 98]. Others suggest that they act as reservoirs which funnel energy back to the RC to decrease back-transfer to the bulk antenna pigments where radiationless decay can occur, increasing the efficiency of the light harvesting process [78] or that they help to maintain optimal energy equilibration within the antenna [98].

Currently, most research on PS I involves the determination of the exact structural nature and assignment of the red state pigments. The location of at least some of the red states had been linked to the trimerization region in *Synechocystis* PCC 6803, as mutants that lacked the PsaL and PsaM protein subunits, which are responsible for the formation of trimers, show ~ 30% less red state absorption at C708 when compared to PS I trimers [95]. Mutants that lacked the Psa F or Psa K subunits, located at the opposite side of the

trimeric domain, showed normal C708 absorption. Another study has shown that the strength of C708 and C714 absorption depends on the ratio of trimeric/monomeric PS I [99]. Thus, it is inferred that the Chl dimer or trimer responsible for the C708 state is bound to either of the core PsaA or PsaB subunits and near the interfacial region with PsaL and PsaM. Based on this and other experimental observations (see above), Small and coworkers have suggested that the two most strongly coupled dimers in the core PS I antenna, A38-A39 and B36-B37, are responsible for the C708 and C714 red state bands in *Synechocystis* PCC 6803, respectively [16, 94, 95]. In *Thermosynechococcus*, an extra trimer (B31-B32-B33) is bound that is not present in *Synechocystis* and is thought to be the origin of either the C708 or C714 state [78], with the other previously mentioned dimers being responsible for the remaining red states. While these assignments have been supported [98], other groups have suggested different Chl dimers as the origin of the red states [91-93]; therefore, these structural assignments must be considered preliminary and tentative at the present time.

1.2.2.c Photosystem II Reaction Center

The other reaction center in oxygenic photosynthesis is the photosystem II RC. Photosystem II is unique in that it is the only RC with a high enough redox potential (~ 1.1-1.7 mV) to oxidize water, which results in O_2 as a by-product [18]. This functional ability has allowed oxygenic photosynthetic organisms to create the oxidizing atmosphere of our current global ecosystem. The structure of PS II is interesting in that it shows high homology to the bacterial RC (e.g. *Rb. Sphaeroides*) [65, 100-105]. Like the bacterial RC, primary charge separation in PS II occurs between a Chl primary donor (P680 in PS II) and a pheophytin acceptor (Pheo). After primary charge separation, the electron is

A

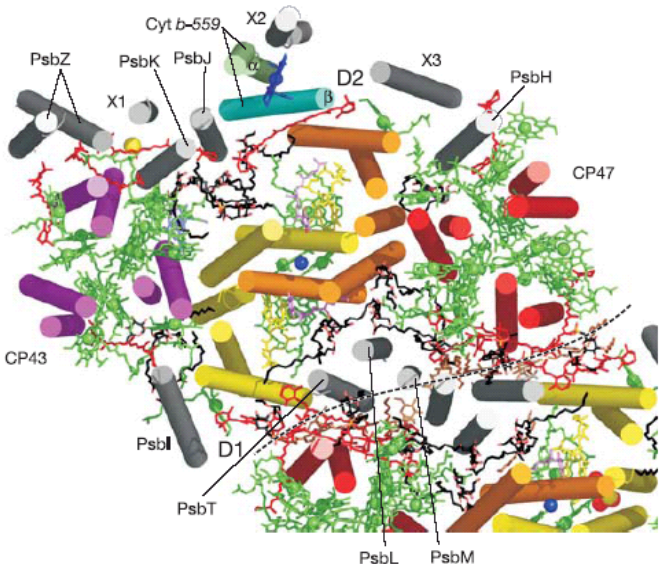

B

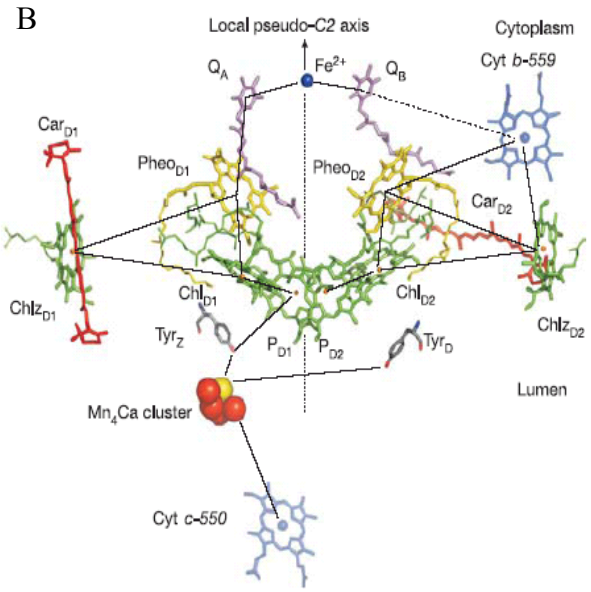

C

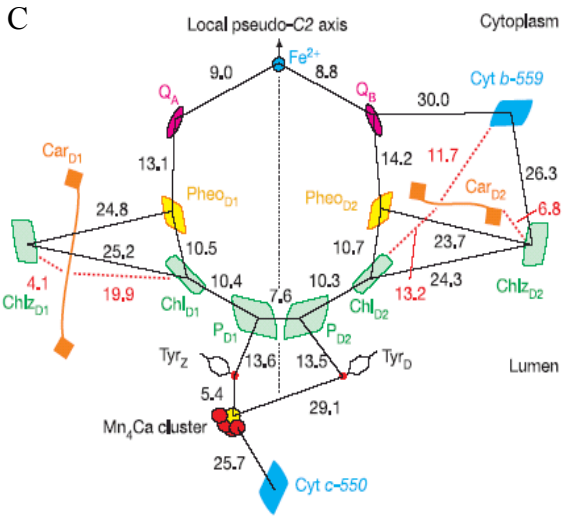

Figure 9. PS II X-ray structure at 2.5 Å resolution from Zouni et al. [108]. In (A), the PS II monomer from the cytoplasmic side is shown. The D_1, D_2 proteins are respectively colored yellow and orange, the CP43 and CP47 antenna complexes are purple and red, while a and b of cyt b_{559} are colored green and cyan. In (B), the structure and orientation of the RC cofactors is shown, while in (C) the respective distances (in Å) between the cofactors are shown. P_{D1}, P_{D2} are the P_1, P_2 Chls which are analogous the bacterial special pair (P_A, P_B) Chls. The labeling convention for the other cofactors follows correspondingly.

transferred to quinone acceptors, Q_A and Q_B (plastoquinone in PS II). The redox potentials of these reducing cofactors are very similar to those of the bacterial RC [106]. The shape of the PS II RC is also analogous. Specifically, P_1, P_2 in PS II are counterparts to the bacterial special pair, Chl_1, Chl_2 are accessory Chl counterparts to the bacterial B_1, B_2 molecules, and $Pheo_1$, $Pheo_2$ are pheophytin counterparts to the BPh_A. BPh_B molecules. However, there are also two additional Chls on the periphery of the PS II RC, designated Chl_{Z1} and Chl_{Z2}. These "linker" Chls are essentially decoupled from the RC (with ~ 25 Å distance to the nearest RC pigment). The function of these linker Chls is as of yet unknown, but it has been suggested they may play a photoprotective role for the PS II RC [107]. Recently, Zouni et al. have determined the X-ray structure of PS II at a resolution of 2.5 Å [108], which allows for almost complete resolution of all the cofactors (see Fig. 9).

Conversely, the PS II RC has some very different physical properties compared to the bacterial RC, due to its aforementioned functional purpose. Unlike the bacterial RC, in which the RC Q_y pigment transitions absorb over ~ 2,500 cm^{-1}, the PS II RC Q_y spectrum spans only ~ 600 cm^{-1}. Also, the bacterial special pair is a strongly coupled dimer where the upper and lower excitonic levels are split by ~ 1350 cm^{-1} at 4K. The strongest coupling in the PS II RC is between $P_1$and P_2 and is much weaker ($\geq$ 300 cm^{-1} at ~ 4K), even though the Mg-Mg center-center distance is comparable to the bacterial special pair at ~ 7.6-8.2 Å, due to the unfavorable orientation of the Chl dipole planes [47, 108]. Thus, P870* (lowest excitonic level of the dimer) is highly localized on the special pair Chls, while in P680* this cannot be assumed. It is plausible then to think of the primary donor state as being delocalized over the RC chlorin pigments. In light of

this, Durrant et al. [109] have proposed a "multimer" model for energy and electron transfer within the PS II RC. In this model, the RC pigments (P_1, P_2, Chl_1, Chl_2, $Pheo_1$, $Pheo_2$) are excitonically coupled in the dipole-dipole approximation; however, the inhomogeneous broadening of the individual Q_y states is comparable (~ 210 cm^{-1}) to these couplings, due to intrinsic structural disorder. This results in P680* being heterogeneous and not well defined. The multimer model predicts a similar intensity distribution of the Q_y states when compared to experimental spectra, with the two lowest states absorbing between 680-684 nm and the other states between 665-676 nm. However, there are some flaws with the multimer model. For example, the multimer model predicts that the reduction or oxidation of any cofactor should result in strong bleaching in the 680-684 nm region, due to the fact that there is significant contribution from all the cofactors to the lowest state [110].

Jankowiak et al. found, though, that in experiments on PS II RC-5 samples (see below) reduced by sodium dithionite, no prominent bleach at ~ 680 nm was seen. Instead, there was a resulting decrease in absorption at 668 nm, which was assigned to a Q_y state localized on $Pheo_2$ [111]. This reduction step was confirmed to be selective for $Pheo_2$ based on an additional $Pheo_2$ Q_x bleach (at ~ 544 nm) from the dithionite exposure [112] and that $Pheo_1$ can only be reduced by white light illumination and dithionite exposure [113]. In fact, reduction with dithonite and white light illumination by Jankowiak et al. on RC-5 samples showed a prominent bleach at ~ 680 nm, indicating that $Pheo_1$ is excitonically coupled to the other RC cofactors [112]. Jankowiak concluded then that $Pheo_2$ was excitonically decoupled from the other RC cofactors through dielectric screening caused by the local surrounding protein environment (e.g. an acidic

environment or π-π stacking forces which tautomerize the $Pheo_2$ macrocyle, thereby reducing excitonic coupling to the other cofactors). Therefore, a "pentamer" model was proposed where $Pheo_2$ is excitonically decoupled from the other five RC cofactors [110]. Like the multimer model, the excitonic couplings in the pentamer model were assumed to be in the dipole-dipole approximation. Random disorder of the cofactor transition energies, resulting from the PS II structural heterogeneity, was accounted for in the pentamer model by Monte Carlo simulations where the transition energies of the cofactors are convolved against a Gaussian site distribution function with a width of 210 cm^{-1}. As a result, the site distribution energy functions (SDFs) of the cofactors are uncorrelated in the pentamer model. This is an important feature as spectral hole-burning studies have shown that the SDFs of Qy states are uncorrelated in several photosynthetic complexes. [23]

The pentamer model developed by Jankowiak et al. correctly predicts the low energy features of the PS II RC Q_y absorption spectrum (i.e. the lowest exciton state is the most strongly absorbing and located at ~ 680 nm). Like the multimer model, the pentamer model predicts that the composition of the lowest exciton state is heterogeneous due to intrinsic structural heterogeneity of the protein environment, with delocalization over both the D_1/D_2 branches. However, the pentamer model provides some unique insights into the nature of P680* over the multimer model. Simulations of experimental triplet bottleneck hole burned spectra of RC-5 using the pentamer model by Jankowiak and coworkers showed that best fits were obtained when the triplet ($P680^{+}Pheo_1^{-} \rightarrow P680^{*3}Pheo_1$) from charge recombination was localized on Chl_1, not P_1, P_2. This is important as recent work by van Grondelle et al. have proposed, through

ultrafast vibrational spectroscopy experiments, that the triplet state is localized on Chl_1 [114]. They also argue that the since the triplet state is localized on Chl_1, it is most likely the primary donor state (P680*). However, they do not recognize the prediction of this phenomenon by the pentamer model, which also predicts that even though the triplet is localized on Chl_1, the primary donor composition is still heterogeneous and not localized on any particular cofactor.

The delocalization of the primary donor state predicted by the pentamer and multimer models has very important implications regarding the primary charge separation kinetics of PS II. Numerous groups have reported conflicting primary charge separation rates for both room temperature, (i.e. (0.4 ps^{-1}) [113, 1115], (3 ps^{-1}) [116-118], (8 ps^{-1}) [119], (21 ps^{-1}) [120]), and low temperature, (i.e. (~ 2-5 ps^{-1}) [121-126]), experiments. In addition, Prokhorenko and Holzwarth have reported low temperature (1.3 K) photon echo experiments in which theoretical modeling of the experimental spectra imply that the primary charge separation kinetics are highly dispersive (~ 2 ps-2 ns) and not single exponential [127]. Recently, HB experiments and theoretical simulations published by our group (see Chapter 4) have given further support to the heterogeneous nature of P680* suggested by the multimer and pentamer models. This heterogeneity manifests as highly dispersive primary charge separation kinetics where the primary donor state has the highest probability of being localized on either the P_1, P_2, or Chl_1 pigments but with significant contribution from all other coupled RC pigment cofactors.

After charge separation, the primary radical pair ($P680^+ Pheo_1^-$) is formed, where $Pheo_1$ is assumed to be the electron acceptor due to its stronger coupling to the other RC pigments compared to $Pheo_2$ [110] and by analogy with the bacterial RC. Then the

electron is transferred to Q_A in 300-500 ps and then to Q_B in 200 μs [2]. During this process the oxygen-evolving complex (OEC) reduces $P680^+$. The overall reaction of this process is given by the following equation: $2H_2O \rightarrow O_2 + 4H^+ + 4e^-$ [2]. From this it can be seen that this is a four-electron process while the process of charge separation in the RC is a one-electron process. Therefore, the OEC has evolved the *S-state mechanism* that consists of five states, S_0 through S_4, which represent consecutively higher oxidative states of the OEC. Only when the OEC reaches S_4 does oxygen evolution occur. This mechanism is significant because it allows the synchronization of one or many RCs per OEC. It has been shown that the S states represent the different oxidative forms of the four Mn atom cluster bound by the OEC [128, 129]. Still, the S-state mechanism is not completely understood and several pathways have been proposed though as to how the OEC exactly oxidizes water. For a more detailed review of the physics and chemistry of this important process and of the OEC complex, the following references are suggested [2, 128].

Unlike the PS I RC, the P SII RC can be prepared in different forms since the D_1, D_2 proteins only bind the RC cofactors and not any antenna pigment complexes. The PS II RC can be prepared for study in "isolated" form, where the PS II RC complex is purified with just the D_1, D_2, cytochrome b_{559}, PsbI, and PsbW proteins. However, these preparations lack quinones for secondary electron transfer and the ability to evolve oxygen. "Core" PS II complexes (see Section 1.2.1) and "supercore" PS II complexes (with the peripheral LHCII and CP29/26 antenna proteins along with the core CP43/47 antenna proteins included) can be also be prepared [130]. In "supercore" PS II complexes, oxygen-evolving capabilities are maintained [130]. All these purification

methods have several protocols and have shown varying levels of purity [130, 131]. In "isolated" PS II RC complexes, some preparations lack one peripheral Chl (RC-5) while other preparations provide the intact RC with all six Chls (RC-6) [119, 132]. In isolated RC-5 preparations, there is a pronounced shoulder at 684 nm that absorbs lower than the main absorption band at 680 nm. The nature of this 684 state has been debated extensively [133]. The most current interpretations suggest that the 684 nm state is the lowest energy state of the primary donor (P684) that originates from intact RC complexes, with the P680 state being the lowest energy state of that originates from the primary donor (P680) of perturbed RC complexes. Therefore, it was concluded that it is the intrinsic structural heterogeneity of these PS II RC complexes that results in the formation of P684 (see Chapter 4). Supercore RC complexes have shown interesting spectroscopic properties when compared to isolated RC complexes. Krausz et al have reported that P680 is red shifted in supercore complexes, as illumination at 685-700 nm results in efficient charge separation. They also report that deep spectral holes with lifetimes of 40-300 ps can be burned in the P680 band at low temperatures (~ 4 K). They explain this phenomenon as a result of "slow" energy transfer from the core CP43/CP47 antenna complexes to the RC. This slow energy transfer mechanism is supported by their experiments on "core" PS II samples in which time-resolved and transient absorption multiexponential decay times at room temperature are ~ 2x longer in CP47-RC "core" complexes versus isolated RC complexes [44-46].

Currently, the exact nature of charge separation and energy transfer in the PS II RC still eludes researchers. A higher resolution (< 2.5 Å) X-ray structure for PS II is clearly needed for certain assignment of pigment distances and positions. However,

promising developments in this area [108] along with high-resolution experimental methods such as single molecule spectroscopy (see Chapter 6) may help to provide a clearer understanding of this important photosynthetic complex.

1.3 Thesis Organization

In this dissertation, the early photophysical and photochemical events - light harvesting energy transfer and initial charge separation in oxygenic reaction centers - are studied. Following the introduction to photosynthesis and background of studied photosynthetic pigment-protein complexes given in Chapter 1, Chapter 2 gives a brief but detailed overview of the developed theories used to model energy transfer and primary electron transfer processes in these photosynthetic complexes. The processes include Förster and Dexter theories of energy transfer, molecular excitonic interactions in photosynthetic complexes, and energy transfer via exciton-phonon scattering. Chapter 3 provides an overview of hole-burning and single-molecule spectroscopy; moreover, high resolution experimental spectroscopic techniques used to study the EET and electron transfer events in various photosynthetic complexes are described. Chapters 4 to 6 are published research papers. In Chapter 4, hole-burning spectroscopy coupled with electric field and high-pressure was used to investigate the lowest energy donor state (P680) of the PS II RC of green plants. Theoretical modeling of HB experiments, along with excitonic calculations of energy transfer in the PS II RC, was also performed to help characterize these hole-burning experiments. In Chapter 5, hole-burning spectroscopy and theoretical calculations were used to investigate the energy transfer properties of PS I-CP43′ supercomplexes of cyanobacteria that form under iron-stress conditions. These experiments specifically probe the connectivity in EET between the CP43′ antenna

complex and PS I. In Chapter 6, bulk hole-burning spectroscopy experiments and single-molecule spectroscopy experiments of on single PS I complexes were performed to characterize the connectivity of energy transfer between different pools of red state antenna pigments in *Synechocystis* PCC 6803 and *Thermosynechococcus elongatus*. Lastly, Chapter 7 provides a short introduction of current and future research on PCs that is impacting the developing field of molecular electronics, while Chapter 8 presents preliminary data for using trimeric photosynthetic PS I RC complexes as a basis for the nanoscale molecular electronic architecture for these types of devices. As stated before, photosynthetic pigment-protein complexes serve as an ideal model for photovoltaic cells, which will be needed in the 21st century due to exhaustion of traditional fossil fuel sources. Considering that the earth receives about 5.2 x 10^{21} kJ/year [10] of solar energy, the development of higher efficiency photovoltaics would have an enormous impact for renewable energy technology.

References

1. Lawlor, D.W., *Photosynthesis: Metabolism, Control, and Physiology*; Longman Scientific & Technical: Essex, England; 1987.
2. Blankenship, R. *Molecular Mechanisms of Photosynthesis*; Blackwell Science: Oxford, England, 2002.
3. Kamen, M.D., *Primary Processes in Photosynthesis*; Academic Press: New York, 1963.
4. Govindjee, In *Bioenergetics of Photosynthesis*, Govindjee, Ed.; Academic Press: New York, 1975; p. 1.
5. Danks, S.M., Evans, E.H., Whittaker, P.A., *Photosynthetic Systems: Structure, Function, and Assembly*; John Wiley and Sons: New York, 1983.
6. Campbell, N.A. and Reece, J.B., *Biology*, 6th Ed; Benjamin Cummings: California, 2001.
7. Mauseth, J.D*., Botany: an introduction to plant biology*, 2nd ed.; Jones and Bartlett: Sudbury, Massachusetts, 1995.
8. Hall, D.O. and Rao, K.K., *Photosynthesis*, 6th ed.; Cambridge University: Cambridge, England, 1999.
9. Nunzi, J.-M., In *Photovoltaic and Photoactive Materials – Properties, Technology, and Applications*, Marshall, J.M. and Dimova-Malinovska, D., Eds.; Kluwer Academic: Dordrecht, The Netherlands, 2002; p. 197.
10. Green, M.A., *Third Generation Photovoltaics*; Springer-Verlag: Berlin, Heidelberg, New York, 2003.

11. Kodis, G., Liddell, P. A., de la Garza, L., Clausen, P. C., Lindsey, J. S., Moore, A. L., Moore, T. A.; Gust, D., *J. Phys. Chem. A.* **2002**, 106, p. 2036.

12. Gust, D., Moore, T. A., Moore, A. L., Kennis, J. T. M., *J. Phys. Chem. B.* **2004**, 108, p. 414.

13. Lee, J. W. Lee, E. Greenbaum, *Phys. Rev. Lett.* **1999**, 79, p**.** 3294.

14. R. Das, P. J. Kiley, M. Segal, J. Norville, A. A. Yu, L. Wang, S. A. Trammell, L. E. Reddick, R. Kumar, F. Stellacci, N. Lebedev, J. Schnur, B. D. Bruce, S. Zhang, M. Baldo, *Nano Lett*. **2004**, 4, p. 1079.

15. Mauzerall, D., Greenbaum, N.L., *Biochim. Biophys. Acta* **1989**, 974, p. 119.

16. Reinot, T., Zazubovich, W., Hayes, J. M. and Small, G. J. *J. Phys. Chem. B* **2001**, 105, p. 5083.

17. Gobets, B., van Grondelle, R., *Biochim. Biophys. Acta*, **2001**, 1507, p 80.

18. Barber, J., Archer, M.D., *J. Photochem. Photobiol. A* **2001**, 142, p. 97.

19. Sundstrom, V., Pullertis, T., van Grondelle, R., *J. Phys. Chem. B* **1999**, 103, p. 2327.

20. Wu, H.-M., Rätsep, M., Jankowiak, R., Codgell, R.J., Small, G.J., *J. Phys. Chem. B* **1997**, 101, p. 7641.

21. Jankowiak, R., Zazubovich, V., Ratsep, M., Matsuzaki, S., Alfonso, M., Picorel, R., Seibert, M., Small, G.J., *J. Phys. Chem. B* **2000**, 104, p. 11805.

22. Camara-Artigas, A., Blankenship, R.E., Allen, J. P., *Photosynth. Res.* **2003**, 75, p. 49.

23. Matsuzaki, S., Zazubovich, V., Rätsep, M., Hayes, J.M., Small, G.J., *J. Phys. Chem. B* **2000**, 104, p. 9564.

24. Prokhorenko, V.I., Holzwarth, A.R., Nowak, F.R., Aartsma, T.J., *J. Phys. Chem. B* **2002**, 106, p. 9923.

25. Wendling, M., Przyjalgowski, M. A., Gulen, D., Vulto, S. I. E., Aartsma, T. J., van Grondelle, R., van Amerongen, H., *Photosynth. Res.* **2002**, 71, p. 99.

26. Brixner, T., Stenger, J., Vaswani, H. M., Cho, M., Blankenship, R. E., Fleming, G. R., *Nature* **2005**, 434, p. 625.

27. McDermott, G., Prince, S.M., Freer, A.A., Hawthornthwaite-Lawless, A.M., Papiz, M.Z., Cogdell, R.J., Isaacs, N.W., *Nature* **1995**, 374, p. 517.

28. Koepke, J., Hu, X., Muenke, C., Schulten, K., Michel, H., *Structure* **1996**, 4, p. 581.

29. Karrasch, S., Bullough, P.A., Ghosh, R., *EMBO J.* **1995**, 14, p. 631.

30. Walz, T,, Jamieson, S.J., Bowers, C.M., Bullough, P.A., Hunter, C.N., *J. Mol. Biol*. **1998**, 282, p. 833.

31. Ketelaars, M., van Oijen, A.M., Matsushita, M., Kohler, J., Schmidt, J., Aartsma, T.J., *Biophys. J.* **2001**, 80, p. 1591.

32. Ketelaars, M., van Oijen, A.M., Matsushita, M., Kohler, J., Schmidt, J., Aartsma, T.J., *Biophys. J.* **2001**, 80, p. 1604.

33. Kühlbrandt, W., Wang, D.N., Fujuyoshi, Y., *Nature* **1994**, 367, p. 614.

34. van Amerongen, H. and van Grondelle, R., *J. Phys. Chem. B* **2001**, 105, p. 604.

35. Liu, Z., Yan, H.W.K., Kuang, T., Zhang, J., Gui, L., An, X., Chang, W., *Nature* **2004**, 428, p. 287.

36. Barzda, V., Gulbinas, V., Kananavicius, R., van Amerongen, H., van Grondelle, R., Valkunas, L., *Biophys. J.* **2001**, 80, p. 2409.

37. Pieper, J., Irrgang, K.-D., Rätsep, M., Jankowiak, R., Schroetter, Th., Voigt, J., Small, G.J., Renger, G., *J. Phys. Chem. A* **1999**, 103, p. 2422.

38. Green, B.R., Durnford, D.G., *Ann. Rev. Plant Physiol. Mol. Biol.* **1996**, 47, p. 685.

39. Durnford, D.G., Deane, J.A., Tan, S., McFadden, G.I., Gantt, E., Green, B.R., *J. Mol. Evol.* **1999**, 48, p. 59.

40. Melkozernov, A.N., Schmid, V.H.R., Schmidt, G.W., Blankenship. R.E., *J. Phys. Chem. B* **1998**, 102, p. 8183.

41. Melkozernov, A.N., Schmid, V.H.R., Lin, S., Paulsen, H., Blankenship, R.E., *J. Phys. Chem. B* **2002**, 106, p. 4313.

42. Novoderexhkin, V., Salverda, J.M., van Amerongen, H., van Grondelle, R., *J. Phys. Chem. B* **2003**, 107, p. 1893.

43. Linnanto, J., Martiskainen, J., Lehtovuori, V., Ihalainen, J., Kananavicius, R., Barbato, R., Korppi-Tommola, J., *Photosynth. Res.* **2006**, 87, p. 267.

44. Krausz, E., Hughes, J. L., Smith, P., Pace, R., Peterson Arskoeld, S., *Photochem. Photobiol. Sci.* **2005**, 4, p. 744.

45. Hughes, J. L., Prince, B. J., Krausz, E., Smith, P. J., Pace, R. J., Riesen, H., *J. Phys. Chem. B* **2004**, 108, p. 10428.

46. Smith, P. J., Peterson, S., Masters, V. M., Wydrzynski, T., Styring, S., Krausz, E.; Pace, R.J., *Biochemistry* **2002**, 41, p. 1981.

47. Ferreira, K.N., Iverson, T.M., Maghlaoui, K., Barber, J., Iwata, S., *Science* **2004**, 303, p. 1831.

48. Jankowiak, R., Zazubovich, V., Ratsep, M., Matsuzaki, S., Alfonso, M., Picorel, R., Seibert, M., Small, G.J., *J. Phys. Chem. B* **2000**, 104, p. 11805.

49. Bricker, T.M., *Photosynth. Res*. **1990**, 24, p. 1.

50. Rhee, K.-H., Morris, E.P., Zheleva, D., Hankamer, B., Kuhlbrandt, W., Barber, J., *Nature* **1997**, 389, p. 522.

51. Zheleva, D., Sharma, J., Panico, M., Morris, H.R., Barber, J., *J. Biol. Chem.* **1998**, 273, p. 16122.

52. Groot, M.-L., Frese, R.N., Weerd, F.L., Bromek, K., Petterson, A., Peterman, E.J.G., van Stokkum, I.H.M., van Grondelle, R., Dekker, J.P., *Biophys J.* **1999**, 77, p. 3328.

53. Chang, H.-C., Jankowiak, R., Yocum, C.F., Picorel, R., Alfonso, M., Seibert, M., Small, G.J., *J. Phys. Chem. B* **1994**, 98, p. 7717.

54. Chang, H.-C., Jankowiak, R., Yocum, C.F., Picorel, R., Alfonso, M., Seibert, M., Small, G.J., *J. Phys. Chem. B* **1994**, 98, p. 7725.

55. Miloslavina, Y., Szczepaniak, M., Mueller, M.G., Sanger, J., Nowaczyk, M., Roegner, M., Holzwarth, A.R., *Biochemistry* **2006**, 45, p. 2436.

56. Andrizhiyevskaya, E.G., Schwabe, T.M.E., Germano, M., D'Haene, S., Kruip, J., van Grondelle, R., Dekker, J.P., *Biochim. Biophys. Acta* **2002**, 1556, p. 265.

57. Myers, J., *Photosynth. Res.* **1994**, 40, p. 303.

58. Emerson, R. and Arnold, W., *J. Gen. Physiol.* **1932**, 15, p. 391.

59. Emerson, R., and Arnold, W., *J. Gen. Physiol.* **1932**, 16, p. 191.

60. Gaffron, H. and Wohl, K., *Naturwissenschaften* **1936**, 24, p. 81.

61. Govindjee and Knox, R.S., *Photosynth. Res*. **1996**, 48, p. 1.

62. Wild, A., and Ball, R., *Photosynthetic Unit and Photosystems: History of Research and Current View (Relationship of Structure and Function)*; Backhuys: Leiden, The Netherlands, 1997.

63. Michel, H., *J. Mol. Biol.* **1982**, 158, p. 167.

64. Deisenhofer, J., Epp, O., Miki, K., Huber, R., Michel, H., *J. Mol. Biol.* **1984**, 180, p. 385.

65. Deisenhofer, J., Epp, O., Miki, K., Huber, R., Michel, H., *Nature* **1985**, 318, p. 618-624.

66. Allen, J.P., Feher, G., Yeates, T.O., Rees, D.C., Deisenhofer, J., Michel, H., Huber, R., *Proc. Natl. Acad. Sci.* **1986**, 83, p. 8589.

67. Chang, C.H., Tiede, D.M., Tang. J., Smith, U., Norris, J., Schiffer, M., *FEBS Lett.* **1986**, 205, p. 82.

68. Camara-Artigas, A., Brune, D., Allen, J.P., *Proc. Natl. Acad. Sci.* **2002**, 99, p. 11055.

69. Feher, G., *Photosynth. Res.* **1998**, 61, p. 1.

70. Johnson, S.G., Tang, D., Jankowiak, R., Hayes, J.M., Small, G.J., *J. Phys. Chem.* **1989**, 93, p. 5953.

71. Haffa, A.L.M., Lin. S., Katilius, E., Williams, J.C., Taguchi, A.K.W., Allen, J.P., Woodbury, N.W., *J. Phys. Chem. B* **2002**, 106, p. 7376.

72. Kirmaier, C., Holten, D., Parson, W.W., *Biochim. Biophys. Acta* **1985**, 810, p. 49.

73. Kirmaier, C., Holten, D., Parson, W.W., *Biochim. Biophys. Acta* **1985**, 810, p. 33.

74. Martin, J.-L., Breton, J., Hoff, A.J., Migus, A., Antonetti, A., *Proc. Natl. Acad. Sci.* **1986**, 83, p. 957.

75. Woodbury, N.W., Becker, M., Middendorf, D., Parson, W.W., *Biochemistry* **1985**, 24, p. 7516.

76. Tang, D., Jankowiak, R., Small, G. J., Tiede, D. M., *Chem. Phys.* **1989**, 131, p. 99.

77. Reddy, N.R.S., Lyle, P.A., Small, G.J., *Photosynthesis Research* **1992**, 31, p. 167.

78. Jordan, P., Fromme, P., Witt, H.T., Klukas, O., Saenger, W., Krauss. N., *Nature* **2001**, 411, p. 909.

79. Schubert, W.-D., Klukas, O., Krauss, N., Saenger, W., Fromme, P., Witt, H.T., *J. Mol. Biol.* **1997**, 272, p. 741.

80. Ihalainen, J.A., Rätsep, M., Jensen, P.E., Scheller, H.V., Croce, R., Bassi, R., Korppi-Tommola, J.E.I., Freiberg, A., *J. Phys. Chem. B* **2003**, 107, p. 9086.

81. Gobets, B. and van Grondelle, R., *Biochim. Biophys. Acta.* **2001**, 1507, p. 80.

82. Gobets, B., van Stokkum, H.M., Rogner, M., Kruip, J., Schlodder, E., Karapetyan, N.V., Dekker, J.P., van Grondelle, R., *Biophys. J.* **2001**, 81, p. 407.

83. Savikhin, S., Xu, W., Martinsson, P., Chitnis, P.R., Struve, W.S., *Biochemistry* **2001**, 40, p. 9282.

84. Kumazaki, S., Ikegami, I, Furusawa, H., Yasuda, S., Yoshihara, K., *J. Phys. Chem. B* **2003**, 107, p. 3228.

85. Muller, M., Niklas, J., Lubitz, W., Holzwarth, A.R., *Biophys. J.* **2003**, 85, p. 3899.

86. Setif, P. and Brettel, K., *Biochemistry* **1993**, 32, p. 7846.

87. Joliot, P. and Joliot, A., *Biochemistry* **1999**, 38, p. 11130.

88. Xu, W., Chitnis, P.R., Valieva, A., van der Est, A., Brettel, K, Guergova-Kuras, M., Pushkar, Y.N., Zech, S.G., Stehlik, D., Shen, G., Zybailov, B., Golbeck, J.H., *J. Biol. Chem.* **2003**, 278, p. 27876.

89. Gibasiewicz, K., Ramesh, V.M., Lin, S., Woodbury, N.W., Webber, A.N., *J. Phys. Chem. B* **2002**, 106, p. 6322.

90. Gobets, B., van Stokkum, I.H.M., van Mourik, F., Dekker, J.P., van Grondelle, R., *Biophys. J.* **2003**, 85, p. 3883.

91. Damjanovic, A., Vaswani, H.M., Fromme, P., Fleming, G.R., *J. Phys. Chem. B* **2002**, 106, p. 10251.

92. Byrdin, M., Jordan, P., Krauss, N., Fromme, P., Stehlik, D., Schlodder, E., *Biophys. J.* **2002**, 83, p. 433.

93. Bruggemann, B., Sznee, K., Novoderezhkin, V., van Grondelle, R., May, V., *J. Phys. Chem. B* **2004**, 108, p. 13536.

94. Hayes, J.M., Matsuzaki, S., Rätsep, M., Small, G.J., *J. Phys. Chem. B* **2000**, 104, p. 5625.

95. Rätsep, M., Johnson, T.W., Chitnis, P.R., Small, G.J., *J. Phys. Chem. B* **2000**, 104, p. 836.

96. Trissl, H.-W., *Photosynth. Res.* **1993**, 35, p. 247.

97. Trissl, H.-W. and Wilhelm, C., *Trends Biochem. Sci.* **1993**, 18, p. 415.

98. Grotjohann, I. and Fromme, P., *Photosynth. Res.* **2005**, 85, p. 51.

99. Satoh, S. and Tanaka, A., *FEBS Lett.* **2002**, 528, p. 235.

100. Trebst, A.Z., *Naturforsch* **1985**, 41, p. 20.

101. Sayre, R.T., Anderson, B., Bogorad, L., *Cell* **1986**, 47, p. 601.

102. Ruffle, S.V., Donnelly, D., Blundell, T.L., Nugent, J.H.A., *Photosynth. Res.* **1992**, 34, p. 287.

103. Seibert, M., In *The Photosynthetic Reaction Center*, Deisenhofer, J., Norris, J., Eds.; Academic Press: San Diego, 1993; Vol**.** 1, p. 319.

104. Svensson, B., Etchebest, C., Tuffery, P., van Kan, P., Smith, J., Styring, S., *Biochemistry* **1996**, 35, p. 14486.

105. Xiong, J. Subramanian, S., Govindjee, R. *Photosynth. Res.* **1998**, 56, p. 229.

106. Barber, J., *Biochim. Biophys. Acta* **1998**, 1365, p. 269.

107. Stewart, D.H. and Brudvig, G.W., *Biochim. Biophys. Acta* **1998**, 1367, p. 63.

108. Loll, B., Kern, J., Saenger, W., Zouni, A., Biesiadka, J., *Nature* **2005**, 438, p. 1040.

109. Durrant, J.R., Klug, D.R., Kwa, S.L.S., van Grondelle, R., Porter, G., Dekker, J.P., *Proc. Natl. Acad. Sci. U.S.A.* **1995**, 92, p. 4798.

110. Jankowiak, R., Hayes, J.M., Small, G.J., *J. Phys. Chem. B* **2002**, 106, p. 8803.

111. Jankowiak, R., Ratsep, M., Picorel, R., Seibert, M., Small, G.J., *J. Phys. Chem. B* **1999**, 103, p. 9759.

112. Tang, D., Jankowiak, R., Seibert, M., Yocum, C.F., Small, G.J., *J. Phys. Chem.* **1990**, 94, p. 6519.

113. Groot, M.L., van Mourik, F., Eijckelhoff, C., van Stokkum, I.H.M., Dekker, J.P., van Grondelle, R., *Proc. Natl. Acad. Sci. U.S.A.* **1997**, 94, p. 4389.

114. Groot, M. L., Pawlowicz, N. P., van Wilderen, L. J. G. W., Breton, J.; van Stokkum, I. H. M., van Grondelle, R., *Proc. Natl. Acad. Sci. U.S.A.* **2005**, 102, p. 13087.

115. Wasielewski, M.R., Johnson, D.G., Seibert, M., Govindjee, R., *Proc. Natl. Acad. Sci. U.S.A.* **1989**, 86, p. 524.

116. Wiederrecht, G.P., Seibert, M., Govindjee, R., Wasielewski, M.R., *Proc. Natl. Acad. Sci. U.S.A.* **1994**, 91, p. 8999.

117. Schelvis, J.P.M., van Noort, P.I., Aartsma, T.J., van Gorkom, H.J., *Biochim. Biophys. Acta* **1994**, 1184, p. 242.

118. Gatzen, G., Müller, M.G., Griebenow, K., Holzwarth, A.R., *J. Phys. Chem.* **1996**, 100, p. 7269.

119. Greenfield, S.R., Seibert, M., Govindjee, Wasielewski, M.R., *J. Phys. Chem. B* **1997**, 101, p. 2251.

120. Merry, S.A., Kamzaki, S., Tachibana, Y., Joseph, D.M., Porter, G., Yoshohara, K., Barber, J., Durrant, J.R., Klug, D.R., *J. Phys. Chem. B* **1996**, 100, p. 10469.

121. Jankowiak, R., Tang, D., Small, G. J., Seibert, M., *J. Phys. Chem*. **1989**, 93, p. 1649.

122. Tang, D., Jankowiak, R., Seibert, M., Small, G. J., *Photosynth. Res.* **1991**, 27, p. 19.

123. Wasielewski, M. R., Johnson, D., Govindjee, Preston, C., Seibert, M., *Photosynth. Res.* **1989**, 22, p. 89.

124. Visser, H. M., Groot, M.-L., van Mourik, F., van Stokkum, I. H., Dekker, J. P., van Grondelle, R., *J. Phys. Chem.* **1995**, 99, p. 15304.

125. Greenfield, S. R., Seibert, M., Wasielewski, M. R., *J. Phys. Chem. B* **1999**, 103, p. 8364.

126. Jankowiak, R., Rätsep, M., Hayes, J. M., Zazubovich, V., Picorel, R., Seibert, M., Small, G. J., *J. Phys. Chem. B* **2003**, 107, p. 2068.

127. Prokhorenko, V. I. and Holzwarth, A. R., *J. Phys. Chem. B* **2000**, 104, p. 11563.

128. Britt, R.D., *Oxygen evolution.* In:*Oxygenic Photosynthesis: The Light Reactions*, Ort, D.R., Yocum, C.F., Eds.; Kluwer Academic: Dordrecht, The Netherlands, 1996; p. 137.

129. Yachandra, V.K., Derose, V.J., Latimer, M.J., Mukerji, I., Sauer, K., Klein, M.P., *Science* **1993**, 260, p. 675.

130. Dekker, J.P. and van Grondelle, R., *Photosynth. Res.* **2000**, 63, p. 195.

131. Eijckelhoff, C., van Roon, H., Groot, M.L., van Grondelle, R., *Biochemistry* **1996**, 35, p. 12864.

132. Vacha, F., Joseph, D.M., Durrant, J.R., Tefler, A., Klug, D.R., Porter, G., Barber, J., *Proc. Natl. Acad. Sci. U.S.A.* **1995**, 92, p. 2929.

133. Jankowiak, R., Rätsep, M., Small, G.J., Zazubovich, V., *J. Phys. Chem. B* **2004**, 108, p. 10346.

CHAPTER 2 – ENERGY TRANSFER IN PHOTOSYNTHETIC COMPLEXES

2.1 Introduction

Probably the most unique physical aspects of photosynthetic complexes (PCs) are their complex, inter-connected energy transfer processes. These arise from the special arrangements and couplings of different photosynthetic pigment molecules to account for specific events during energy collection and eventual charge separation; resulting in a wide variation of energy transfer channels, rates, and yields [1-7]. Consequently, energy transfer in PCs has been modeled through many different approximations. For example, energy transfer has been modeled as localized Förster donor - acceptor states [8] in the weakly coupled B800 dimer ring of purple bacterial LH2 [1, 2]. Energy transfer has also been modeled through exciton formation [10], as in the PS II reaction center (RC) [6, 34], and through coherent excitonic relaxation in strongly coupled antenna systems, such the Fenna-Matthews-Olsen (FMO) light harvesting antenna complex [7].

Thus, it is important to understand the physical picture of EET for photosynthetic systems, which can be described in terms of two limiting cases: weak and strong coupling between donor and acceptor molecules (states) [11, 12]. In the weak coupling limit, energy transfer can be thought of as hopping process between independent, localized states. In the strong coupling limit, the electronic states cannot be thought of as localized on individual molecules, as new intermolecular coherent eigenstates (excitonic states, see Section 2.4) are formed by virtue of strong electronic coupling, and EET is thought of as a perturbation induced relaxation process between these coherent excitonic states.

Photosynthetic pigment systems, however, usually do not lie at the extremes of these limiting cases but somewhere in-between. The ratio of the electronic coupling between donor and acceptor pigments, V, and the disorder (inhomogeneous broadening), Δ, is an important factor for deciding whether energy transfer occurs through incoherent hopping, and can be modeled with Förster and Dexter theories [8, 14] or excitonic relaxation [13]. If $V/\Delta << 1$, then it can be assumed that interactions are in the weak coupling limit and incoherent hopping energy transfer can be assumed; however, if $V/\Delta >> 1$, then strong coupling interaction is present and energy transfer can be "pictured" through excitonic relaxation [1].

2.2 Förster Energy Transfer Theory

Energy transfer between weakly coupled photosynthetic pigment molecules often can adequately be described through Förster theory [8]. In the Förster model, energy transfer is characterized as an incoherent hopping process from an emitting donor molecule to an absorbing acceptor molecule in the weak interaction limit ($V/\Delta << 1$). The energy transfer rate from this process can be calculated, in the absence of static disorder, by using a Fermi-Golden rule approximation [9]. In this approximation, for energy transfer to occur from the donor to the acceptor molecule, there must be spectral overlap between the donor fluorescence and acceptor absorption along with sufficient electrostatic coupling. This transfer rate, as determined by Förster, is given as

$$k_{DA} = \frac{2\pi}{\hbar}\left|\langle D^* A|V_{DA}|D\ A^*\rangle\right|^2 \int_0^\infty dv J(v) \qquad (2.1)$$

where $\left|\langle D^* A|V_{DA}|D\ A^*\rangle\right|^2$ is the electronic coupling between the donor molecule, D, and acceptor molecule, A. $J(v)$ is the spectral overlap between the donor emission and the

acceptor absorption, normalized to unit area on an energy scale [8]. Also, it is assumed that the electronic transition moment does not change upon molecular nuclear motions and that the thermalization of molecular vibrations and bath phonons occur on a time scale much faster than energy transfer.

In Förster theory, dipole-dipole coupling can safely be assumed when the electronic transitions of *D* and *A* are weakly coupled and the distance between them is greater than the size of the molecules, i.e. there is no wavefunction overlap [8, 15]. Usually this corresponds to a separation distance between the donor-acceptor of ~ 1-10 nm. If these requirements are met, higher order multipole terms along with antisymmetrization (electron exchange) terms can be neglected and the electronic coupling matrix element between *D* and *A*, in Eq. 2.1 is

$$\langle D^* A | V_{DA} | DA^* \rangle \equiv V_{DA} = \frac{\kappa \left| \vec{\mu}_D \right\| \vec{\mu}_A \right|}{R_{DA}{}^3} \tag{2.2}$$

where $\vec{\mu}_D$ and $\vec{\mu}_A$ are the electronic transition dipole moment vectors of *D* and *A*, respectively. V_{DA} is dependent only on the electronic wavefunctions since the Born-Oppenheimer approximation is invoked during the derivation of Eq. 2.1. R_{DA} is the distance between the center of *D* and the center of *A* in angstroms. κ is the orientation factor and is defined as: $\kappa \equiv \hat{\mu}_D \cdot \hat{\mu}_A - 3(\hat{\mu}_D \cdot \hat{\mathrm{R}}_{DA})(\hat{\mathrm{R}}_{DA} \cdot \hat{\mu}_A)$ where the circumflex symbol (^) represents the unit vector of the corresponding vector. Depending on the orientation, κ can range in value from –2 to 2 (see Fig. 1). As shown in Fig. 1, κ^2 is largest, and the transfer rate is enhanced, when $\vec{\mu}_D$ and $\vec{\mu}_A$ is in either a head-to-head or

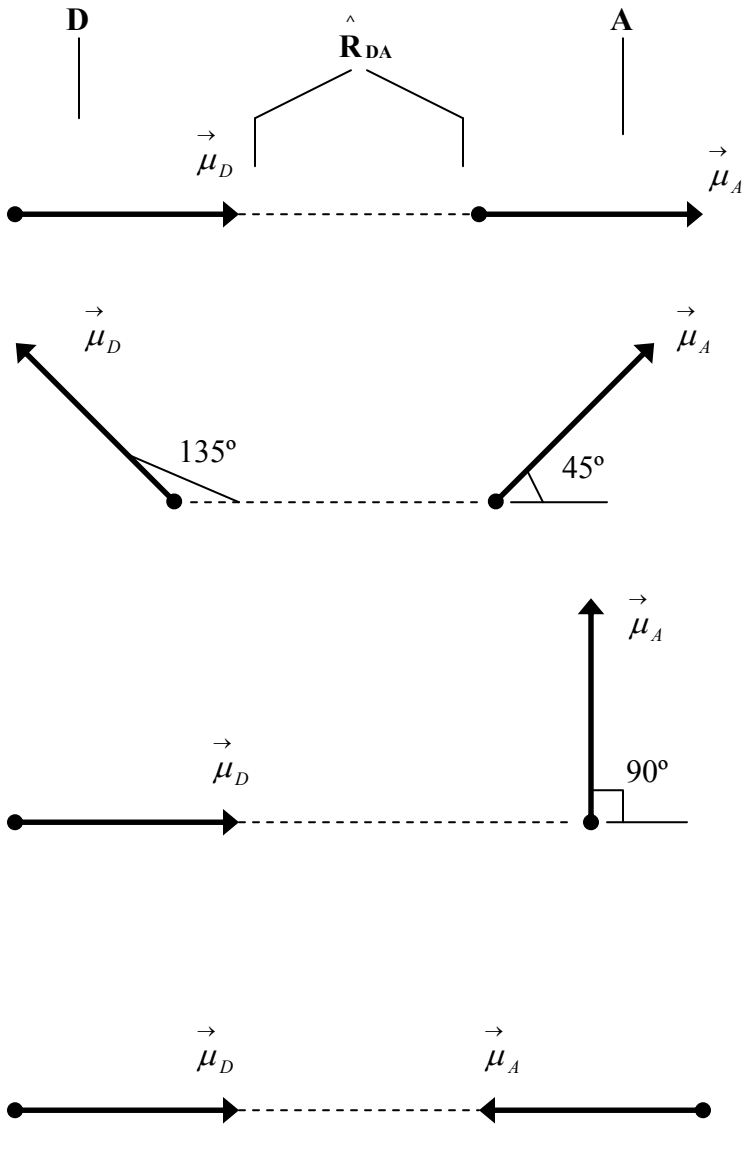

Figure 1. Examples of donor-acceptor dipole orientation factors, κ. The solid arrows represent the dipole vectors of the donor, $\vec{\mu}_D$, and acceptor, $\vec{\mu}_A$, molecules. The dashed line that connects the vectors represents the distance, $\hat{\mathbf{R}}_{DA}$, between the two molecules. It is assumed here, for simplification, that both the donor and acceptor molecules are in the same plane. However, this cannot be assumed for real molecular systems.

head-to-tail orientation. For molecules with random orientations of dipole vectors, κ = 2/3 [16].

The spectral overlap, $J(\nu)$, term in Eq. 2.1 is another result of invoking the Born-Oppenheimer approximation. In the Born-Oppenheimer approximation [17], separation of the electronic and vibrational wavefunctions is allowed as the nuclear motions of the atoms are assumed to be on a much slower timescale compared to the motions of the electrons during the optical excitation of either *D* or *A*. Therefore, the vibrational transitions of *D* and *A* are expressed in $J(\nu) = \varepsilon_A(\nu) \cdot F_D(\nu) \cdot 1/\nu^4$, where $\varepsilon(\nu)$ is the molar decadic extinction coefficient of *A* in L/(mol·cm), $F_D(\nu)$ is the normalized emission spectrum of D, and ν is the wavenumber in cm^{-1}. $\varepsilon_A(\nu)$ and $F_D(\nu)$ are expressed as

$$\varepsilon_A(\nu) = \frac{8\pi^3 N' \nu}{3hcn\ln(10)} \mu_A^2(\nu) \tag{2.3}$$

and

$$F_D(\nu) = \frac{64\pi^3 n\nu^3 \tau}{3h} \mu_D^2(\nu) \tag{2.4}$$

where N' is Avogadro's constant divided by 1000, *h* is Planck's constant, *c* is the speed of light in vacuum and units of cm^2/s, *n* is the refractive index of the solvent, and τ is the total dephasing time of *D* (for the definition of pure dephasing time, see Chapter 3, Sect 3.1). $\mu_D^2(\nu)$ and $\mu_A^2(\nu)$ are the vibronic transition dipole moments averaged over all thermal and vibrational levels, respectively. Thus, $J(\nu)$ is referred to as the Franck-Condon factor weighted density of states [16, 18] (for a more detailed description of the

A

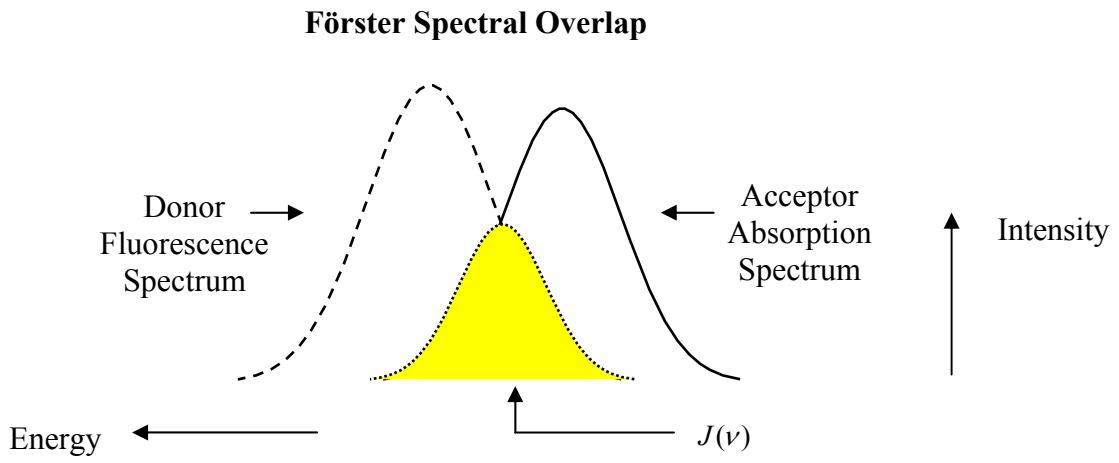

B

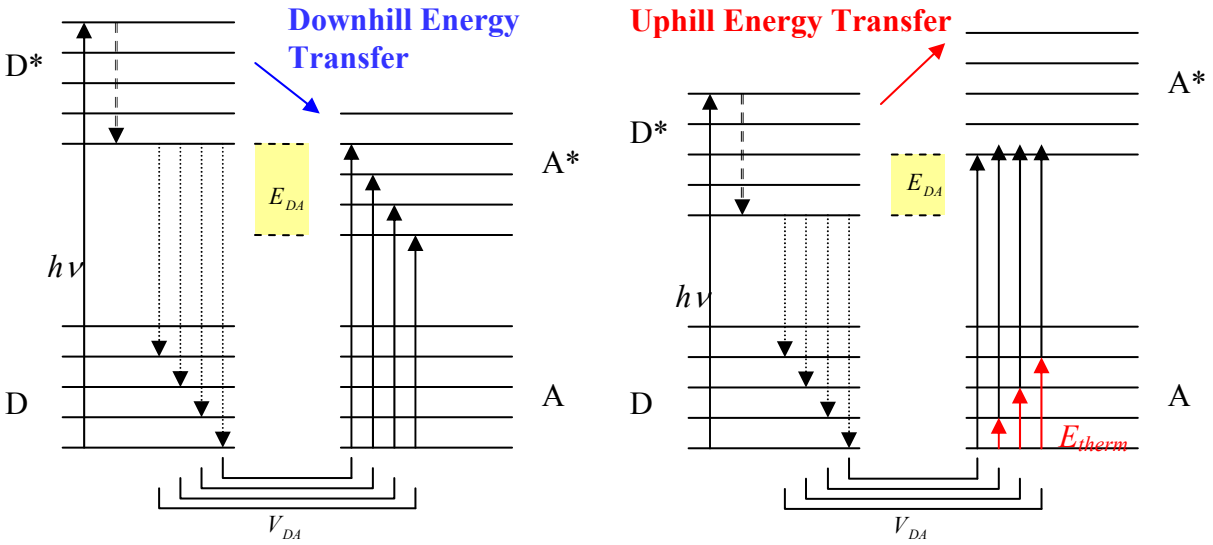

Figure 2. In frame (A), a conceptual schematic of the spectral overlap, $J(\nu)$, is shown [16]. While energy transfer does not occur through a fluorescence-absorption process, $J(\nu)$, is directly proportional to the Förster energy transfer probability, and can range from 0 to 1. In frame (B), the resonance energy transfer condition between the donor (D) and acceptor (A) molecule is illustrated. After excitation by $h\nu$, D vibrationally relaxes (dashed arrow) and energy is transferred to A via dipole-dipole coupling (V_{DA}). Both downhill and uphill energy transfer schemes are shown. In uphill energy transfer, energy must be obtained from the thermal surroundings (E_{therm}) to fulfill the resonance conditions (see text).

Franck-Condon principle, see Chapter 3, Sect. 3.1). The value of $J(\nu)$ can range from 0 to 1, with a value of 1 indicating perfect spectral overlap (see Fig. 2A).

With terms such as spectral overlap, donor fluorescence, and acceptor emission, one may think that energy transfer in Förster theory occurs radiatively, with *D* emitting a photon that is captured by *A*. This is incorrect; however, energy transfer in Förster theory is a quantum mechanical non-radiative process that occurs between two states that are resonant in energy [8, 15, 19]. This resonance condition is required by conservation of energy, so that the energy of the system is same after energy transfer as it was before, because of this Förster energy transfer is often referred to as Förster resonance energy transfer (FRET) [20]. For an illustration of the resonance condition, see Fig. 2B.

The Förster rate equation (Eq. 2.1) can also be recast [8, 21] in a slightly more elegant form

$$k_{DA} = \frac{1}{\tau}\left(\frac{R_0}{R}\right)^6 , \tag{2.5}$$

where R is the distance between the centers of molecules *D* and *A* and R_0 is expressed as

$$R_0^6 \equiv \frac{9\ln(10)}{128\pi^5 n^4 N'}\kappa^2 \int d\nu * \frac{F_D(\nu)\varepsilon_A(\nu)}{\nu^4} \tag{2.6}$$

and is defined as the distance where energy transfer is 50% efficient. Eq 2.5 shows that the energy transfer rate is inversely proportional to the distance between *D* and *A* to the sixth power and that when $R_0 = R_{DA}$, the energy transfer rate is equal to the total dephasing time of *D*.

While Eqs. 2.1 and 2.5 are relatively straightforward, there are implications and limits with Förster theory that must be recognized. As mentioned previously, Förster theory assumes that phononic and vibrational relaxation, which is on the order of ~ 1 ps,

occurs on a faster timescale than energy transfer [22]. For sub-picosecond *D*-*A* energy transfer processes, this assumption cannot be made.

Förster theory also assumes that *D* and *A* are identical molecules, which is not always the case when studying photosynthetic pigments or other biological systems. If *D* and *A* are not identical molecules, there is an energy gap, E_{D-A}, that is equal to the difference between the respective 0-0 electronic transitions, as vibrational relaxation occurs on a timescale faster than energy transfer in Förster theory. Energy transfer is usually most efficient when E_{D-A} is positive and less than $h\nu_D$ ($h\nu_D$ is the 0-0 electronic transition energy of *D*), which allows for increased spectral overlap [23]. This is referred to as "downhill" energy transfer (see Fig.2A). Energy transfer can still occur if E_{D^*-A} is negative, though. However, if this is the case, there will usually not be enough energy after the excited donor vibrationally relaxes to make a pure electronic transition in *A*. Instead, energy must be obtained from the thermal surroundings and/or dephasing processes must be present for transfer to take place. This thermally activated energy transfer process is referred to as "uphill" energy transfer (see Fig. 2B).

Eqs. 2.1 and 2.5 are not always valid when the donor or acceptor lineshapes are appreciably inhomogeneously broadened. If the inhomogeneous broadening of the lineshape is comparable to the electronic coupling between *D* and *A*, then multiple $E_{D\text{-}A}$ can be present which can result in dispersive energy transfer (non-exponential) kinetics. Typically, for photosynthetic pigments, spectral lines are inhomogeneously broadened by ~ 100-300 cm^{-1} and electronic couplings range from ~ 50-900 cm^{-1}. Therefore, when studying energy transfer in photosynthetic pigments, Förster theory must often be modified to account for inhomogeneous broadening [25].

Lastly, since dipole-dipole coupling is only valid when the *D-A* distance is greater than the size of the molecules, closely spaced molecules cannot be modeled in this approximation. When the *D-A* distances are small enough for wavefunction overlap, electron exchange interactions must be taken into account for the electronic coupling (see Fig. 3). Electron exchange energy transfer occurs in strongly coupled pigment dimers and the primary electron donors of RC complexes. For example, primary charge separation in the bacterial RC has been modeled through a Marcus formalism via a Dexter coupled electron exchange reaction [23, 24]. However, primary electron transfer for other photosystems (i.e. PS I and PS II) is more sophisticated, and cannot be assumed to follow this approximation. Interestingly, higher order coulombic terms (e.g. monopole-monopole, dipole-quadrapole) can activate energy transfer between allowed-forbidden transitions; however, these transitions are only weakly allowed and usually only significant when the electronic coupling is considered to be stronger. This assumption of higher order electronic coupling terms to trigger energy transfer is referred to as Dexter theory [14] and models have been developed to account for these for energy transfer between photosynthetic pigment molecules [26-28].

2.4.1 Molecular Excitons

While Förster and Dexter type theories are good approximations for weakly coupled pigments, they start to lose their physical meaning for more strongly coupled systems where excitations cannot assume to be localized. Instead, excitons (coherent inter-molecular excited states) form in these photosynthetic systems [6, 7, 29]. Here, the basic physics of excitons are described, and then, in later sections, applied to energy transfer in photosynthetic pigment complexes.

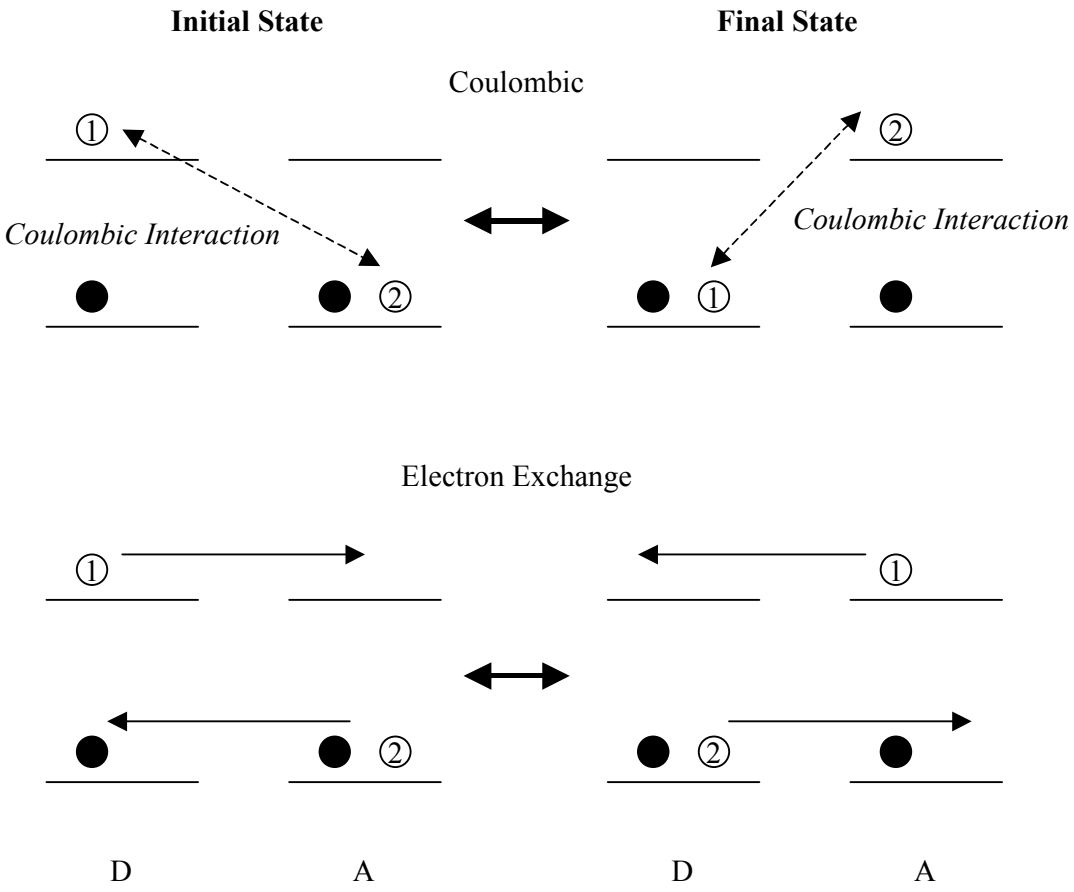

Figure 3. Coulombic energy transfer (Förster) vs. electron exchange (Dexter). Coulombic energy transfer is a Förster energy transfer mediated process with electronic dipole-dipole coupling, V_{DA}. For energy transfer via electron exchange (Dexter theory), the electronic coupling, V_e, has an exponential dependence upon the D-A distance, $V_e = \exp(-\beta d)$, where β is a parameter describing the D-A distance dependence and D is the D-A distance.

In a periodic, ordered molecular system, such as a molecular aggregate, the excitation of a single molecule can be represented by

$$\left[\sum_{n} H_n + \sum_{n,m}{}' \frac{1}{2} V_{nm} - E_{ex}\right] |\varphi\rangle = 0 \tag{2.7}$$

where H_n designates the energy operator of the nth molecule and φ is the wavefunction of the system. V_{nm} is the interaction energy between the excited molecule and its nearest neighbor, second nearest neighbor, and so on; E_{ex} is the molecular excitation energy [10]. The system wavefunction, φ, is defined as the antisymmetrized product of the individual molecular wavefunctions

$$\varphi_{ex} = \varphi_n^{ex} \prod_{\substack{m \\ n \neq m}} \varphi_m^g \tag{2.8}$$

where φ_n^{ex} is the excited state wavefunction of the nth molecule and φ_m^g are the ground state wavefunctions of the other molecules in the aggregate [10].

When the interaction energy in Eq. 2.7 is large enough, the excitation is no longer localized on the αth molecule but is transferred to the other molecules in the crystal, spreading as an excitation wave, which travels as an electrostatically bound electron-hole pair that eventually recombines and annihilates. This collective excitation is referred to as an *exciton*. Excitons are defined between two limiting cases, where the electron-hole pair is either tightly bound (Frenkel exciton) or loosely bound (Mott-Wannier exciton) [10]. In Frenkel excitons, the excited electron is located on the same molecule or atom along with the hole. However, as the excitation travels as a wave through the crystal or ordered aggregate, the electron-hole pair "hops" from molecule to molecule (see Fig 4A). Frenkel excitons are the type of excitons that are discussed in this section, and usually

occur in molecular crystals and ordered aggregates, e.g. photosynthetic pigment complexes [6, 7, 29]. They are often referred to as molecular excitons. In Mott-Wannier excitons, the electron and hole are much farther apart, with distances larger than that of a lattice constant, and occur in ionic crystals (such as semiconductors and dielectrics) with a high dielectric constant. In terms of band theory, a Mott-Wannier exciton corresponds to an excitation where an electron is promoted from a filled valence band to an empty conduction band [30-32] (see Fig 4B).

Since an excited state is not localized in molecular excitons, the wavefunctions defined in Eq. 2.8 are not stationary states. Instead, the system wavefunction can be represented as a superstition of all the wave functions in the aggregate in the Bloch waveform:

$$\psi_{ex}(\mathbf{k}) = N^{-1/2}\sum_{n}\psi_{n}^{ex}\exp(i\mathrm{kn}) \tag{2.9}$$

where wavevector **k** indicates the excitation wave in the crystal and spans N discrete values

$$\mathrm{k} = \sum_{i=1}^{3}\frac{2\pi}{N_i}\nu_i \mathrm{b_i}\,, \qquad -\frac{N_i}{2} < \nu_i \le \frac{N_i}{2} \tag{2.10}$$

and $\mathbf{b}_i$ are the basis vectors of the reciprocal lattice, which are orthonormal to the basis vectors of the lattice ($\mathbf{b}_i\mathbf{a}_j = \delta_{ij}$). It is also noted that the unit cell here is assumed to be a parallelepiped with three noncoplanar basis vectors $\mathbf{a}_1$, $\mathbf{a}_2$, $\mathbf{a}_3$, edges $N_1\mathbf{a}_1$, $N_2\mathbf{a}_2$, $N_3\mathbf{a}_3$, and only one molecule per unit cell (for simplicity) so that the total number of molecules in the unit cell is $N = N_1N_2N_3$.

Then, if we let the ground state wavefunctions of the aggregate be represented as

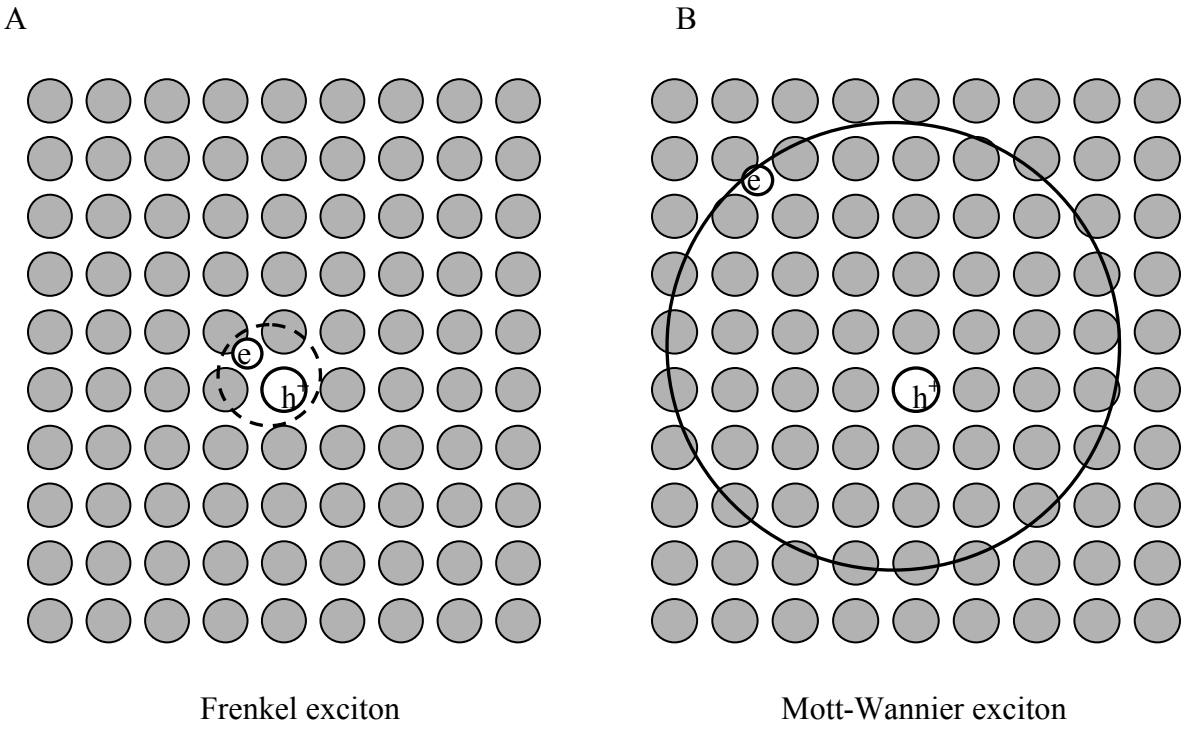

Figure 4. (A) Schematic of a Frenkel exciton. The electron (e^-) - hole (h^+) pair is tightly bound and as it travels through the molecular lattice, with an electron-hole separation distance less than the unit cell length. However, the excitation is considered a superposition of all the wavefunction in the lattice (Bloch form) and is thus considered to be delocalized over all the molecules in the lattice. (B) Schematic of a Mott Wannier exciton. The electron-hole pair is loosely bound, which results in electron-hole separation distances greater than the unit cell length. Mott-Wannier excitons are not observed in organic molecular systems due to their low dielectric constants. For Mott-Wannier excitons to form, a large dielectric constant is needed so that electron hole interaction is sufficiently weak to allow large electron hole separation distances [30].

$$\psi_g = \prod_n \varphi_n^g \tag{2.11}$$

the excitation energy for an excited state in the aggregate can be determined by taking the difference between the excited state and ground state energies, which is given by:

$$E_{ex}(\mathrm{k}) = \varepsilon_{ex} + D_{ex} + L_{ex}(\mathrm{k}) \tag{2.12}$$

where ε_{ex} is the excitation energy of one molecule in the aggregate, D_{ex} is the change in interaction energy of one molecule with all other molecules from the ground to excited state,

$$D_{ex} = \sum_m{}' \left\langle \left|\varphi_n^{ex}\right|^2 \left| V_{nm} \right| \left|\varphi_m^g\right|^2 \right\rangle - \left\langle \left|\varphi_n^g\right|^2 \left| V_{nm} \right| \left|\varphi_m^g\right|^2 \right\rangle \tag{2.13}$$

and L_{ex} is the transition of excitation between molecule **n** and all other molecules.

$$L_{ex}(\mathrm{k}) = \sum_m{}' \left\langle \varphi_n^g \varphi_m^{ex} \left| V_{nm} \right| \varphi_m^g \varphi_n^{ex} \right\rangle \exp\{i\mathrm{k}(\mathrm{n}-\mathrm{m})\} \tag{2.14}$$

Eq 2.12 specifically shows how a single excitation is not localized on one molecule, but is a collective excitation of all molecules in the aggregate. Eq 2.12 is also a function of N different values of the wave vector **k**, resulting in a non-degenerate exciton band with N sublevels.

2.4.2 Excitonically Coupled Dimer

Coherent molecular excitons can also form in linear or cyclic molecular aggregates where there is short-range, but no long-range periodic order, such as strongly coupled chlorophyll molecules in PCs. While there are many types of chlorophyll molecule aggregates, the simplest is the excitonically coupled dimer [33]. The excitonically coupled dimer can be thought of as the building block for more complex cyclic and linear photosynthetic aggregates.

A dimer in this sense refers to a pair of electrostatically interacting chlorophyll pigment molecules (either identical or non-identical) that are spatially separated, and not necessarily in van der Waals contact. For two identical molecules, though, the Hamiltonian due this interaction is

$$\left\langle \varphi_1^g \varphi_2^g \left| H_1 + H_2 + V \right| \varphi_1^g \varphi_2^g \right\rangle = E_g \tag{2.15}$$

where the ground state wavefunction of the dimer is taken to be a product of the molecular wavefunctions, as in molecular crystals:

$$\psi_g = \varphi_1^g \varphi_2^g \tag{2.16}$$

and the ground state energy of the dimer can be expressed as

$$E_g = \varepsilon_1^g + \varepsilon_2^g + D_g \tag{2.17}$$

Thus, the coupling between the two molecules shifts the ground state energy of the dimer by $D_g \equiv V_{00} \equiv \left\langle \varphi_1^g \varphi_2^g \left| V \right| \varphi_1^g \varphi_2^g \right\rangle$. D_g is often referred to as the *ground dispersion energy*.

The excited state wavefunction of the dimer can be represented as

$$\psi_{ex} = \frac{1}{\sqrt{2}} \left[\varphi_1^{ex} \varphi_2^g \pm \varphi_1^g \varphi_2^{ex} \right] \tag{2.18}$$

or more simply by

$$\psi_{ex} = \frac{1}{\sqrt{2}} \left[\psi_{ex}^1 \pm \psi_{ex}^2 \right] \tag{2.19}$$

$$\psi_{ex}^1 = \varphi_1^{ex} \varphi_2^g$$

$$\psi_{ex}^2 = \varphi_1^g \varphi_2^{ex}$$

where the wavefunction is both normalized and orthogonal.

Then the excited state Hamiltonian for the excited dimer can be written as

$$\langle \psi_{ex} | H_1 + H_2 + V | \psi_{ex} \rangle = E_{ex} \tag{2.20}$$

By expanding the wavefunction (which can be seen most clearly by putting Eq. 2.20 in determinant matrix form)

$$\begin{vmatrix} \varepsilon_1^{ex} + V_{11} - E_{ex} & V_{12} \\ V_{21} & \varepsilon_2^{ex} + V_{22} - E_{ex} \end{vmatrix} = 0 \tag{2.21}$$

and if we recognize that $V_{11} \equiv V_{22} \equiv D_{ex}$ and $V_{12} \equiv V_{21} \equiv V_{res}$, the matrix can be diagonalized and the Hamiltonian solved for the eigenenergies, which is given by:

$$E_{ex}^1 = \varepsilon_1^{ex} + D_{ex} + V_{res} \tag{2.22.a}$$

$$E_{ex}^2 = \varepsilon_2^{ex} + D_{ex} - V_{res} \tag{2.22.b}$$

with

$$D_{ex} = \langle \varphi_2^g \varphi_1^{ex} | V | \varphi_1^{ex} \varphi_2^g \rangle = \langle \varphi_2^{ex} \varphi_1^g | V | \varphi_1^g \varphi_2^{ex} \rangle \tag{2.23}$$

$$V_{res} = \langle \varphi_2^g \varphi_1^{ex} | V | \varphi_1^g \varphi_2^{ex} \rangle = \langle \varphi_2^{ex} \varphi_1^g | V | \varphi_1^{ex} \varphi_2^g \rangle \tag{2.24}$$

Thus, it is easy to see that the excited excitonic band is split into two non-degenerate bands (Eqs. 2.22.a and 2.22.b) by an energy separation of $2V_{res}$ (Davydov splitting) [10, 33] and are delocalized over both molecules. Eqs. 2.22.a and 2.22.b also show that the energy difference between the ground and excited states (transition energy) has dropped compared to a single molecule. V_{res} is the *resonance transfer matrix element* and is the Coulomb coupling responsible for energy transfer between the two pigment molecules, which is clearly shown in Eq. 2.24. D_{ex} is the *excited dispersion energy*, and like the ground dispersion energy, shifts the excited state energy. Together, D_{ex}–D_g is the *solvent shift* or shift in excitation energy that occurs when a molecule goes from the gas to

condensed phase [16, 33]. The solvent shift usually causes a decrease in excitation energy, yielding a red shift of the excitonic absorption bands (see Fig 5).

Since the Coulomb coupling of V_{res} is usually considered in the dipole-dipole approximation, the relative orientation of the molecular transition dipole moment vectors in the dimer determines the oscillator strength and absorption intensity of each excitonic state. In the case where the dimer consists of two identical molecules, its transition dipole strength, I_{dim}, from the ground to the one quantum excited state, for each excitonic state, is [33]

$$I_{\dim}(\pm) = \left|\left\langle \psi_g \left| \mu_1 + \mu_2 \right| \psi_{ex} \right\rangle\right|^2 = I_{mol}(1 \pm \cos\theta) \qquad (2.25)$$

where $\mu_{n=1,2}$ is the dipole moment operator of the respective molecules, I_{mol} is the molecular dipole strength, and θ is the angle between the molecular transition dipole moment vectors. The + and - labeling refers to the split excitonic states of the dimer (Eqs. 2.22.a and 2.22.b, respectively). For illustration, possible orientations of the transition dipole moment vectors in an excitonically coupled dimer of chlorophyll pigment molecules are diagrammed in Fig. 6, along with how these orientations determine the magnitude/sign of V_{res} and dipole (oscillator strength) of the excitonic bands.

In photosynthetic complexes, pigment molecules experience different local environments due to the surrounding protein matrix. Therefore, it cannot always be assumed that the site energies of pigment molecules will be the same. If a dimer is composed of two molecules with inequivalent excitation site energies of difference δ, then their energies can be "rezeroed" to δ/2 and -δ/2, respectively. The Hamiltonian

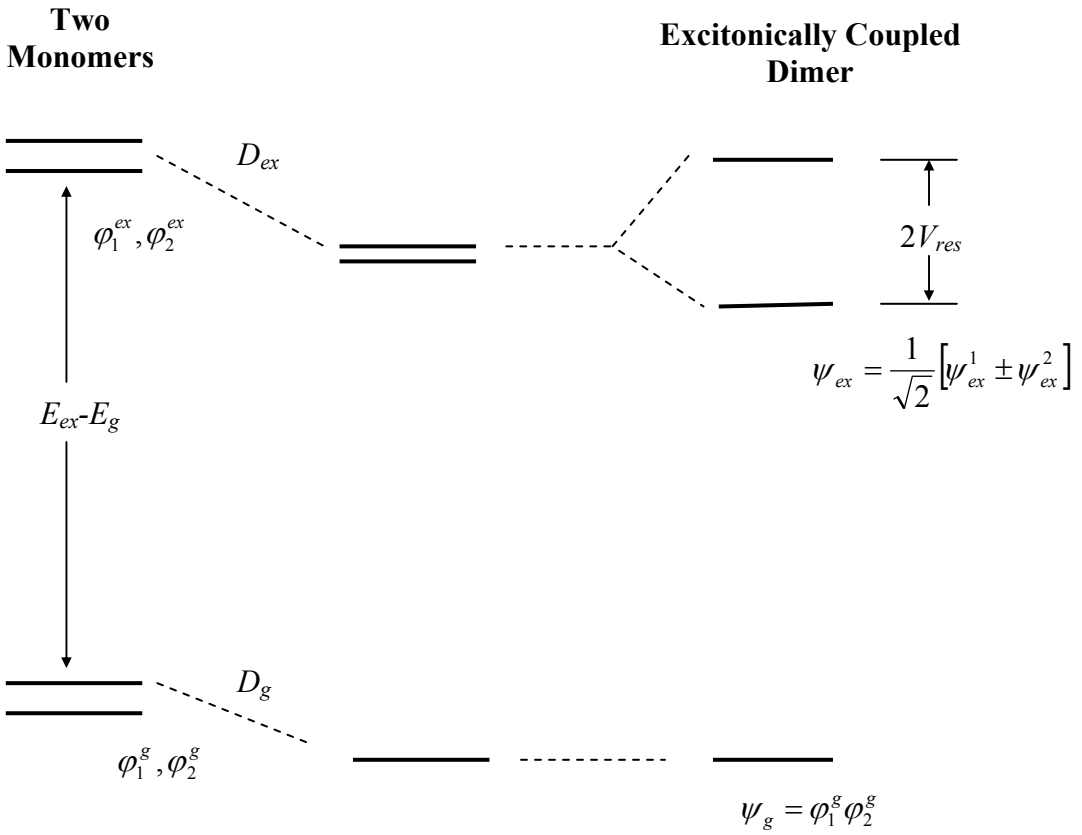

Figure 5. Schematic of the energy level shifts that occurs when two monomers are coupled as an excitonic dimer [10, 33]. D_{ex} and D_g are the excited and ground dispersion energy shifts, respectively. The difference between them (D_{ex}–D_g) is referred to as the *solvent energy shift*. The excited state energies of the dimer are then split by $2V_{res}$. The orientation of the molecules determines the energies and oscillator strengths of the excitonic bands (see Fig. 6). The excitonic wavefunctions of the dimer are labeled as ψ_{ex} and ψ_g while the molecular wavefunctions of the monomer are labeled as φ_i^{ex} and φ_i^g (i = 1,2).

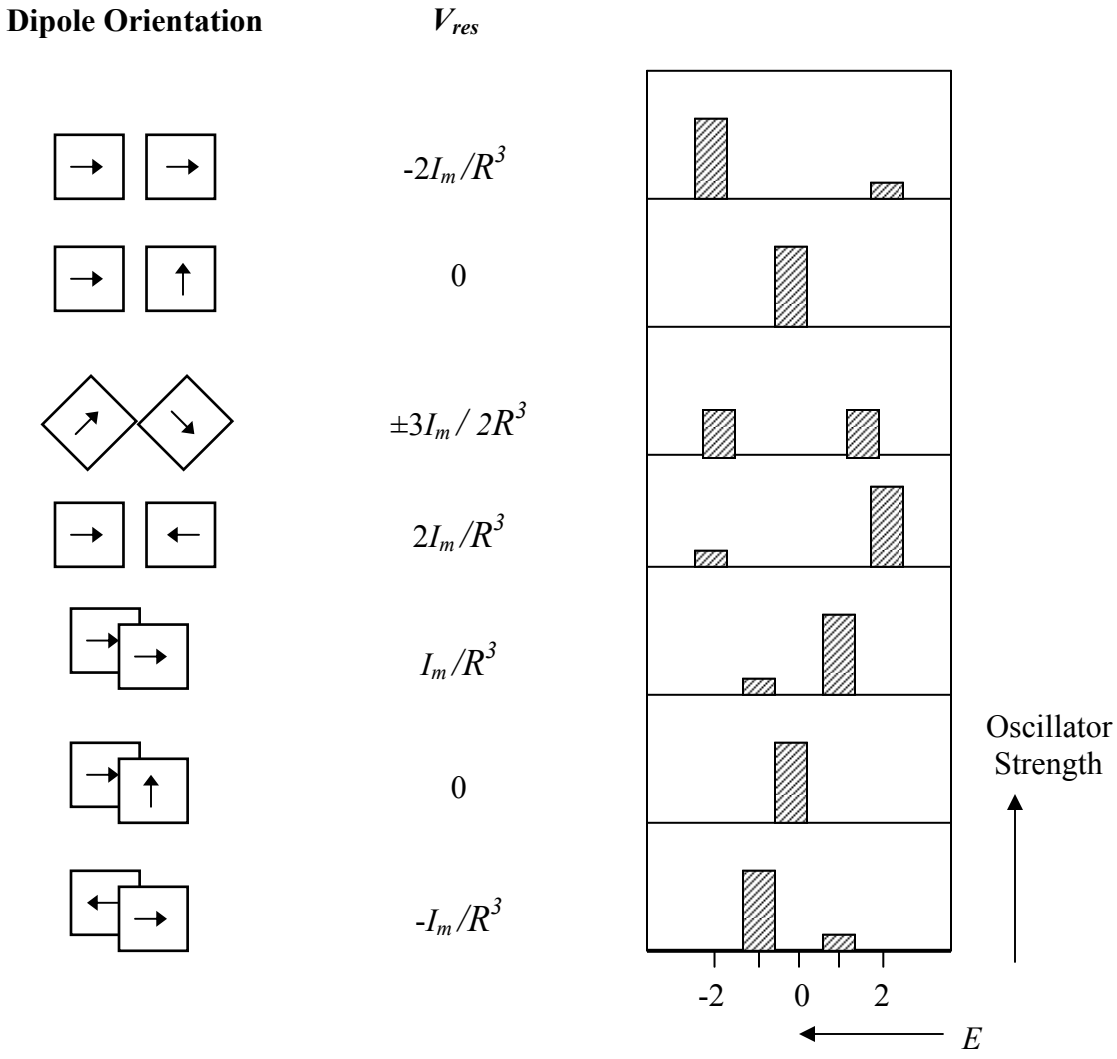

Figure 6. Schematic of excitonic band dipole orientations, oscillator strengths, and energies [34]. In the leftmost column, the orientation of the molecules and their dipole moments are shown. The squares represent molecular planes and the solid arrows, the transition dipole moment vectors. The excitonic coupling between the molecules is assumed to be dipole-dipole and is given by $V_{res} = V_{DA} \equiv \kappa I_m/R^3$ where $I_m = |\vec{\mu}_D||\vec{\mu}_A|$ (see Eq. 2.2). The energy, E, (in units of I_m/R^3) and oscillator strength of the split excitonic bands are shown in the right most column.

matrix for this dimer is then

$$\begin{vmatrix} \delta/2 - E_{ex} & V_{res} \\ V_{res} & -\delta/2 - E_{ex} \end{vmatrix} = 0 \tag{2.26}$$

where the D_{ex} term has been omitted for simplicity. After diagonalizing Eq. 2.46, the exciton energies are

$$E_{ex} = +\frac{\delta}{2}\sqrt{1+\frac{2V_{res}^2}{\delta^2}} \tag{2.27.a}$$

$$E_{ex} = -\frac{\delta}{2}\sqrt{1+\frac{2V_{res}^2}{\delta^2}} \tag{2.27.b}$$

It can be easily seen that there are two limiting case for Eqs. 2.27.a and 2.27.b. If V >> δ, 2.27.a and 2.27.b approach the energies and splittings of the identical molecule dimer (Eqs. 2.22.a and 2.22.b) where the exciton states are delocalized over both molecules. If V << δ, 2.27.a and 2.27.b approach the energies of the uncoupled molecules, where they are split by δ/2 and the excited states are localized on the individual molecules.

2.4.3 Photosynthetic Excitons - Coherent Excitons in Photosynthetic Aggregates and Complexes

Moving beyond the simple excitonic dimer leads to ordered systems, such as linear and cyclic aggregates, where the excitonic and environmental interactions of the chlorin molecules are more complex [33, 35]. As before, a good example is the PS II RC of cyanobacteria and green plants, a wish-boned shaped aggregate of 6 Chls and 2 Pheos, that is neither cyclic nor linear, where the excitonic couplings are weak when compared to the energy disorder due to local protein environment effects. This results in the primary donor state being poorly defined and not always localized on one particular chlorin molecule.

In such aggregates, the excited state Hamiltonian is:

$$H = \sum_{n,m} \varepsilon_n^{ex} \delta_{nm} + \sum_{n,m}{}' V_{nm} \tag{2.28}$$

(where the excited state dispersion energies are discarded for simplicity) and the normalized excited state wavefunctions for the coupled chlorin molecules are

$$\varphi_{ex,n} = \sum_n \varphi_n^{ex} \prod_{\substack{m \\ n \neq m}} \varphi_m^g \tag{2.29}$$

By then taking the wavefunctions in Eq. 2.29 and expanding them about the Hamiltonian in Eq. 2.28 the following result is obtained

$$H = \sum_n \varepsilon_n^{ex} \left\langle \varphi_n^{ex} \middle| \varphi_n^{ex} \right\rangle + \sum_{n,m}{}' \left\langle \varphi_n^{ex} \middle| V_{nm} \middle| \varphi_m^{ex} \right\rangle \tag{2.30}$$

which shows that the Hamiltonian depends only on the excited state wavefunctions and energies. This expansion generates a $n \times n$ matrix and can be diagonalized to solve for the excitonic energies (E_α) and wavefunctions ($|\alpha\rangle$).

The excitonic wavefunctions are simply

$$|\alpha\rangle = \sum_n c_{\alpha n} \left| \varphi_n^{ex} \right\rangle \tag{2.31}$$

where the excited state molecular wavefunctions serve as a basis for the normalized and orthogonal excitonic wavefunctions, and the coefficients determine the contribution of each molecular wavefunction to the excitonic band. The coefficients can also be used to determine the excitonic transition dipoles

$$\hat{\boldsymbol{\mu}}_{\boldsymbol{\alpha}} = \sum_n c_{\alpha n} \hat{\mu}_n \quad , \tag{2.32}$$

where $\hat{\mu}_n$ is the transition dipole vector for chlorin molecule *n*. Therefore, the oscillator strength contribution of each chlorin for each excitonic band, or occupation number, is determined by $|c_{\alpha n}|^2$. The delocalization of the excitonic bands is given by

$$N_{\text{del}} = \frac{1}{\sum_n |c_{\alpha n}|^4} \tag{2.33}$$

where N_{del} represents the number of chlorin molecules per excitonic state α [35].

While the above equations are relatively straightforward, determination of the photosynthetic excitonic spectra is not so easily done. Modeling of such excitonic spectra by Jankowiak et al. [6, 35] and Durrant et al. [36, 37] for the PS II RC, and Aartsma et al. [38] for the FMO antenna complex, has shown a marked difference to the observed experimental spectra, regarding overall band shapes and widths. In references [35-37], the chlorins are all assumed to have identical site energies, which in a first-order approximation is valid due to the width of the overall excitation spectrum for both complexes (~ 500 cm^{-1}), and a dipole-dipole coupling mechanism. However, the site energies are most likely not identical and along with the electrostatic coupling redistributing the oscillator strength among the chlorins, complicates the chlorin transition energies and strengths, which cannot be determined experimentally. The broadening of the excitonic bands also plays an important role, since the homogeneous broadening depends on the exciton-phonon coupling strength and the inhomogeneous broadening is determined by the amount of disorder induced by the surrounding protein matrix and motional narrowing via delocalization of the excitonic bands [35].

In addition, the arguments above assume that the structure of photosynthetic complexes is precisely known, this is usually not the case. High-resolution X-ray

crystallography structures (≤ 1.6 Å) [39] are not available for most PCs [40-42]. Therefore, the precise positions of the chlorin molecules to calculate the electrostatic coupling are not available, and, more importantly, since the chlorin-chlorin distances are not adequately defined, what coupling approximation should be used, e.g. dipole-dipole, full Coulomb, etc.

2.4.4 Energy Transfer via Relaxation in Photosynthetic Excitons

As discussed previously, when $V/\Delta >> 1$ the Condon approximation breaks down and the treatment of individual photosynthetic pigments as localized donor and acceptor eigenstates that transfer energy through an incoherent hopping process is no longer valid. Instead, energy transfer occurs through coherence and relaxation of excitonic states. In this "exciton picture", the energy transfer can be calculated using a Fermi-Golden rule expression, like the Förster equation, that is derived from first-order perturbation theory. The perturbation in excitonic relaxation, however, is not the electronic coupling (V), as in Förster theory, but the electron-phonon coupling (dynamic disorder) [1, 25].

Since the Condon approximation is no longer valid, the electronic wavefunction coordinates are no longer independent of the vibrational wavefunction coordinates and the excitonic Hamiltonian must be modified. The electron-phonon perturbation can be expressed by partitioning the excitonic Hamiltonian into H_0, the zero order contribution (Eq. 2.28), and ΔH, the perturbation operator,

$$H^{ex} = H_0 + \Delta H \tag{2.34}$$

The perturbation operator, also referred to as the non-adiabaticity operator or Born-Oppenheimer correction term, takes into account the dependence of the electron-phonon interaction potential, V_{int}, for a fixed configuration of the phonon "promoting mode"

coordinates, q_{p}^{0}, and is responsible for energy transfer via scattering between exciton levels. It is written as

$$\Delta H = \sum_{\mathrm{p}} q_{\mathrm{p}} \left(\frac{\partial V_{\mathrm{int}}}{\partial q_{\mathrm{p}}} \right)_0 \tag{2.35}$$

where the promoting modes have a frequency of ω_{p}, and are not necessarily required to be Franck-Condon active [25, 44].

The perturbation operator then enters into the Fermi-Golden rule rate expression as

$$\frac{2\pi}{\hbar} \left| \langle \Psi_{\mathrm{F}} | \sum_{\mathrm{p}} q_{\mathrm{p}} \left(\frac{\partial V_{\mathrm{int}}}{\partial q_{\mathrm{p}}} \right)_0 | \Psi_{\mathrm{I}} \rangle \right|^2 \rho(\Omega) \tag{2.36}$$

where $\rho(\Omega) = \int_0^\infty d\omega \; J(\Omega)$ and is referred to as the spectral density of states; Ψ_{F} and Ψ_{I} are the final and initial electronic excited state wavefunctions, respectively. If it is recognized that the phonon coordinate, q_{p}, can be written in terms of ladder operators [45]

$$q_{\mathrm{p}} = \left(\frac{\hbar}{2\omega_{\mathrm{p}}} \right)^{1/2} (b_{\mathrm{p}} + b_{\mathrm{p}}^{+}) \tag{2.37}$$

(b_{p}^{+} and b_{p} are the creation and annihilation operators, respectively) then Eq. (2.36) can be expanded about the appropriate vibrational wavefunctions to give

$$\sum_{p} \frac{\pi}{\omega_{\mathrm{p}}} \left| \langle \Psi_{\mathrm{F}} | \left(\frac{\partial V_{\mathrm{int}}}{\partial q_{\mathrm{p}}} \right)_0 | \Psi_{\mathrm{I}} \rangle \right|^2 \langle \tilde{n}_{\mathrm{p}} + 1 \rangle \; \rho(\Omega - \omega_{\mathrm{p}}) \; , \tag{2.38}$$

since $\left|\left\langle n_{\mathrm{p}}+1\left|b_{\mathrm{p}}+b_{\mathrm{p}}^{+}\right|n_{\mathrm{p}}\right\rangle\right|^{2}=\left\langle\tilde{n}_{\mathrm{p}}+1\right\rangle$, where $\left|n_{\mathrm{p}}, n_{\mathrm{p}}+1\right\rangle$ are the vibrational wavefunctions for the promoting mode(s) and $\tilde{n}_{\mathrm{p}}$ is the thermal occupation number, $\left[\exp(\hbar\omega_{\mathrm{p}}/kT)-1\right]^{-1}$ [45]. The spectral density in Eq 2.38 is reduced by ω_{p} due to one-phonon emission; if there is one-phonon absorption ($\left\langle\tilde{n}_{\mathrm{p}}\right\rangle$), the spectral density is increased by ω_{p} [16].

To determine explicit expressions for the exciton-phonon interaction (perturbation operator, ΔH) in Eq 2.41, the excitonic Hamiltonian (Eq. 2.28) is expanded in a Taylor series about the lattice coordinates $\{\mathbf{R}=0\}$, which the phonon coordinates, q_{p}, are dependent upon. In this expansion all the linear terms are collected, along with quadratic terms that describe harmonic phonons. This results in the following equation [10, 46]

$$H^{ex}(R)=H_0(R)+H_{PH}(R)+H_{EX-PH(1)}(R)+H_{EX-PH(2)}(R) \tag{2.39}$$

$H_0(R)$, the zero-order contribution (see above), determines the crude adiabatic energies for the exciton bands and is written as

$$H_0(R)=\sum_n\left[\varepsilon_n^{ex}+D_n^{ex}(R)\right]B_n^{+}B_n+\sum_{n,m}V_{nm}(R)\;B_n^{+}B_m\;, \tag{2.40}$$

where the excited state dispersion energies are included, in Eq. 2.40 $D_n^{ex}(R)=\sum_{m\neq n}D_{ex,nm}(R)$ and the expanded Hamiltonian is expressed in terms of ladder operators. $H_{PH}(R)$, the phonon Hamiltonian, is

$$H_{PH}(R)=\sum_{\mathbf{q}s}\hbar\omega_s(\mathbf{q})b_{\mathrm{q}}^{+}b_{\mathrm{q}}\;, \tag{2.41}$$

where $\omega_s(\mathbf{q})$ is the phonon frequency for the *s*-th phonon branch with wave vector **q**. Eq. 2.41 does not describe high frequency phonons that occur via intramolecular vibrations. $H_{EX-PH(1,2)}(R)$ are the exciton-phonon coupling expressions responsible for exciton relaxation and which enter into Eq. 2.38 as the perturbation operator terms.

$$H_{EX-PH(1)}(R) = \sum_{n,m} B_n^+ B_m \sum_{j=1}^{6} \left[R_n^j \left(\frac{\partial V_{nm}}{\partial R_n^j} \right)_0 + R_m^j \left(\frac{\partial V_{nm}}{\partial R_m^j} \right)_0 \right] \tag{2.42}$$

$$H_{EX-PH(2)}(R) = \sum_{n,m} B_n^+ B_m \sum_{j=1}^{6} \left[R_n^j \left(\frac{\partial D_{nm}^{ex}}{\partial R_n^j} \right)_0 + R_m^j \left(\frac{\partial D_{nm}^{ex}}{\partial R_m^j} \right)_0 \right] \tag{2.43}$$

In Eqs. 2.42-3, $j = 1,2,3$ and $j = 4,5,6$ indices represent the translational and rotational degrees of freedom of the excited molecule, respectively.

It is more transparent, though, to switch $H_{EX-PH(1,2)}(R)$ terms from a localized representation to an exciton representation that also contains phonon b^+ and b ladder operators. This is accomplished using the following relations [46, 47]

$$B_n = N^{-1/2} \sum_k B(\mathbf{k}) e^{-i\mathbf{k}\cdot\mathbf{n}} \ , \tag{2.44}$$

where B(**k**) is the delocalized exciton operator with wave vector **k**, and

$$R_n^j = N^{-1/2} \sum_{\mathbf{q}s} \frac{q_s(\mathbf{q})}{I_j} e_s^j(\mathbf{q}) e^{i\mathbf{q}\cdot\mathbf{n}} \ , \tag{2.45}$$

where *N* is the number of sites, $q_s(\mathbf{q})$ is the phonon coordinate associated with mode **q***s*, and I_j is the moment of inertia associated with the *j*-th degree of freedom. Eqs. 2.42 and 2.43 then become:

$$H_{EX-PH(1)}(R) = N^{-1/2} \sum_{\mathbf{k},\mathbf{q}s} B^+(\mathbf{k}+\mathbf{q}) B(\mathbf{k}) F_s(\mathbf{k},\mathbf{q}) (b_{\mathbf{q}s} + b_{-\mathbf{q}s}^+) \tag{2.46}$$

$$H_{EX-PH(2)}(R) = N^{-1/2}\sum_{\mathbf{k},\mathbf{q}s} B^{+}(\mathbf{k})B(\mathbf{k})\chi_s(\mathbf{q})(b_{\mathbf{q}s} + b^{+}_{-\mathbf{q}s}) \ , \tag{2.47}$$

where

$$F_s(\mathbf{k},\mathbf{q}) = \sum_{j,m(\neq 0)} \alpha(s,\mathbf{q}) e_s^j(\mathbf{q}) \left[\left(\frac{\partial V_{0m}}{\partial R_0^j} \right)_0 + e^{i\mathbf{q}\cdot(\mathbf{m})} \left(\frac{\partial V_{0m}}{\partial R_m^j} \right)_0 \right] e^{i\mathbf{k}\cdot(\mathbf{m})} \tag{2.48}$$

$$\chi_s(\mathbf{q}) = \sum_{j,m(\neq 0)} \alpha(s,\mathbf{q}) e_s^j(\mathbf{q}) \left[\left(\frac{\partial D_{0m}^{ex}}{\partial R_0^j} \right)_0 + e^{i\mathbf{q}\cdot(\mathbf{m})} \left(\frac{\partial D_{0m}^{ex}}{\partial R_m^j} \right)_0 \right] \tag{2.49}$$

with $\alpha(s,\mathbf{q}) = \left(\hbar / 2\omega_s(\mathbf{q}) I_j\right)^{-1/2}$. Eqs. 2.46 and 2.47 both assume that there is only one molecule per unit cell, and thus only one exciton branch. Thus, the final expression for energy transfer is obtained trivially by inserting these expressions into Eq. 2.38, which contain the delocalized excitonic and nuclear wavefunctions.

It is noted that Eqs. 2.46 and 2.47 imply two limiting cases for exciton-phonon scattering, when $H_{EX-PH(1)} >> H_{EX-PH(2)}$ and when $H_{EX-PH(1)} < H_{EX-PH(2)}$. If the former is the limiting case, the modulation of the *V* term is dominant, and the exciton-phonon coupling is considered to be weak and non-local. In this case, exciton scattering, and thus energy transfer, occurs from one **k**-value to another (see Fig. 7). If the latter is the limiting case, the modulation of the *D* term is dominant, and the exciton-phonon coupling is considered to be strong and local. In this case, exciton scattering occurs, but there is no change in **k**-value and energy transfer from one band to another does not occur. Instead, this modulation of the molecular energy *D* term shifts the equilibrium of the intermolecular coordinates, deforming the lattice around the excited molecule. If the electron-phonon coupling is strong enough, this deformation can localize or even trap the exciton. These *self-trapped excitons* should not be viewed as being “localized" in space

Exciton-Phonon Scattering

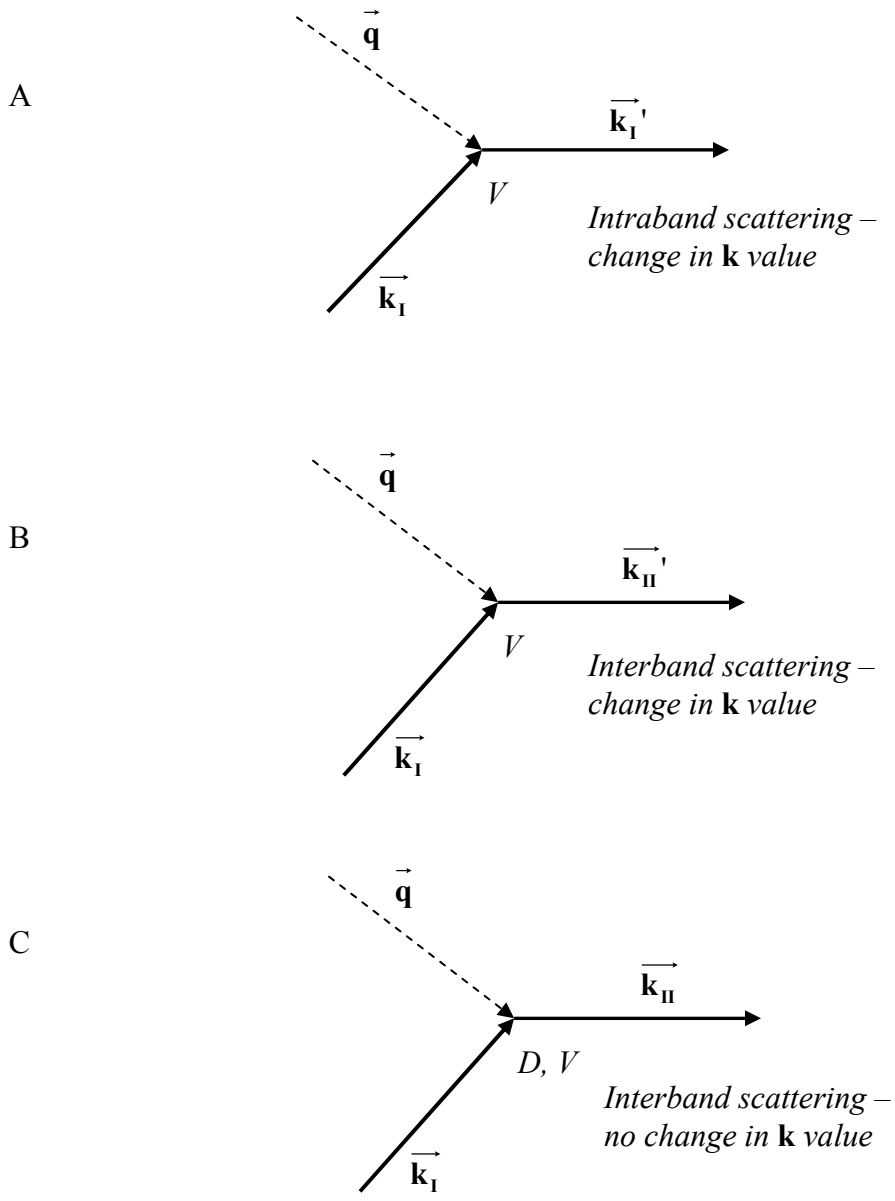

Figure 7. Energy transfer via exciton-phonon scattering processes are shown schematically [46]. The exciton wavevectors (**k**) are the solid arrows, with **I** and **II** representing different exciton branches, while the phonon wavevectors (**q**) are the dashed arrows. In (A), intraband exciton-phonon scattering with a change in exciton *k*-value is modulated by the *V* term (Eq. 2.68). When there is more than one molecule per unit cell then interband scattering is possible. In (B), interband exciton-phonon scattering with a change in *k*-value is modulated by the *V* term. While in (C), interband exciton-phonon scattering with no change in *k*-value is modulated by the *D* and *V* terms (Eqs. 2.48-2.49).

and time, but rather moving through the lattice at a slow velocity. Self-trapped excitons in photosynthetic complexes [48, 49] are analogous to *polarons* in molecular crystals [30].

Alternatively, exciton relaxation can also be modeled through a density matrix picture approach, which allows for a time-evolution description of the coherence of the excitonic matrix elements. Thus, the downward energy cascading between excitonic bands can be followed through time. This approach is specifically called Redfield relaxation theory [50, 51]. In Redfield theory, the density operator ρ is projected into a reduced Liouville space that describes the electronic excitation degrees of freedom but averages out the phonon degrees of freedom. A second-order expansion of the Hamiltonian is then performed to determine the exciton-phonon Hamiltonian, which reduces the density matrix equation to [1, 33]

$$\frac{d\rho_{nm}(t)}{dt} = \frac{-i}{\hbar}[H_0, \rho]_{nm} - \sum_{pq} \mathbf{R}_{nm,pq}\rho_{pq}(t) \tag{2.50}$$

where $\rho_{\alpha\beta}$ is the density matrix operator for states α and β, respectively. The first term on the R.H.S. in Eq. 2.50 details the coherence of the system, which depends on the zero-order Hamiltonian (see Eq 2.30), while the second term on the R.H.S. details the coherence loss due to the system-bath interaction described by the Redfield tensor **R**. The Redfield tensor $\mathbf{R}_{nm,pq}$ is dependent on the electron-phonon coupling expressions from Eqs. 2.46-7 and connects all the density matrix elements. $\mathbf{R}_{nn,mm}$ is the rate constant for the population transfer from the m^{th} to the n^{th} state; $\mathbf{R}_{nm,nm}$ is the dephasing of the coherence between the m^{th} and n^{th} states; and $\mathbf{R}_{nm,pq}$ is the coherence transfer term between p and q states to n and m states.

The formal solution to Eq 2.50 is $\rho(t) = e^{Lt}\rho(0)$ where L is the Liouville operator and t is time [51]. However, for a system with N elements, the Liouville tensor has N^2 elements. Therefore, the diagonalization algorithm scales to N^6, which is impractical to solve for systems with more than a few degrees of freedom. Instead, an iterative approach can be used where the explicit form of the Redfield operator is not needed [52, 53]. This approach is based on the short-iterative Arnoldi procedure [54, 54] and is independent of the vibronic basis size and converges much faster than traditional Runge-Kutta algorithms. [56, 57]

A formal derivation and explanation of Redfield relaxation theory will not be given here, however. The derivation, while straightforward, is lengthy and detailed. Also, the research in this thesis does not use Redfield theory to describe energy transfer, due to the frequency domain spectroscopy techniques used. Therefore, any interested readers are directed to the following outstanding reviews of Redfield relaxation theory and its application to energy transfer in photosynthetic light harvesting antennas and reaction center complexes [50, 51, 58, 59].

References

1. Sundstrom, V., Pullertis, T., van Grondelle, R., *J. Phys. Chem. B* **1999,** 103, p. 232.
2. Hofmann, C., Ketelaars, M., Matsushita, M., Michel, H., Aartsma, T.J., Kohler, J., *Phys. Rev. Lett.* **2003**, 90, p. 013004/1.
3. Hayes, J.M., Matsuzaki, S., Ratsep, M., Small, G.J., *J. Phys. Chem B* **2000**, 104, p. 5625.
4. van Amerongen, H. and van Grondelle, R., *J. Phys. Chem. B* **2001**, 105, p. 604.
5. Jankowiak, R., Zazubovich, V., Ratsep, M., Matsuzaki, S., Alfonso, M., Picorel, R., Seibert, M., Small, G.J., *J. Phys. Chem. B* **2000**, 104, p. 11805.
6. Riley, K., Jankowiak, R., Rätsep, M., Small, G.J., Zazubovich, V., *J. Phys. Chem. B* **2004**, 108, p. 10346.
7. Brixner, T., Stenger, J., Vaswani, H. M., Cho, M., Blankenship, R. E., Fleming, G. R., *Nature* **2005**, 434, p. 625.
8. Förster, Th., *Ann. Phys.* [Series 6] **1948**, 2, p. 55.
9. Levine, Ira N. *Quantum Chemistry,* 5th ed.; Prentice Hall: New Jersey, 2000; p. 96.
10. Davydov, A.S., *Theory of Molecular Excitons*; Plenum: New York, 1971.
11. Reddy, N.R.S., Picorel, R., Small, G.J., *J. Phys. Chem.* **1992**, 96, p. 6458.
12. Rahman, T.S., Knox, R.S., Kenkre, V.M., *Chem. Phys.* **1979**, 44, p. 197.
13. Kühn, O., Renger, T., May, V., Voigt, J., Pullerits, T., Sundström, V., *Trends in Photochem. Photobiol.*; 1997; Vol. 4, p. 213.
14. Dexter, D.L., *J. Chem. Phys.* **1953**, 21, p. 836.

15. Scholes, G.D., Jordanides, X.J., Fleming, G.R., *J. Phys. Chem. B* **2001**, 105, p. 1640.

16. Wu. H.-M., Ph.D. Thesis, Iowa State University, 1998.

17. Levine, Ira N. *Quantum Chemistry,* 5th ed.; Prentice Hall: New Jersey, 2000; p. 96.

18. Coolidge, A. S, James, H. M., Present, R. D., *J. Chem. Phys*. **1936**, 4, p.193.

19. Mukamel, S. *Principles of Nonlinear Optical Spectroscopy*; Oxford University Press: New York, 1995.

20. Clegg, R.M., *Chemical Analysis* **1996**, 137, p. 179.

21. Förster, Th., *Discuss. Faraday Soc*. **1959**, 27, p. 7.

22. McHale, J.L., *Molecular Spectroscopy*; Prentice Hall: New Jersey, 1999.

23. Blankenship, R. *Molecular Mechanisms of Photosynthesis*; Blackwell Science: Oxford, England, 2002.

24. Marcus, R.A.J., *Chem. Phys.* **1956**, 24, p. 966.

25. Kolaczkowski, S.V., Hayes, J.M., Small, G.J., *J. Phys. Chem* **1994**, 98, p. 13418.

26. Czikklely, V., Forsterling, H.D., Kuhn, H., *Chem. Phys. Lett.* **1970**, 6, p. 207.

27. Chang, J.C., *J. Chem. Phys.* **1977**, 67, p. 3901.

28. Krueger, B.P., Scholes, G.D., Fleming, G.R., *J. Phys. Chem. B* **1998**, 102, p. 5378.

29. Zazubovich, V., Jankowiak, R., Small, G.J., *J. Phys. Chem. B*. **2002**, 106, p. 6802.

30. Kittel, C., *Introduction to Solid State Physics*; 5th ed.; John Wiley and Sons: New York, 1976.

31. Dresselhaus, G., *Phys. Chem. Solids* **1956**, 1, p. 14.

32. Elliot, R.I., *Phys. Rev.* **1957**, 108, p. 1384.

33. van Amerongen, H., Valkunas, L., van Grondelle, R., *Photosynthetic Excitons*; World Scientific Publishing: New York, 2000; p. 50-71.,

34. Kasha, M., Rawls, H.R., El-Bayoumi, M.A., *Pure Appl. Chem.* **1965**, 11, p. 371.

35. Jankowiak, R., Hayes, J.M., Small, G.J., *J. Phys. Chem. B* **2002**, 106, p. 8803.

36. Merry, S.A., Kamazaki, S., Tachibana, Y., Joseph, D.M., Porter, G., Yoshoara, K., Barber, J., Durrant, J.R., Klug, D.R., *J. Phys. Chem.* **1996**, 100, p. 10469.

37. Leegwater, J.A., Durrant, J.R., Klug, D.R., *J. Phys. Chem.* **1997**, 101,1, p. 7205.

38. Louwe, R.J.W., Vrieze, J., Hoff, A.J., Aartsma, T.J., *J. Phys. Chem. B* **1997**, 101, p. 11273.

39. Drenth J., *Principles of Protein X-Ray Crystallography;* Springer-Verlag: New York, 1999.

40. McDermott, G., Prince, S.M., Freer, A.A., Hawthornthwaite-Lawless, A.M., Papiz, M.Z., Cogdell, R.J., Isaacs, N.W., *Nature* **1995**, 374, p. 517.

41. Ferreira, K.N., Iverson, T.M., Maghlaoui, K., Barber, J., Iwata, S., *Science* **2004**, 303, p. 1831.

42. Jordan, P., Fromme, P., Witt, H.T., Klukas, O., Saenger, W., Krauss. N., *Nature* **2001**, 411, p. 909.

43. Loll, B., Kern, J., Saenger, W., Zouni, A., Biesiadka, J., *Nature* **2005**, 438, p. 1040.

44. Englman, R., *Nonradiative Decay of Ions and Molecules in Solids*; North-Holland: Amsterdam, 1979.

45. Cochran, W., In *Phonons In Perfect Lattices and In Lattices with Point Imperfections*, Stevenson, R.W.H., Ed.; Plenum: New York, 1966; p. 53.

46. Burland, D.M. and Zewail, A.H., *Adv. Chem. Phys.* **1979**, 40, p. 369.

47. Johnson, C.K, and Small, G.J., In *Excited States*, Lim, E.C., Ed.; 1982; Vol. 6, p. 97.

48. Freiberg, A., Ratsep, M., Timpmann, K., Trinkunas, G., Woodbury, N. W., *J. Phys. Chem. B* **2003**, 107; p. 11510.

49. Timpmann, K.; Ratsep, M.; Hunter, C. N.; Freiberg, A., *J. Phys. Chem. B* **2004**, 108, p. 10581.

50. Redfield, A.G., *Adv. Magn. Reson.* **1965**, 1, p. 1.

51. Jean, J.M., *J. Phys. Chem. A* **1998**, 102, p. 7549.

52. Pollard, W.T., Felts, A.K., Friesner, R.A., *Adv. Chem. Phys.* **1996**, 93, p. 77.

53. Pollard, W.T., Friesner, R.A., *J. Chem. Phys.* **1994**, 100, p. 5054.

54. Arnoldi, W.E., *Q. Appl. Math.* **1951**, 9, p. 17.

55. Friesner, R.A., Tuckerman, L.S., Dornblaser, B.C., Russo, T.V., *J. Sci. Comput.* **1989**, 4, p. 327.

56. Runge, C. *Math. Ann.* **46**, 167, p. 1895.

57. Arfken, G. *Mathematical Methods for Physicists,* 3rd ed.; Academic Press: Orlando, Florida, 1985; p. 492.

58. Novoderezhkin, V., Salverda, J. M., van Amerongen, H., van Grondelle, R., *J. Phys. Chem. B* **2003**; 107, p. 1893.

59. Novoderezhkin, V. I., Yakovlev, A. G., van Grondelle, R., Shuvalov, V. A, *J. Phys. Chem. B* **2004**, 108, p. 7445.

CHAPTER 3 – HOLE-BURNING AND SINGLE-MOLECULE SPECTROSCOPY

3.1 Spectral Lineshape Theory

Optical excitation of a molecule involves absorption of a quantum of light energy which promotes an electron from a ground state (E_g) to a higher quantized electronic energy level (E_{ex}). This excited electron can then return to the ground electronic state by emitting a photon or through radiationless energy decay. Since this excitation-decay process is quantum mechanical in nature, the Heisenberg uncertainty principle (H.U.P.) must be satisfied. The familiar form of H.U.P. is given by

$$\Delta x \Delta p \geq \frac{h}{2\pi} \tag{3.1}$$

where x is the position of the electron, p is its' momentum, and h is Planck's constant [1]. However, for optical spectroscopic processes, this relation can be recast in a more useful form as

$$\Delta E \Delta t \geq \frac{h}{2\pi} \tag{3.2}$$

where E is the energy of the electron and t is the time the electron spends at this particular energy [1]. It can be seen then that when the electron is promoted to a higher quantum energy level, the energy cannot be precisely known. Along with this, the time that this electron spends in this higher energy level cannot be precisely known; so to determine either the energy or time of a particular transition more precisely sacrifices the accuracy of the other. Therefore, the spectral lineshape of an optical transition is necessarily broadened by this condition, which is called *uncertainty or homogeneous broadening* [2].

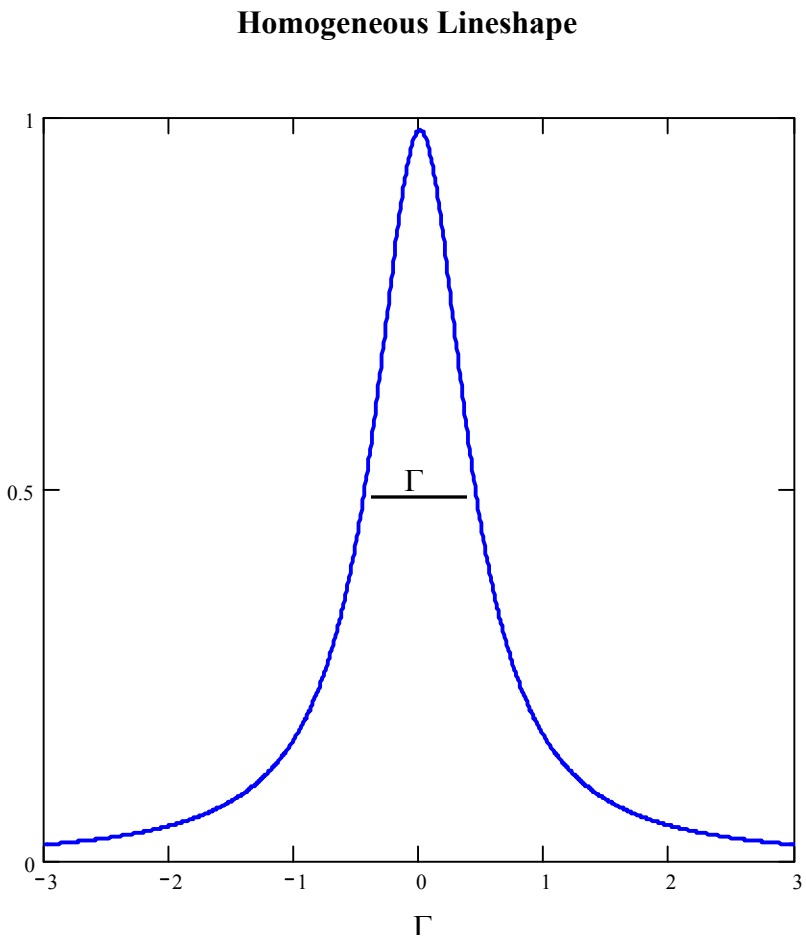

Figure 1. Natural or homogeneous lineshape of a ZPL [3]. The homogeneous profile is Lorentzian and carries a full width at half maximum (FWHM) of $\Gamma = 1/2\pi cT_1$, as defined by the Heisenberg uncertainty principle (Eq 3.2).

This is often referred to as the *natural or homogeneous lineshape* of an optical transition (see Fig. 1).

For guest-host systems, such as molecular impurities in solid-state matrices (e.g. crystals, glasses, proteins), the homogeneous linewidth of an optical transition for a guest molecule at the zero point temperature (T = 0) has a characteristic time, referred to as the *energy relaxation time*. From Eq. 3.2, this relationship can be expressed as [3]

$$\Gamma(0) = \frac{1}{2\pi\, cT_1} \tag{3.3}$$

where $\Gamma(0)$ is the homogeneous linewidth in cm^{-1} at T = 0, c is the speed of light, and T_1 is the relaxation time. Unlike gas-phase optical transitions, Doppler broadening is not present since the guest molecule is attached to mass of the host matrix [3]. At T = 0, the homogeneous linewidth is appreciably narrow (10^{-4}-10^{-3} cm^{-1}) with a relaxation time of $T_1 \approx 10^{-7}$-10^{-8} s [3]. At $T \neq 0$, the homogeneous lineshape begins to broaden due to dephasing processes induced by thermally activated phonon modes of the host matrix.

The dephasing induced by phonons results from quasi-elastic scattering of a phonon by the molecular impurity, which changes the phonon's direction of propagation and a negligible change to its energy. For the impurity, this scattering results in a change in the phase of the excited electronic state wavefunction so that the time dependent part, $\exp(iE_{ex}t/\hbar)$, acquires an additional random phase component, δ, and changes to $\exp[(iE_{ex}t/h)+i\,\delta]$ [3]. Consequently, the lifetime of the excited quantum state is shortened, and the spectral linewidth carries additional uncertainty broadening. Therefore, at $T \neq 0$ the homogeneous linewidth must be described in terms of the energy relaxation and dephasing times:

$$\Gamma(\mathrm{T})\ \left[\mathrm{cm}^{-1}\right] = \frac{1}{\pi\ cT_2} = \frac{1}{\pi\ c}\left[\frac{1}{2T_1} + \frac{1}{T_2^*}\right] \tag{3.4}$$

where T_2 is the coherence time and T_2^* is (pure) dephasing time of the excited electronic state [4]. For electronic transitions from one quantum state to another where no phonons are created or destroyed, no additional dephasing occurs. The homogeneous lineshape for these transitions is called the *zero-phonon line* or ZPL [3]. ZPLs can either result from purely electronic transitions or from vibronic transitions (simultaneous electronic and vibrational transitions) (see Fig. 1).

For transitions from one quantum state to another where phonons are created or destroyed, through coupling of the impurity molecule to the phonon modes of the matrix (electron-phonon coupling), a broad continuous band, called the *phonon sideband*, is seen along with the ZPL with a characteristic width of Γ_{PSB}. The strength of the phonon side band (PSB) can be explained through the Franck-Condon principle (see Fig. 2) [3]. For weak electron-phonon coupling, the geometry change of the impurity molecule is relatively small in the excited electronic state and thus the normal lattice coordinate of the host matrix is also small, leading to a weak PSB feature. For strong electron-phonon coupling, the geometry change of the impurity molecule is relatively large in the excited electronic state and thus the normal lattice coordinate of the host matrix is also large, leading to a strong PSB feature. Large geometry changes between excited and ground state molecular configurations also increase the probability of vibronic transitions, which can lead to very strong electron-phonon coupling due to pseudo-localized phonons of the probe molecule. Therefore, depending on the mixed solid system, the PSB structure can

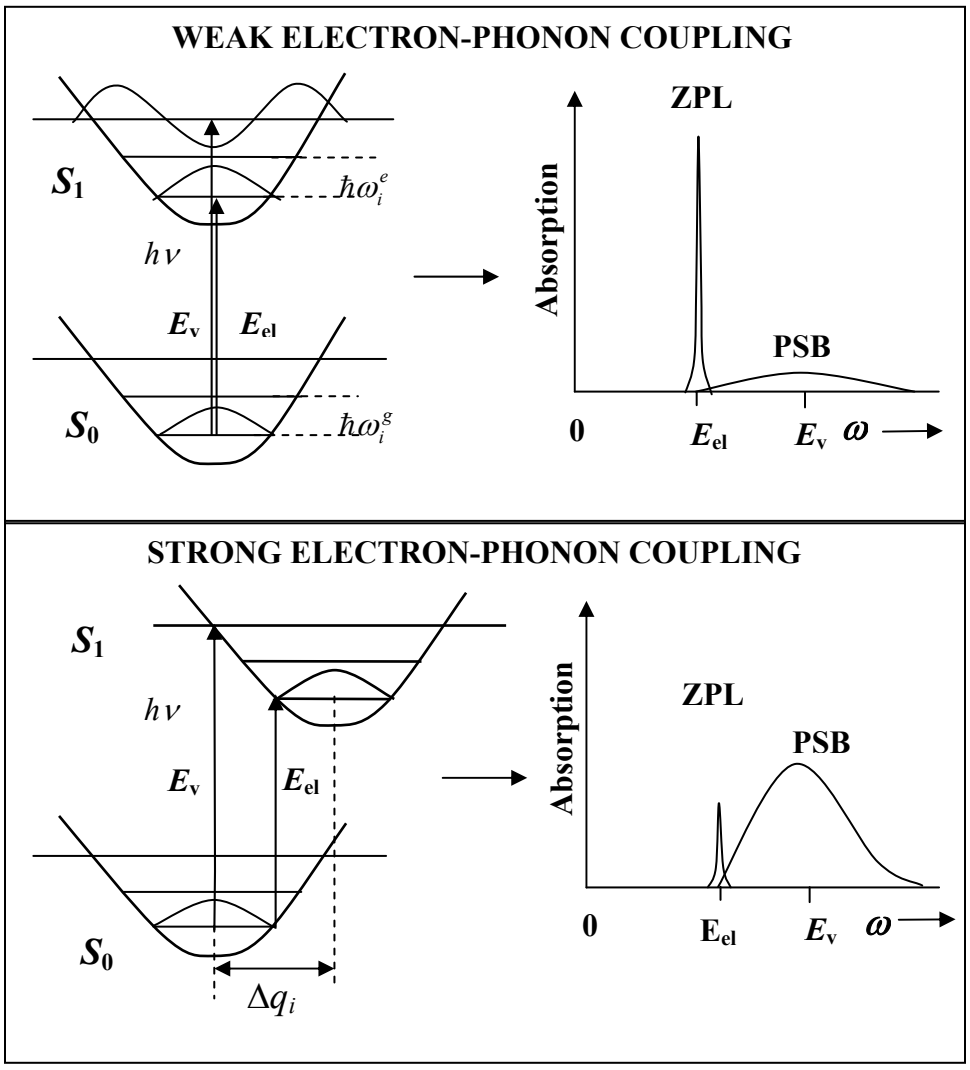

Figure 2. Schematic of the electron-phonon coupling of a guest impurity molecule in a low temperature solid host matrix via the Franck-Condon principle [9]. After excitation by $h\nu$, the molecule makes a transition from the ground electronic state, S_0, to the excited electronic state, S_1. The lattice coordinate displacement, Δq, determines the overlap between the ground and excited state vibrational wavefunctions; the stronger the overlap, the stronger the PSB feature. E_{el} and E_v represent the pure electronic and vertical transition energies, respectively. $\hbar\omega_i^g$ and $\hbar\omega_i^{ex}$ are the ground and excited state vibrational energy levels, respectively. [9]

be due to delocalized phonons of the host or pseudo-localized phonons associated with the probe molecule [5, 6].

More specifically, the PSB arises from the linear electron-phonon coupling [7]. The interaction of phonon quanta with the molecular impurity can be described using a harmonic oscillator model and be written in the following form [8]:

$$V = \sum_i A_i q_i + \sum_{ij} B_{ij} q_i q_j . \tag{3.5}$$

where the first term in Eq. 3.5 describes the linear electron-phonon coupling with A_i being the linear coupling coefficients while the second term describes the quadratic electron-phonon coupling with B_{ij} being the quadratic coupling coefficients. The quadratic electron-phonon coupling describes the energy change in the excited state due to the change in the normal oscillator frequencies during an excitation. For no coordinate change during excitation, or when $i = j$, the quadratic electron-phonon coupling gives rise to homogeneous broadening of the ZPL (see above). When the normal oscillator frequencies change during excitation, or $i \neq j$, the quadratic coupling describes the energy change due to the mixing of lattice normal coordinates [9]. This coordinate mixing is referred to as normal coordinate (Dushinsky) rotation [10].

The spectral intensities of both the ZPL and PSB features can be characterized using the Debeye-Waller factor (DWF), α (also known as the FC factor) [6, 11, 12]:

$$\alpha = \frac{I_{\mathrm{ZPL}}}{I_{\mathrm{ZPL}} + I_{\mathrm{PSB}}} \tag{3.6}$$

where I_{ZPL} and I_{PSB} are the relative integrated intensities of the ZPL and the PSB, respectively. At $T \sim 0$ in the harmonic oscillator model for N phonon modes, the DWF factor is given by

$$\alpha = \exp(-S) \ , \tag{3.7}$$

where S is the dimensionless Stokes shift (also known as the Huang-Rhys factor) and is expressed as [11]:

$$S(T=0) = \frac{M_i \omega_i}{2\hbar} \sum_i (\Delta q_i)^2 \ . \tag{3.8}$$

In Eq. 3.8, M and ω_i are the reduced mass and frequency of the phonon mode i, respectively, and Δq_i is the change in equilibrium of lattice normal coordinate q_i. From Eq. 3.8, we see that $S \propto (\Delta q_i)^2$. Thus, S can be used to characterize the strength of the electron-phonon coupling. In general, electron phonon coupling is weak when $S < 1$. For $S > 1$, the electron-phonon coupling is strong [6, 12].

The DWF is temperature dependent. It decreases rapidly and, usually, monotonically as temperature increases, i. e. increasing temperature results in a rapid decease of ZPL intensity. The temperature dependent DWF is given by [13]:

$$\alpha(T) = \exp\left[-\sum_i^N S(2\bar{n}_i + 1) \right] , \tag{3.9}$$

where thermal occupation number, $\bar{n}_i = \left[\exp(\hbar\omega_i / kT) - 1\right]^{-1}$, is the average number of phonons of mode i at temperature T. $\alpha(T)$ reaches its maximum value at very low temperatures (T $\leq$ 10 K for most organic glasses).

3.2 Inhomogeneous Broadening

The preceding section discussed homogeneous lineshapes for a *single* impurity molecule in a host matrix. An ensemble of impurity molecules, however, will show a different characteristic spectrum. If the host matrix is not perfectly ordered so that each molecule experiences an identical environment, each molecule will experience a *different*

local nanoenvironment. These different local environments rise from the particular inhomogeneities in the host matrix (e.g. point, linear, surface defects; stress field variation; irregular molecular ordering) that shift the ground and excited states of the guest impurity molecules, and in solid matrices this is always the case [14]. Therefore, the coupling of each impurity molecule to the host matrix will be different and result in a distribution of homogeneous lineshape frequencies. This phenomenon is called *inhomogeneous broadening* [14, 15].

In order to characterize the inhomogeneous broadening it is convenient to introduce the inhomogeneous distribution function (IDF), $G(\omega)$, which is most commonly assumed to be a smooth Gaussian shaped function [14, 15, 16]. The bandwidth (Γ_{inh}) of the IDF is always larger than the homogeneous width, $\Gamma(0)$. Even for impurity doped Shpol'skii systems where the guest molecules are embedded in a highly ordered crystalline host, the disorder is large enough that $\Gamma_{inh} \approx$ 1-5 cm^{-1} [14]. For glasses and proteins the magnitude is significantly greater with $\Gamma_{inh} \approx$ 100-400 cm^{-1}, a factor of 10^5-10^6 greater than $\Gamma(0)$ [15]. To see the effects of inhomogeneous broadening, one only needs to convolve the single site spectrum of one molecule, $\Gamma(T) + \Gamma_{PSB}$, with $G(\omega)$. As seen in Fig. 3, this convolution results in broadening of the ZPL and PSB features in a Shpol'skii host system but a complete elimination of any discernable spectral features in a glassy host system. This convolution consequently gives for the ensemble spectrum a characteristic width of about $\Gamma_{inh} + S\omega$, where ω_m is the mean phonon frequency and S is the Huang-Rhys factor as defined above [17, 18, 19].

An inhomogeneous impurity absorption band is therefore a superposition of two parts: a continuous band that is the sum of all the individual PSBs and a sum of sharp

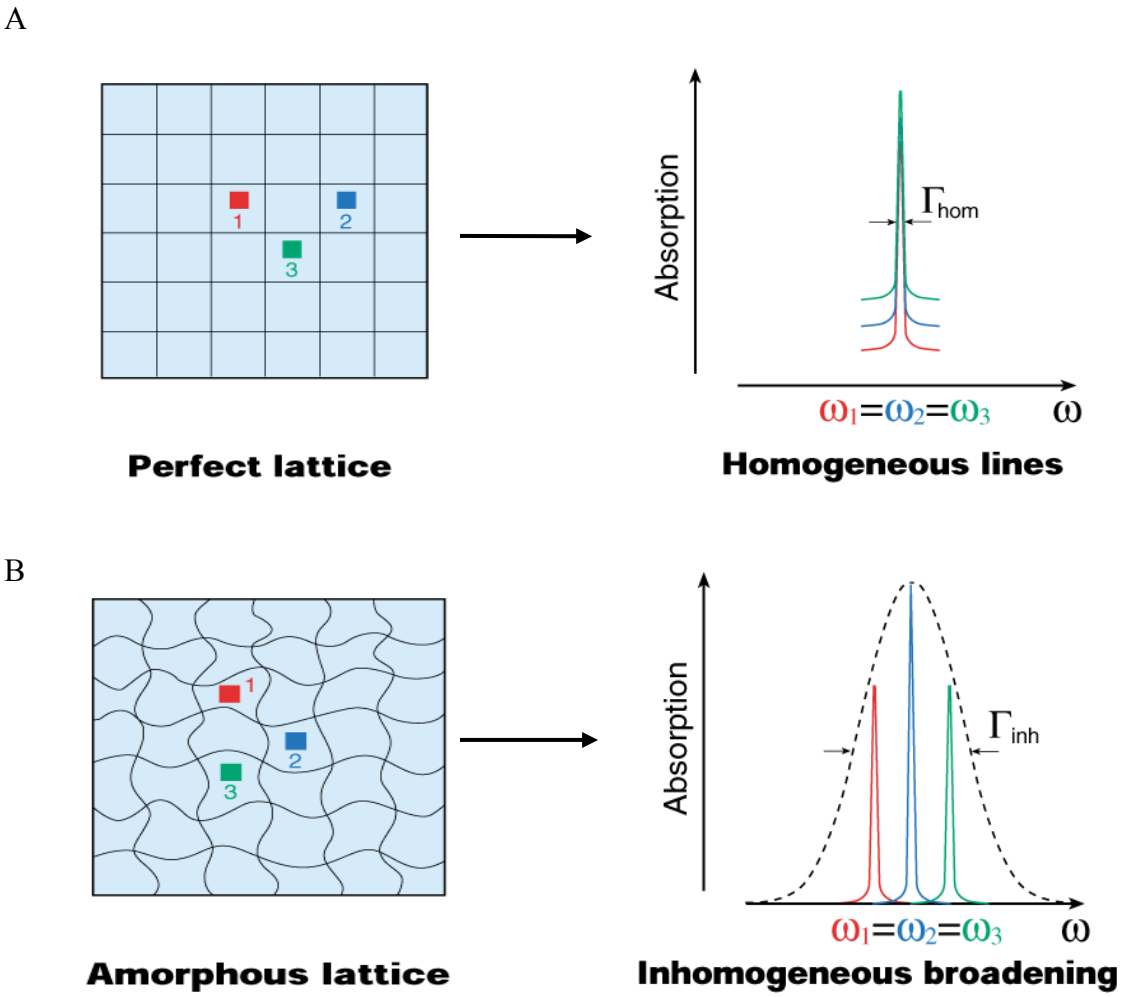

Figure 3. Schematic of homogeneous vs. inhomogeneous broadening. In frame (A), guest impurity molecules are in a perfect host lattice. Homogeneous lines (Γ_{hom}) overlap, resulting in an absorption spectrum with a linewidth = individual ZPL. In frame (B), guest impurity molecules are in a disordered host lattice, so that each impurity molecule absorbs at different frequency. This leads to a distribution of ZPL absorption frequencies and thus, the impurity absorption band is *inhomogeneously broadened*.

ZPL lines, both of which are hidden by the inhomogeneous spectrum. Since the inhomogeneous band obscures the detailed ZPL and PSB information, methods of selective excitation at low temperature are needed. Numerous site selective spectroscopies have been developed to overcome the effects of large inhomogeneous spectral broadening, such as fluorescence line narrowing (FLN) [9, 28], spectral hole-burning (HB) [20-24], photon echo (PE) [25-28], and single-molecule spectroscopy (SMS) [33, 34]. In particular, spectral HB and SMS provide extremely high spectral resolution and sensitivity along with being powerful tools for probing the structural disorder and molecular dynamics of amorphous glassy solids. This is especially true for SMS, which works at the ultimate limit of site-selective spectroscopy- spectrally and spatially selecting out an individual impurity in an ensemble.

3.3 Hole-Burning Spectroscopy

Spectral hole-burning is a powerful site selective spectroscopy of impurities in crystalline and amorphous solids. It can reveal hidden spectral information, such as the homogeneous ZPL linewidth, electron-phonon coupling parameters, and exciton-level structure determination in proteins [35]. Moreover, it has been used as a powerful tool for probing the structural disorder and configurational tunneling dynamics of amorphous and glassy solids at low temperature [3, 35, 48, 69]. Spectral hole-burning was first reported by Personov et al. [36] for perylene and 9-aminoacridine in ethanol at 4.2 K. Similarly, Gorokhovskii et al. [33] reported similar observations for phthalocyanine in a Shpol'skii matrix. For detailed information, excellent reviews of spectral hole-burning can be found in references [19-24. 38, 39].

The basic physical principles of hole-burning (HB) are quite straightforward. To burn a spectral hole, a narrow bandwidth laser (λ_B) is used to excite a small subset of impurity molecules, which can be excited via their ZPLs in an inhomogeneously broadened absorption band. When these molecules are optically excited, they are then photophysically or photochemically transformed so that when they return to their ground electronic state, they no longer absorb at their original frequency. This leaves the inhomogeneous absorption band with a "hole" that has a shape that reveals the ZPL and PSB structure of these selected molecules (see Fig. 4). For sufficiently narrow laser linewidths, only the homogeneous lines that absorb at the exact same frequency will be "burned", thereby revealing the hidden individual homogeneous lineshapes in the inhomogeneously broadened band [38].

The different photophysical and photochemical pathways that result in a spectral hole determines the particular hole burning method. In *photochemical hole-burning* (PHB) *spectroscopy* [3, 27, 29-32], there is a photoreaction (such as tautomerization, bond breaking, and isomerization) of the impurity molecules in the excited electronic state so the chemical identity changes when the molecules return to the ground electronic state. The molecules then no longer have the same optical properties and do not absorb at the original excitation frequency. In *nonphotochemical hole-burning* (NPHB) *spectroscopy* [3, 35, 38], the host-guest matrix undergoes structural rearrangements when the impurity molecules are optically excited [40]. When the photochemically stable impurity molecules return to the ground electronic state the local nanoenvironment is different resulting in an energy shift of the impurity molecules, resulting in a spectral hole. Most commonly, NPHB is

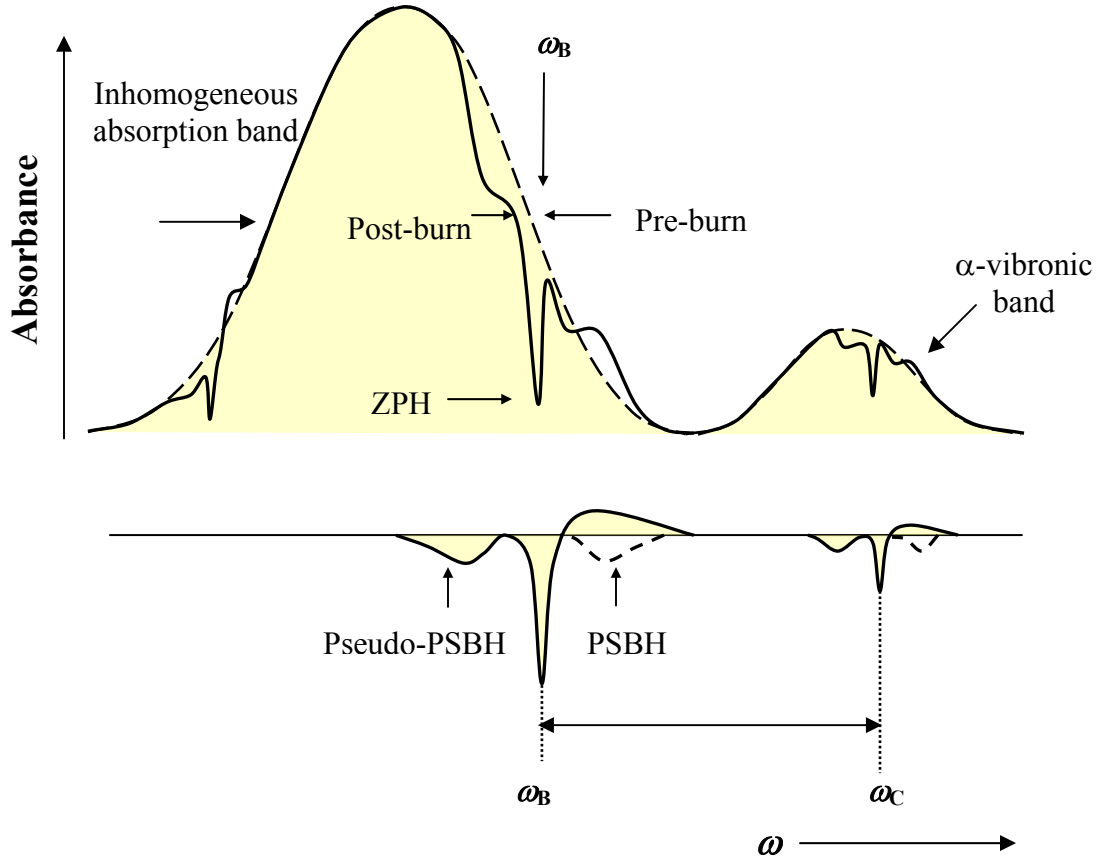

Figure 4. Spectral hole-burning in an inhomogeneously broadened absorption band [47]. Two curves represent the pre-burn (dashed-line) and the post-burn (solid line) absorption spectrum. After hole burning at frequency ω_B, the resulting hole-burning spectrum is shown about the zero line (the difference between the pre-burn and post-burn absorption spectrum). Spectral holes form at ω_B and ω_C. The hole at ω_B consists of a zero-phonon hole (ZPH) component, which forms from burning out the ZPLs that are excited at ω_B. There are also phonon side band hole (PSBH) and pseudo-PSBH components. The PSBH forms from burning out the PSBs that are excited at ω_B. The pseudo-PSBH results from burning out the ZPLs that lie lower in energy to ω_B, and burn via their PSBs. Another hole also forms at ω_C by burning into the α-vibronic band of the main electronic absorption band.

observed in low temperature amorphous systems (glasses, polymers, and protein hosts) because of their inherent configurational host-guest interactions.

Unlike crystals whose low temperature properties are determined by phonons, glasses and proteins are determined by a different low temperature excitation, two-level systems (TLS) [35, 41, 42]. TLS are atoms or groups of atoms that can occupy different energetic configurations. It is the coupling of the impurity molecules to these TLS that accounts for the phenomenon of NPHB and is shown by a scheme of TLS transitions coupled to an impurity (extrinsic two-level system, TLS_{ext}) in Fig. 5 [40, 43, 44]. The superscripts α and β label the ground and excited electronic states of the probe. It is considered that excitation of the zero-phonon transition of a chromophore at frequency ω_B occurs in the left well, and is followed by a tunneling process in the excited state. The hole burning process of the chromophore competes with the relaxation to the ground state as depicted on the right well. The left to right relaxation that takes place in the excited electronic state leads to a blue-shifted anti-hole.

Based on optical dephasing studies [43, 45], it was suggested that for hole-burning two types of TLS - extrinsic (TLS_{ext}) and intrinsic (TLS_{int}) – are important. TLS_{ext} are associated with the impurity molecule and its inner shell of solvent molecules. In NPHB, the TLS_{ext} are responsible for the initiation of the hole formation. TLS_{int} of the host are connected with the excess free volume of glasses [46]. It is the coupling of the impurity molecules to the TLS_{int} and low frequency phonon modes that are responsible for optical dephasing in glassy solids. When the impurity molecule is optically excited, this triggers the rearrangement of the host environment, which then initiates the phonon-assisted tunneling process that leads to hole formation. Therefore, it is the

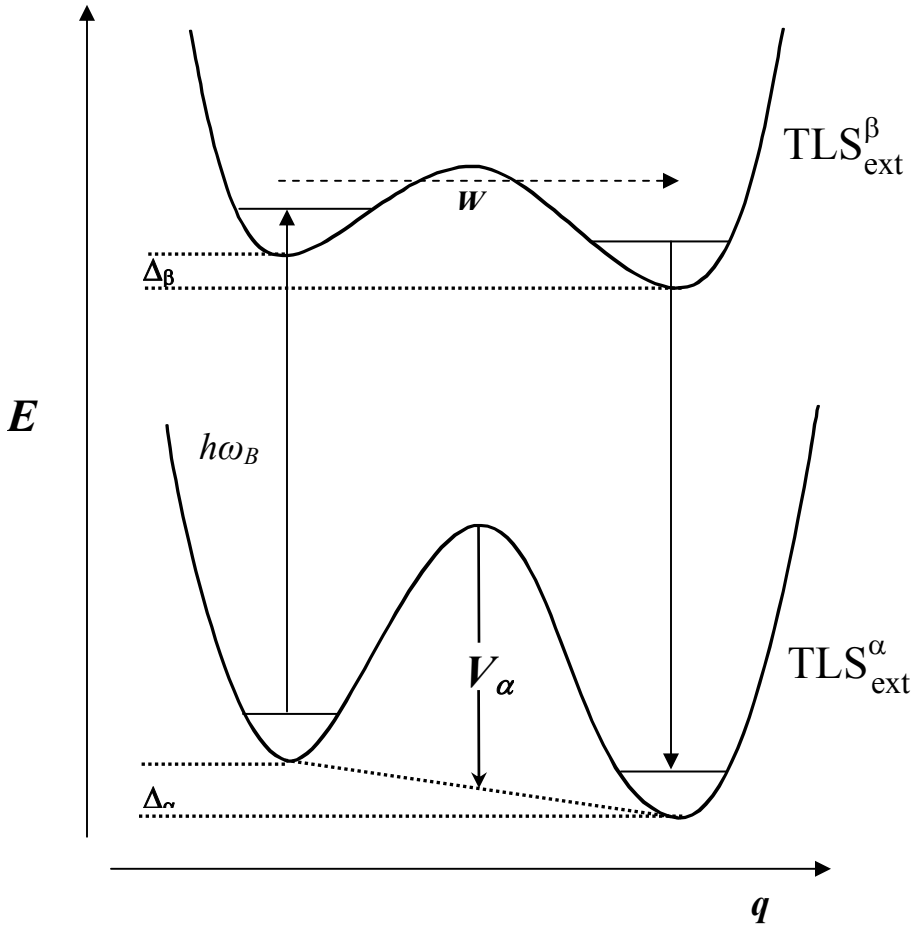

Figure 5. Schematic of the NPHB mechanism [35, 43, 47]. The diagram shows the extrinsic two level system (TLS_{ext}) of a guest molecule in the ground state (α) and excited state (β). After excitation ($h\omega_B$) at the burn frequency (ω_B) to β, the TLS_{ex} flips, due to the much lower barrier height (V_α) compared to the ground state, through phonon assisted tunneling (PAT), which is represented by the tunneling frequency, W. The molecule then decays to the ground state and finds itself in a different host configuration, and therefore absorbs at a different frequency. This results in the formation of a persistent spectral hole that can be observed experimentally. Δ_α and Δ_β are the double well asymmetry parameters in the ground and excited state, respectively. q represents the intermolecular coordinate, ω_B is the burn frequency.

phonon-assisted tunneling in TLS_{ext}^{β} that is the rate-determining step in NPHB. The TLS_{ext}^{β} energy diagram in Fig. 5 depicts the situation where phonon-assisted tunneling in the excited state involves phonon emission and the anti-hole site absorbs at higher energy of ω_B. There are seven other energy level schemes [43]. Four of the eight lead to blue-shifted anti-hole sites, whereas the other four lead to red-shifted sites. Four of the schemes involve phonon absorption; the other four involve phonon emission. Extensions beyond the TLS model have also been made [48]; Shu and Small have proposed multi-level systems (MLS) in glasses and proteins, where several energetic configurations are present to further explain the NPHB phenomenon [43, 44].

Both PHB and NPHB are referred to as persistent hole burning methods, since the holes can be observed on an experimental timescale longer than it takes to burn them. This is in contrast to *transient spectral hole-burning*, where the holes can only be observed an a timescale equal to or shorter than the experimental timescale it takes to burn them [49]. In transient spectral hole burning, (or *triplet bottleneck hole-burning* (TBHB)), the triplet state is used as a reservoir to store excited impurity molecules in resonance with the laser line. While the impurity molecules are pumped into the triplet state, the absorption signal change can be measured with a spectrometer [49], or by using a reference laser beam to monitor the lifetime of the transient hole [50].

In particular, PHB, NPHB, and TBHB are powerful methods for determining the low temperature excitation/energy transfer properties of photosynthetic pigment protein complexes, whose spectra are inhomogeneously broadened due to intrinsic structural disorder of the protein matrix [15, 35, 38]. These spectroscopies can reveal important information, such as: (a) the inhomogeneous broadening of Γ_{inh} of

$S_0 \rightarrow S_1$ (Q_y) chlorophyll pigment protein electronic transitions via ZPH action spectra [35, 51-58], (b) electron-phonon coupling parameters (S and ω_i) and intramolecular Franck-Condon factors via vibronic spectral hole structure [15, 59, 60], (c) the extent of correlation between site-distribution functions (SDF) of different molecular electronic transitions [30], and (d) the excitation energy transfer (EET) and electron transfer rates from the zero-point vibrational level in and between different photosynthetic complexes [30, 43]. Information obtained from (a), (b), and (c) are especially important for photosynthetic EET calculations since they determine the spectral density in the nonadiabatic Förster rate equation (see Chapter 2.2). More recent developments in NPHB spectroscopy involve the coupling with external fields, e.g. electric (Stark), high pressure. [60-64].

In Stark HB spectroscopy, broadening or splitting of the ZPH is observed with applied electric field [65, 66]. This yields the value of $f\Delta\mu$, where $\Delta\mu$ is the permanent dipole moment change and f is the local field correction factor. In the absence of ZPH splitting, the change in $\Delta\mu$ is determined from the change in $\Gamma(0)$ in response to the applied field ($\mathbf{E}_S$). In this case,

$$\Gamma(F) = \Gamma_0 (1 + F^2)^{1/2} \tag{3.10}$$

where Γ_0 is the ZPH linewidth at zero applied field and Γ is in units of circular frequency [65, 67], where F is given by:

$$F = 2f \cdot \Delta\mu \mathbf{E_S} / \hbar\Gamma_0 \tag{3.11}$$

In glasses, the absence of Stark splitting may be expected when the matrix induced component of $\Delta\mu$ is larger than the inherent molecular $\Delta\mu$ component. Large electric

field $f\Delta\mu$ shifts are important because they can separate the excitonic states of closely spaced Chl molecules that are strongly coupled and possess charge transfer character [61, 68].

For high pressure hole burning experiments, the linear pressure shift rates of the ZPH (R_p) for strongly coupled Chl molecules are large (R_p > ~0.2 cm^{-1}/MPa), compared to the ZPH shift rates for excitations localized on a single Chl pigment molecule (R_p ~ 0.05 to -0.15 cm^{-1}/MPa), and thus can be used to separate and characterize excitonic states. The linear pressure shift rates of ZPHs can also be used to identify closely spaced excited states that cannot be easily resolved based on their hole burning characteristics [62, 63].

Several formalisms for the theoretical modeling of HB spectra have been developed [35, 69, 70], with one such formalism developed by Hayes and Small [70]. This has been successfully used to simulate low temperature spectral holes of impurity doped glasses such as APT in glassy water and photosynthetic complexes such as the bacterial RC, photosystem I and II of cyanobacteria, and the FMO antenna complex [19, 62, 71, 72]. By using this master equation, the absorption at Ω after burning with a laser at ω_B for time t at the low temperature limit is given by

$$A(\Omega,t) = \exp(-\sum_k S_k)\prod_k \sum_{R=0}^{\infty}\left(\frac{S_k^R}{R!}\right)\int d\omega\ G(\omega)\exp^{-\sigma P\phi t L(\omega_B-\omega)}\, l_{R,k}(\Omega-\omega-R\omega_k)\ , \quad (3.12)$$

where $G(\omega)$ is the inhomogeneous distribution function introduced previously, σ is the integrated absorption cross section of the impurity molecule (cm^2), P is the photon flux in number of photons (cm^{-2} s^{-1}), and S_k is the Huang-Rhys factor of the kth phonon. ϕ is the hole-burning quantum yield that is given by [73]

$$\phi(\lambda) = \frac{\Omega_0 \exp(-2\lambda)}{\Omega_0 \exp(-2\lambda) + \tau_{fl}^{-1}} = \frac{R}{R + \tau_{fl}^{-1}} \tag{3.13}$$

where τ_{fl} is the fluorescence lifetime. The $l_{R,k}$ are the single site lineshape functions (ZPL+PSB) with R=0,1,2… corresponding to the 0,1,2,… phonon transitions while $l_{R=0}$ is the ZPL lineshape function which is Lorentzian. $L(\omega - \omega_B)$ is the single site absorption spectrum for the ZPL centered at the burning laser frequency, ω_B. Then $L(\omega - \omega_B)$ can be expressed as follows:

$$L(\omega_B - \omega) = \exp(-\sum_k S_k) \prod_k \sum_{R=0}^{\infty} \left(\frac{S_k^R}{R!} \right) l_{R,k}(\omega_B - \omega - R\omega_k) \tag{3.14}$$

The hole burned spectrum is then the difference between the post-burn and pre-burn $[A_0(\Omega, t)]$ spectra, or $A_t(\Omega) - A_0(\Omega)$.

3.3 Single-Molecule Spectroscopy

Single-molecule spectroscopy (SMS) is, as its name implies, the spectroscopy of one single impurity molecule or, in the case of photosynthesis research, one single photosynthetic complex (SCS) at a time. This is usually achieved by using a narrow, tightly focused (through optical elements) laser that excites only one impurity molecule to a higher quantum electronic energy level (E_{ex}) in an adequately dilute sample (see Fig. 6 A-B). By looking at molecules individually, the inhomogeneous broadening of impurity molecules in disordered solids can be eliminated since there are no ensemble averaging effects present. With SMS, the statistical distribution of a parameter can be determined instead of its average value. This can uncover quantum effects and stochastic processes of molecules, which can be hidden because of ensemble averaging. Optical SMS was first reported by Moerner et al. in 1989 [74] and has since grown to be a

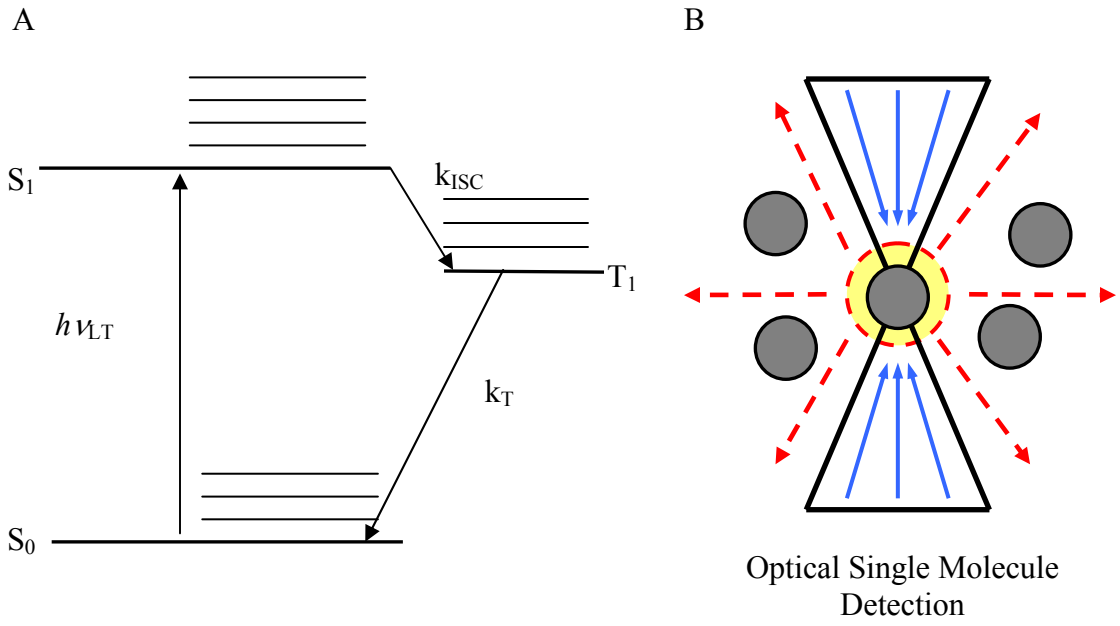

Figure 6. Energy level scheme (A) and illustration (B) of optical fluorescence single-molecule spectroscopy detection [97]. In frame (A), the molecule is excited from the zero point ground to the zero point excited electronic (0-0) transition at low temperatures, $h\nu_{LT}$, so there is no excitation from or into vibrational levels, which will cause optical dephasing. It is also advantageous to have a low intersystem cross rate, k_{ISC}, and a high triplet decay rate, k_T, so the molecule does not enter dark states where is does not fluoresce. In frame (B), a single molecule is detected by focusing the excitation profile (solid arrows), so that only one molecule is resonance, and then detecting the emitted fluorescence (dashed lines).

powerful experimental technique for uncovering atomic and molecular quantitative information. For detailed information regarding SMS theory and experimental techniques, excellent reviews of SMS and its applications can be found in references [75, 76].

Through single molecule experiments, information can be obtained that is impossible to glean under ensemble averaged experiments. For example, the homogeneous linewidths of individual molecules or complexes can be determined, such as the vibronic spectrum and the local dynamics of an impurity molecule [77-80], spectral diffusion resulting from the dynamical processes of the chromophore and protein matrix can be observed [81], and molecular transition dipole directions can be determined through polarization experiments [81-83]. SMS has also been used to detect molecular triplet state probabilities, the magnetic resonance of one spin [84, 85], and the correlation properties of emitted photons [86, 87]. Currently, fluorescence resonance energy transfer (FRET) between single biomolecules [88] and other single protein molecules [89-91] has been observed. The excitonic structure for single light harvesting systems [92] has also been determined with SMS.

Single molecules are detected optically when only one molecule is in resonance with the excitation laser beam at a time in the probe volume area and the signal to noise ratio (SNR) > 1 during the experimental timescale (see Fig. 6A). Ensuring that only one molecule is spectrally selected can be achieved by either using a sample with very low concentration (~ 10^{-7} - 10^{-10} M) or by a using sample with very large Γ_{inh} and tuning the laser excitation frequency into the wings of the inhomogeneous absorption band, where the number of resonance molecules is low. Several fluorescence microscopy optical

techniques have been successfully used for single molecule detection such as near-field optical scanning microscopy [93], confocal microscopy [94], and far-field techniques such as epiflourescence and total internal reflection microscopy [95, 96].

After this, the most challenging task for achieving SMS is to optimize the signal-to-noise ratio (SNR). For single molecule detection (using fluorescence excitation) in a solid, the SNR can be approximated by the following equation [97, 98]:

$$\mathrm{SNR} = \frac{D\phi_{\mathrm{F}}\left(\frac{\sigma^{\mathrm{P}}}{A}\right)\left(\frac{P_0}{h\nu}\right)\tau}{\sqrt{\frac{\left(D\phi_{\mathrm{F}}\sigma^{\mathrm{P}}P_0\tau\right)}{Ah\nu} + C_{\mathrm{b}}P_0\tau + N_{\mathrm{d}}\tau}} \tag{3.15}$$

where D is the overall efficiency for the detection of emitted photons (see [98, 99] for detailed description), ϕ_{F} is the fluorescence quantum yield, σ^{P} is the peak absorption cross-section, P_0 is the laser power, A is the focal spot area, $h\nu$ is the photon pump energy, τ is the detector counting interval, N_{d} is the dark count rate, and C_{b} is the background count rate per Watt of excitation power. In Eq. 3.15, the numerator represents the peak detected fluorescence counts from one molecule in time interval τ while the three terms in the denominator represent shot noise contributions from the emitted fluorescence, background, and dark signal, respectively.

According to Eq. 3.15, to maximize the SNR, the experimental conditions should be optimized for the smallest possible focal volume containing the probe molecule, thereby minimizing the background signal. In addition, the chosen probe molecule should (a) ideally have a large peak absorption cross-section, (b) high photostability and fluorescence quantum yield, (c) low triplet bottleneck probability, and (d) illumination

below the saturation of the molecular absorption [75]. The issues and concerns with each of these conditions are thus explained further.

Having a large peak absorption cross-section, σ^{P}, is extremely important for achieving SMS detection. Since the absorption probability of a single molecule from an incident photon is σ^{P}/A, maximizing σ^{P} is important for both maximizing the photon absorption from the incident laser beam and minimizing the background signals from any unabsorbed photons. At room temperature (RT), the peak absorption cross-section is given by

$$\sigma_{RT}^{P} = 2.303\varepsilon / N_{A} \tag{3.16}$$

in units cm^2, where ε is the molecular extinction coefficient (L mol^{-1} cm^{-1}) and N_A is Avogadro's constant. The low temperature peak absorption cross-section, σ_{LT}^{P} is calculated using [100]:

$$\sigma_{LT}^{P} = 3\sigma_{RT}^{P}(\Gamma_{RT} / \Gamma_{LOW}) \ , \tag{3.17}$$

where Γ_{RT} and Γ_{LOW} are the width of the absorption spectrum at room temperature and of the ZPL at low temperature, respectively.

An alternative method of estimating the peak absorption cross-section at low temperature is [98]:

$$\sigma_{LT}^{P} = 2c\tau_{2}\left(\frac{O}{N_{tot}}\right)_{ZPL} \tag{3.18}$$

where c is the speed of light, τ_2 is the total dephasing time, O is the integrated absorption, and N_{tot} is the number density of absorbers producing O (units cm^{-2}). According to Eqs. 3.17 and 3.18, σ^{P} is inversely proportional to the ZPL linewidth (and directly

proportional to τ_2). Therefore, a narrow ZPL linewidth at low temperature gives a large peak absorption cross-section [3, 98].

In addition, the impurity molecule should be photostable and show weak hole burning at the excitation laser frequency. Since spectral hole burning causes the molecule to change its resonance frequency, it is necessary to provide sufficient time averaging of the single-molecule signal before it changes appreciably or moves to another spectral position. The fluorescence quantum yield of the molecule should be high as well, i.e. approach unity. The fluorescence quantum yield, ϕ_F, is given by [97]:

$$\phi = \frac{k_{\text{rad}}}{k_{\text{rad}} + k_{\text{nonrad}}} = \frac{\tau_F}{\tau_{\text{rad}}}, \tag{3.19}$$

where k_{rad} is the radiative rate (Einstein A coefficient), k_{nonrad} is the sum of all nonradiative rates (e.g. internal conversion, intersystem crossing), τ_F is the excited state lifetime, and τ_{rad} is the radiative lifetime [75]. The best fluorescing molecules are those with rigid structures that will decay via photon emission instead of non-radiatively through vibrational or rotational coupling. Strongly emitting molecules can have lifetimes that are on the order of ns, with a maximum photon emission rate of $\sim 10^8$ s^{-1}.

Optical saturation during excitation should also be avoided, as saturation leads to excess background signal and loss of absorption intensity since the molecule cannot efficiently decay back to the ground state. For organic molecules, saturation of the optical transitions becomes evident when the laser power $P_{laser} \geq 1$ W cm^{-2}. The dependence of the emission rate $R(I)$ of an excited molecule on the saturation intensity, I_S, is given by the following expression [97, 98]:

$$R(I) = R_\infty \frac{I / I_S}{(1 + I / I_S)} \tag{3.20}$$

where I is the excitation laser intensity. R_∞ is the maximum emission rate of the excited molecule and is given by

$$R_\infty = \frac{\left(k_{21} + k_{\mathrm{ISC}}\right)\ \phi_{\mathrm{F}}}{2 + \left(k_{\mathrm{ISC}} / k_{\mathrm{T}}\right)}\ , \tag{3.21}$$

where k_{21} is the decay rate from S_1 to S_0, k_{ISC} is the rate of intersystem crossing, and k_{T} is the total decay rate from the triplet state (T_1) back to S_0.

The dependence of molecular absorption on I_{S} is given by [97, 98]:

$$\sigma^{\mathrm{P}} = \frac{\sigma_0^{\mathrm{P}}}{\left(1 + I / I_{\mathrm{S}}\right)}\ , \tag{3.22}$$

where σ_0^{P} is the low power peak absorption cross-section. The characteristic saturation intensity depends on the energy level structure of the molecule. For optical transitions of a molecule that approximate a ground to excited state electronic transition, the saturation intensity is given by [75]:

$$I_{\mathrm{S}} = \frac{h\nu}{2\sigma^{\mathrm{P}}\tau_{\mathrm{F}}} \tag{3.23}$$

where τ_{F} is fluorescence lifetime. However, intersystem crossing from singlet states into triplet states can represent a bottleneck and causes cessation of both absorption of photons and photon emission for a relatively long time equal to the triplet state lifetime. This effect results in premature saturation of the emission rate from the molecule and reduction of the absorption cross-section σ^{P}. Therefore, the premature saturation of the optical transition is dependent on whether the molecules have large triplet bottleneck probabilities. The saturation intensity for a molecule with a triplet bottleneck can be estimated using the following expression [97, 98]:

$$I_S = \frac{h\nu k_{21}}{2\sigma^P}\left[\frac{1+(k_{ISC}/k_{21})}{1+(k_{ISC}/2k_T)}\right]. \quad (3.24)$$

In Eq. 3.24, the factor outside the brackets represents the saturation intensity if there was no triplet bottleneck, giving an upper limit for the saturation intensity. According to this equation, in order to minimize the triplet bottleneck probability, ideal impurity molecules should be those which give small values of k_{ISC} and large values of k_T. Commonly, organic rigid, planar aromatic molecules, such as chlorin pigment molecules, satisfy these requirements [74, 75].

3.3 SMS Experimental System

While many optical techniques for SMS have been developed (see above), epiflourescence and confocal microscopy detection schemes remain ubiquitous for SMS due their excellent combination of spatial and spectral selectivity [74, 75, 97]. For the single molecule experiments presented in this dissertation, a unique low temperature confocal microscopy experimental system was developed for detection of single photosynthetic complexes.

The optical system was based on a home-built confocal microscope with a Newport 60x 0.85 NA achromatic objective attached to the sample holder inside an immersion liquid helium cryostat (Janis). In order to reduce sample movements due to temperature expansion, the rod of the sample holder was made from fused quartz. The sample was moved in relation to the objective along the objective axis using an electromagnet with two parallel coils, one superconducting (for T < 7K) and the other made from copper wire. A computer-controlled scanning mirror was used to move the focal spot across the sample plane. Excitation was performed with a Coherent CR-699 laser with Exciton LD-688 dye (650-720 nm), and with intra-cavity etalons removed,

providing a linewidth of several GHz. After adjustment and to ensure that the photosynthetic complex containing sample was indeed in the focal plane of the objective, the scanning mirror was moved while the fluorescence (excited at 675-680 nm) was collected (at $\lambda > 700$ nm) by an avalanche photodiode (Perkin-Elmer, dark count < 25 s^{-}). In order to focus on individual complexes, the mirror was then moved to positions determined from the raster-scan image and spectroscopic measurements were performed. Fluorescence excitation spectra were recorded with either a Princeton Instruments PI-MAX intensified CCD camera or a liquid nitrogen-cooled, back–illuminated CCD camera. A Jobin-Yvon Triax 320 spectrometer with a resolution of 0.4 nm was used to record fluorescence emission spectra. For photosystem I (PS I) single complex experiments, an Omega AELP 700 long-pass filter and DRLP 710 dichroic mirror were used since PS I emits > 700 nm. Also, in order to reduce background (mainly broadband dye fluorescence) an Omega 3rd Millennium SP700 short-pass filter was placed after the laser power stabilizer (BEOC). The experimental setup is schematically depicted in Fig. 7.

Samples for single complex experiments were prepared by first diluting a concentrated photosynthetic complex solution (~ 10^{-3}-10^{-4} M) with suitable buffer to achieve a Chl *a* concentration of approximately 10^{-7} M, where the concentration is determined by absorption. Then the solution is diluted again in a buffer/glycerol mixture (3:1) by a factor of ~ 1000, and then spin-coated on a plasma-cleaned sapphire plate yielding a film thickness of less than 1 μm. The use of glycerol here was not meant to facilitate formation of a transparent glass, but to adjust the viscosity of the solution for better thin film formation. Polymers were not used for sample preparation because,

based on our experience (unpublished results), the photosynthetic complexes embedded in dry polymer films are disrupted compared to those studied in typical bulk experiments. Samples were then placed in a cold (< 0º C), dark, oxygen-free cryostat and the temperature was lowered to liquid helium temperature in about 20 minutes. Experiments were performed at 10 K in helium gas or at 2 K in superfluid helium. To avoid sample degradation, all room-temperature sample-handling procedures were performed in dim light as quickly as possible.

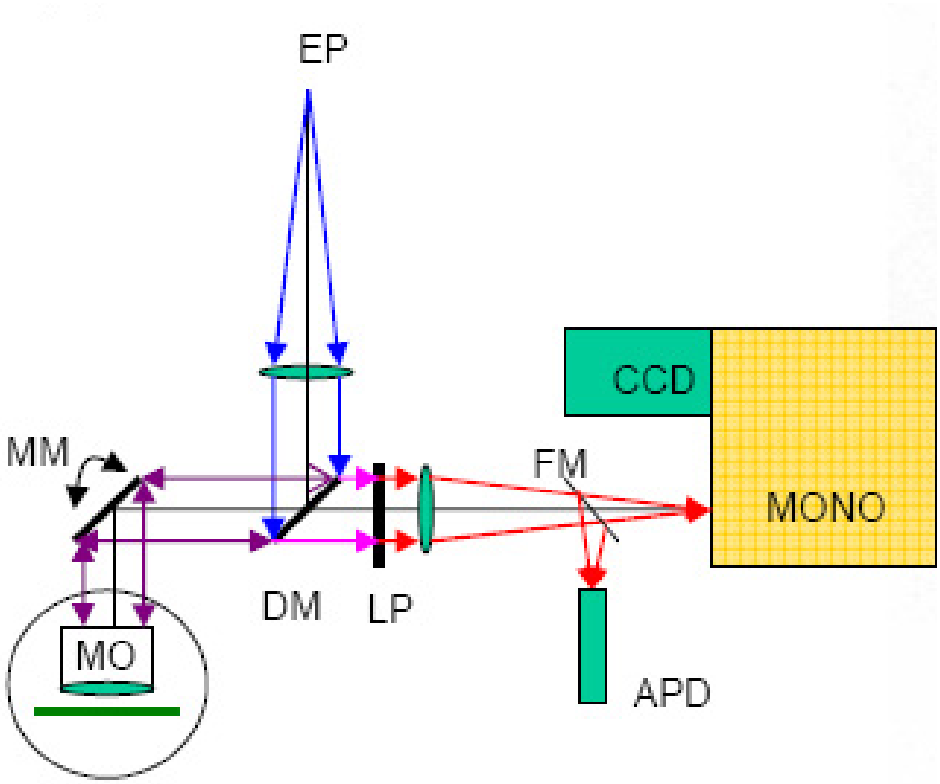

Figure 7. Schematic of confocal microscope used for single complex spectroscopy. EP is the excitation pinhole, DM is the dichroic mirror, MM is the motorized mirror, MO is the microscope objective, LP is the long-pass filter, and FM is the flipping mirror. The APD aperture and the monochromator's slit were used as detection pinholes.

References

1. Levine, Ira N. *Quantum Chemistry,* 5th ed.; Prentice Hall: New Jersey, 2000; p. 96-97.
2. Ingle, J.D. and Crouch, S.R., *Spectrochemical Analysis*; Prentice-Hall: New Jersey, 1988; p. 209.
3. Moerner, W. E., Ed., In *Topics in Current Physics, Persistent Spectral Hole Burning: Science and Applications*; Springer-Verlag: New York, 1988, p. 17.
4. Allen, L., Eberly, J.H., *Optical Resonance and Two-Level Atoms*; Wiley-Interscience: New York, 1975.
5. Dawber, P. G. and Elliott, R. J., *Proc. Roy. Soc. (London)* **1963**, A273, p. 222; Maradudin, A. A., Montroll, E. W., and Weiss, G. H., *Solid St. Phys;* Academic: London, 1963, Suppl. 3; Stevenson R.mW. H., Ed., *Phonons in Perfect Lattices and in Lattices with Point Imperfections*; Oliver and Boyd: London, 1966; Bak, T.A., Ed., *Phonons and Phonon Interactions*; Benjamin, W. A.: New York, 1965; Wallis, R. F., Ed., *Lattice Dynamics*; Pergamon: New York, 1965; Small, G. J., *Chem. Phys.* **1970**, 52, p. 656.
6. Personov, R. I., In *Spectroscopy and Excitation dynamics of Condensed Molecular Systems*, Agranovich, V. M. and Hochstrasser, R. M., Eds.; North-Holland: Amsterdam, 1983; p. 555.
7. Pryce, M.H.L., In *Phonons In Perfect Lattices and In Lattices with Point Imperfections*, Stevenson, R.W.H., Ed.; Plenum: New York, 1966; p. 403.
8. Sapozhnikov, M. N., *Phys. Stat. Sol.* (*b*) **1976**, 75, p. 11

9. Jankowiak, R., In *Shpol'skii Spectroscopy and Other Site Selection Methods: Applications in Environmental Analysis, Bioanalytical Chemistry, and Chemical Physics*, Gooijer, C., Ariese, F. and Hofstraat, J. W., Eds.; John Wiley & Sons: New York, 2000; p. 235.
10. Dushinsky, F., *Acta Physiochem*. **1937**, **7**, p. 51.
11. Rebane, K. K., *Impurity Spectra of Solids*, Plenum: New York, 1970.
12. Osadko, I. S., In *Advances in Polymer Science*, Dusek, K., Ed.; Springer-Verlag: Berlin, Heidelberg, New York, 1988, p. 123.
13. van der Zaag, P. J., Galaup, J. P. and Völker, S., *Chem. Phys. Lett.* **1990**, 166, p. 263.
14. Moerner, W. E., Ed., In *Topics in Current Physics, Persistent Spectral Hole Burning: Science and Applications*; Springer-Verlag: New York, 1988; p. 27.
15. Reddy, N.R.S., Lyle, P.A., Small, G.J., *Photosynthesis Research* **1992**, 31, p. 169.
16. Jankowiak, R., Richert, R., Bässler, H., *J. Phys. Chem.* **1985**, 89, 4569-4574.
17. Jankowiak, R., Hayes, J.M., Small, G.J., *Chem. Rev.* **1993**, 93, p. 1471.
18. Hayes, J.M., Gillie, J.K., Tang, D., Small, G.J., *Biochim, Biophys, Acta* **1988**, 932, p. 287.
19. Hayes, J.M., Lyle, P.A., Small, G.J., *J. Phys. Chem.* **1994**, 98, p. 7337.
20. Sild, O. and Haller, K., Eds., *Zero-Phonon Lines and Spectral Hole Burning in Spectroscopy and Photochemistry*; Springer-Verlag: New York, 1988.
21. Völker, S., In *Relaxation Processes in Molecular Excited States*, Fünfschilling, J., Ed.; Kluwer: Dordrecht, The Netherlands, 1989; p. 113.

22. Moerner, W. E., Ed., In *Topics in Current Physics, Persistent Spectral Hole Burning: Science and Applications*; Springer-Verlag: New York, 1988.

23. Maier, H., Kharlamov, B. and Haarer, D., In *Tunneling Systems in Amorphous and Crystalline Solids*, Esquinazi, Ed.; Springer: New York, 1998; p. 317.

24. Creemers, T. M. H and Volker, S., In *Shpol'skii Spectroscopy and Other Site Selection Methods: Applications in Environmental Analysis, Bioanalytical Chemistry, and Chemical Physics*, Gooijer, C., Ariese, F. and Hofstraat, J. W., Eds.; John Wiley & Son: New York, 2000, Chapter 9, p. 273.

25. Mukamel, S., *Principles of Nonlinear Optical Spectroscopy*, Oxford University: New York, 1995; Chapter 9 - 11, p. 261.

26. Hesselink, W. H. and Wiersma, D. A., In *Spectroscopy and Excitation dynamics of Condensed Molecular Systems*, Agranivich, V. M. and Hochstrasser, R. M., Eds.; North-Holland, Amsterdam, The Netherlands, 1983; p. 249.

27. Narasimhan, L. R., Littau, K. A., Pack, D. W., Bai, Y. S., Elschner, A, Fayer, M.D., *Chem. Rev.* **1990**, 90, p. 439.

28. Koedijk, J. M. A., Wannemacher, R., Silbey, R. J. and Völker, S., *J. Phys. Chem.* **1996**, 100, p. 19945.

29. Völker, S., MacFarlane, R. M., Genack, A. Z., Trommsdorff, H. P., and van der Waals, J. H., *J. Chem. Phys.* **1977**, 67, p, 1759.

30. Dick, B. *Chem. Phys.* **1989**, 136, p. 429.

31. van den Berg, R., Visser, A. and Völker, S., *Chem. Phys. Lett.* **1988**, 144, p. 105.

32. Lee, I.-J., Small, G. J. and Hayes, J. M., *J. Phys. Chem.* **1990**, 94, p. 3376.

33. Basche, Th., Moerner, W. E., Orrit, M., Wild, U., Eds., In *Single Molecule Optical Detection, Imaging and Spectroscopy*; VCH: Weinheim, New York, 1996.

34. Basche, Th., Orrit, M., Rigler, R., Eds., *Single Molecule Spectroscopy - Nobel Conference Lectures*; VCH: Weinheim, New York, 1996.

35. Reinot, T., Zazubovich, W., Hayes, J. M. and Small, G. J. *J. Phys. Chem. B* **2001**, 105, p. 5083.

36. Kharlamov, B. M., Personov, R. I., Bykovskaya, L. A., *Opt. Commun*. **1974**, 12, p. 191.

37. Gorokhovskii, A. A., Kaarli, R. K., Rebane, L. A. *JETP Lett*. **1974**, 20, p. 216.

38. Jankowiak, R., Hayes, J.M., Small, G.J., *Chem. Rev.***1993**, 93, p. 1471.

39. Jankowiak, R., and Small, G.J., *Science* **1987**, 237, p. 618.

40. Hayes, J.M. and Small, G.J., *Chem. Phys.* **1978**, 21, p. 151.

41. Anderson, P.W., Halperin, B.I., Varma, C.M., *Philos. Mag.* **1972**, 25, p. 1.

42. Phillips, W.A., J. *Low Temp. Phys.* **1972**, 7, p. 351.

43. Shu, L. and Small, G.J., *J. Opt. Soc. Am. B* **1992**, 9, p. 724.

44. Shu, L. and Small, G. J. *Chem. Phys.* **1990**, 141, p. 447.

45. Hayes, J. M., Stout, R. P., Small, G. J. *J. Phys. Chem.* **1981**, 74, p. 4266.

46. Cohen, M.H. and Grest, G.S., *Phys. Rev. Lett.* **1980**, 45, p. 1271.

47. Dang, N.C., Ph.D. Thesis, Iowa State University, 2005.

48. Reinot, T. and Small, G.J., *J. Chem. Phys.* **2001**, 114, p. 9105.

49. Szabo, A., *Phys. Rev Lett.* **1970**, 25, p. 924.

50. Erickson, L. E. *Phys. Rev. B* **1975**, 11, p. 4512.

51. Wu. H.-M., Ratsep, M., Jankowiak, R., Cogdell, R.J., Small, G.J., *J. Phys. Chem. B* **1997**, 101, p. 7641.

52. Wu. H.-M., Ratsep, M., Jankowiak, R., Cogdell, R.J., Small, G.J., *J. Phys. Chem. B* **1997**, 101, p. 4023.

53. Reddy, N.R.S., Picorel, R., Small, G.J., *J. Phys. Chem.* **1992**, 96. p. 6458.

54. den Hartog, F.T.H., Dekker, J.P., van Grondelle, R., Völker, S., *J. Phys. Chem. B* **1998**, 102, p. 11007.

55. Jankowiak, R., Rätsep, M., Picorel, R., Siebert, M., Small, G.J., *J. Phys. Chem. B* **1999**, 103, p. 9759.

56. den Hartog, F.T.H., Vacha, G., Lock, A.J., Barber, J., Dekker, J., Volker, S., *J. Phys. Chem. B* **1998**, 102, p. 9714.

57. Fetisova, Z.G., Mauring, K, *FEBS Lett.* **1993**, 323, p. 159.

58. Psencki, J., Polivka, T., Nemec, P., Dian, J., Kudrna, J., Maly, P., Hala, J., *J. Phys. Chem. A* **1998**, 102, p. 4392.

59. Jankowiak, R. and Small, G.J., In *Photosynthetic Reaction Centers*, Diesenhofer, J, Norris, J., Eds.; Academic Press: New York, 1993.

60. Zazubovich, V., Tibe, I., Small, G.J., *J. Phys. Chem. B* **2001**, 105, p. 12410.

61. Reinot, T., Zazubovich, W., Hayes, J. M., Small, G. J. *J. Phys. Chem. B* **2001**, 105, p. 5091.

62. Rätsep, M., Johnson, T.W., Chitnis, P.R., Small, G.J., *J. Phys. Chem. B* **2000**, 104, p. 836.

63. Zazubovich, V, Jankowiak, R., Small, G.J., *J. Phys. Chem. B* **2002**, 106, p. 6802.

64. Hsin, T.-M., Zazubovich, V., Hayes, J. M., Small, G. J. *J. Phys. Chem. B* **2004**, 108, p. 10515.

65. Kohler, M., Friedrich, J., Fidy, J., *Biochimica et Biophysica Acta* **1998**, 1386, p. 255.

66. Marchetti, R.J.A.P., Scozzafava, M., Young, R.H., *Chem. Phys. Lett.* **1977**, 51, p. 424.

67. Kador, L., Haarer, D., Personov, R, *J. Chem. Phys*. **1989**, 86, p. 5300.

68. Haarer, D and Philpott, M., In *Spectroscopy and Excitation Dynamics of Condensed Molecular Systems*; Agranovich, V.M., Hochstrasser, R.M., Eds.; North-Holland: Amsterdam, The Netherlands, 1983; p. 27.

69. Reinot, T.; Dang, N. C.; Small, G. J, *J. Chem. Phys*. **2003**, 119, p. 10404.

70. Hayes, J.M., Gillie, J.K., Tang, D., Small, G.J., *Biochim. Biophys, Acta.* **1988**, 932, p. 287.

71. Matsuzaki, S., Zazubovich, V., Rätsep, M., Hayes, J.M., Small, G.J., *J. Phys. Chem. B* **2000**, 104, p. 9564.

72. Matsuzaki, S., Zazubovich, V., Johnson, T. W., Hayes, J. M, Chitnis, P. R., Small, G. J., *Chem. Phys.* **2002**, 275, p. 47.

73. Kenney, M.J., Jankowiak, R., Small, G.J., *Chem. Phys.* **1990**, 46, p. 47.

74. Moerner, W.E. and Kador, L., *Phys. Rev. Lett.* **1989**, 62, p. 2535.

75. Basche, Th., Moerner, W. E., Orrit, M., Wild, U., Eds., *Single Molecule Optical Detection, Imaging and Spectroscopy*; VCH: Weinheim, New York, 1996.

76. Basche, Th., Orrit, M., Rigler, R., Eds., *Single Molecule Spectroscopy - Nobel Conference Lectures*; VCH: Weinheim, New York, 1996.

77. Ambrose, W. P., Basche, Th. and Moerner, W. E., *J. Chem. Phys.* **1991**, 95, p. 7150.

78. Thenio, P., Myers, A. B. and Moerner, W. E., *J. Lumines.* **1993**, 56, p. 1.

79. Orrit, M. and Bernard, J., *Phys. Rev. Lett.* **1990**, 65, p. 2716.

80. Fluery, L. Zumbusch, A., Orrit, M., Brown, R. and Bernard, J., *J. Lumines.* **1993**, 56, p. 15.

81. Moerner, W.E., *J. Chem. Phys.* **2002**, 117, p. 10925.

82. Mei, E., Tang, J., Vanderkooi, J.M., Hochstrasser, R.M., *J. Am. Chem. Soc.* **2003**, 125, p. 2730.

83. Hofmann, C., Ketelaars, M., Matsushita, M., Michel, H., Aartsma, T.J., Kohler, J., *Phys. Rev. Lett.* **2003**, 90, p. 013004/1.

84. Kohler, J., Disselhorst, J. A. J. M., Donckers, M. C. J. M., Grouenen, E., Schmidt, J. and Moerner, W. E., *Nature* **1993**, 363, p. 242.

85. Wrachtrup, J., von Borczyskowski, C., Bernard, J., Orrit, M. and Brown, R., *Nature* **1993**, 363, p. 244.

86. Bernard, J., Fluery, Talon, H., and Orrit, M., *J. Chem. Phys.* **1993**, 98, p. 850.

87. Zumbusch, A., Fluery, L., Brown, R., Bernard, J. and Orrit, M., *Phys. Rev. Lett.* **1993**, 70, p. 3584.

88. Weiss, S., *Science* **1999**, 283, p. 244.

89. Funatsu, T., Harada, Y., Tokumaga, M., Saito, K. and Yanagida T., *Nature* **1995**, 374, p. 555.

90. Noji, H., Yasuda, R., Yoshida, M. and Kinosita, K., *Nature* **1997**, 386, p. 299.

91. Dickson, R. M., Cubitt, A. B., Tsien R. and Moerner W. E., *Nature* **1997**, 388, p. 355.

92. van Oijen, A. B., Ketelaars, M., Kohler, J. Aartsma, T. J., Schmidt, J., *Science* **1999**, 285, p. 400.

93. Betzig, E. and Chichester, R.J., *Science* **1993**, 262, p. 1422.

94. Nie, S. and Chiu, D.T., Zare, R.N., *Science* **1994**, 266, p. 1018.

95. Trautman, J.K. and Macklin, J.J., *Chem. Phys.* **1996**, 205, p. 221.

96. Dickson, R.M. et al., *Science* **199**6, 274, p. 966.

97. Moerner, W. E. and Fromm, D. P., *Review Scientific Instruments* **2003**, 74, p. 3597.

98. Moerner, W. E., In *Single Molecule Optical Detection, Imaging and Spectroscopy*, Basche, Th., Moerner, W. E., Orrit, M., Wild, U., Eds.; VCH: Weinheim, New York, 1996; p. 1.

99. Basche, Th., Ambrose, W. P. and Moerner, W. E., *J. Opt. Soc Am.* **1992**, B9, p. 829.

100. Reinot, T. and Small, G. J., *J. Chem. Phys.* **2000**, 113, p. 10207.

CHAPTER 4 – EVIDENCE FOR HIGHLY DISPERSIVE PRIMARY CHARGE SEPARATION KINETICS AND GROSS HETEROGENEITY IN THE ISOLATED PS II REACTION CENTER OF GREEN PLANTS

A submitted paper that was modified and published in the *J. Phys Chem. B* **2004**, 108, p. 10346-10356.

Kerry Riley, Ryszard Jankowiak, Margus Rätsep, Gerald. J. Small and Valter Zazubovich

Abstract

Despite the availability of an X-ray structure and many spectroscopic studies, important issues related to structural heterogeneity, excitonic structure, primary charge separation (CS) and excitation energy transfer dynamics of the isolated reaction center (RC) of photosystem II (PS II) remain unresolved. The issues addressed here include (1) whether or not the primary CS kinetics at low temperatures are highly dispersive (due to structural heterogeneity), as proposed by Prokhorenko and Holzwarth (*J. Phys. Chem. B* **2000**, 104, 11563), and (2) the nature of the weak lowest-energy Q_y absorption band at ~ 684 nm that appears as a shoulder on the intense primary electron donor band (P680). Results of low temperature non-photochemical hole burning (NPHB) and triplet bottleneck hole burning (TBHB) spectroscopic experiments (including effects of pressure and external electric (Stark) fields) are presented for the RC from spinach with one of the two peripheral chlorophylls removed. Both NPHB and TBHB are observed with excitations within the P680 and 684 nm bands. Both types of hole spectra exhibit a weak

dependence on the burn wavelength (λ_B) between 680 and 686 nm. Furthermore, the permanent dipole moment change ($f\,\Delta\mu$), as determined by Stark-NPHB spectroscopy, is identical (0.9±0.1 D) for the two bands, as are the linear electron-phonon coupling parameters (Huang-Rhys factors $S_{17} = 0.7$ and $S_{80} = 0.2$ for 17 cm^{-1} and 80 cm^{-1} phonons). These similarities, together with published fluorescence line narrowed spectra lead us to favor the gross heterogeneity model in which the 684 nm band is the primary electron donor band (P684) of a subset of RCs that may be more intact than P680-type RCs. Based on the linear pressure shift rates for the P680 and P684 nm bands, it is concluded that population of either P680* (* ≡ Q_y state) or P684* results in both TBHB (due to charge recombination of the primary radical ion pair) and NPHB. It was found that the values of parameters (e.g. electron-phonon coupling, site distribution function) used to simulate the NPHB spectra also provided reasonable fits to the TBHB spectra. Acceptable theoretical simulations of the line-narrowed TBHB spectra were not possible using a single primary CS time. However, satisfactory fits (including λ_B and burn intensity dependences) were achieved using a distribution of CS times. The observed TBHB is due to P680- and P684-type RCs with the faster CS kinetics since the persistent non-photochemical holes were saturated prior to measuring the TBHB spectra. (RCs exhibiting the most efficient NPHB have slower CS kinetics as well as higher fluorescence quantum yields.) For the TBHB spectra the same distribution (Weibull) was used for the P680- and P684-type RCs. The distribution describes quite well the distribution of Prokhorenko and Holzwarth for CS times shorter than 25 ps. Finally, the data indicate that electron exchange contributes only weakly (relative to electrostatics) to the inter-pigment excitonic interactions.

Introduction

Since its isolation in 1987, [1] the $Q_y(S_1)$ excitonic structure, excitation energy transfer and charge separation dynamics of the photosystem II (PS II) reaction center (RC) have been the subjects of intense study (as reviewed in [2]). The recently determined X-ray structure (3.8 Å resolution) of the PS II RC [3] has stimulated greater activity and confirmed that the structural arrangement of the core chlorins (Figure 1) is similar to that of the bacterial RC. P_1, P_2, Chl_1 and Chl_2 are chlorophyll *a* molecules and $Pheo_1$ and $Pheo_2$ are pheophytin *a* molecules. The subscripts denote the polypeptides to which the chlorins are bound, D_1 and D_2, which are analogous to the L and M polypeptides of the bacterial RC. P_1 and P_2, for example, are the structural counterparts of P_L and P_M (bacteriochlorophyll molecules) of the bacterial RC, the special pair. It is the lowest excited state of the special pair of the bacterial RC that serves as its primary electron donor state (see [4] for a review). The X-ray structure also located the two peripheral Chl *a* molecules, Chl_{Z1} and Chl_{Z2} that are bound to D_1 and D_2 [3]. In what follows the RC with 6 Chl *a* molecules will be referred to as RC-6. The RC with one of the two peripheral Chls removed [5] will be referred to as RC-5. Because of their peripheral locations Chl_{Z1} and Chl_{Z2} are not expected to have a significant effect on the Q_y excitonic structure of the core chlorins [6].

Despite the availability of an X-ray structure and an earlier structural model [7], several important issues related to excitonic structure and dynamics have yet to be resolved [2]. To a considerable extent this is due to the severe spectral congestion of the $S_0 \rightarrow Q_y$ absorption spectrum that spans a range of only ~ 500 cm^{-1}, Figure 1. It is

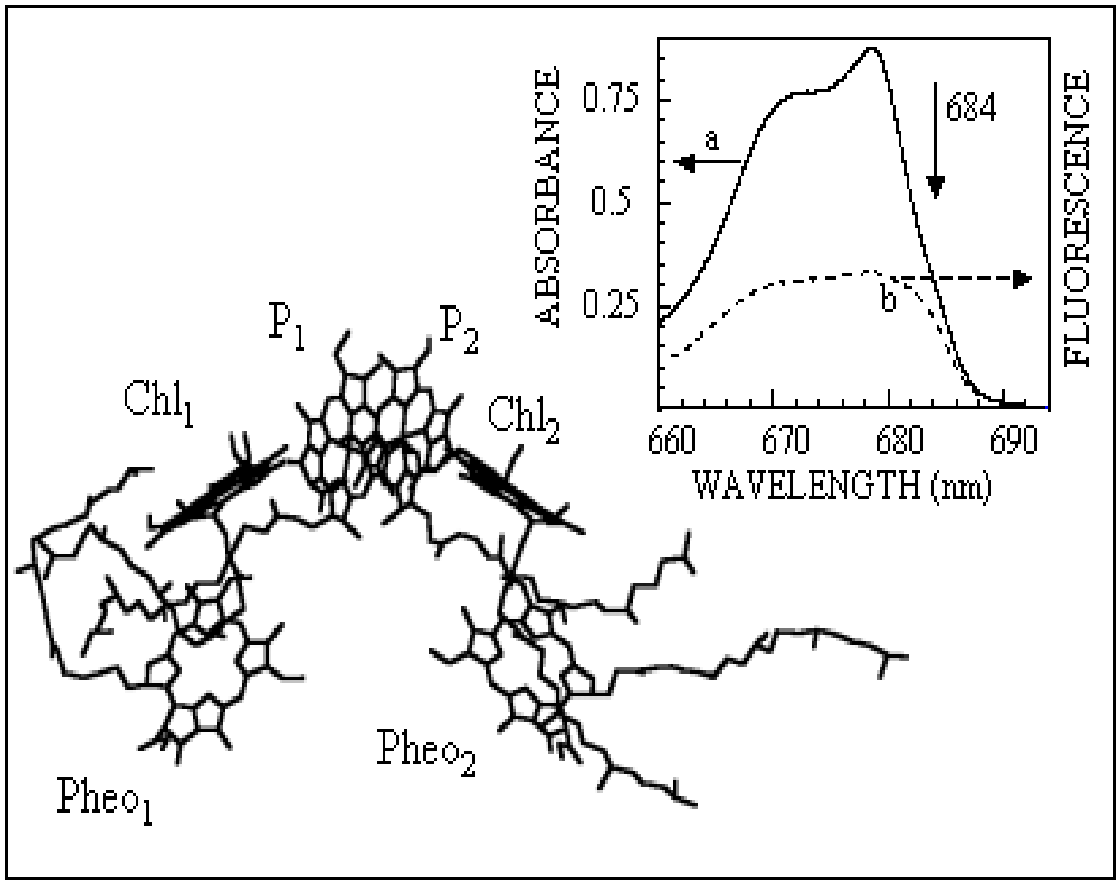

Figure 1. Structure of the isolated PS-II RC (peripheral chlorophylls not shown). Insert: Absorption (a; solid line) and fluorescence excitation (b; dashed line) spectra of PS II RC-5 sample at 5 K. Both spectra are measured in the same experiment and with the same sample. Vertical arrow indicates the shoulder at ~ 684 nm.

generally agreed, however, that the primary electron donor of the isolated PS II RC, P680, contributes significantly to the 680 nm absorption band. The main issues to be addressed in this paper are the effects of structural heterogeneity on (1) the excitonic composition of the primary electron donor state (P680*) and on (2) the primary charge separation kinetics, as well as (3) the nature of the relatively weak absorption shoulder at ~ 684 nm indicated by the arrow in Figure 1 for RC-5. Such absorption also exists in RC-6, *vide infra*.

In early works it was assumed, by analogy with the bacterial RC, that P_1 and P_2 form a special pair whose lowest excited dimer state is P680*, the primary electron donor state. This assumption was called into question by Tetenkin et al. [8] and later by Durrant et al [6] who introduced the so-called multimer (excitonic) model for the six core chlorins. The RC structure used was based on that of the bacterial RC but with the P_1-P_2 distance (Mg…Mg) set at 10 Å, rather than the value of 7.6 Å for P_L-P_M. The calculations took into account diagonal energy disorder; coupling energies were calculated using the point dipole-dipole approximation. It was found that the Q_y states are delocalized over ~ 3 chlorins, mainly on either the D_1 or D_2 branch. Thus, a lowest energy, primary donor state highly localized on P_1 and P_2 did not emerge from the calculations. Calculations of a similar vein, but based on the model structure of Svensson et al. [7] and/or the X-ray structure [3] were performed later [9]. The results for the two structures were similar, with the Q_y states mainly delocalized over ~ 3-4 chlorins. However, it was *not* found that the states are mainly delocalized over either the D_1 or D_2 branches, consistent with the results of [10]. Significantly improved fitting of hole-burned and other spectra was achieved with $Pheo_2$ decoupled from the other five

chlorins. It was found that the two lowest Q_y states are the most strongly absorbing with the absorption strength of the lowest equivalent to 2.3 Chl *a* molecules and that of the adjacent state equivalent to 1.1 Chl *a* molecules. The calculated splitting between these two states is ~ 90 cm^{-1}. A key point for consideration of the 684 nm absorbing chlorin molecule is that all calculations to date do not predict a lowest energy state that is weakly absorbing. Concerning the composition of the lowest energy state, P680*, it was found that, on average, P_1 and P_2 make the largest contributions although the contributions from Chl_1, $Pheo_1$ and, to a lesser extent, Chl_2 are significant [9]. Compositional analysis of the lowest energy state of single complexes revealed that its excitonic composition varies significantly from complex to complex. This provides support for the conclusion of Prokhorenko and Holzwarth [11] that the primary charge separation kinetics at low temperatures are highly dispersive. It should be noted that a recent refinement of the X-ray structure has led to a P_1-P_2 distance of 8.6 Å, [12] 1.4 Å shorter than the value reported in [3] and used in [9]. This distance may be short enough for the electron exchange coupling to be significant.

Concerning the primary charge separation rate at or near room temperature for RC-6, values of $(0.4\ ps)^{-1}$ [13], $(3\ ps)^{-1}$ [14-17], $(8\ ps)^{-1}$ [18], and $(21\ ps)^{-1}$ [19] have been reported. At liquid helium temperatures several groups have reported values in the $(2–5\ ps)^{-1}$ range [13, 20-25]. (The results in [25] led to the conclusion that the primary charge separation rate of RC-6 and RC-5 in the low temperature limit are very similar.) However, Prokhorenko and Holzwarth recently reported photon echo data obtained at 1.3 K which, on the basis of theoretical simulations, indicate that there is not a well-defined primary charge separation rate, i.e. the kinetics of primary charge separation are highly

dispersive, with charge separation times ranging from a couple of ps to several ns. The dispersive kinetics would be a consequence of the structural heterogeneity leading to a lower energy Q_y state whose chlorin composition varies significantly from RC to RC. Of relevance to this paper is that the simulations of the triplet bottleneck hole burned (TBHB) spectra of P680 presented in [25] assumed that the primary charge separation kinetics are non-dispersive.

Concerning the weak 684 nm absorption band, it was suggested early on that it corresponds to the lowest energy band of the special pair (P_1, P_2) with the higher energy and more strongly absorbing dimer level located at 680 nm [26]. The same group later argued against that interpretation [27]. It was reported in [21] that the 684 nm absorbing chlorin(s) is fragile, e.g. easily disrupted by the detergent TX-100 at concentrations of TX-100 too low to significantly affect the P680 band. It was also observed that the intensity of the 684 nm absorbing chlorin varied in different samples. These observations led to the suggestion that the 684 nm absorbing Chl(s) is a solvent exposed 'linker' pigment that may serve to shuttle excitation energy from the proximal antenna complexes to the RC at biological temperatures. The 'linker' was later assigned to one of the two peripheral Chl molecules [28].

New insights on the 684 nm absorbing pigment(s) emerged from the experiments of Völker and coworkers [29, 30]. Based on zero-phonon hole (ZPH) action spectra they determined that the width of the site (state) excitation frequency distribution function (SDF) of the 684 nm absorbing Chl is ~ 140 cm^{-1} and ~ 150 cm^{-1} for RC-6 and RC-5, respectively, with the Gaussian SDF centered near 684 nm. These widths represent static inhomogeneous broadening. Very narrow ($\lesssim$ 1 GHz) ZPH widths were observed (T $\leq$

4.2 K) and convincingly attributed to pure dephasing from electron-two level system coupling. Thus, the excitation energy transfer and/or primary charge separation times must be very long (ns time scale) for the 684 nm Chl *probed by persistent hole burning*. For that reason the 684 nm state was referred to as a trap state [30]. It has been suggested that this state may be due to a subset of the RCs for which primary charge separation is highly forbidden on energetic grounds [2]. Since such a model does not predict a distinct 684 nm absorption band, the same group proposed that the 684 nm band is the origin band of the primary donor state with the 680 nm band corresponding to a phononic transition involving a ~ 80 cm^{-1} mode [31]. Another interpretation put forth is that the 684 nm absorption band is due to the primary donor P684 of intact RC and that the procedure used to obtain the isolated RC results in structural changes that blue-shift the primary donor band of the majority of the RC to 680 nm. Very recently, Smith et al. [32] reported magnetic circular dichroism spectra (1.7 K) for the O_2-evolving PS II complex from spinach and assigned a narrow (~ 45 cm^{-1}) spectral feature at 683.5 nm to the primary electron donor (P684).

We present the results of persistent nonphotochemical hole burning (NPHB) and TBHB experiments designed to provide new insights on primary charge separation and the 684 nm absorbing Chl *a*. High pressure and external electric (Stark) fields are combined with hole burning to enhance spectroscopic selectivity. The experimental data and theoretical simulations are consistent with a model in which gross heterogeneity leads to two types of RC, one in which the primary electron donor absorbs at ~ 680 nm (P680) and the other at ~ 684 nm (P684). Intrinsic structural heterogeneity in each type of RC leads to highly dispersive primary charge separation kinetics. The model suggests

that the lowest energy Q_y state of RCs (of both types) with the slowest charge separation is the trap state referred to above. Potential problems with the model are considered as well as alternative explanations of the data.

Experimental

PS II RC-5 complexes containing ~ 5.3 Chl *a* molecules per two Pheo *a* molecules were prepared and purified from market spinach as described in [18]. Samples were dissolved in a mixture of MES buffer (pH = 6.5) containing 2 mM dodecylmaltoside and 5 mM imidizole. Glycerol was added (v/v ratio of 1:2) to ensure formation of high optical quality glasses upon cooling to liquid helium temperatures.

Moderate resolution (0.5 cm^{-1}) absorption and hole burned spectra were measured with a Bruker HR120 FT spectrometer. The burn laser was a Coherent 699 ring dye laser with the intra-cavity assembly (ICA) removed (2 GHz linewidth). This setup was used in some Stark (external electric field) experiments and all high pressure experiments.

Persistent zero-phonon hole (ZPH) action spectra [33] were obtained with the ICA installed (long term laser linewidth < 20 MHz). Action spectra were obtained in both the transmission and fluorescence detection modes. For the former, light transmitted through the sample was detected with a diode assembly based on a UDT-10 DPI photodiode, optimized for high sensitivity and slow response. For the latter mode, fluorescence was detected by a Hamamatsu 2949 PMT at 90° relative to the excitation beam direction. A 730 nm cut-off filter was used to suppress scattered laser light. Spectra were corrected for the transmission characteristics of the neutral density filters (LOMO, Russia). Spectra obtained in the excitation mode with different filter sets were essentially identical after correction. ZPH were well-fitted with Lorentzian profiles.

Fractional hole depths were calculated as the ratio of ΔOD at the peak of ZPH divided by OD prior to burning (transmission mode). For the fluorescence detection mode, the fractional hole depth was calculated as the fluorescence intensity decrease after burning divided by the intensity prior to burning.

Triplet bottleneck hole burned (TBHB) spectra were obtained following saturation of the persistent nonphotochemical hole (NPHB) spectrum, as described in [25]. This procedure ensures that TBHB spectra correspond to RCs undergoing efficient primary charge separation. The Stark hole burning apparatus is described in [34]. The setup allows for determination of the response of the ZPH with laser polarization parallel and perpendicular to the applied field. For 665 nm $\leq \lambda_B \leq$ 679 nm, a spectral resolution of 0.5 cm^{-1} was used, *vide supra*. Burn fluences ranged from ~ 10 J/cm^2 to ~ 75 J/cm^2. For $\lambda_B \geq$ 680 nm, holes were burned and read with a resolution of 20 MHz (fluorescence excitation mode). In this mode a burn fluence of 1.5 mJ/cm^2 was used. The high pressure apparatus used is described in [35]. When the desired pressure exceeded the pressure of helium solidification at the temperature of the hole burning experiment (~ 6 K), the cell was pressurized at ~ 60 K and then cooled to 6 K.

Results

Absorption, excitation and ZPH action spectra. Absorbance (A) and fluorescence excitation (B) spectra for the Q_y-region of RC-5 are shown in the insert of Figure 1. The absorption spectrum, with a maximum at ~ 679 nm and shoulder at ~ 684 nm, is very similar to those presented in [29, 30, 36, 37]. The fluorescence excitation spectrum differs significantly from the spectra reported by den Hartog et al. [30]. The maximum at ~ 679 nm in Figure 1 is broader and much less pronounced. This difference

cannot be attributed to sample degradation since the absorption spectrum was recorded immediately after recording the excitation spectrum. We note that fluorescence excitation spectra obtained without correction for the transmission characteristics of the neutral density filters were quite similar to those of den Hartog et al. The difference between the two spectra in Figure 1 establishes that the fluorescence quantum yield is not constant as the excitation is tuned across the absorption spectrum. The decrease in fluorescence quantum yield for excitation wavelengths in the vicinity of 680 nm might be expected given that primary charge separation involving P680 occurs on a time scale as short as a few picoseconds.

Figure 2 shows persistent ZPH action spectra obtained in the transmission mode (frame A) and fluorescence excitation mode (frame B) with a burn fluence of 3 mJ/cm^2. (The excitation action spectrum obtained with 0.3 mJ/cm^2 was very similar to that in frame B). The action spectra correlate with the spectra in Figure 1, e.g. the maximum of the spectrum in frame A and of spectrum a (absorbance) in Figure 1 are at ~ 680 nm, and both spectra feature a relatively weak shoulder at ~ 684 nm. The action spectrum in frame A could be well-fitted for $\lambda \geq 676$ nm with two Gaussian profiles at 679.9 nm and 683.9 nm with widths of 110 and 90 cm^{-1}, respectively, and the amplitude of the former (dashed curve) a factor of 2.4 higher than that of the latter (dotted curve). We note that the action spectrum obtained in the transmission mode is very similar to that reported in [37], which was obtained with a burn fluence of 15 J/cm^2 and measured with a resolution of 0.5 cm^{-1}. Fitting of the ZPH action spectrum obtained in the fluorescence excitation mode with a single Gaussian led to a SDF centered at 683.5 nm with an inhomogeneous

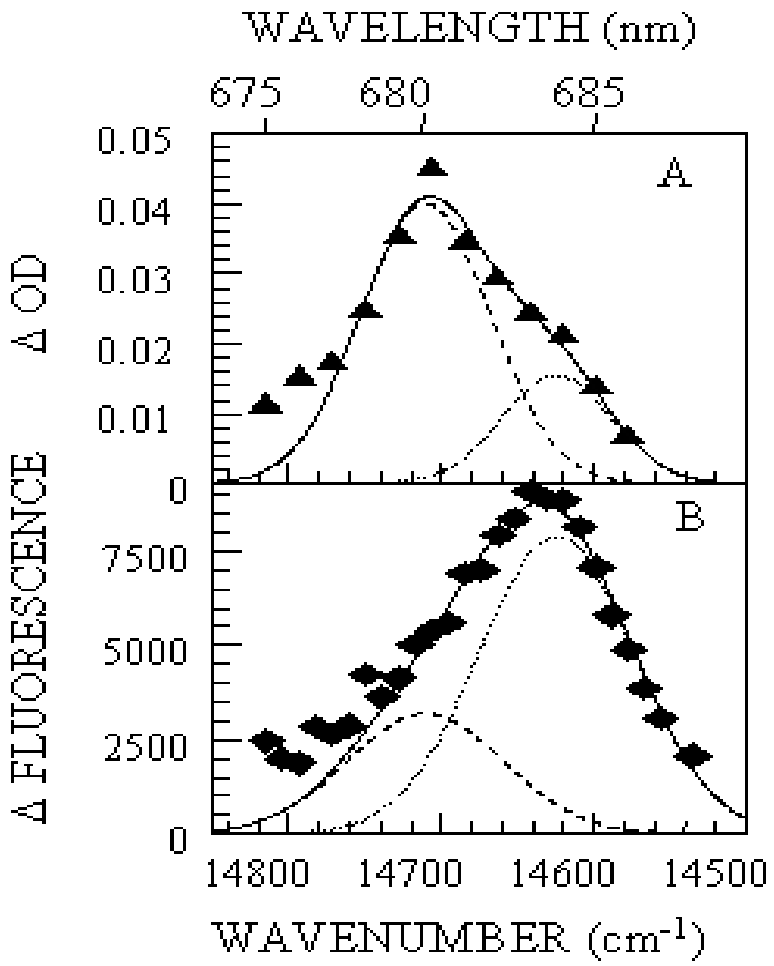

Figure 2. Action spectra obtained in transmission (A; triangles) and fluorescence excitation (B; diamonds) modes with 3 mJ/cm^2 irradiation. Frame A: The best parameters for two-Gaussian fit are (peak position / width): 679.9 nm / 110 cm^{-1} (dashed line) and 683.9 nm / 90 cm^{-1} (dotted line) with the amplitude ratio 2.4:1. Frame B: The best fit parameters are 680.0 nm / 120 cm^{-1} (dashed line) and 683.9 nm / 110 cm^{-1} (dotted line) with the amplitude ratio of 1:2.4. Solid curves are sums of dashed and dotted curves.

width of 130 cm^{-1}, values close to those reported by den Hartog et al. [30]. A better fit was obtained by using two Gaussians at 679.9 (dashed curve) and 683.9 nm (dotted curve) with the amplitude of the latter a factor of 2.4 higher than that of the former, frame B of Figure 2. This situation is roughly the reverse of that for the action spectrum in frame A of Figure 2.

The results of Figure 2 establish that states absorbing at ~ 680 and ~ 684 nm undergo persistent nonphotochemical hole burning (NPHB). Prior to the introduction of the multimer model, it was proposed that [37, 38] the state at 680 nm responsible for NPHB is localized on $Pheo_1$ since the non-line narrowed hole profile obtained with non-resonant excitation is very similar to the bleach profile resulting from white light plus dithionite reduction of $Pheo_1$ (primary electron receptor) at 4 K. An additional consideration was that NPHB was not observed for the primary donor absorption band (P870) of the purple bacterium *Rb. sphaeroides,* a consequence of the primary charge separation rate (~ 1 ps)$^{-1}$, being several orders of magnitude higher than the NPHB rate. The possibility that P680→P680* excitation can result in both NPHB and TBHB is considered in section 4.

Pressure dependent results. In earlier studies it was shown that the TBHB spectra of the isolated PS II RC-6 obtained at liquid helium temperatures under non-line narrowing conditions consists of two components centered near 680 and 684 nm [21]. Formation of the triplet state is a result of charge recombination of the radical ion pair associated with primary charge separation. To gain further insight on the two components, non-line narrowed TBHB spectra (6 K) were obtained at pressures of 0.1, 12, 154, 298 and 402 MPa (λ_B = 665 nm). The 0.1 and 402 MPa spectra are shown in

Figure 3, along with fits obtained using two Gaussians. At ambient pressure they are centered at 680.0 nm (14705 cm^{-1}) and 684.3 nm (14614 cm^{-1}), with widths of 115 and 85 cm^{-1}, respectively. Note that these values are very similar to those obtained from the action spectrum in frame A of Figure 2. At 402 MPa the Gaussians are peaked at 14655 and 14554 cm^{-1}, with widths of 125 and 90 cm^{-1}. The linear pressure shift rates for the 680 and 684 nm components (states) obtained using the spectra for all five pressures are -0.12 ± 0.01 cm^{-1}/MPa and -0.15 ± 0.01 cm^{-1}/MPa, respectively. The shift rates of persistent ZPH burned into the 680 and 684 nm bands are, within experimental uncertainty, the same as those given above. The results for λ_B (burn wavelength) = 680 nm and 686 nm are shown in Figure 4. The respective shift rates are 0.11 ± 0.005 and 0.16 ± 0.01 cm^{-1}/MPa. We emphasize that λ_B = 686 nm is highly selective for the 684 nm absorbing pigment(s).

Stark hole-burning spectroscopy. Stark hole-burning spectroscopy has proven to be a powerful approach for determining the permanent dipole change ($\Delta\mu$) associated with the $S_0 \rightarrow Q_y(S_1)$ transitions of photosynthetic complexes [39-41]. Typically, one monitors the dependence of the ZPH profile (coincident with λ_B) with the laser polarization parallel and perpendicular to the applied electric (Stark) field. In the absence of splitting of the ZPH in either polarization, $\Delta\mu$ is obtained from the dependence of the ZPH width (Γ) on the applied field ($\mathbf{E}_S$) [42, 43].

$$\Gamma(F) = \Gamma_0 (1 + F^2)^{1/2} \qquad (1)$$

where Γ_0 is the width (fwhm) of the ZPH at zero applied field and

$$F = 2f \cdot \Delta\mu E_s / \hbar\Gamma_0 \qquad (2)$$

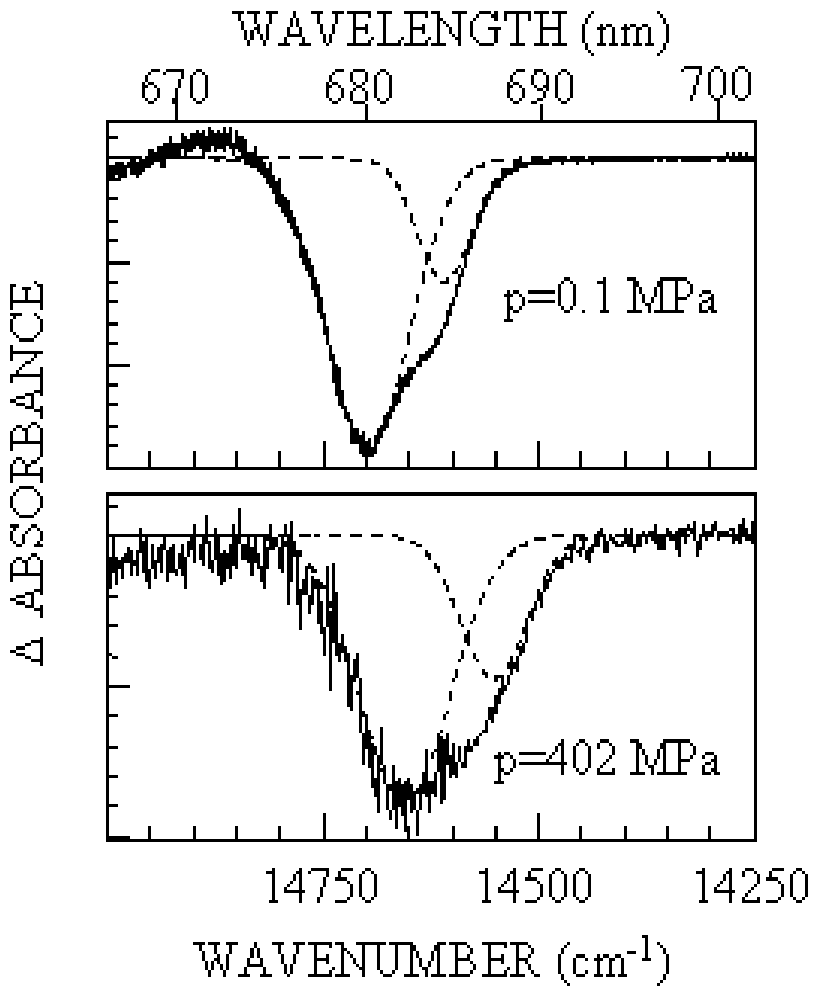

Figure 3. Frame A: Triplet bottleneck hole spectrum resulting from excitation at 665 nm with ~ 200 mW/cm^2, p=0.1 MPa. The hole is best fitted by a sum of two Gaussians (dashed curves), peaked at 14705 cm^{-1} (680.0 nm) and 14614 cm^{-1} (684.3 nm). The widths of these Gaussians are 115 and 85 cm^{-1}, respectively. Frame B: Triplet bottleneck hole at 402 MPa; the best fit parameters are 14655 / 125 and 14554 / 90 cm^{-1}.

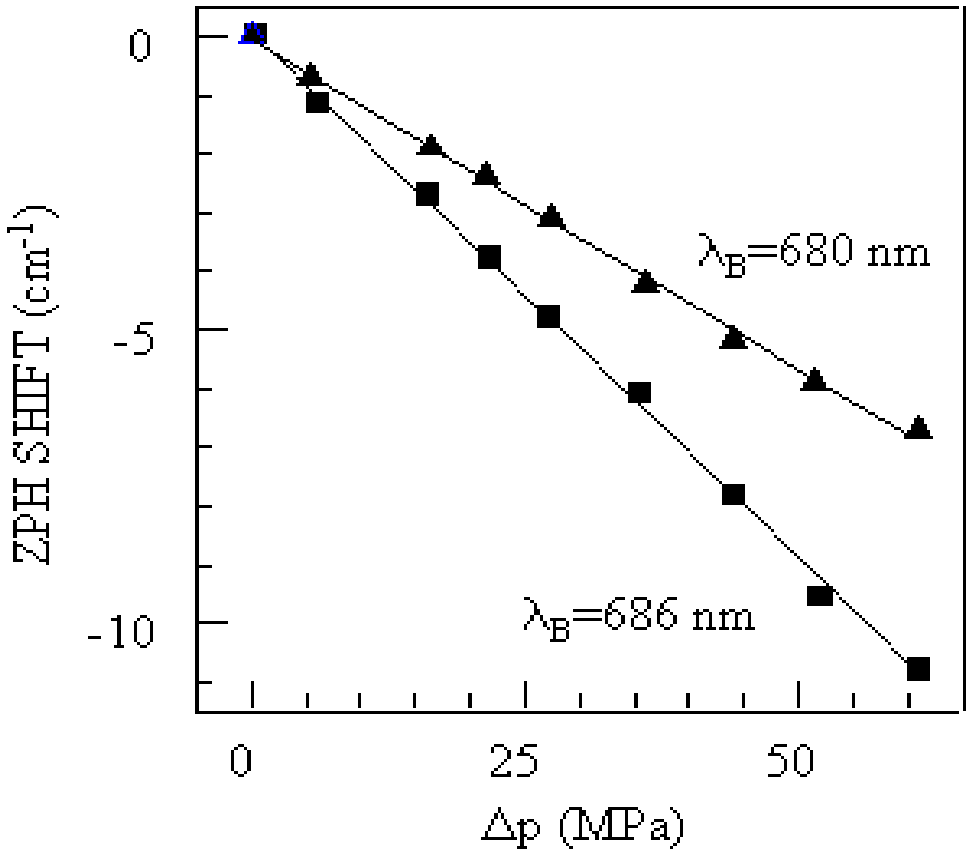

Figure 4. Pressure-induced shifts of the ZPHs burned at 680 nm (triangles) and 686 nm (squares). The shift rates are –0.11 and –0.16 cm^{-1}/MPa, respectively.

with f the local field correction factor. The unit of Γ is circular frequency. The absence of Stark splitting of the ZPH in both polarizations is expected when the matrix-induced contribution to $\Delta\mu$ dominates the intrinsic contribution of the chromophore and is random in a vectorial sense [42]. Stark hole burning data (2.0 K) were obtained for λ_B-values between 665.0 and 686.5 nm. The $f \cdot \Delta\mu$ values, in the unit of Debye (D), are listed in Table 1 for $\mathbf{E}_S$ parallel (||) and perpendicular ($\perp$) to the laser polarization $\mathbf{E}_\ell$. Values in italic and Roman were obtained in the fluorescence excitation mode (20 MHz resolution) and transmission mode (0.5 cm^{-1} resolution with FT spectrometer), respectively. Representative Stark ZPH broadening data for λ_B = 680 nm, λ_B = 686 nm and $\mathbf{E}_\ell$ parallel to $\mathbf{E}_S$ are shown in Figure 5. Again, λ_B = 686 nm is highly selective for the 684 nm absorbing chlorin. The solid and dashed curves are the fits to the data obtained with Eq. (1).

The $f \cdot \Delta\mu$ values in Table 1 are interesting in a couple of respects. First, they are essentially constant (~ 0.9 D) for $\lambda_B \gtrsim$ 679 nm, which means that the 680 and 684 nm absorbing states cannot be distinguished on the basis of permanent dipole moment change. Second, $f \cdot \Delta\mu$ values are smaller for λ_B < 679 nm and, furthermore, $f \cdot \Delta\mu$ values in the range ~ 0.4–0.6 D are typical for a Chl *a* monomer in polymers and in proteins. The small differences (~ 10%) between $f \cdot \Delta\mu$ values for $\mathbf{E}_S \perp \mathbf{E}_\ell$ and $\mathbf{E}_S$ || $\mathbf{E}_\ell$ for some of the burn wavelengths may be due to anisotropy of the molecular polarizability and/or the interplay between the molecular, random matrix and non-random matrix dipole moment changes.

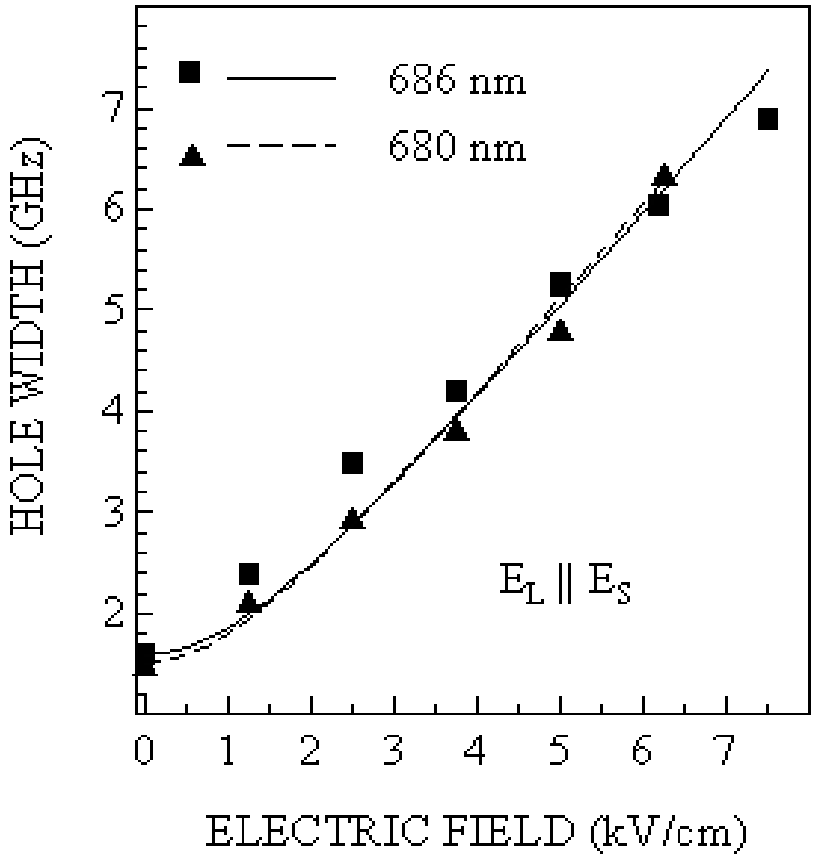

Figure 5. Dependence of the ZPH width on the external electric field for $\lambda_B = 680$ nm (triangles) and 686 nm (squares). Dashed and solid curves, respectively, are the fits to the data with Eqs. 1 and 2. Laser light polarization was parallel to the external field. $f\Delta\mu = 0.9$ D for both wavelengths.

Table 1. Dipole moment change $f\,\Delta\mu$ at different wavelengths [a].

Wavelength (nm)	f Δμ (D), $E_S \parallel E_I$	f Δμ (D), $E_s \perp E_I$
665	0.4±0.1	0.4±0.1
668	0.6±0.1	0.6±0.1
671	0.7±0.1	0.6±0.1
673	–[b]	0.7±0.1
675	–[b]	0.8±0.1
679	1.0±0.1	0.9±0.1
680	*0.91±0.05*	–[b]
681	0.9±0.1	0.85±0.1
682	*0.91±0.05*	*0.81±0.05*
683	1.0±0.1	0.8±0.1
684	*0.93±0.05*	*0.75±0.05*
685	0.9±0.1	–[b]
686	*0.93±0.05*	0.8±0.1
686.5	0.9±0.1	0.8±0.1

[a] Numbers in Roman and italic obtained in the transmission and fluorescence excitation modes, respectively.

[b] Not measured.

Dependence of hole burned spectra on burn intensity and burn wavelength.

Persistent NPHB spectra (A-D) and transient TBHB spectra (E-H) obtained with λ_B = 680, 682, 684 and 686 nm at 5 K are shown in Figure 6. The burn fluences used to obtain the three spectra in each of frames A-D and the burn intensities (I_B) used to obtain the four spectra in each of frames E-H are given in the caption. The sharpest feature in each spectrum is the ZPH coincident with λ_B. The solid and dashed upward arrows locate the pseudo- and real-phonon sideband holes (PSBH) displaced by 17 cm^{-1} from the ZPH. The spectra in frames A and E are similar to those reported in [25] for RC-6 and $\lambda_B \sim 680$ nm. Of particular importance is that the dependence of the NPHB spectra on λ_B is weak and that the electron-phonon coupling of the TBHB spectra would appear to be significantly stronger than that of the NPHB spectra, as judged by the intensity of the ZPH relative to that of the phonon sideband hole structure. The apparent difference in electron-phonon coupling strength has been investigated [35]. For $\lambda_B \sim 680$ nm, the theoretical simulations led to $S_{17} \sim 0.7$ and $S_{17} \sim 1.6$ for the NPHB and TBHB spectra, respectively, where S_{17} is the Huang-Rhys factor for the 17 cm^{-1} phonons. In fitting the TBHB spectra it was assumed that the primary charge separation rate is not distributed. That the two values of S_{17} differ significantly was taken as evidence that the chlorin pools (states) responsible for the two types of hole spectra are different. It is shown in section 4 that this need not be the case when the primary charge separation rate is dispersive (distributed).

Hole spectra in Figure 6 were simulated using the theory of Hayes et al. [44] that has been successfully applied to several photosynthetic complexes, including the

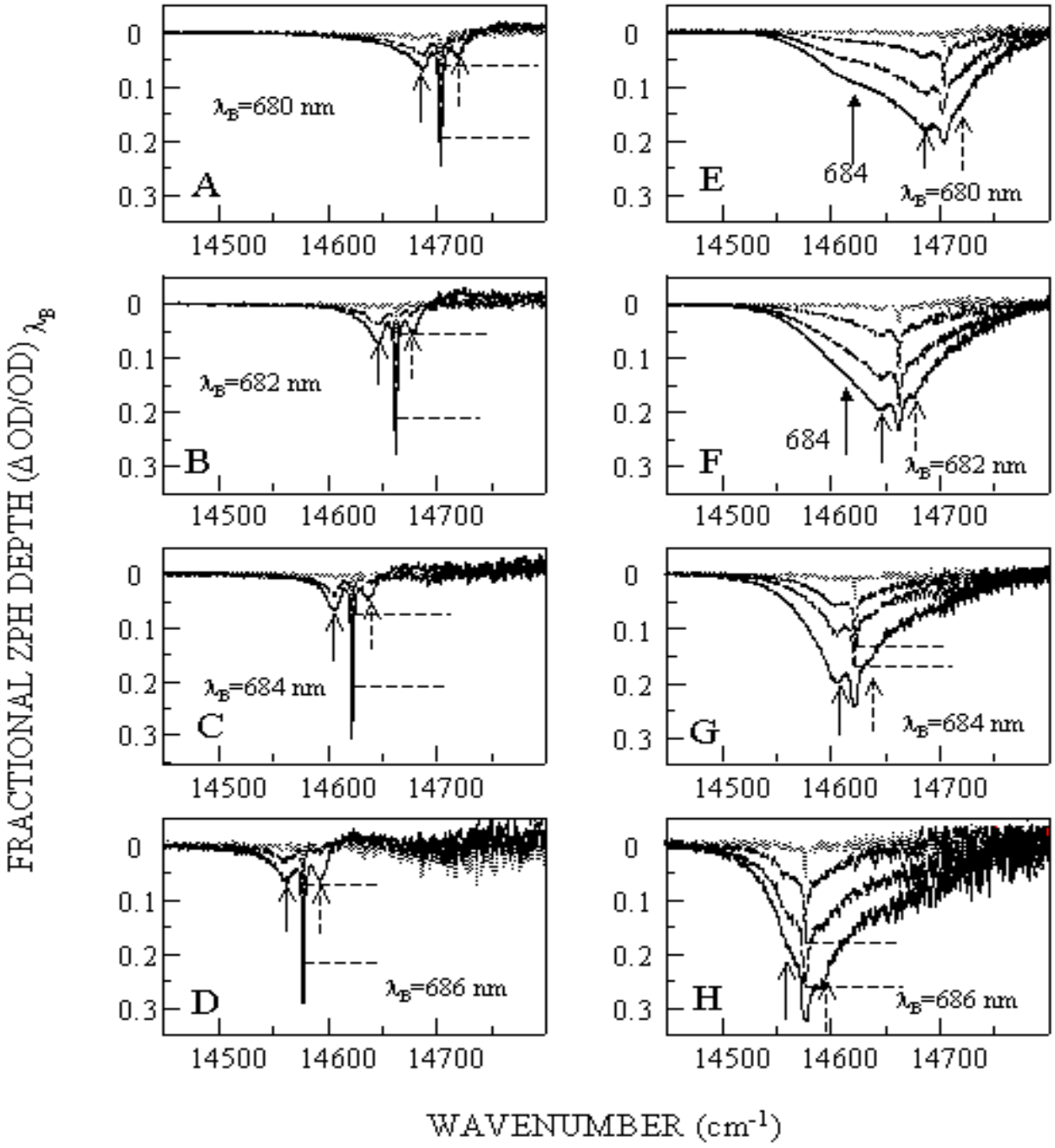

Figure 6. Frames A-D: Persistent NPHB spectra for λ_B = 680, 682, 684 and 686 nm, respectively. Burn fluences are 2.4 J/cm^2 for dotted curve, 170 J/cm^2 for dashed curve and 1600-1800 J/cm^2 for solid curve. Frames E-H: Triplet bottleneck hole spectra for λ_B = 680 – 686 nm, respectively. Burn intensities are 2, 40, 200 and 600 (at 684-686 nm) or 700 (at 680-682 nm) mW/cm^2. Vertical solid arrows indicate pseudo-PSBH peaked at 17 cm^{-1} from the ZPH. Vertical dashed arrows indicate the real-PSBH. Dashed horizontal lines represent the depths of the ZPH, which are obscured by deeper holes. In frames E, F the additional solid arrows indicate the broad satellite hole at 684 nm.

bacterial RC [45], the FMO antenna complex [46], and photosystem I of cyanobacteria [39, 40]. The absorption at Ω following burning at ω_B with photon flux P for time τ is given by (low temperature limit)

$$A_\tau(\Omega) = e^{-\sum_k S_k} \prod_{k=1,n} \sum_{R=0}^{\infty} \left(\frac{S_k{}^R}{R!} \right) \int d\omega\, G(\omega) e^{-\sigma P \phi \tau L(\omega_B - \omega)} \ell_{R,k}(\Omega - \omega - R\omega_k) \quad (3)$$

where G(ω) is the site (or state) energy distribution function (SDF) of the ZPL, σ the integrated absorption cross-section, ϕ the hole burning quantum yield and S_k and ω_k the Huang-Rhys factor and frequency of the k-th phonon. The $\ell_{R,k}$ are line shape functions with R = 0, 1, 2,… corresponding to the 0-, 1-, 2-,… phonon transitions. $\ell_{R=0}$ is the ZPL shape function (a Lorentzian). $L(\omega_B - \omega)$ is the single site absorption spectrum for the ZPL centered at the burn frequency ω_B:

$$L(\omega_B - \omega) = \exp(-\sum_k S_k) \prod_{k=1,n} \sum_{R=0}^{\infty} \left(\frac{S_k^R}{R!} \right) \ell_{R,k}(\omega_B - \omega - R\omega_k) \quad . \quad (4)$$

The hole spectrum is the difference between post-burn and pre-burn ($A_0(\Omega)$) spectra:

$$A_\tau(\Omega) - A_0(\Omega) \quad . \quad (5)$$

We emphasize that Eqs. 3 and 5 account for the fluence broadening of the ZPH.

We consider first simulations of the persistent NPHB spectra. Quality of the fits should be based on the ZPH and the pseudo-PSBH since the real-PSBH is interfered with

by the anti-hole, [47] which is not accounted for in Eq. 3. In addition to the 17 cm^{-1} phonons, the 80 cm^{-1} phonons active in the fluorescence line-narrowed (FLN) spectra of the isolated PS II RC [30] were included in the simulations. The first approximations to the one-phonon profiles of the 17 cm^{-1} and 80 cm^{-1} phonons could be obtained directly from the FLN spectra. The Huang-Rhys factors S_{17} and S_{80} were adjustable parameters. It was not possible to simultaneously fit the persistent NPHB spectra for the four λ_B-values with a SDF that is a single Gaussian, but it was possible using a sum of two Gaussians, as suggested by the ZPH action spectrum in frame A of Figure 2. All best fit parameter values are listed in Table 2. In frame A of Figure 7 the experimental hole burned spectrum (λ_B = 680.0 nm, burn fluence ~ 1700 J/cm^2) is compared with three calculated spectra. The best fit (red curve) was obtained with the parameter values in Table 2 (see Figure 7 caption for parameters of other simulated spectra). The experimental hole spectrum for λ_B = 686 nm (burn fluence ~ 1700 J/cm^2) is shown in frame B of Figure 7. The fit (dashed curve) was obtained with the parameter values in Table 2. As in frame A, the fit to the right of the ZPH is poor because of the neglect of the anti-hole.

Turning next to the TBHB spectra (E–H) of Figure 6, it was also found that significantly improved fits were obtained when a SDF that is the sum of two Gaussians was used, consistent with the non-line narrowed TBHB spectra in Figure 3. However, it was not possible to obtain satisfactory fits to spectra for λ_B = 680, 682, 684 and 686 nm and the four burn intensities. This is illustrated in frame D of Figure 8 for λ_B = 686 nm and burn intensities of 40, 200 and 600 mW/cm^2. Calculated spectra are shown for S_{17} =

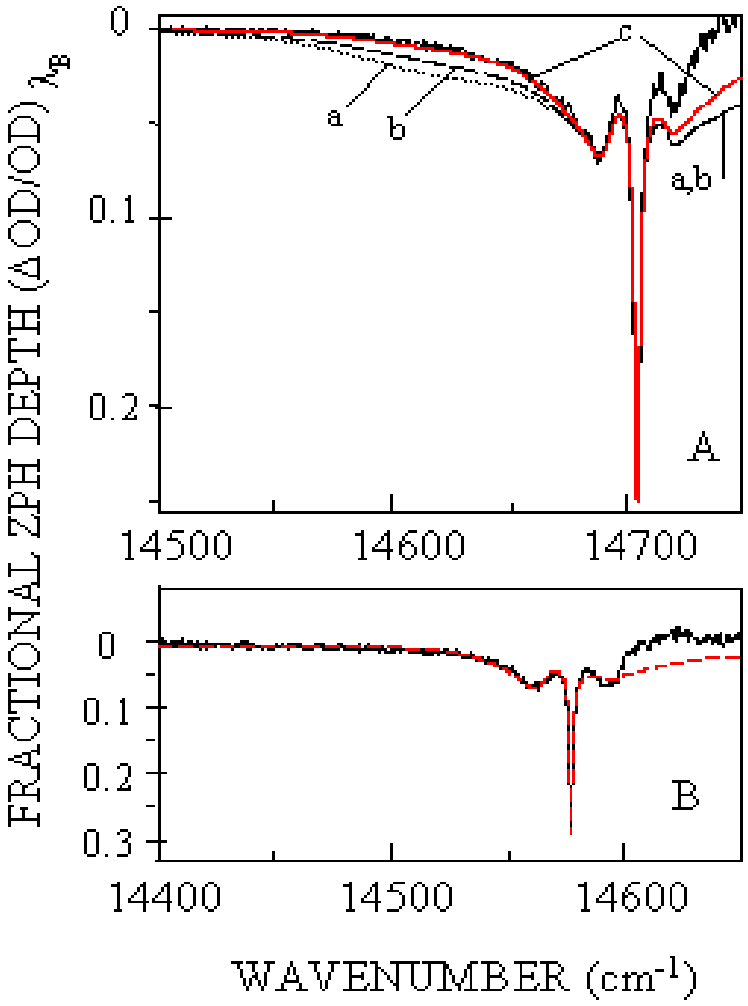

Figure 7. Saturated persistent holes burned at 680 nm (A) and 686 nm (B), black solid curves, and their fits according to the model by Hayes et al. [45] (see Table 2 for parameters). In frame A dotted (a) and dashed (b) curves are for $S_{17} = S_{80} = 0.7$, the parameters deduced from FLN spectra [31]. Ratio of peak intensities of 680 and 684 nm SDFs was 2.5:1 (a) and 5:1 (b). Red curve corresponds to $S_{17} = 0.7$, $S_{80} = 0.2$ and the SDF peak ratio of 2.5:1. In frame B only the spectrum calculated with latter parameters is shown (red) along with the experimental spectrum (black).

Table 2. Parameters used to fit persistent and triplet bottleneck hole spectra.

Parameter	686 nm holes	680 nm holes
P684 SDF[a] peak / width	684.7±0.5 nm / 90±10 cm^{-1}	
P680 SDF peak / width	680.3±0.5 nm / 110±10 cm^{-1}	
Peak intensity ratio (P680 : P684) ≡ R	2.5 : 1	
Phonon frequency ω_1:	17±1 cm^{-1}	
One-phonon profile (ω_1)[b].	11±1 cm^{-1} / 16±2 cm^{-1},	
Huang-Rhys factor S_{17}	0.7±0.1	
Phonon frequency (ω_2)	80±5 cm^{-1}	
One-phonon profile (ω_2)	90±10 cm^{-1}	
Huang-Rhys factor S_{80}	0.2±0.1	
Homogeneous ZPL width for persistent holes	0.5 cm^{-1}	1.0 cm^{-1}
Homogeneous ZPL width for triplet bottleneck holes	Subject to Weibull distribution with α=1.2 and maximum at 0.6 cm^{-1}.	

[a] SDF ≡ site (state) excitation frequency distribution function. [b] Gaussian shape on low-energy side (fwhm=11±1 cm^{-1}) and Lorentzian shape on high-energy side (fwhm=16±2 cm^{-1}). [c] Gaussian with fwhm of 90±10 cm^{-1}. [d] Resolution-limited

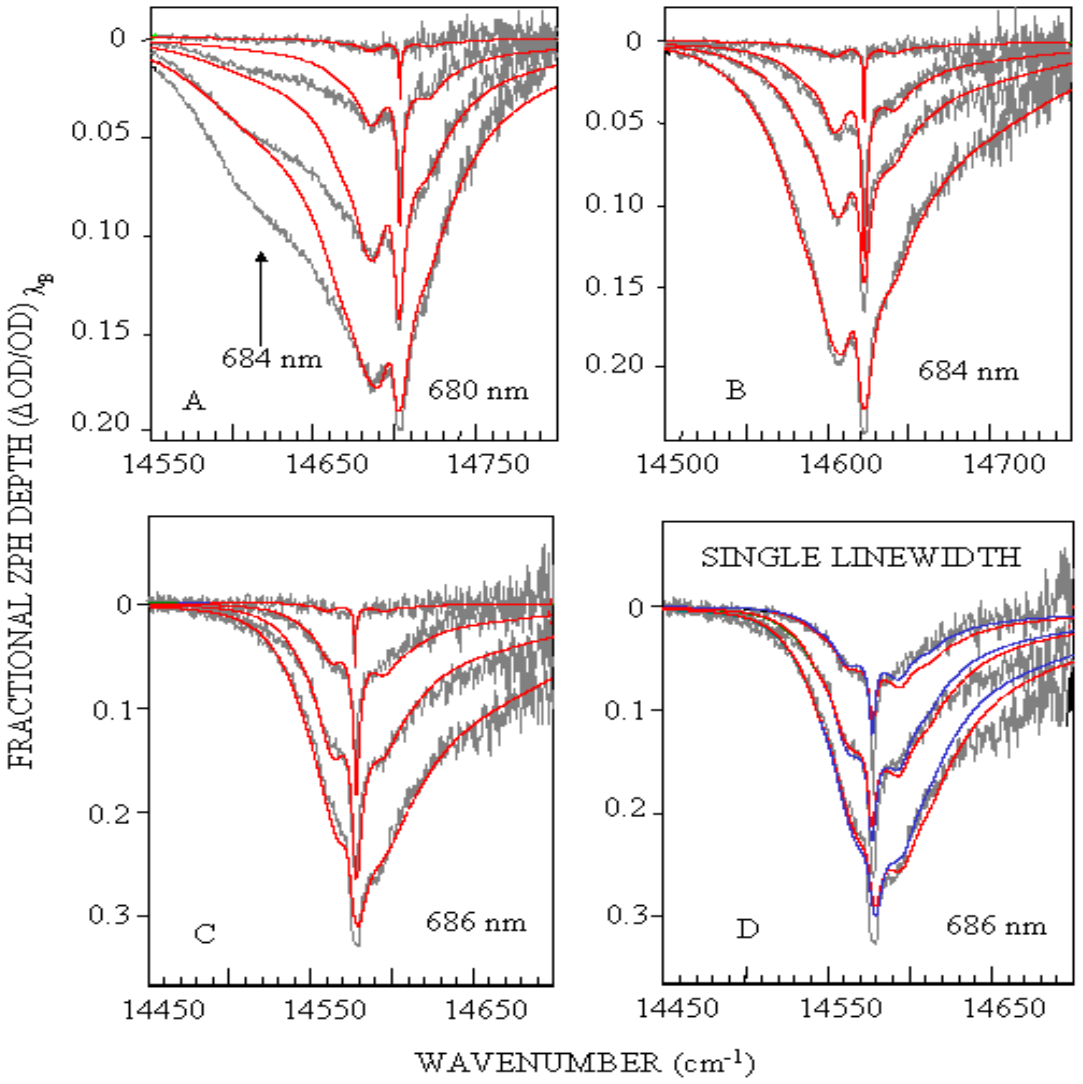

Figure 8. Frames A-C: Experimental (black) and calculated (red) triplet bottleneck hole spectra obtained with the same electron-phonon coupling parameters as used to fit persistent holes ($S_{17} = 0.7$, $S_{80} = 0.2$) and a distribution of homogeneous ZPL widths depicted in Figure 9. (Burn wavelengths are 680, 684 and 686 nm in frames A-C, respectively). Frame D: The hole spectra for $\lambda_B = 686$ nm and their fits with no ZPL width distribution, fixed ZPL width of 2 cm^{-1} and strong electron-phonon coupling. Blue curve: $S_{17} = 1.25$, red curve: $S_{17} = 1.5$.

1.25 (blue curve) and 1.50 (red curves); all other parameter values are as given in Table 2 except that the ZPL width was set equal to 2 cm^{-1} and the shape of the one-phonon profile of the 17 cm^{-1} mode changed slightly to improve the fits. The 2 cm^{-1} width corresponds to the primary charge separation time of ~ 5 ps reported in [25], T= 5.0 K. It proved impossible to simulate the peak intensity and width of the ZPH and the intensity and shape of the phonon sideband hole structure using a *fixed* ZPL width. In the following section it is shown that a distribution of ZPL widths (charge separation rates) results in significantly better fits to the TBHB spectra.

Discussion

We begin by considering possible assignments for the 684 nm absorbing chlorin(s). Following that the question of whether or not the primary charge separation kinetics are highly dispersive is addressed or, equivalently, the question of whether or not the primary electron donor state (lowest energy Q_y state) is well defined. The section ends with some remarks on the strength of the excitonic couplings between the core chlorins.

A. Nature of the 684 nm absorbing chlorin. The absorption spectrum in Figure 1 and hole burned spectra in Figures 2, 3 and 6 provide convincing evidence for the existence of the 684 nm absorbing chlorin(s). In view of the multimer model one might propose that the weak 684 nm band is due to the lowest energy exciton level of the core chlorins. However, the excitonic calculations are inconsistent with this since they predict that the lowest energy Q_y-state should be the most strongly absorbing, not weakly absorbing [6, 9, 10]. Also inconsistent with this are the TBHB spectra shown in frames

G and H of Figure 6 obtained with λ_B = 684 and 686 nm, wavelengths quite highly selective for the 684 nm band. The spectra are devoid of any intense satellite hole structure that lies to higher energy of the hole peaked at λ_B (the spectral region higher in energy than 14800 cm^{-1} (676 nm), which is not shown in frames G and H, also showed no hole structure). Such satellite hole structure would be a natural consequence of the weak 684 nm band corresponding to the lowest energy Q_y-state. A nice example of such satellite hole structure is the special pair of the RC of *Rps. viridis* [48]. It was shown that a hole burned in the lower dimer band (P_) of the special pair produced a satellite hole in the higher energy upper dimer band (P_+).

A second interpretation of the 684 nm band was that it is the origin of the primary electron donor's absorption with the P680 band corresponding to the one-quantum transition of a ~ 80 cm^{-1} vibration (phonon) [2]. This interpretation is untenable since the absorption spectrum (Figure 1) and TBHB spectra (Figure 3) lead to a Huang-Rhys factor (S_{80}) of ~ 2. The Franck-Condon progression for $S_{80} \sim 2$ would exhibit a maximum for the two-quantum transition at 2×80 cm^{-1} = 160 cm^{-1}, which is clearly absent in the TBHB spectra of Figure 3. We note also that a lengthy Franck-Condon progression in an 80 cm^{-1} mode is absent in the TBHB spectrum shown in frame H of Figure 6. Also, the observation that the 684 nm band is fragile while the P680 band is much less so is also inconsistent with the above interpretation.

In the absence of gross structural heterogeneity, a more likely assignment for the 684 nm band is that it corresponds to a localized Q_y transition of a particular RC chlorin that lies lower in energy than the primary electron donor's absorption (P680). Such a state would serve as a trap state. Because of the aforementioned fragility, it was

proposed that the responsible chlorin is one of the two peripheral Chls [38]. (It is known with certainty that one of the peripheral Chls absorbs near 670 nm [2].) There are, however, potential problems with this assignment. First, the results of the fs pump-probe experiments on RC-5 and RC-6 at room temperature indicate that both peripheral Chls absorb near 670 nm [5]. Second, the Q_y absorption spectrum for RC-5 calculated with either the multimer or pentamer excitonic Hamiltonians for the *core chlorins*, when added to the absorption of the peripheral Chl, does not fit well the observed spectrum unless the latter absorption is located near 670 nm, not 684 nm [6, 9, 10]. A third (possible) problem is related to motional narrowing of the inhomogeneous broadening of the site (chlorin) Q_y transition due to excitonic delocalization. It was determined in [37] that the site inhomogeneous broadening is, on average, ~ 200 cm^{-1}. Motional narrowing resulted in reduction of this width to ~ 120 cm^{-1} for the observed 'delocalized' transitions [37, 9]. The observed inhomogeneous width for the 684 nm band is only ~ 90 cm^{-1} (Table 1), slightly narrower than the inhomogeneous width of the P680 band which one expects to be motionally narrowed. The 90 cm^{-1} width would seem to be too narrow to be attributed to a transition localized on a single chlorin. This line of reasoning can be used to argue against the 684 nm band being due to a transition localized on any of the core chlorins. Nevertheless, the possibility that the 684 nm band is due to such a localized state cannot be excluded at this time.

Model for the 684 nm absorbing chlorin(s) based on gross structural heterogeneity. In this model the P680 and 684 nm bands are considered to arise from the same 'subset' of pigments. At low temperatures the oxygen-evolving PS II (D_1/D_2-cyt b_{559} RC plus CP43 and CP47 proximal antenna complexes) of spinach and

cyanobacteria exhibits a primary electron donor absorption band near 684 nm (P684) [32, 49] rather than 680 nm. The possibility that the biochemical procedure used to isolate and solubilize the RC shifts the P684 nm band of the majority of the *intact* RCs to 680 nm, while leaving a smaller fraction of RCs that still absorb at 684 nm, is worthy of consideration. Removal of the CP43 and CP47 antenna complexes might destabilize the RC, leading to a blue shift of the P684 band. An additional consideration is that the two plastoquinones of the RC are removed during the isolation procedure [2]. This 'P680-P684 model' for the isolated RC would appear to be consistent with the observation that the 684 nm absorbing chlorin(s) of the isolated RC are especially fragile. However, our intent is to be more general and explore the possibility that the isolated RC consists of two subpopulations with primary electron donor absorption bands at 680 nm (P680) and 684 nm (P684), regardless of the origin of heterogeneity.

This possibility is supported by the experimental results presented here. First, those in frames E-H of Figure 6 show that TBHB spectra of comparable intensity result from excitation at 680 nm and 686 nm, with the latter wavelength selective for the 684 nm state (P684*). Given that triplet state formation is the result of charge recombination of a primary radical ion pair [20, 50], it appears certain that P680* and P684* have in common that they serve as primary electron donor states. Second, the permanent dipole moment change for the $S_0 \rightarrow$P680* and $S_0 \rightarrow$P684* transitions are identical within experimental uncertainty, $f \cdot \Delta\mu \sim 0.9$ D, Table 2. Third, the linear pressure rates of –0.12 cm^{-1}/MPa and –0.15 cm^{-1}/MPa for the 680 nm and 684 nm absorption bands, respectively, are nearly the same. We note that this shift rate is linearly proportional to the local compressibility κ [42] so that, all other things being equal, a ~ 20% difference in

κ would account for the difference between the two shift rates. Fourth, the fluorescence line narrowed spectra obtained with laser excitation wavelengths between 679 nm and 686 nm exhibited identical vibronic structures (vibrational frequencies and relative vibronic intensities) [31]. This is consistent with the observation that the persistent NPHB spectra in frames A-D of Figure 6 are essentially independent of λ_B. More specifically, the hole spectra can be fitted using the same set of electron-phonon coupling parameter values for both the 680 and 684 nm states (Table 1). Examples are shown in Figure 7 for λ_B = 680 nm and 686 nm.

The above results establish that the properties of the 680 nm and 684 nm states are very similar. Such similarity would not be expected if the latter state was localized on a single chlorin molecule while P680* is delocalized over P_1 and P_2 and other pigments [9]. One has, therefore, an additional argument against the 684 nm state being localized. On the other hand, the results support the P680-P684 (gross structural heterogeneity) model. In this model the excitonic compositions of the 680 nm and 684 states are, on average, similar; this despite the 4 nm shift that may be due mainly to non-excitonic interactions (dispersion, van der Waals, H-bonding).

B. Simulation of triplet bottleneck hole-burned (TBHB) spectra with dispersive charge separation kinetics. The results in Figure 6 show that both persistent NPHB and transient TBHB spectra can be generated throughout the 680 nm and 684 nm absorption bands. In the first hole burning studies of the isolated PS II RC, in which λ_B was near the maximum of the 680 nm absorption band, the TBHB spectra were assigned to P680*, the primary electron donor state [20, 28]. The persistent NPHB was attributed to a Q_y state localized on $Pheo_1$ for reasons given above. As a result, the 680 nm

absorption band was proposed to be due mainly to P680 but with a significant contribution from $Pheo_1$, whose absorption is quasi-degenerate with that of P680. In view of the hole burned spectra presented here for λ_B = 684 and 686 nm (Figure 6), one might propose, with the P680-P684 model in mind, the same scenario for the 684 nm absorption band.

Recent results, however, suggest an alternative model in which (for both the 680 nm and 684 nm bands) the 'same' Q_y state is responsible for both NPHB and TBHB. (In this model the existence of P680 and P684 due to gross heterogeneity is retained.) First, the photon echo data (1.3 K) of Prokhorenko and Holzwarth [11] strongly indicate that the kinetics of primary charge separation are highly dispersive, with time constants ranging from a few nanoseconds to a couple of picoseconds. Even for the most efficient nonphotochemical hole burning systems the rate constant is only ~ $(10\ ns)^{-1}$ [51]. Thus, with the just mentioned dispersive kinetics for charge separation, the quantum yield for NPHB would vary over several orders of magnitude and the most efficient nonphotochemical hole burning RCs would also have the highest fluorescence quantum yields. We note that Groot et al. [52] reported a fluorescence quantum yield of 0.07 for RC-6. Second, and as pointed out earlier, all calculations on the Q_y excitonic structure of the core chlorins do not predict a transition highly localized on $Pheo_1$.

In using the alternative (new) model to simulate the TBHB spectra in Figure 6 a distribution function that describes the dispersion of charge separation times (or, equivalently, the distribution of zero-phonon linewidths; 1 ps$\rightarrow$ 5 cm^{-1}) is required. The Weibull function $W(x) = \alpha x^{\alpha-1}\exp(-x^{\alpha})$ was chosen, in part, because it provides an acceptable description of the shorter charge separation times reported by Prokhorenko

and Holzwarth [11]. To reduce the number of free parameters, the value of α was taken to be the same for both the 680 nm and 684 nm states, which is reasonable within the P680-P684 model. In addition, the electron-phonon coupling parameters for both states were then taken to be the same and independent of burn wavelength. With reference to Eqs. 3 and 5, the quantum yield for charge separation can be set equal to unity since the TBHB spectra were obtained under conditions which ensure that only RCs with charge separation times much shorter than a few ns (Chl *a* natural radiative lifetime) contribute. Thus, the simulations with Eq. 5 simply involved allowing for a distribution (Weibull) of widths for the zero-phonon line shape function ($l_{R=0}$ in Eq. 3). We note that this width is automatically added to the widths of the phonon sideband transitions associated with the 17 cm^{-1} and 80 cm^{-1} modes. The relative values of the burn intensities for each burn wavelength were *not* adjustable parameters, i.e. they were determined by the experimental intensities.

The simulated spectra (red curves) are compared against the experimental TBHB spectra in frames A, B and C of Figure 8 for λ_B = 680, 684 and 686 nm, respectively. A surprising and interesting finding was that the values of the electron-phonon coupling and SDF parameters (see Table 1) that provide reasonable fits to the persistent NPHB spectra (examples shown in Figure 7) also provide acceptable fits to the TBHB spectra. The Weibull distribution function (α = 1.2) that led to these best overall fits is shown in Figure 9. Note that it is offset along the abscissa. The reason for the offset is that the TBHB spectra were obtained after saturating *persistent* NPHB at λ_B (see section 2). This protocol was originally introduced to eliminate interference from NPHB due to $Pheo_1$ to the TBHB spectra of P680 [20]. What this means for the model being considered is that

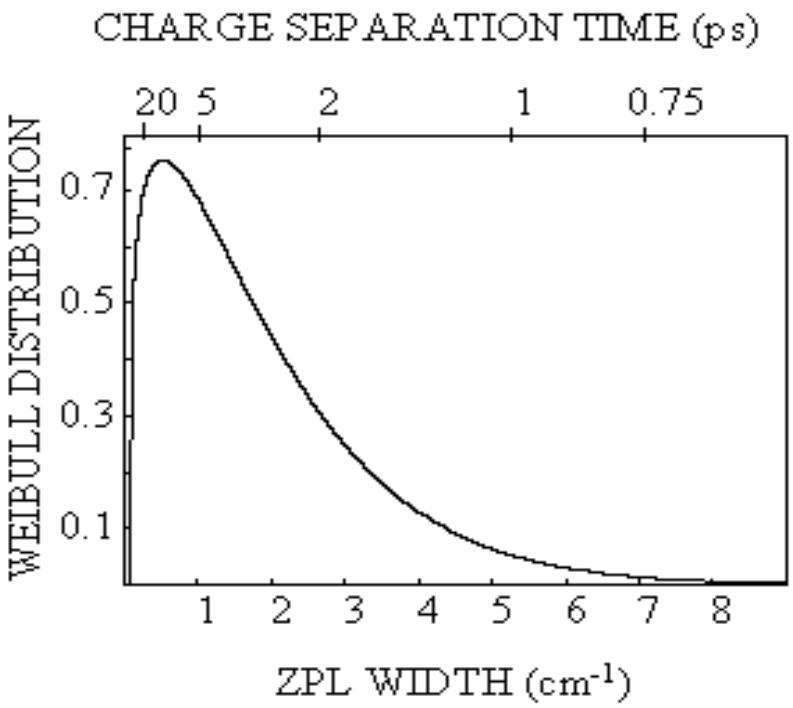

Figure 9. Weibull distribution of the homogeneous ZPL widths used in this work. Distribution is offset along the ZPL width axes by 0.2 cm^{-1} and peaked at 0.6 cm^{-1} (9 ps primary charge separation time).

the RCs with the slowest charge separation kinetics have been burned away (persistently) and, therefore, do not contribute to the TBHB spectra. The offset was an adjustable parameter; its value in Figure 9 is 0.2 cm^{-1} (25 ps). Thus, only RCs with a charge separation time shorter than ~ 25 ps contribute to the TBHB spectra.

For all λ_B values a distribution of ZPL widths gave considerably better fits than a single ZPL width (charge separation time). This can be seen for λ_B = 686 nm by comparing the spectra in frame C with those in frame D (fixed ZPL width), Figure 8. (The spectra for the lowest burn intensity are not shown in frame D because of very poor agreement between the observed and simulated spectra.) The red and blue curves in frame D were calculated, respectively, with Huang-Rhys factor S_{17} = 1.5 and 1.25. The simulated spectra in frame D reveal the problem encountered with all burn wavelengths; namely, that it is impossible to achieve acceptable fits to both the phonon sideband hole (PSBH) structure and the zero-phonon hole (ZPH) when the width of the ZPL is assigned a constant value. The increase in width of the ZPH with increasing burn intensity in the simulated spectra shown in frame D is due to fluence broadening [53, 54], which is accounted for in the hole burning theory used. The fits of the simulated spectra shown in frame C, obtained with a distribution of charge separation times, are clearly superior. Now the increase of ZPH width with increasing burn intensity is due to both fluence broadening and spectral dynamics (the induced absorption rate is inversely proportional to the width of the ZPL which, in turn, is inversely proportional to the primary charge separation time). The agreement between the simulated and experimental spectra obtained with distributed charge separation kinetics and λ_B = 684 nm is also quite satisfactory, frame B of Figure 8. This is also the case for λ_B = 680 nm, frame A. The

apparent discrepancies at ~ 684 nm (also seen for λ_B = 682 nm, not shown) do not signal a problem with the model. The broad feature near 684 is a satellite hole due to downward energy transfer to the lowest energy exciton level of P684-type RCs following excitation at 680 nm of the second lowest energy exciton level. Such energy transfer is not accounted for in Eq. 3.

The results in Figures 7 and 8 (and others not shown) establish that the persistent NPHB spectra and TBHB spectra can be understood in terms of the P680-P684 model and a common set of values for the parameters that define the electron-phonon coupling and the SDF for both P680 and P684 *provided the charge separation kinetics are taken to be dispersive*. Of considerable interest is that in the simulation of the TBHB spectra dispersive charge separation kinetics results in weak electron-phonon coupling (S_{17} = 0.7), while non-dispersive kinetics results in strong coupling (S_{17} ~ 1.5). The latter value is similar to those reported earlier [28, 36]. In those works it was assumed that the kinetics are non-dispersive. A detailed understanding of how dispersive kinetics results in an 'apparent' weakening of the coupling is rather involved because the hole burned spectrum consists of four contributions [55]: the ZPH; the real-PSBH that builds, in a Franck-Condon sense, on the ZPH; the pseudo-PSBH that is the result of 'sites' whose ZPLs lie lower in energy than ω_B and which absorb via their phonon sideband. Hole burning ensues following relaxation of the phonons and population of the zero-point level; and the phonon structure that builds on the pseudo-PSBH in a Franck-Condon sense. One should also keep in mind that the ZPHs of RCs with the slowest charge separation kinetics will saturate (reach maximum depth) first since the induced absorption rate is proportional to the charge separation time (or inversely proportional to

homogeneous width of the ZPL). Fluence broadening of the ZPH increases rapidly as saturation is approached [53, 54]. In the case of single exponential kinetics, the increase of ZPH width seen in frames E-H of Figure 6, with increasing burn intensity would be due solely to saturation broadening. For a given range of burn intensities (starting at the shallow burn limit), the greater the increase in width, the larger S_{17}. To a reasonable approximation the Franck-Condon factor for the ZPH is $\exp(-2S_{17})$ [45]. Thus, for a given homogeneous width of the ZPH, the burn intensity required to saturate the ZPH decreases with increasing S_{17}. In case of dispersive kinetics, such as described by the Weibull distribution in Figure 9, the ZPH broadening is due to both fluence broadening and spectral dynamics, the latter associated with charge separation kinetics. Thus, correcting the observed broadening for the contribution due to spectral dynamics would lead to less broadening due to fluence broadening and, as a consequence, a lower value of S_{17}. One additional point has to do with the contribution of the ZPH to the spectral 'pedestal' region of the real-PSBH and pseudo-PSBH. For a fixed homogeneous width of the Lorentzian ZPH, the larger the ratio of the integrated intensity of the underlying pedestal to that of the ZPH (which is superimposed on the pedestal), the stronger the electron-phonon coupling. Given the Weibull distribution in Figure 9 and the 2 cm^{-1} ZPH width used to fit the TBHB spectra in frame D of Figure 8, it is clear that the contribution to the pedestal in the case of dispersive kinetics would be greater than in the case of nondispersive kinetics, especially at the later stages of hole burning. This would also lead to a lower value of S_{17} in the case of dispersive kinetics.

C. Excitonic couplings between the core chlorins. As discussed in the Introduction, excitonic calculations [6, 9, 10] based on the X-ray structure of the PS II

RC and guided by the observation that the Q_y absorption spectrum spans a range of only ~ 500 cm^{-1}, as well as an experimental value for the width of the SDF of the core chlorins (~ 200 cm^{-1}), indicate that the Q_y states of the core cofactors are delocalized over ~ 3-4 chlorins. This, despite the fact that the strongest pairwise coupling is only ~ 150 cm^{-1} (between P_1 and P_2). Jankowiak et al. [9] found that several types of optical spectra (low temperature) were best fitted if $Pheo_2$ was decoupled from the other core chlorins (P_1, P_2, Chl_1, Chl_2, $Pheo_1$). One has, therefore, a 'pentamer' model for the Q_y states. Decoupling would require a significant weakening of the interaction between $Pheo_2$ and Chl_2 relative to the interaction between $Pheo_1$ and Chl_1 (see Figure 1). Recently, Frese et al. [56] reported that $f \cdot \Delta\mu$ for the $S_0 \rightarrow Q_x$ transitions of $Pheo_1$ and $Pheo_2$ are very different, 3.0 D and 0.6-1.0 D, respectively. The difference is most likely due to the 'matrix' induced contribution to $f \cdot \Delta\mu$ on the D_2 side of the RC being much larger than on the D_1 side. Interestingly, the very recently reported X-ray structure (3.7 Å resolution) of PS II from *Thermosynechococcus vulcanus* revealed that the two carotenoid molecules for the RC are located on the D_2 side, quite close to $Pheo_2$ [57]. Thus, there are some reasons to speculate that $Pheo_2$ could be decoupled, e.g. dielectric screening might lead to significant weakening of the $Pheo_2$-Chl_2 coupling.

It is worthwhile to compare the low temperature absorption spectrum of RC-5 calculated with the pentamer Hamiltonian given in [9] with the experimental spectrum. The shorter dashed curve in frame A of Figure 10 is the calculated spectrum for the core chlorins (peripheral Chl not included). The six underlying dotted curves are the absorption bands of the six Q_y states. That of the decoupled $Pheo_2$ is marked by the

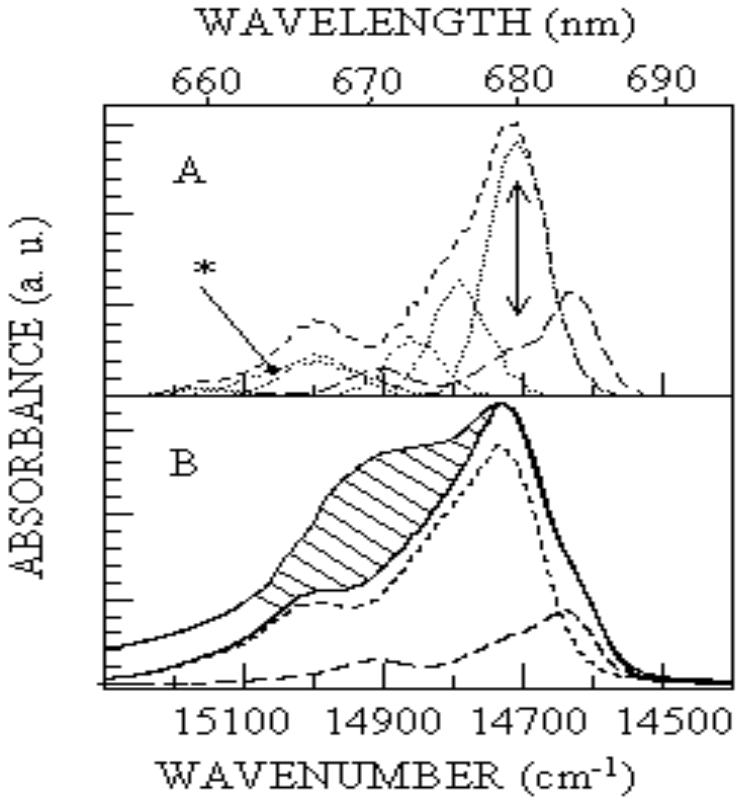

Figure 10. Simulations of absorption spectra. Dotted lines in frame A represent the excitonic states (and the state localized on the decoupled $Pheo_2$ at 668 nm; marked with a slanted arrow with an asterisk) of the pentamer model by Jankowiak et al. [9] neglecting electron-phonon coupling. Short-dashed line is the sum of the dotted curves. Long-dashed line represents the spectrum of the P684-type RCs. Short- and long-dashed curves in frame B are the result of convolution of the respective curves from frame A with the single site spectrum. Thin solid curve is the sum of long- and short-dashed curves. Thick solid curve is the experimental absorption spectrum. Shaded region represents the absorption of the peripheral Chl *a* peaked at ~ 670 nm. Vertical arrow in frame A indicates that the lowest state of P680-type RCs and the second-lowest state of P684-type RCs are degenerate.

asterisk and is located at 668 nm with a fwhm of 180 cm^{-1}. The other five bands correspond to the delocalized states. For these states the SDFs of the five coupled chlorins were centered at 671 nm (fwhm ~ 180 cm^{-1}) [9], values close to those given in [9]. With the P680-P684 model in mind, the shorter dashed curve should be viewed as the absorption spectrum of P680-type RCs, less the peripheral Chl. The longer dashed spectrum is that of P684-type RCs, a 4 nm shifted replica of the P680-type spectrum. (Based on the action spectra in Figure 2 and the TBHB spectra in Figure 3 we estimated that the ratio of intensity of the P680 absorption band to that of the 684 nm band is ~ 2.5. This leads to the result that the P684-type RCs contribute ~ 25% of the total absorption, in reasonable agreement with the spectra in frame A of Figure 2.) The two spectra do not include electron-phonon coupling. We used the electron-phonon coupling parameter values in Table 1 to define a single site absorption spectrum which was convolved with the six inhomogeneously broadened absorption bands of both the P680 and P684 RCs. The resulting (summed) spectra are the short dashed (P680) and long dashed (P684) in frame B of Figure 10. Their sum is the thin solid line spectrum, which should be compared with the experimental spectrum (thick solid line). The fit to lower energy of the maximum of the 680 nm band is satisfactory. The discrepancy to higher energy (hatched area) is most reasonably assigned mainly to the single peripheral Chl (~ 670 nm) that was not included in the simulations, i.e. it seems unlikely that the 684 nm absorption band is due to the peripheral Chl. We note that vibronic transitions that build on the origin bands at 680 and 684 nm should make a weak contribution to the absorption at ~ 670 nm.

Concerning the pairwise excitonic interactions (electrostatic) of the core chlorins of the PS II RC, we note that although they are rather small ($\lesssim$ 150 cm^{-1}), the Q_y states tend to be delocalized because the larger interactions are comparable in magnitude to the differences between the chlorin site excitation energies, as well as the width of the site excitation energy distribution functions [8, 10]. (There is no physical basis for asserting that all the Q_y states are localized, as Diner and coworkers have [58].) The question arises as to whether or not any experimental data indicate that electron-exchange coupling contributes significantly to pairwise interactions (the most likely one being between P_1 and P_2). Such coupling introduces charge transfer character to the excited states, as reviewed in [4]. Three indicators for appreciable electron-exchange coupling are the electron-phonon coupling strength, the permanent dipole moment change and linear pressure shift of the $S_1(Q_y)\leftarrow S_0$ transitions. These three properties are generally positively correlated (see references (refs.) [39, 40] and refs. therein). As discussed in those works, the linear pressure rate (R_p) for the $S_1(\pi\pi^*)\leftarrow S_0$ transition frequency is ~ –0.05 to –0.15 cm^{-1}/MPa for *monomer* chromophores in glasses and polymers at low temperatures, $f\cdot\Delta\mu$ ~ 0.4–0.6 D for the Chl *a* monomer in polymers or a localized Q_y state and, finally, the total Huang-Rhys factor (S_t) for low frequency phonons is most often less than 1 (weak linear electron-phonon coupling). As reviewed in [59] for Chl dimers, $|R_p| \gtrsim 0.3$ cm^{-1}/MPa, $f\cdot\Delta\mu \gtrsim 1$ D and $S_t >> 1$ (strong coupling) are values which indicate that the monomers are strongly interacting with electron exchange coupling making a significant contribution. Examples of such a Chl *a* dimer state are the red-most antenna state of the cyanobacteria *Synechocystis* PCC 6803 and *Synechococcus elongatus* at 714

nm and 719 nm, respectively, for which $R_p \sim -0.5$ cm^{-1}/MPa, $f \cdot \Delta\mu \sim 2.4$ D and $S_t \sim 2.0$ [39, 40]. The values for P680 and P684 of the isolated PS II RC are ~ -0.14 cm^{-1}/MPa, ~ 0.9 D and 0.9, values that are inconsistent with appreciable electron exchange coupling between the cofactors, in particular P_1 and P_2.

Acknowledgements

Research at the Ames Laboratory was supported by the Division of Chemical Sciences, Office of Basic Energy Sciences, U. S. Department of Energy. Ames Laboratory is operated for USDOE by Iowa State University under Contract W-7405-Eng-82. Authors are thankful to Drs. Tõnu Reinot and John M. Hayes (ISU), Dr. Thomas Renger (Humboldt University, Berlin), Dr. Rafael Picorel (E. E. Aula Dei, Zaragoza), Dr. Michael Seibert (NREL, Golden, Colorado), Drs. Ronald Pace and Elmars Krausz (The Australian National University) and Dr. Valentin Prokhorenko (Max-Planck-Institut für Strahlenchemie, Mülheim a.d. Ruhr) for fruitful discussions.

References

1. Nanba, O., Satoh, K., *Proc. Natl. Acad. Sci. U.S.A*. **1987**, 84, p. 109.
2. Dekker, J. P., van Grondelle, R., *Photosynth. Res.* **2000**, 63, p. 195.
3. Zouni, A., Witt, H. T., Kern, J., Fromme, P., Krauβ, N., Saegner, W., Orth P., *Nature* **2001**, 409, p. 739.
4. Small, G. J., *Chem. Phys.* **1995**, 197, p. 239.
5. Vacha, F., Joseph, D. M., Durrant, J. R., Telfer, A., Klug, D. R., Porter, G., Barber, J., *Proc. Natl. Acad. Sci. U.S.A.* **1995**, 92, p. 2929.
6. Durrant, J. R., Klug, D. R., Kwa, S. L. S., van Grondelle, R., Porter, G., Dekker, J. P., *Proc. Natl. Acad. Sci. U.S.A.* **1995**, 92, p. 4798.
7. Svensson, B., Etchebest, C., Tuffery, P., van Kan, P., Smith, J., Styring, S., *Biochemistry* **1996**, 35, p. 14486.
8. Tetenkin, V. L., Gulyaev, B. A., Seibert, M., Rubin, A. B., *FEBS Lett.* **1989**, 250, p. 459.
9. Jankowiak, R., Hayes, J. M., Small, G. J., *J. Phys. Chem. B* **2002**, 106, p. 8803.
10. Renger, T., Marcus, R. A., *J. Phys. Chem. B* **2002**, 106, p. 1809.
11. Prokhorenko, V. I., Holzwarth, A. R., *J. Phys. Chem. B* **2000**, 104, p. 11563.
12. Vasil'ev, S., Orth, P., Zouni, A., Owens, T. G., Bruce, D., *Proc. Natl. Acad. Sci. U.S.A.* **2001**, 98, p. 8602.
13. Groot, M. L., van Mourik, F., Eijckelhoff, C., van Stokkum, I. H. M., Dekker, J. P., van Grondelle, R., *Proc. Natl. Acad. Sci. U.S.A.* **1997**, 94, p. 4389.
14. Wasielewski, M. R., Johnson, D. G., Seibert, M., Govindjee, *Proc. Natl. Acad. Sci. U.S.A.* **1989**, 86, p. 524.

15. Wiederrecht, G. P., Seibert, M., Govindjee, Wasielewski, M. R., *Proc. Natl. Acad. Sci. U.S.A.* **1994**, 91, p. 8999.

16. Schelvis, J. P. M., van Noort, P. I., Aartsma, T. J., van Gorkom, H. J., *Biochem. Biophys. Acta* **1994**, 1184, p. 242.

17. Gatzen, G., Müller, M. G., Griebenow, K., Holzwarth, A. R., *J. Phys. Chem.* **1996**, 100, p. 7269.

18. Greenfield, S. R., Seibert, M., Govindjee, Wasielewski, M. R., *J. Phys. Chem. B* **1997**, 101, p. 2251.

19. Merry, S. A., Kamzaki, S., Tachibana, Y., Joseph, D. M., Porter, G., Yoshohara, K., Barber, J., Durrant, J. R., Klug, D. R., *J. Phys. Chem. B* **1996**, 100, p. 10469.

20. Jankowiak, R., Tang, D., Small, G. J., Seibert, M., *J. Phys. Chem.* **1989**, 93, p. 1649.

21. Tang, D., Jankowiak, R., Seibert, M., Small, G. J. *Photosynth. Res.* **1991**, 27, p. 19.

22. Wasielewski, M. R., Johnson, D., Govindjee, Preston, C., Seibert, M., *Photosynth. Res.* **1989**, 22, p. 89.

23. Visser, H. M., Groot, M.-L., van Mourik, F., van Stokkum, I. H., Dekker, J. P., van Grondelle, R., *J. Phys. Chem.* **1995**, 99, p. 15304.

24. Greenfield, S. R., Seibert, M., Wasielewski, M. R., *J. Phys. Chem. B* **1999**, 103, p. 8364.

25. Jankowiak, R., Rätsep, M., Hayes, J. M., Zazubovich, V., Picorel, R., Seibert, M., Small, G. J., *J. Phys. Chem. B* **2003**, 107, p. 2068.

26. van Kan, P. J. M., Otte, S. C. M., Kleinherenbrink, A. M., Nieveen, M. C., Aartsma, T. J., van Gorkom, H. J., *Biochim. Biophys. Acta* **1990**, 1020, p. 146.

27. Otte, S. C. M., van der Vos, R., van Gorkom, H. J., *Photochem. Photobiol. B: Biol.* **1992**, 15, p. 5.

28. Chang, H.-C., Jankowiak, R., Reddy, N. R. S., Yocum, C. F., Picorel, R., Seibert, M., Small, G. J., *J. Phys. Chem*. **1994**, 98, p. 7725.

29. Groot, M. L., Dekker, J. P., van Grondelle, R., den Hartog, F. T. H., Völker, S., *J. Phys. Chem.* **1996**, 100, p. 11488.

30. den Hartog, F. T. H., Vacha, F., Lock, A. J., Barber, J., Dekker, J. P., Völker, S., *J. Phys. Chem. B* **1998**, 102, p. 9174.

31. Peterman, E. J. G., van Amerongen, H., van Grondelle, R., Dekker, J. P., *Proc. Natl. Acad. Sci. U.S.A.* **1998**, 95, p. 6128.

32. Smith, P. J., Peterson, S., Masters, V. M., Wydrzynski, T., Styrling, S., Krausz, E., Pace, R. J., *Biochemistry* **2002**, 41, p. 1981.

33. Reddy, N. R. S., Picorel, R., Small, G. J., *J. Phys. Chem.* **1992**, 96, p. 6458.

34. Rätsep, M., Wu, H.-M., Hayes, J. M., Blankenship, R. E., Cogdell, R. J., Small, G. J., *J. Phys. Chem. B* **1998**, 102, p. 4035.

35. Chang, H.-C., Jankowiak, R., Reddy, N. R. S., Small, G. J., *Chem. Phys.* **1995**, 197, p. 307.

36. Kwa, S. L. S., Eijckelhoff, C., van Grondelle, R., Dekker, J. P., *J. Phys. Chem.* **1994**, 98, p. 7702.

37. Jankowiak, R., Rätsep, M., Picorel, R., Seibert, M., Small, G. J., *J. Phys. Chem. B* **1999**, 103, p. 9759.

38. Chang, H.-C., Small, G. J., Jankowiak, R., *Chem. Phys.* **1995** 194, p. 323.

39. Rätsep, M., Johnson, T. W., Chitnis, P. R., Small, G. J., *J. Phys. Chem. B* **2000**, 104, p. 836.

40. Zazubovich, V., Matsuzaki, S., Johnson, T. W., Hayes, J. M., Chitnis, P. R., Small, *Chem. Phys.* **2002**, 275, p. 47.

41. Wu, H.-M., Rätsep, M., Young, C. S., Jankowiak, R., Blankenship, R. E., Small, G. J., *Biophys. J.* **2000**, 79, p. 1561.

42. Köhler, M., Friedrich, J., Fidy, J., *Biochim. Biophys. Acta* **1998**, 1386, p. 255.

43. Kador, L., Haarer, D., Personov, R., *J. Chem. Phys* **1987**, 86, p. 5300.

44. Lyle, P. A., Kolaczkowski, S. V., Small, G. J., *J. Phys. Chem*. **1993**, 97, p. 6924.

45. Hayes, J. M., Lyle, P. A., Small, G. J., *J. Phys. Chem*. **1994**, 98, p. 7337.

46. Matsuzaki, S., Zazubovich, V., Rätsep, M., Hayes, J. M., Small, G. J., *J. Phys. Chem. B* **2000**, 104, p. 9564.

47. Lee, I.-J., Small, G. J., *J. Phys. Chem.* **1990**, 94, p. 3376.

48. Reddy, N. R. S., Kolaczkowski, S. V., Small, G. J., *J. Phys. Chem*. **1993**, 97, p. 6934.

49. Hillmann, B., Brettel, K., van Mieghem, F., Kamlowski, A., Rutherford, A. W., Schlodder, E., *Biochemistry* **1995**, 34, p. 4814.

50. Vink, K. J., de Boer, S., Plijter, J. J., Hoff, A. J., Wiersma, D. A., *Chem. Phys. Lett*. **1987**, 142, p. 433.

51. Reinot, T., Small, G. J., *J. Chem. Phys*. **2000**, 113, p. 10207.

52. Groot, M.-L., Peterman, E. J. G., van Kan, P. J. M., van Stokkum, I. H. M., Dekker, J. P., van Grondelle, R., *Biophys. J.* **1994**, 67, p. 318.

53. Völker, S., *J. Luminescence* **1987**, 36, p. 251.

54. van der Zaag, P. J., Galaup., J. P., Völker, S., *Chem. Phys. Lett.* **1990**, 174, p. 467.

55. Pieper, J., Voigt, J., Renger, G., Small, G. J., *Chem. Phys. Lett*. **1999**, 310, p. 296.

56. Frese, R. N., Germano, M., de Weerd, F. L., van Stokkum, I. H. M., Shkuropatov, A. Y., Shuvalov, V. A., van Gorkom, H. J., van Grondelle, R., Dekker, J. P., *Biochemistry* **2003**, 42, p. 9205.

57. Kamiya, N., Shen, J.-R., *Proc. Natl. Acad. Sci. USA* **2003**, 100, p. 98.

58. Diner, B., Rappaport, F., *Annu. Rev. Plant Biol.* **2002**, 53, p. 551.

59. Reinot, T., Zazubovich, V., Hayes, J. M., Small, G. J., *J. Phys. Chem. B* **2001**, 105, p. 5083.

CHAPTER 5 – FREQUENCY-DOMAIN SPECTROSCOPIC STUDY OF THE PS I - CP43′ SUPERCOMPLEX FROM THE CYANOBACTERIUM *SYNECHOCYSTIS* PCC 6803 GROWN UNDER IRON STRESS CONDITIONS

A submitted paper that was modified and published in the *J. Phys Chem. B* **2006**, 110, p. 22436-22446.

Kerry J. Riley, Valter Zazubovich, and Ryszard Jankowiak

Abstract

Absorption, fluorescence excitation, emission and hole burning (HB) spectra were measured at liquid helium temperatures for the PS I - CP43′ supercomplexes of *Synechocystis* PCC 6803 grown under iron stress conditions and for respective trimeric PS I cores. Results are compared with those of room temperature, time-domain experiments (Melkozernov et al, *Biochemistry* **2003**, 42, 3893) as well as with the low-temperature steady-state experiments on PS I - CP43′ supercomplexes of *Synechococcus* PCC 7942 (Andrizhiyevskaya et al, *BBA* **2002**, 1556, 265). In contrast to the CP43′ of *Synechococcus* PCC 7942, CP43′ of *Synechocystis* PCC 6803 possesses two low-energy states analogous to the quasi-degenerate states A and B of CP43 of photosystem II (Jankowiak et al, *J. Phys. Chem. B* **2000**, 104, 11805). Energy transfer between the CP43′ and the PS I core occurs, to significant degree, through the state A, characterized with broader site distribution function (SDF). It is demonstrated that the low temperature (T = 5K) excitation energy transfer (EET) time between the state A of CP43′ (*IsiA*) and

the PS-I core in PS I - CP43′ supercomplexes from *Synechocystis* PCC 6803 is about 60 ps, which is significantly slower than the EET observed at room temperature. Our results are consistent with fast (≤ 10 ps) energy transfer from state B to state A. Energy absorbed by the CP43′ manifold has, *on average,* a greater chance of being transferred to the reaction center (RC) and utilized for charge separation than energy absorbed by the PS I core antenna. This indicates that energy is likely transferred from the CP43′ to the RC along a well-defined path and that the "red antenna states" of the PS I core are localized far away from that path, most likely on the B7-A32 and B37-B38 dimers in the vicinity of the PS I trimerization domain (near PsaL subunit). We argue that the A38-A39 dimer does not contribute to the red antenna region.

Introduction

The evolution of photosynthetic organisms has resulted in the development of different strategies to adapt their photosynthetic apparatuses to various conditions of illumination or nutrient supply. One such strategy involves changing the extent and structure of phycobilisomes [1, 2]. In an iron-deficient environment, the phycobiliprotein content and photosystem I (PS I) to photosystem II (PS II) ratio are reduced [3]. This is compensated by an accumulation of *IsiA* (CP43′) [4-6] protein, a chlorophyll *a* (Chl *a*) binding protein genetically very similar to CP43 of photosystem II (PS II) [7, 8]. In particular, the typical reaction of some cyanobacteria to iron stress is to surround the (trimeric) PS I core with 18 [7, 9, 10] (or 17 for the PS I lacking PsaF and PsaJ subunits [11]) copies of CP43′. The PS I core monomer contains protein subunits PsaA … PsaX; most of the chlorophyll (Chl) molecules, including the reaction center (RC) chlorophylls, are bound to PsaA and PsaB subunits, which are approximately related to each other by C_2 symmetry [12]. An arrangement involving 18 copies of CP43′ was observed for *Synechococcus* PCC 7942 [9] and *Synechocystis* PCC 6803 [10]. It is interesting that a similar structural arrangement was also adopted by deep-water (low-illumination) strains of *Prochlorococcus marinus* [13], although, in this case, antenna complexes and probably also the PS I core contain Chl b_2 (divinyl derivative of Chl *b* with similar spectral properties). Recently, several groups engaged in studying spectral properties and energy transfer dynamics in CP43′ and PS I - CP43′ supercomplexes of cyanobacteria [14-16]. These works agree that the CP43′ ring effectively transfers energy (within 2 ps at room temperature) to the PS I core, although an increase of total trapping time (compared to separate PS I cores) was also observed [14, 16]. Note, however, that the transient

difference absorption spectra (Figure 5 in ref. [14]) indicate that a large fraction of excitation remains at ~ 680 nm even after 10 ps. Thus, 2 ps may be the fastest, not the average CP43′ → PS I core excitation energy transfer (EET) time. The high-resolution structure of the CP43′ complex is not known, but the three-dimensional structure of the PS I - CP43′ supercomplex has been modeled by merging low-resolution cryo-microscopy data [17] with available high-resolution data on PS I from *Thermosynechococcus elongatus* [12] and CP43 from PS II [18], see Figure 1. Only 12 chlorophyll molecules per CP43 were identified in ref. [18] and only [11] are depicted in Figure 1 and in ref. [17], while according to the more recent X-ray diffraction data there are 13 [19, 20] or even 14 [21] chlorophylls per CP43. However, one should be careful comparing CP43 and CP43′ since CP43′ has ~ 130 fewer amino acids than CP43 due to the absence of a hydrophilic loop joining the lumenal ends of the transmembrane helices 5 and 6 [17]. That said, if one assumes that the CP43′ complexes bind chlorophylls in the same way as CP43, then the closest distances between Chl *a* molecules of adjacent CP43′ complexes may be as small as 10 Å, which could result in sub-picosecond energy equilibration within the CP43′ ring at room temperature. It also appears that there are three regions per PS I monomer where Chl *a* molecules belonging to CP43′ are close enough (within ~ 20 Å) to the Chl *a* molecules of the PS I core to justify excitation energy transfer on an ~ 2 ps timescale at room temperature [7, 14, 16, 17]. One of the intriguing results of [17] is that one of these contact regions of the PS I core incorporates chlorophylls labeled B31, B32 and B33 (labeling according to [12]), which, as argued in ref. [12], is a possible origin of one of the red antenna states of the PS I core (see below).

The second region includes chlorophylls J1-J3 and the third region, chlorophylls A8, A10, A12-A14, A18 and K2. Note that six CP43′ complexes are in non-equivalent positions relative to the PS I core monomer (see Figure 1; see also [17]) and, therefore, the reported CP43′ → PS I core energy transfer rates may be an average of several different rates.

Spectral hole burning (SHB) has been successfully applied to various photosynthetic complexes, including trimeric cyanobacterial PS I [22-24] and CP43 isolated from PS II of higher plants [25, 26]. The widths of spectral holes are inversely proportional to the lifetimes of the excited states. This feature makes SHB very useful in exploring energy transfer processes in photosynthetic complexes. In case of the CP43, SHB was applied to demonstrate that this complex possesses two quasi-degenerate, low-energy states, labeled A and B in [25], characterized by different inhomogeneous widths and different permanent dipole moment differences between ground and excited state, as well as different intersystem crossing yields. For PS I, SHB was mainly employed to resolve different red antenna states (i.e. the antenna states absorbing at lower energy than the primary donor, P700) and to prove that these states originate from aggregates of strongly coupled chlorophyll molecules (and not from monomeric Chl *a* whose red-shifted energies are the result of peculiar interactions with the protein environment [22-24]). Three red antenna states were resolved by SHB for *Synechococcus elongatus* [22] and two for *Synechocystis* PCC 6803 [23, 24]. It is interesting that the lowest-energy states of the PS I of the above two cyanobacteria, C719 and C714, respectively, have very similar properties and therefore most likely originate from the same chlorophyll aggregate

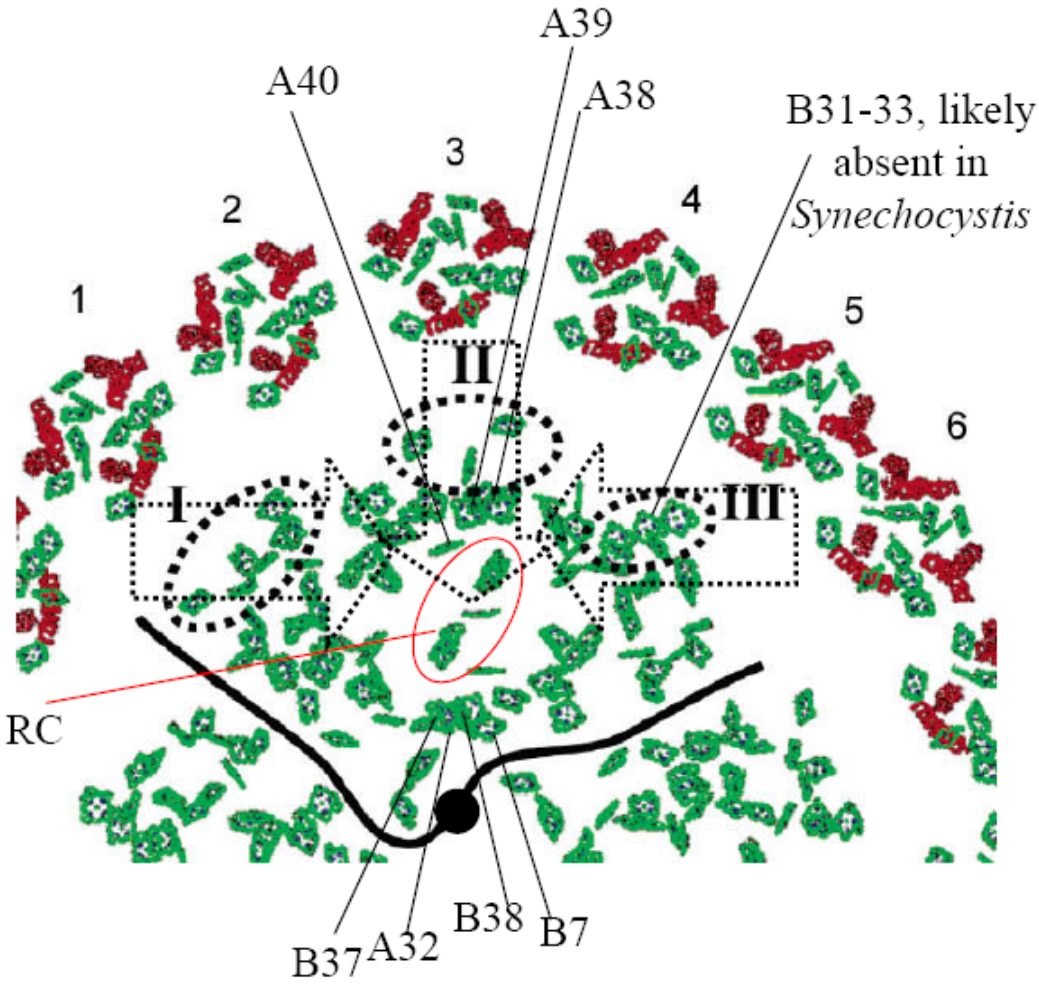

Figure 1. (Modified from [17].) Arrangement of trimeric PS I and CP43′ antenna complexes in the PS I - CP43′ supercomplex, based on X-ray diffraction data for PS-I of *Synechococcus elongatus* [12] and CP43 [18] and low-resolution cryomicroscopy data [17]. Regions of most probable CP43′ to PS I core energy transfer are labeled by roman numbers. Arabic numbers 1-6 refer to CP43′ complexes in non-equivalent positions in relation to the PS I core monomer. Core chlorophyll molecule labeling is according to [12]. Dotted arrows indicate most likely paths of the CP43′ to PS I core energy transfer. Dark solid circle indicates the center of the PS I trimer.

[22-24]. However, there is no agreement regarding the correspondence between the red antenna states and particular chlorophyll aggregates. So far, at least 12 different Chl *a* aggregates were suggested and several combinations of them were considered [22, 27-31]. The lack of agreement concerning the red state assignments is due to the problems associated with calculating inter-pigment electrostatic couplings, and especially chlorophyll site energies, with sufficient precision.

Although the works [14-16] provided extensive and valuable data on the functioning of the PS I - CP43′ supercomplex, several issues remain unresolved. First, to achieve a satisfactory fit to the absorption spectra of PS I - CP43′ supercomplex from *Synechococcus* PCC 7942, it had to be assumed that there are 17-18 Chl *a* molecules per CP43′ complex [15], rather than 13 as suggested by structural data on CP43 [18]. The results of [15] also indicated that one of the low-energy states (i.e. B state [22]) present in CP43 could be missing in CP43′. It is unclear if those differences between CP43 and CP43′ are real or resulted from the partial disruption of the samples during the preparation/isolation procedures. Second, existing data on energy transfer for both *Synechococcus* PCC 7942 [16] and *Synechocystis* PCC 6803 [14] were only obtained at room temperature using ultra-fast spectroscopy which, by its nature, lacks spectral resolution. Therefore, the goal of this work is to utilize high resolution spectral hole burning (SHB) to gain additional insight into the properties of PS I - CP43′ complexes from *Synechocystis* PCC 6803 by comparing the SHB results with those previously obtained by means of time-domain spectroscopy [14]. In addition, SHB results are compared with the steady-state spectroscopy results obtained for *Synechococcus* PCC

7942 [15]. Here the goal is to determine if the lowest-energy states similar to those observed in the isolated CP43 from PS II [22] are present in CP43′ and, if so, how these states affect energy transfer from CP43′ to the PS I core. The details of energy transfer in the PS I - CP43′ supercomplex from *Synechocystis* PCC 6803 are of particular interest since the B31-B32-B33 trimer (see above) is absent and/or significantly disrupted in *Synechocystis* PCC 6803. This could strongly affect or even eliminate one of possible CP43′ → PS I core energy transfer channels. The lack of this trimer is supported by the absence of the histidine residues coordinating Chls B31-B32-B33 [24].

Experimental

PS I trimers and PS I - CP43′ supercomplexes were isolated as described in [14] and stored at –77 ºC. Immediately before the experiment, a sample/buffer solution was mixed with glycerol at a ratio 1:2 in order to ensure formation of good-quality glass upon cooling. This mixture was placed into plastic vials 9 mm in diameter and slowly frozen in the dark in a Janis 10DT liquid helium cryostat. Temperature was measured and stabilized with a Lakeshore model 330 temperature controller.

Absorption spectra were measured with a Bruker IFS-120HR Fourier-transform spectrometer with the resolution of 2 cm^{-1}. Broadband fluorescence excitation spectra were measured while scanning the laser (COHERENT CR-699 with intra-cavity etalons removed, i.e. with a line-width of several GHz) wavelength over the whole dye range (LD688 dye, 650-720 nm) and collecting the fluorescence at $\lambda > 730$ nm with the photomultiplier (Hamamatsu), positioned at 90^0 angle with respect to the excitation beam. Fluorescence excitation spectra were corrected to take into account the (weak) wavelength dependence of the transmission of neutral filters. Emission spectra were

measured with ~1 nm resolution using a McPherson 2061 1-m focal length monochromator with Princeton Instruments diode array as a detector. Samples were diluted to $OD_{680} < 0.1$ per 1 cm thickness (to avoid re-absorption) and placed into glass vials with a diameter of 1.5 mm; the vials, in turn, were placed into a Janis SVT-100 cryostat. Fluorescence was excited by Ar-ion laser with about 15 mW at 514 nm. The collected emission spectra were corrected for the response function of the spectrometer/detector system.

Persistent hole spectra are the difference between post-burn and pre-burn absorption spectra. Triplet bottleneck hole burned spectra (measured after saturation of persistent holes) are the difference spectra between the absorption spectra measured with the laser on and that measured with the laser off. Non-resonant satellite hole spectra were measured with 2 cm^{-1} resolution using Bruker IFS-120HR spectrometer. Holes used for constructing the hole burning action spectrum (i.e. hole depth dependence on the wavelength for fixed burn dose) in absorption/transmission mode were measured with the same spectrometer at 0.5 cm^{-1} resolution. Burn intensities and times are reported in text and figure captions. Burn intensities were adjusted using neutral density filters (LOMO) and laser power stabilizer/controller (BEOC). The COHERENT CR-699 ring dye laser with a line-width of several GHz was used for hole burning. The lifetime(s) of the lowest energy state(s) of CP43' were determined using the CR-699-29 (Autoscan) laser at 0.2 GHz resolution in fluorescence excitation mode. After a series of burns, the sample was heated in the dark to ~ 150 K in order to refill the holes. After the sample cooled back to 4.2 K, the absorption spectrum was measured and compared to that obtained at the very beginning of the experiment, to ensure that the sample was still intact and the spectral holes had been fully filled (i.e. erased).

Results

Absorption spectra. The 5 K absorption spectra of PS I - CP43′ supercomplexes (a) and corresponding PS I cores (b) are presented in Figure 2A. The spectrum of PS I cores is almost identical to the spectra of *Synechocystis* PCC 6803 PS I reported in [23, 24], although the PS I explored in these works was obtained from a different source. Similar intensities of the red antenna state region in this work and [23, 24] indicate that the PS I cores in this work are indeed trimeric. Curve (c) in Figure 2A is the difference spectrum between absorption spectra of PS I - CP43′ and the PS I trimeric core. Before calculating the difference spectrum, the spectrum of the PS I core was renormalized so that the low-energy edges of the two spectra matched as closely as possible. (Assuming that absorption spectrum of the CP43′ ought to resemble that of the CP43 of higher plants, both should have negligible absorption at $\lambda > 695$ nm. Thus, all absorption at $\lambda >$ 695 nm should belong to the PS I core.) Therefore, the difference spectrum (curve c) should be treated as the absorption spectrum of CP43′ complexes. The main broad absorption band is located near 668.3 nm with an additional narrow peak at 681.2 nm; the intensity ratio of the two bands is ~ 2:1. There is also a prominent shoulder near 675-676 nm. These spectral features are similar to those observed for CP43, where the respective bands were observed at 669, 682.4, and ~ 678 nm [25]. The spectrum of CP43 from [25] is shown in the insert of Figure 2A (dashed line) along with the difference spectrum assigned to the CP43′ complex (solid line). It is apparent that the absorption spectra of

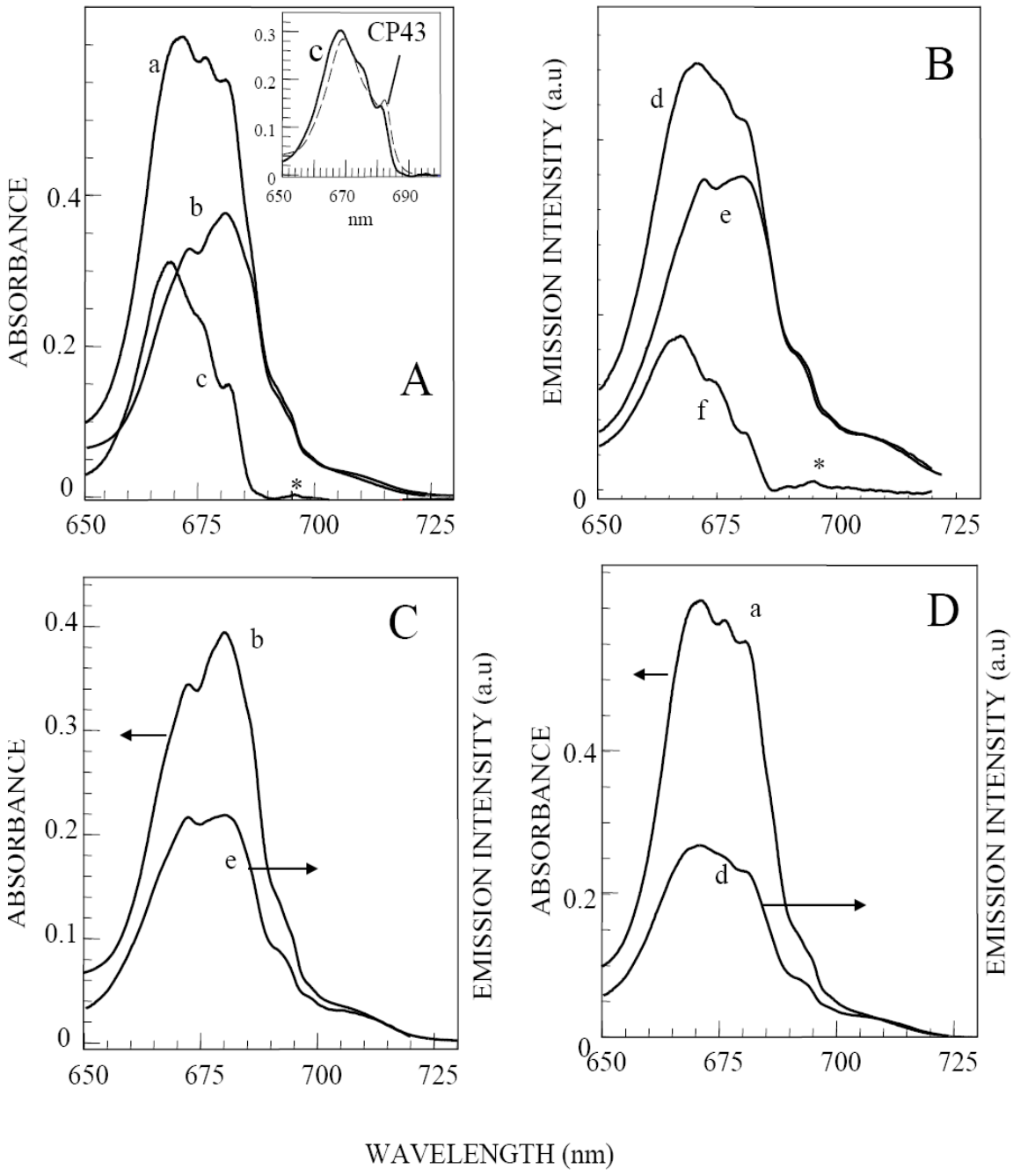

Figure 2. Frame A: 5 K absorption spectra of the PS I - CP43′ supercomplex (a), PS I core (b) and their difference spectrum ascribed to CP43′ (c = a–b). Insert compares 5 K absorption spectra of the CP43′ (solid curve, (c) in the main picture) and CP43 (dashed curve). Frame B: 5 K fluorescence excitation spectra of the PS I - CP43′ supercomplex (d), PS I core (e) and their difference spectrum ascribed to CP43′ (curve f). Asterisk in Frames A and B refers to a weak feature at ~ 695 nm, see text. Frame C: Absorption (b) and fluorescence excitation (e) spectra of the PS I core. Frame D: Absorption (a) and fluorescence excitation (d) spectra of the PS I - CP43′ supercomplex.

CP43′ and CP43 are fairly similar, i.e. both contain a weak narrow band near 682 nm.

Fluorescence excitation spectra. The fluorescence excitation spectra of the PS I - CP43′ supercomplexes (curve d) and trimeric PS I cores (e) are presented in Figure 2B. Since a significant part of the energy harvested by the bulk antenna is transferred to the RC and not to the red emitting states, the shapes of spectra (d) and (e) differ from the shapes of absorption spectra (a) and (b), respectively. Different shapes indicate that excitation may not fully equilibrate over the whole antenna system before being transferred to either the RC or red states at low temperatures. In other words, the fluorescence excitation spectrum is proportional to the absorption spectrum of a sub-ensemble of chlorophylls which, in the end, transfer energy to the red antenna states and not to the RC. A similar effect was reported for trimeric PS I of *Synechocystis* PCC 6803 obtained from a different source [24] and for the isolated reaction center of photosystem II [32]. The difference between spectra (d) and (e) corresponds to the fluorescence excitation spectrum of the CP43′ (see curve f). As expected, spectrum (f) closely resembles the absorption spectrum of CP43′ (curve c). It contains a feature at 681 nm, although that feature is not as well resolved as in spectrum (c). As in the case of the absorption difference (spectrum c), spectrum (f) also reveals a weak feature near 695 nm. Therefore, we suggest that this feature is not a renormalization/subtraction artifact, but that it originates from the shift of the band of some core pigment(s) due to the interaction with CP43′.

Emission spectra. Next, the non-selectively excited (at 514 nm) emission spectra of PS I -CP43′ supercomplexes and PS I cores were measured. The emission

spectra of PS I - CP43′ supercomplexes obtained at various temperatures are shown in Figure 3. The spectra are qualitatively very similar to those observed for the PS I - CP43′ complex of *Synechococcus* [15]. The main fluorescence band at 720 nm with FWHM of 25 nm (T = 5 K) is assigned to the emission from the C714 red antenna state of the *Synechocystis* PS I core in agreement with ref. [23]. A similar but slightly narrower band (FWHM=22 nm) red-shifted by 1 nm, was observed for the PS I core sample (data not shown). The additional 685.2 nm band, observed in Figure 3, is absent in the emission spectra of the PS I core and therefore most likely belongs to the CP43′. Its width is about 7 nm (150 cm^{-1}) when measured as twice the higher-energy half-width of the band. The ratio of the integrated areas of the 720 nm band and the 685 nm band (integrated from 670 nm to 800 nm) is at least 15:1 at 4.2 K.

Hole-burned spectra. In the case of isolated CP43, two quasi-degenerate low-energy states were reported [25]. States A and B were resolved as satellite holes using triplet bottleneck and persistent hole burning, respectively. (Satellite holes form due to hole-burning following excitation energy transfer from directly excited higher-energy chlorophylls to lower-energy chlorophylls.) To verify whether similar states are present in CP43′, we measured the satellite hole spectra for PS-I-CP43′ and PS-I core samples. Satellite persistent holes for PS I - CP43′ (a) and PS I core (b) obtained at 665 nm with laser power density of ~ 460 J/cm^2 are presented in Figure 4. (PS I core hole spectrum was normalized so that the PS I core absorption is equal for both samples.) For the

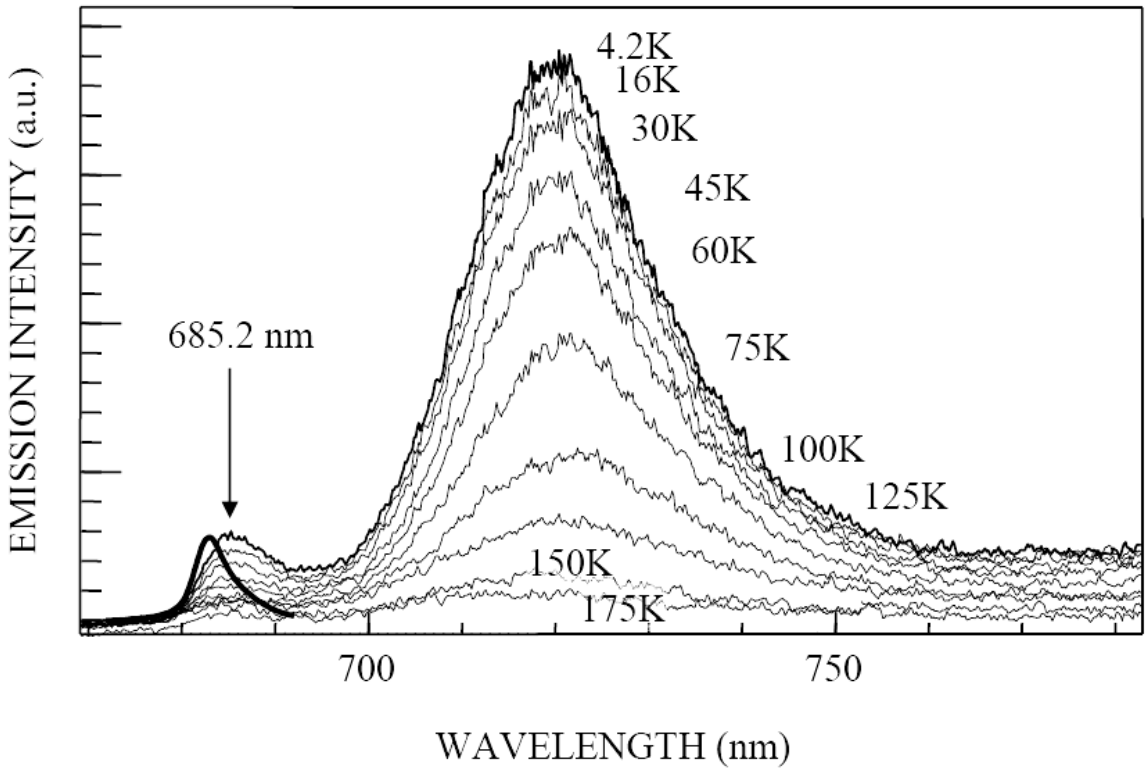

Figure 3. Thin noisy curves: emission spectra of the PS I - CP43′ supercomplex at various temperatures. Bold curve: Emission spectrum of the CP43 of higher plants [25].

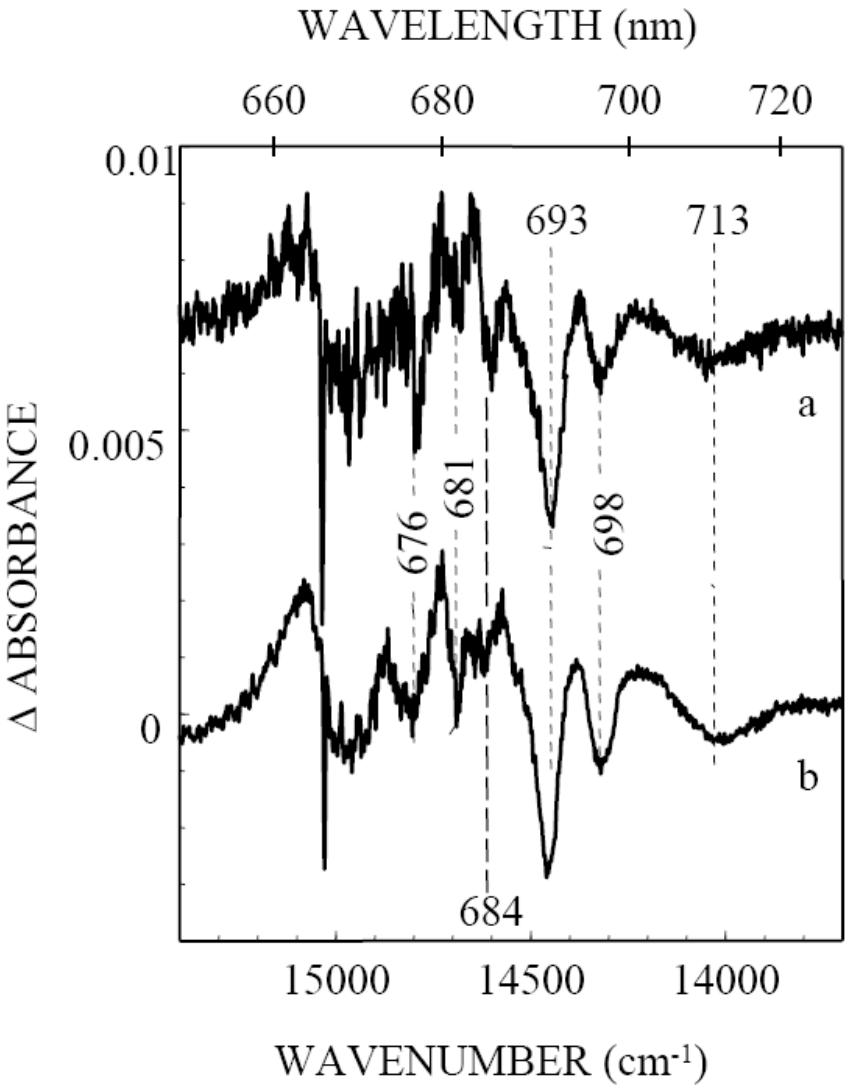

Figure 4. Spectral holes in the absorption spectra resulting at 5 K from the illumination at 665 nm with ~ 460 J/cm^2 for PS I - CP43′ supercomplex (a) and PS I core (b). Short-dashed lines point at the satellite hole features equally represented in both spectra. Long-dashed line refers to the hole at 684 nm, which is significantly stronger in spectrum (a).

CP43′- PS I supercomplex, the deepest satellite hole is at 693 nm, but there are also prominent holes at 676, 681, 684 and 698 nm and a broad lowest-energy hole at 713 nm. The 713 nm hole is assigned to the lowest-energy "red state" of the core, i.e. C714 state in agreement with ref. [23]. All of these features (except for the one at 676 nm, which is obscured by the pseudo-phonon sideband of a resonant hole) could be also observed at the same wavelengths upon irradiation at 670 nm (data not shown), indicating that they are not the vibronic replicas of the resonant hole. A comparison of the hole spectrum (a) to that of the PS I core (b) reveals that most of the satellite hole structure is also preserved for the PS I cores. The main difference is that the 684 nm feature is several times stronger in the PS I - CP43′ supercomplex. (Interestingly, the 681 nm persistent satellite hole obtained at similar experimental conditions was significantly deeper in the PS I core of *Synechocystis* PCC 6803 grown by a different group [23].) No triplet bottleneck satellite holes could be observed.

Zero phonon hole (ZPH) action spectra. In order to gain additional insight about the number and properties of the lowest-energy states of the CP43′, we measured the hole burning action spectra of the PS I - CP43′ supercomplexes and the PS I cores. Hole burning action spectrum is the dependence of the hole depth on the burn wavelength for a fixed burning dose [33]. This type of spectroscopy can easily resolve the lowest-energy states of photosynthetic complexes [25, 32, 33]. ZPH action spectra for the PS I - CP43′ supercomplex and the PS I core are presented in Figure 5A. As in the case of the absorption spectra (see Figure 2), the PS I core ZPH action spectra were normalized to make the PS I core absorption equal for both samples. Only very shallow holes were

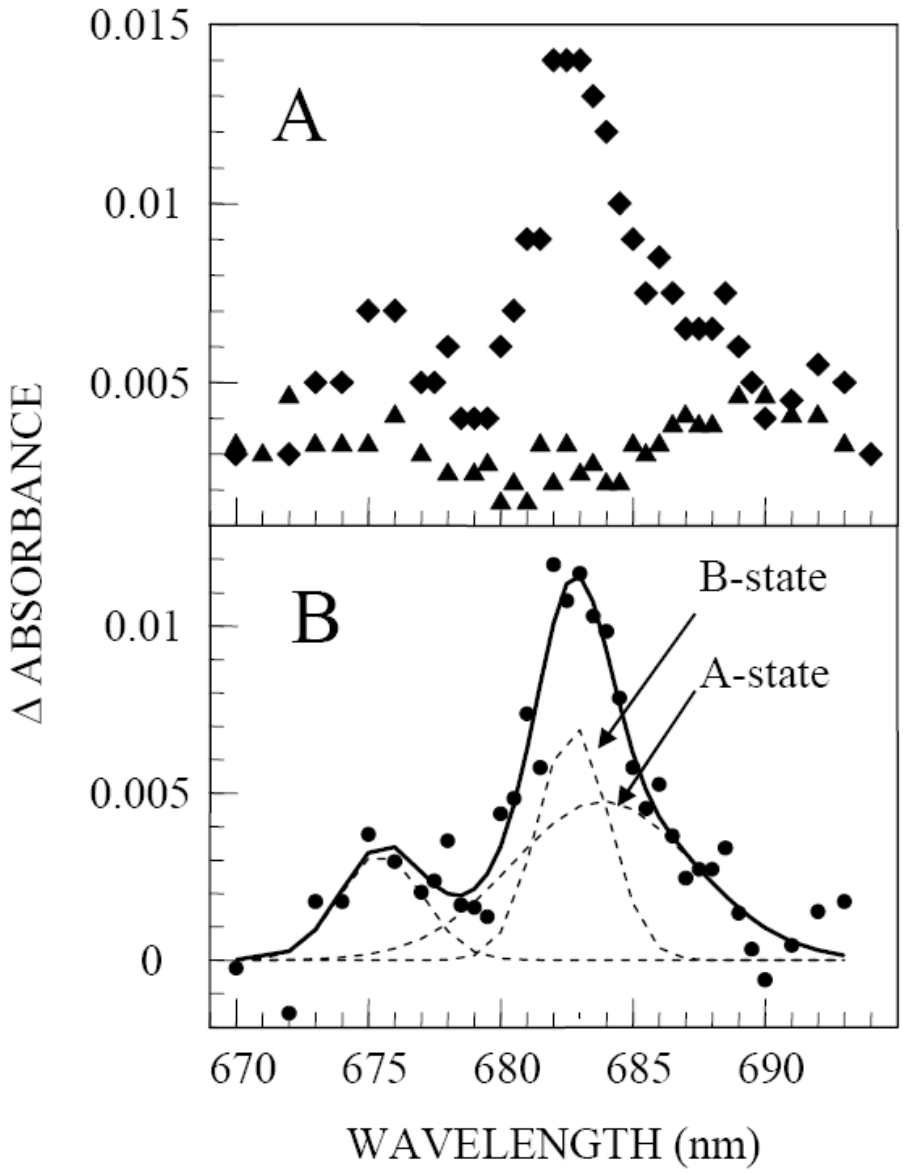

Figure 5. Frame A: 5 K hole burning action spectra (hole depth versus wavelength for fixed burn dose) of PS I - CP43′ supercomplex (diamonds) and PS I core (triangles). Burn dose was 5 J/cm^2. Frame B: Difference of the two action spectra from the Frame A (action spectrum of the CP43′) and its best fit.

observed for both the PS I - CP43′ supercomplex and PS I core at wavelengths between 695 and 705 nm. For the results presented in Figure 5, the burn time was 1 minute and the intensity 80 mW/cm^2, i.e. the burning dose was ~ 5 J/cm^2. Such irradiation resulted in ~ 3% fractional hole depths for the PS I - CP43′ supercomplex, which corresponds to ~ 10% holes in the CP43′ spectrum (see Figure 2A). The irradiation of PS I - CP43′ complexes with 0.5 J/cm^2 was attempted but did not yield holes with reasonable fractional depth and/or signal to noise ratio, at least at 0.5 cm^{-1} resolution (see below). Note that the irradiation with less than 0.5 J/cm^2 was employed with the isolated CP43 [25] in order to burn ~ 10%-deep holes. This is the first indication (see Discussion for details) that the lifetime of the state(s) exhibiting persistent spectral hole burning is significantly shorter in CP43′ within the PS I - CP43′ supercomplex than in isolated CP43. It is interesting to note that even for the increased burning dose of 20 J/cm^2 the action spectra did not exhibit significant maxima at 693 and 698 nm, where the deepest satellite holes were observed in Figure 4. While the ZPH-action spectrum of the PS I core (triangles in Figure 5A) does not contain prominent features between 670 and 692 nm, the same cannot be said about ZPH- action spectrum obtained for the PS I - CP43′ supercomplex (diamonds). The difference of the two ZPH-action spectra (Figure 5B; circles) has two maximums at 682.5 nm and at ~ 676 nm. These two features must belong to the CP43′ complex. The maximum at ~ 682.5 nm is close to the wavelength of the non-resonantly burned hole at ~ 684 nm, which is strong in PS I - CP43′ and weak in PS I core (see Figure 4). While the quality of the action spectrum does not allow us to make definite conclusions concerning the number of quasi-degenerate states at ~ 682-685 nm, a better fit to the difference of the two ZPH-action spectra (solid line in Figure 5B)

involves three bands with absorption peaks / inhomogeneous widths (FWHM) of 675.6 nm / 80 cm^{-1}, 682.6 nm / 70 cm^{-1} and 683.9 nm / 160 cm^{-1}, respectively. The latter two bands most likely correspond to states B and A, respectively, observed in the isolated CP43 [25]. The relative intensities of the two bands in the ZPH-action spectrum are also fairly similar to those reported for isolated CP43. The broader of these two bands is most likely the main origin of the 685 nm emission.

Energy transfer times. To determine the lifetime(s) of the lowest state(s) of the CP43′ complex (CP43′ → PS I core energy transfer times), we measured the widths of shallow holes burned into the absorption spectrum of the PS I - CP43′ supercomplex at 679-688 nm. Holes were measured in fluorescence excitation mode. If the CP43′ complex possesses two states in this region, the contribution of the narrow 682.6 nm band to the lower-energy part of this region should be negligible. The shallow holes burned in this region exhibited widths of about 7-8 GHz at 5 K. The pre-burn absorption spectrum and the hole (burned at 685.5 nm with 0.1 J/cm^2) measured in fluorescence excitation mode along with its Lorentzian fit, are shown in Figure 6. The fractional depth of this hole is 2.5% and the width is 7.3 GHz. Assuming that about 2 GHz at 5 K is the contribution from pure dephasing [25] one could arrive at a CP43′ → PS I core energy transfer time of about 70 ps. It is evident from Figure 6, however, that in addition to the narrow Lorentzian hole described above, the spectra contain another, much broader component. The latter observation is in agreement with the hole-growth curve obtained for the very same hole and depicted in the insert of Figure 6, which yields fractional hole depth of ~ 4% instead of 2.5%. (The hole-growth curve corresponds to the decrease in

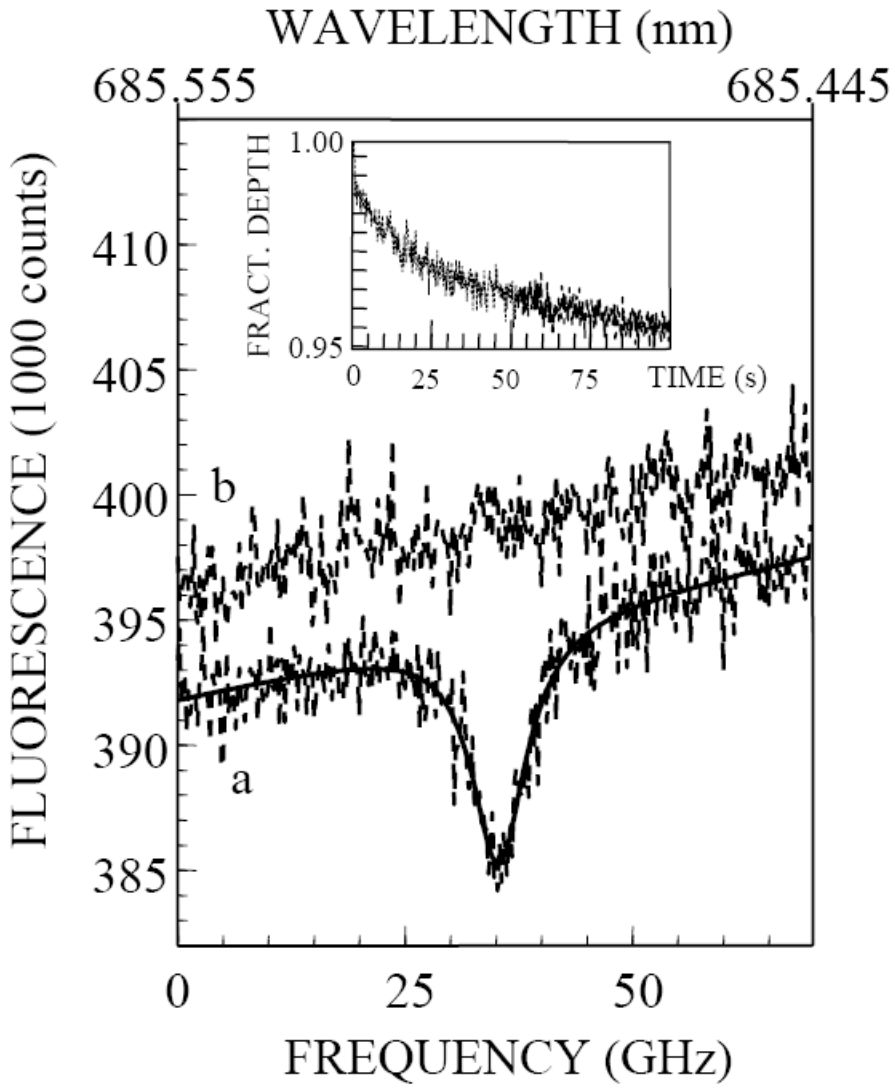

Frame 6. High-resolution hole spectrum (a) with respective pre-burn spectrum (b) measured in fluorescence excitation mode (noisy curves) and a Lorentzian fit (smooth thick curve) to the narrow spectral hole. FWHM = 7.3 GHz, T = 5 K, burning wavelength was 685.5 nm and the burn dose was 0.1 J/cm^2. Insert: Growth curve for the hole depicted in the main frame.

fluorescence signal while sample is irradiated with a laser of constant wavelength.) The similar behavior was observed for all holes burned in the 679 - 688 nm wavelength region, with the relative intensity of the broad contribution varying from spectrum to spectrum without apparent correlation with burn wavelength (or dose; several additional irradiation doses were employed at some wavelengths). Therefore, we did not attempt to assign that contribution, or to derive any quantitative data characterizing it.

The narrow ~ 7 GHz components of the holes burned with 0.1 J/cm^2 in fluorescence excitation mode were used to construct a different action spectrum, which can be compared to the one obtained in transmission/absorption mode (see Figure 5). The results are presented in Figure 7. Surprisingly, the shape of the low-irradiation-dose ZPH-action spectrum (solid triangles) closely resembles the shape of the broader band (state A) used to fit the higher-dose, lower-resolution transmission mode action spectrum presented in Figure 5. State B does not seem to contribute significantly to the high-resolution low-irradiation action spectrum. (This cannot be explained by sample degradation, since the absorption spectrum was measured after the action spectrum depicted in Figure 7 had been obtained, and that spectrum had the same shape as spectrum (a) in Figure 2A, which was acquired in the beginning of the experiment.)

Discussion

Low-energy states of the CP43′. The main difference between the CP43′ absorption spectrum shown in Figure 2A (curve c) and that reported in ref. [15] is the presence of a narrow band peaked at 681.2 nm. The inset compares curve (c) with the absorption spectrum of CP43 [25] (dashed curve). Comparison reveals that spectrum (c) resembles the spectrum of CP43 much more closely than that measured for the *Synechococcus* PCC 7942 CP43′ [15]. Our results are also consistent with the absorption

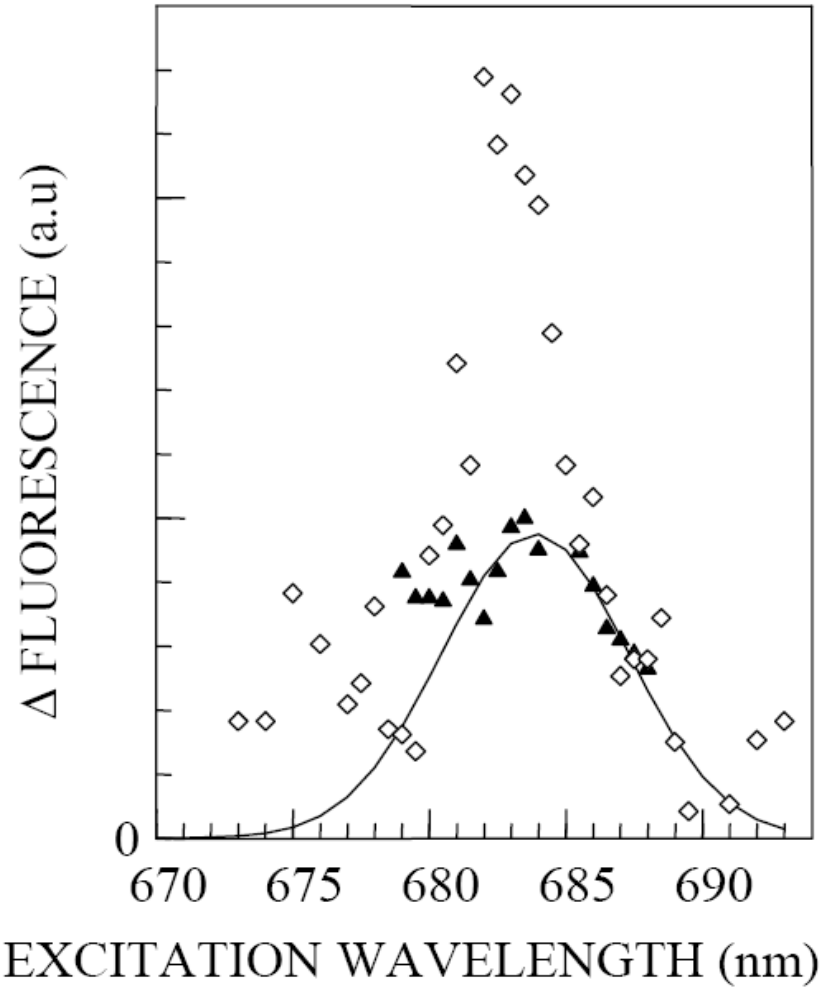

Figure 7. The hole burning action spectra (hole depth versus wavelength for fixed burn dose) of PS I - CP43′ supercomplex obtained with 5 J / cm^2 in absorption / transmission mode (0.5 cm^{-1} resolution; open diamonds) and with 0.1 J / cm^2 in fluorescence excitation mode (0.2 GHz resolution; solid triangles). The lower-dose action spectrum is normalized to fit the solid curve, which is the broader component of the fit to the higher-dose action spectrum (see Fig. 6).

spectrum reported for *Synechocystis* PCC 6803 at 77 K [34]. We hasten to add that the spectra in [15] and [34] were obtained directly for the isolated CP43′ complexes. Although the 681.2 nm band is somewhat weaker than the 682.5 nm band observed in CP43 [25], this characteristic band is definitely present in curve c = a–b assigned (*vide supra*) to the CP43′ complex. Thus, by analogy with CP43, one could suggest that CP43′ possesses two quasi-degenerate lowest-energy states. Further support for this assignment is provided by the hole burning action spectra shown in Figure 5 and emission spectra in Figure 3. Since the HB data revealed that for the lowest-energy state(s) of CP43 the electron-phonon coupling is weak [25, 26], it is unlikely that the emission peaked at 685.2 nm originates from the narrow absorption band peaked at 681.2 nm. Note that a Stokes shift of only ~ 6 cm^{-1} (0.2-0.3 nm) was observed for the lowest-energy states of CP43 [25]. Another important point about the emission spectra presented in Figure 3 is the relatively small intensity of the 685 nm emission in comparison with the major emission band near 720 nm. This comparison indicates that the CP43′ complexes transfer energy effectively to the PS I core.

Energy transfer from CP43′ to the PS I core: analysis of the absorption and fluorescence excitation spectra. It is instructive to compare the integral intensity ratios of spectra (a) and (b) with (d) and (e), respectively, of Figure 2. The intensity ratio of spectra (a) and (b), integrated between 600 and 730 nm, is 1.58. The integrated intensity ratio of spectra (d) and (e) is 1.33 (for 650-720 nm). The ratio difference of about 20% exceeds the error that may result from the renormalization of spectra being compared or from difference in integration ranges. (We confirmed that the ratio of areas below (a) and (b) is still ~ 1.6 for the 650-720 nm integration range. This can also be considered as an

indication that the spectra in frame A are indeed superimposed properly.) Let us consider several different (d) to (e) integral intensity ratios:

The ratio of ~ 1 would require that all of the energy absorbed by the CP43′ is either directly emitted from the CP43′ or transferred selectively to the RC (and consumed for charge separation) and not to the emitting red states of the core. This is because the experimental setup used to measure fluorescence excitation spectra strongly favors registration of emission at $\lambda > 730$ nm over the emission of CP43′, expected at 682-685 nm. Thus, in this case, excitation energy would not be transferred to the emitting red state of PS I core.

A ratio of 1.58 (*vide supra*) would mean that all of the energy absorbed by the CP43′ is transferred to the core and then distributed between the RC and the red states in exactly the same manner as in isolated PS I core. In other words, the energy would equilibrate between CP43' manifold and higher-energy chlorophylls of the PS I core relatively quickly, faster than it is trapped by either RC or the red states.

A ratio larger than 1.58 (corresponding to large relative intensity of difference spectrum f) would mean that energy from the CP43′ gets preferentially transferred to the red states of the PS I core and not to the RC.

A ratio of 1.33 (i.e. between 1 and 1.58) suggests that energy absorbed by the CP43′ ring has on average a somewhat higher chance of ending up used for charge separation in the RC than the energy absorbed by the core bulk antenna states.

Based on results presented in ref. 15 and our fluorescence data depicted in Figure 3, we assume that only a small fraction of energy absorbed by the CP43′ is emitted from the CP43′; thus for the time being this small fraction will be ignored. We denote this

fraction $P_{CP43'\_EM}$. The integral intensities of absorption (curve b in Figure 2A) and normalized fluorescence excitation spectrum (curve e in Figure 2B) for the PS I core are compared in Frame C of Figure 2. This comparison reveals that about 60% of the energy absorbed by the PS I core is emitted at ~ 720 nm; that is ~ 40 % gets utilized for charge separation. We label this fraction as P_{core_RC}. A similar result was reported in [24]. Following the same logic, the probability that energy absorbed by the CP43′ will be transferred to the red states of the PSI core and emitted from there $P_{CP43'\_red\ states}$ is equal to the ratio of the (properly normalized) integrated areas of the fluorescence excitation and absorption spectra of CP43′. The latter two spectra are shown as curve (f) in Figure 2B and curve (c) in Figure 2A, respectively. Let A_1 be the integral intensity (area below the spectrum) of core absorption. Then the integral intensity of the absorption spectrum of the PS I - CP43′ supercomplex will be $A_{S,Abs} = 1.58A_1$ and the integral intensity of the core fluorescence excitation spectrum will be $A_{C,FluorExc} = 0.6A_1$. The integral intensity of the supercomplex fluorescence excitation spectrum will be $A_{S,FluorExc} = 1.33x0.6A_1$. The integral intensity of the CP43′ absorption is $A_{CP43'Abs} = A_{S,Abs} - A_1 = 0.58A_1$ and the integral intensity of the CP43’ fluorescence excitation spectrum is $A_{CP43'FluorExc} = A_{S,FluorExc} - A_{C,FluorExc} = 0.2A_1$. Consequently, the $P_{CP43'\_red\ state} = 0.2A_1 / 0.58A_1 = 34\%$, compared to 60% for the probability of transfer from the core to the red antenna states. Thus, on average, the excitation of the CP43′ indeed results in a charge separation that is significantly more efficient than resulting from the excitation of PS I core. Thus we suggest that the energy transfer between the CP43′ ring and the reaction center of the core occurs, at least at low temperatures, along a relatively well-defined pathway, carefully avoiding the chlorophylls responsible for the “red antenna states.” This

argument is supported by Figure 1, which is adopted from [17]. Dotted arrows roughly indicate the possible pathways of EET that most likely avoid the B37-B38 and A32-B7 "red aggregates" [22, 27-29]. It was demonstrated in [23, 35] that red aggregates are most likely located close to the trimerization domain of the PS I (solid black dot in Figure 1). Note that in order to avoid being transferred to the B37-B38 and A32-B7 aggregates, the energy would likely travel to the RC through the chlorophylls labeled A38-A40. The result that the A38-A39 is not a red state is in agreement with the results of [36], where, based on spectral shifts upon charge separation in the RC, the absorption of those chlorophylls was assigned to 680-695 nm spectral region.

We now wish to estimate the time for EET from the CP43′ to the PS I core. The excitation energy redistribution is schematically shown in Figure 8. Let E be the amount of excitation energy (EE) absorbed by the PS I - CP43′ supercomplex. Of this energy, 60% is absorbed by the PS I core and 40% by the CP43′. Of the energy absorbed by the PS I core, 60% gets emitted from the red-states and 40% is utilized in charge separation. As a function of E, this amounts to 0.36E and 0.24E, respectively. Of the 40% of EE absorbed by the CP43′, $P_{CP43'\_EM}$ is emitted from the CP43′ and $(1- P_{CP43'\_EM})$ is transferred to the core. As was determined above, 66% of the latter amount is utilized in charge separation and 34% is transferred to the red states and emitted from there. As a function of EE, this amounts to $0.4 \times (1- P_{CP43'\_EM}) \times 0.66E$ and $0.4 \times (1- P_{CP43'\_EM}) \times 0.34E$, respectively. The total emission from the red states of the core is then $0.36E + 0.4 \times (1- P_{CP43'\_EM}) \times 0.34\ E = 0.496E - 0.136\ P_{CP43'\_EM}E$. Based on the intensity ratio deduced from Figure 3,

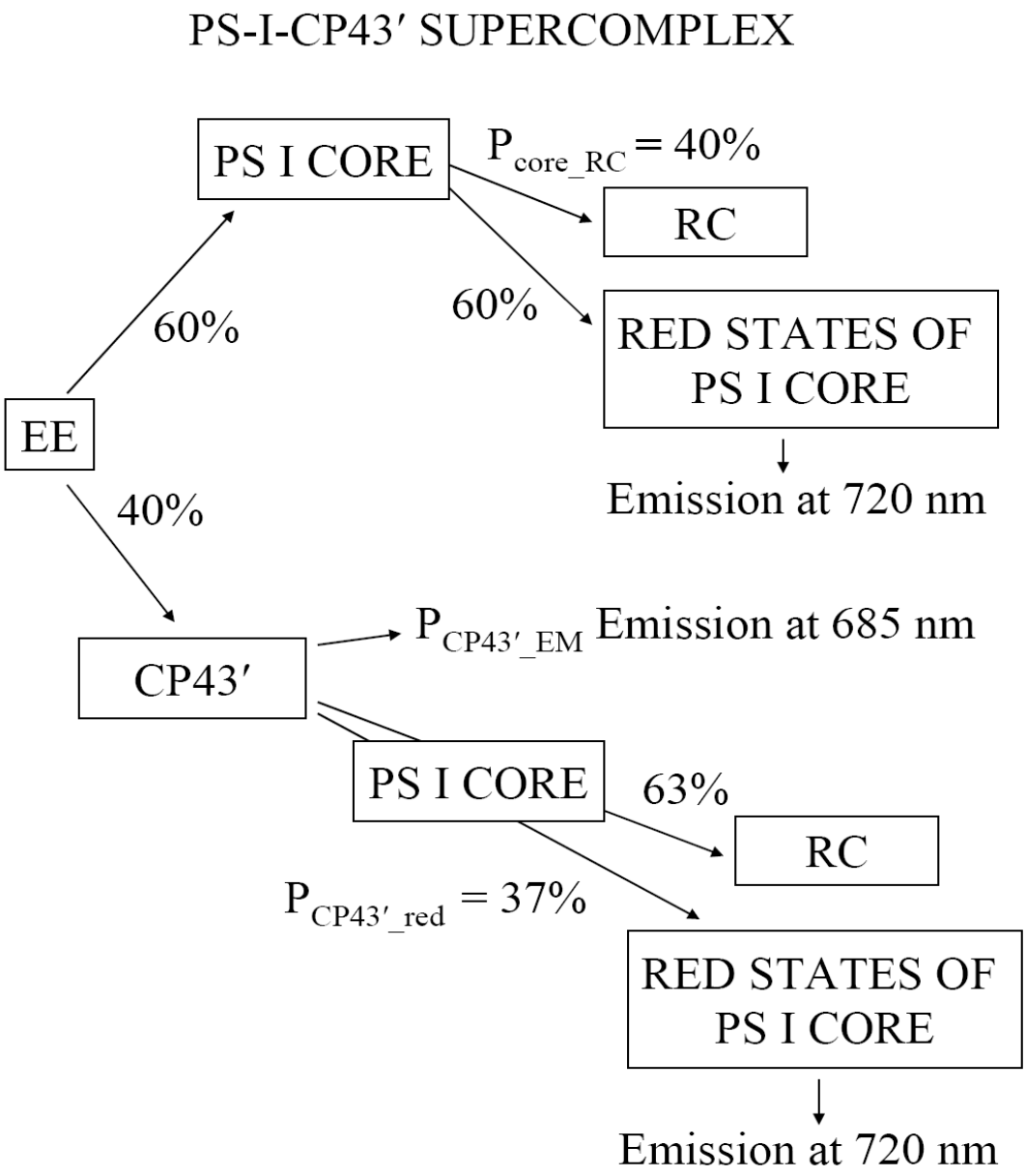

Figure 8. Scheme of the energy transfer processes between the CP43′ and the PS I core and within the PS I core.

$$(0.496E - 0.136\ P_{CP43'\_EM}\ E) : (0.4\ P_{CP43'\_EM}\ E) = 15:1.$$

Solving this equation for $P_{CP43'\_EM}$, one can arrive at a probability of ~ 8% for emission directly from the CP43′, at 685 nm. Taking into account this correction, we can arrive at values of 37% and 63 % (instead of 34% and 66 % as determined above) for the relative amounts of energy transferred from the CP43′ to the emitting red states of the PS I core and the RC, respectively; see Figure 8 for details. Thus, the above conclusion that, on average, the CP43′ transfers energy to the RC much more effectively than the PS I core remains valid. Since the fluorescence lifetime of the emitting state(s) of the CP43′ is not known precisely, the knowledge of the $P_{CP43'\_EM}$ does not allow us to determine the CP43′ → PS I core energy transfer time precisely. Nevertheless, assuming a reasonably realistic fluorescence lifetime of 1 ns, the 8% probability of CP43′ emission requires energy transfer time to be (on average) close to 60 ps.

To conclude this subsection we need to discuss the possibility that we are dealing with a mixture of disconnected CP43′ and PS I cores. If this is true, the above argument is invalid. Based on data shown in Figure 2A, approximately 40% of all excitation energy would be absorbed by CP43′-s and about 60% by the PS I cores. Recall that the fluorescence yield of the PS I cores at liquid helium temperatures is about 60% for excitation at wavelengths shorter than 700 nm (this percentage was determined comparing spectra (b) and (e) in Frames 2A and 2B after normalizing them to equal oscillator strength of the red antenna state region (Figure 2C); see also Figure 4 in [24]). Thus, the 720 nm and 685 nm band integral intensity (area) ratio should be about 1:1 if no EET from CP43′ to PS I took place. Since the observed ratio is at least 15:1, this scenario can be excluded. (We assumed, for the sake of simplicity, that there is not much

non-radiative energy dissipation within the CP43 or CP43′ complexes and, consequently, the fluorescence yield of isolated CP43′ or CP43 should be close to 100%, consistent with the similarity of spectra (c) and (f) in Frames A and B respectively of Figure 2 and the absence of triplet bottleneck holes.) One may also suggest that a small fraction of the CP43′ complexes (or CP43′ aggregates [34]) are disconnected from the PS I cores and only these disconnected CP43′ complexes are the origin of the 685 nm emission. This suggestion, however, contradicts the observation that the temperature dependence of the intensity of the 685 nm emission band (not shown) is much faster than for the isolated CP43′ [15]. The temperature dependences observed for the PS I - CP43′ supercomplex in [15] and in this work are very similar despite the fact that the absorption spectra of the CP43′ complexes in [15] lack the narrow band in the ~ 681-683 nm region.

Energy transfer from CP43′ to the core: Spectral hole burning. The presence of a noticeable persistent satellite hole near 684 nm shown in Figure 4 is in good agreement with a noticeable 685 nm emission. Absence of triplet bottleneck holes upon non-resonant higher-energy excitation in the case of the CP43′ within the supercomplexes indicates that either the lifetime or the intersystem crossing yield or triplet lifetime of state A are significantly reduced in CP43′ of the PS I - CP43′ supercomplex, compared to the isolated CP43. Overall, there are four competing decay processes with different rates for the A state of the CP43′ complex within the PS I - CP43′ supercomplex: τ_{ET}^{-1}, $\tau_{TRIPLET}^{-1}$, τ_{fluor}^{-1} and τ_{HB}^{-1}, which are the rate of the EET to the PS I core, intersystem crossing rate (not to be confused with the [triplet state lifetime]$^{-1}$), fluorescence rate and persistent hole burning rate, respectively. Even for the best hole-burning systems the $\tau_{HB}^{-1} < 0.1 \ldots 0.01 \tau_{fluor}^{-1}$ [37]. Of the four processes

mentioned above, only energy transfer to the core is absent in case of the isolated CP43. Assuming that the properties of state A in CP43 and CP43′ are otherwise similar, it is most likely that excitation energy transfer to the core competes with the intersystem crossing in the PS I - CP43′ complex. In CP43′ the energy transfer to the PS I core takes place in about 60-70 ps (*vide supra*); such fast EET could indeed suppress the triplet bottleneck hole formation, if intersystem crossing rates for Chl *a* are in the ns^{-1} range [38]. Consequently, energy transfer from the CP43′ to the PS I core occurs, to a significant degree, through state A.

Hole burning results of Figure 6 are in agreement with the 60-70 ps energy transfer from state A but suggest that there might be more than one energy transfer rate from the CP43′ to the PS I core. Note that six CP43′ complexes are in non-equivalent positions in relation to the PS I core monomer (see Figure 1) and, therefore, multiple rates of energy transfer from the CP43′ to the PS I core should be expected. Results presented in Figure 7 indicate that there is no significant contribution from the state B to the low-fluence fluorescence excitation mode ZPH-action spectrum, which is an indication of the short lifetime of the B state. This is in agreement with the absence of the B-state emission in Figure 3. The CP43′ emission band would be narrower and less red-shifted than that observed if a significant amount of emission from the B state were present. (See the emission spectrum of CP43 from [25] superimposed on Figure 3. Significant fraction of CP43 emission originates from the narrower B state.) Another possibility to be considered is that energy from state B of the CP43′ is transferred exclusively to the reaction center of the PS I and not to the red emitting states of the core. Taking into account the architecture of the PS I - CP43′ supercomplex and the fact that

some RCs are permanently closed [42], this possibility is highly unlikely. Consequently, one must conclude that the (average) lifetime of state B is significantly shorter than that of state A. Unfortunately, precise determination of the excited state lifetime of the state B by means of spectral hole burning is difficult, since one cannot access this state selectively. However, the widths of spectral holes used to compose the action spectrum in Figure 5 can be used for rough estimation. The widths of the shallow holes burned in the absorption spectrum at ~ 682 nm were in the range of 1.2 - 1.5 cm^{-1}, which corresponds to the lifetime of about 10 ps. Since the holes burned at ~ 682 nm contain contributions from both A and B states, and since the A-state contribution most likely has the resolution-limited width (0.5 cm^{-1}), 10 ps should be considered an upper limit for the B-state lifetime.

Summarizing, we are left with a relatively fast (< 10 ps) energy transfer *from* state B. The nature of the acceptor in this energy transfer process (PS I core versus the state A of the CP43′) is to be determined. In this respect, three scenarios are possible, each leading to certain contradictions either with some results of this work or with the interpretations of the results obtained in [25] for isolated plant CP43. Before we describe these three scenarios, it is necessary to remind the reader that the structural origin of the lowest-energy band(s) of the CP43 is still unknown. It was suggested in [25] that both states A and B are localized on monomeric chlorophylls. In [39] it was argued that chlorophylls labeled 10, 18 and especially 12 are most likely to transfer energy to the PS II RC. In [40] the lowest-energy state of CP43 was assigned to the lowest excitonic state of the aggregate containing chlorophylls 9, 13 and 19 in the notation of [39]. (Different notation was used in [40] which may be obtained by adding 14 to the notation of [39].)

In [21] the lowest state of CP43 was assigned to the aggregate consisting of chlorophylls 11, 13 and 16.

In the first scenario, which is in agreement with [25], the state B serves as a fast (several ps), main channel for energy transfer from the CP43′ to the PS I core. However, taking into account that the energy transfer from the state A to the PS I core occurs in 60-70 ps, it is difficult to explain the relatively high intensity of the 685 nm emission band for the PS I - CP43′ supercomplex (Figure 3).

In the second scenario we invoke fast and effective energy transfer from state B to state A in CP43′ (with state A being the main trap and the main channel for energy transfer to the PS I core). This scenario successfully explains the observations in this work, but contradicts the arguments from [25], where it was suggested that the B state is the primary low-energy trap of the isolated CP43, that energy transfer between the CP43 and the reaction center of the PS II occurs predominantly through state B, and that the energy transfer between states A and B is possible but very slow (~ ns).

According to the third scenario, states A and B both originate from the same chlorophyll molecule or group of molecules. The CP43′ (isolated or in the PS I - CP43′ supercomplex) samples and isolated CP43 samples explored in [25, 26, 41] must have been highly heterogeneous, with some CP43 or CP43′ complexes having their lowest-energy chlorophyll(s) in a very well-defined protein pocket (B-type), and the rest of the complexes having much worse-defined protein pocket (A-type). Differences in spectra between CP43 and CP43′ from different sources could then be explained by different preparations of CP43 and CP43′ containing different proportions of A-type and B-type complexes. Although B-type CP43′ complexes would transfer energy to the PS I core

faster than the A-type CP43′ complexes, due to a relatively small percentage of the B-type complexes, the average transfer rate would not be significantly affected. The transition from B-type to A-type results in a nearly two-fold increase of the permanent dipole moment change $\Delta\mu$ [25], the change of the mean phonon frequency from 24 cm^{-1} to 15 cm^{-1} [26], and, at least in case of the CP43′, a ~ 7-10-fold decrease of the rate of EET to the PS I core, *vide supra*. However, large variations in the properties of the same chlorophyll(s) as described above were never observed for any other photosynthetic complex. In the case of the reaction center of PS II, the isolation process resulted in the shift of the P680 band from ~ 684 to ~ 680 nm in a majority of RCs [32, 43], but other properties of the band remained practically unchanged [32]. Moreover, the PS I - CP43′ supercomplexes were not subjected to the biochemical procedures employed for isolating CP43, and the chlorophylls serving as the energy transfer channel from the CP43′ to the PS I core are not as exposed to the environment as those in isolated CP43. Therefore, the most apparent reasons for disruptions leading to several different types of the same lowest state in CP43 are absent in case of CP43′ in the intact supercomplexes, and the scenario involving heterogeneity of CP43 and CP43′ samples is quite unlikely. On the other hand, there is not enough evidence available at the moment to completely reject that scenario.

Presuming that the results obtained for CP43′ in this work must have larger "weight" than those obtained for a different system (isolated plant CP43), we favor the second scenario, involving fast B $\rightarrow$ A energy transfer. More research, especially on the isolated CP43 and CP43′ is needed to clarify if the results obtained for CP43 need re-interpretation.

Quality of the samples and pigment content of the CP43′ complexes. To determine the pigment content of the CP43′ complexes, the areas under the PS I - CP43′ and the PS I spectra and their difference (assigned to CP43′) in Figure 2 were determined in the wavelength range from 600 to 730 nm. These areas (which include Q_y origin and its vibronic replicas) scale approximately as 5.2:3.3:1.9. Assuming that there are 96 Chl *a* molecules per PS I core monomer [12] and that the PS I - CP43′ super-complex contains 18 CP43′ complexes, one can conclude that the number of Chl *a* molecules in CP43′ is about 10, which is closer to 13 that were found in CP43 by means of X-ray diffraction [19, 20] than the 17-18 molecules reported in [15]. The discrepancy between 10 and 13 may be explained if one remembers that, due to electrostatic interactions between chlorophyll molecules in the adjacent CP43′ complexes as well as in the CP43′ and the PS I core, the spectrum of PS I - CP43′ may differ from the sum of the spectra of the PS I core and 18 CP43′-s even if the complexes are not disrupted. This possibility was not considered when renormalizing the PS-I core absorption spectrum to the lower-energy edge of the PS I - CP43′ absorption spectrum. Electrostatic interactions between chlorophyll molecules of PS I core and CP43′ may also be a reason for the weak (less than 0.2 Chl *a* equivalent) features marked by an asterisk in spectra (c) and (f) in Figures 2A and 2B, respectively. However, it is also possible that our PS I - CP43′ supercomplexes could miss some of the 18 CP43′ subunits, and/or that the intact CP43′ might indeed contain only 10 Chl *a* molecules per complex. The former possibility is more likely as it agrees with the results of [34]. In that work, 77 K absorption and fluorescence excitation spectra of PS I - CP43′ complexes from *Synechocystis* PCC 6803

with different CP43′ content were presented. While the spectra of the PS I - CP43′ with exactly 18 CP43′ complexes per PS I trimer were somewhat less structured than the spectra presented in this work, the spectra of the complexes with less than 18 CP43′ per PS I trimer more closely resembled our 5 K spectra. Based on the results of [34], the results of [15], in which the CP43′ chlorophyll content was estimated as 17-18, could be explained assuming that the CP43′ content was higher than 18 per PS I trimer in that work. The formation of a second CP43′ ring around the first ring of the CP43′ complexes was observed for supercomplexes from *Synechocystis* grown under prolonged iron stress conditions [34]. In this respect it is interesting to note that the 5 K absorption spectrum of the CP43′ complex from *Synechococcus* published in [15] lacks the structure present in the spectrum (c) in Figure 2A and in the spectra of [34], even though the latter were collected at 77 K and consequently should be less structured than the 5 K spectra. Although we do not want to engage in speculations about the origin of the spectra belonging to the different bacterium, we find it worthwhile to mention that less-structured CP43′ spectra were obtained in our laboratory after the sample was accidentally heated while under illumination by the FT spectrometer white light beam. (Moderate heating of the sample in the dark, to about 150 K, typically used to refill the spectral holes, *vide supra*, returned the shape of the absorption spectrum to that observed in the beginning of experiment.) The spectra in this work can be best fitted, assuming that there are 13 Chl *a* molecules per CP43′, if there are ~ 15 CP43′ units per PS I core *trimer*. Aggregates with 12-14 CP43′ units surrounding the PS I core *monomer* were observed in [34]. However, the spectra expected from the latter system would be quite different from those presented in Figure 2. We conclude that the presence of

supercomplexes where the PS I core monomer is surrounded by the CP43′ units is quite unlikely in samples studied in this work.

Conclusions

We have demonstrated that low-temperature energy transfer between the CP43′ manifold and the PS I core is very effective in PS I - CP43′ supercomplexes from *Synechocystis* PCC6803. Average transfer time is about 60 ps. This finding is consistent with very efficient energy transfer observed for the same system at room temperature. The CP43′ of *Synechocystis* PCC 6803 possesses two low-energy states analogous to the quasi-degenerate states A and B of CP43 of photosystem II. Energy transfer between the CP43′ and the PS I core occurs to significant degree through the broader state A. (Possible implications of these results for CP43, including the possibility of fast energy transfer between states A and B, will be the subject of future publication.) It was also demonstrated that energy absorbed by the CP43′ manifold has, on average, a higher chance to be transferred to the RC and utilized for charge separation than energy absorbed by the PS I core. Thus, at low temperatures, the energy transfer from CP43′ to the RC occurs along a relatively well-defined path avoiding the chlorophylls responsible for the "red antenna states." This indicates that the "red antenna states" of the PS I core are most likely localized on the aggregates B7-A32 and B37-B38 located close to the PS I trimerization domain (PsaL subunit). We also argue that the A38-A39 aggregate does not contribute to the red antenna region. No effects were observed that could be attributed to the B31-B32-B33 trimer (most likely absent or disrupted in *Synechocystis*). The lower limit of the chlorophyll content of CP43′ was estimated to be close to 10. However, we consider it more likely that the chlorophyll content of the CP43′ is closer to

13 (observed for CP43), but the number of CP43′ complexes per PS I trimer in our samples was smaller than 18 (i.e. it is most likely ~ 15). In addition, the content of CP43′ monomers or CP43′ aggregates disconnected from the PS I cores in our samples was negligible. It would be very interesting to perform experiments analogous to those described in this work on the PS I - CP43′ supercomplexes from *Synechococcus elongatus*, if and when such samples become available.

Acknowledgements

This research was supported by the Division of Chemical Sciences, Office of Basic Energy Sciences, USDOE. Ames Laboratory is operated for USDOE by Iowa State University under Contract W-7405-Eng-82. Authors are thankful to Drs. Alexander Melkozernov and Robert Blankenship (ASU) for their valuable comments, to Dr. Tõnu Reinot (ISU) and Dr. Nhan Dang (KSU) for help with fluorescence excitation spectra measurements, and to Dr. James Barber (Imperial College, London) who provided the CP43' – PS I supercomplex samples.

References

1. Gantt, E., *BioSciences* **1975**, 25, p. 781.
2. Glazer, A. N., *Annu. Rev. Microbiol*. **1982**, 36, p. 173.
3. Pakrasi, H. B., Riethman, H. C., Sherman, L. A., *Proc. Natl. Acad. Sci. USA* **1985**, 82, p. 6903.
4. Guikema, J., Sherman, L. A., *Plant Physiol.* **1983**, 73, p. 250.
5. Laudenbach, D., Strauss, N. A., *J. Bacteriol.* **1988**, 170, p. 5018.
6. Burnap, R. L., Troyan, T., Sherman, L. A., *Plant Physiol.* **1993**, 103, p. 893.
7. Bibby, T. S., Nield, J., Barber, J., *J. Biol. Chem.* **2001**, 276, p. 43246.
8. Bricker, T. M., Frankel, L. K. *Photosynth. Res.* **2002**, 72, p. 131.
9. Boekma, E. J., Hifney, A., Yakushevska A. E., Piotrowsky, M., Keegstra W., Berry, S., Michel, K.-P, Pistorius, E. K., Kruip, J., *Nature* **2001**, 412, p. 745.
10. Bibby, T. S., Nield, J., Barber, J., *Nature* **2001**, 412, p. 743.
11. Kouril, R., Yeremenko, N., D'Haene, S., Yakushevska, A. E. Keegstra, W., Matthijs, H. C. P., Dekker, J. P., Boekema E. J., *Biochem. Biophys. Acta* **2003**, 1607, p. 1.
12. Jordan, P., Fromme, P., Witt, H. T., Klukas, O., Saenger, W., Krauβ, N. *Nature,* **2001**, 411, p. 909.
13. Bibby, T. S., Nield, J., Partensky, F., Barber, J., *Nature* **2001**, 413, p. 590.
14. Melkozernov, A. N., Bibby, T. S., Lin, S., Barber, J., Blankenship, R. E., *Biochemistry* **2003**, 42, p. 3893.
15. Andrizhiyevskaya, E. G., Schwabe, T. M. E., Germano, M., D'Haene, S., Kruip, J., van Grondelle, R., Dekker, J. P., *Biochem. Biophys. Acta* **2002**, 1556, p. 265.

16. Andrizhiyevskaya, E. G., Frolov, D., van Grondelle, R., Dekker, J. P., *Biochem. Biophys. Acta* **2004**, 1656, p. 104.

17. Nield, J., Morris, E. P., Bibby, T. S., Barber, J., *Biochemistry* **2003**, 42, p. 3180.

18. Zouni, A., Witt, H.-T., Kern, J., Fromme, P., Krauβ, N., Saegner, W., Orth, P., *Nature* **2001**, 409, p. 739.

19. Kamiya, N., Shen, J.-R., *Proc. Natl. Acad. Sci. USA* **2003**, 100, p. 98.

20. Biesiadka, J., Loll, B., Kern, J., Irrgang, K.-D., Zouni, A., *Phys. Chem. Chem. Phys.* **2004**, 6, p. 4733.

21. Ferreira, K. N., Iverson, T. M., Maghlaoui, K., Barber, J., Iwata, S., *Science* **2004**, 303, p. 1831.

22. Zazubovich, V., Matsuzaki, S., Johnson, T. W., Hayes, J. M., Chitnis, P. R., Small, G. J., *Chem. Phys.* **2002**, 275, p. 47.

23. Rätsep, M., Johnson, T. W., Chitnis, P. R., Small, G. J. *J. Phys. Chem. B* **2000**, 104, p. 836.

24. Hsin, T.-M., Zazubovich, V., Hayes, J. M., Small, G. J., *J. Phys. Chem. B* **2004**, 108, p. 10515.

25. Jankowiak, R., Zazubovich, V., Rätsep, M., Matsuzaki, S., Alfonso, M., Picorel, R., Seibert, M., Small, G. J., *J. Phys. Chem. B* **2000**, 104, p. 11805.

26. Hughes, J. L., Prince, B. J., Peterson Årsköld, S., Krausz, E., Pace, R. J., Picorel, R., Seibert, M., *J. Lumin*. **2004**, 108, p. 131.

27. Sener, M. K., Lu, D., Ritz, T., Park, S., Fromme, P., Schulten, K., *J. Phys. Chem. B* **2002**, 106, 7948.

28. Damjanovic, A., Vaswani, H. M., Fromme, P., Fleming, G. R., *J. Phys. Chem. B* **2002**, 106, p. 10251.

29. Byrdin, M., Jordan, P., Krauβ, N., Fromme, P., Stehlik, D., Schlodder, E., *Biophys. J.* **2002**, 83, p. 433.

30. Balaban, T. S., *FEBS Letters* 2003, 545, p. 235.

31. Gobets, B., van Stokkum, I. H. M. van Mourik, F., Dekker, J. P., van Grondelle, R., *Biophys. J.* **2003**, 85, p. 3883.

32. Riley, K., Jankowiak, R., Rätsep, M., Small, G. J., Zazubovich, V., *J. Phys. Chem. B* **2004**, 108, p. 10346.

33. Reddy, N. R. S., Picorel, R., Small, G. J., *J. Phys. Chem.* **1992**, 96, p. 6458.

34. Yeremenko, N., Kouril, R., Ihalainen, J. A., D'Haene, S., van Oosterwijk, N., Andrizhiyevskaya, E. G., Keegstra, W., Dekker, H. L., Hagemann, M., Boekma, E., J., Matthijs, H. C. P., Dekker, J. P., *Biochemistry* **2004**, 43, p. 10308.

35. Pålsson L.-O., Fleming, C., Gobets, B., van Grondelle, R., Dekker, J., Schlodder, E., *Biophys J.* **1998**, 74, p. 2611.

36. Dashdorj, N., Xu, W., Martinsson, P., Chitnis, P. R., Savikhin, S., *Biophys. J.* **2004**, 86, p. 3121.

37. Reinot, T., Zazubovich, V., Hayes, J. M., Small, G. J., *J. Phys. Chem. B* **2001**, 1056, p. 5083.

38. Correa, D. S., de Boni, L., dos Santos Jr., D. S., Barbosa Neto, N. M., Oliveira Jr., O. N., Misoguti, L., Zilio, S. C., Mendonca, C., R., *Appl. Phys. B* **2002**, 74, p. 559.

39. Vasil'ev, S., Orth, P., Zouni, A., Owens, T. G., Bruce, D., *Proc. Natl. Acad. Sci. USA* **2001**, 98, p. 8602.

40. de Weerd, F. L., van Stokkum, I. H. M., van Amerongen, H., Dekker, J. P., van Grondelle, R., *Biophys. J.* **2002**, 82, p. 1586.

41. Groot, M.-L., Frese, R. N., de Weerd, F. L. Bromek, K., Pettersson, Å., Peterman, E. J. G., van Stokkum, I. H. M., van Grondelle, R., Dekker, J. P., *Biophys. J.* **1999**, 77, p. 3328.

42. Brettel, K., *Biochem. Biophys. Acta* **1997**, 1318, p. 322.

43. Peterson Årsköld, S., Prince, B. J., Krausz, E., Smith, P. J., Pace, R. J., Picorel, R., Seibert, M, *J. Lumin.* **2004**, 108, p. 97.

CHAPTER 6 – RED ANTENNA STATES OF PHOTOSYSTEM I FROM CYANOBACTERIA *SYNECHOCYSTIS* PCC 6803 AND *THERMOSYNECHOCOCCUS ELONGATUS:* SINGLE-COMPLEX SPECTROSCOPY AND SPECTRAL HOLE-BURNING STUDY

A submitted paper that was modified and published in the *J. Phys Chem. B* **2007**, 111, p. 286-292.

Kerry J. Riley, Tõnu Reinot, Ryszard Jankowiak, Petra Fromme, and Valter Zazubovich

Abstract

Hole-burning and single photosynthetic complex spectroscopy were used to study the excitonic structure and excitation energy transfer processes of cyanobacterial trimeric photosystem I (PS I) complexes from *Synechocystis* PCC 6803 and *Thermosynechococcus elongatus* at low temperatures. It was shown that individual PS I complexes of *Synechocystis* PCC 6803 (which have two red antenna states, i.e. C706 and C714), reveal only a broad structureless fluorescence band with a maximum near 720 nm, indicating strong electron-phonon coupling for the lowest-energy C714 red-state. The absence of zero-phonon lines (ZPLs) belonging to the C706 red- state in the emission spectra of individual PS I complexes from *Synechocystis* PCC 6803 suggests that the C706 and C714 red antenna states of *Synechocystis* PCC 6803 are connected by efficient energy transfer with a characteristic transfer time of ~ 5 ps. This finding is in agreement with spectral hole burning data obtained for bulk samples of *Synechocystis* PCC 6803. The importance of comparing the results of ensemble (spectral hole burning) and single

complex measurements was demonstrated. The presence of narrow ZPLs near 710 nm in addition to the broad fluorescence band at ~ 730 nm in *Thermosynechococcus elongatus* (Jelezko et al., *J. Phys. Chem. B* **2000**, 104, 8093-8096), has been confirmed. We also demonstrate that high-quality samples obtained by dissolving the crystals of PS I of *Thermosynechococcus elongatus* exhibit stronger absorption in the red antenna region than any samples studied so far by us and other groups.

Introduction

Photosystem I (PS I) is one of the two major photosystems involved in oxygenic photosynthesis and is the largest, most complex membrane protein for which detailed structural and functional information is available [1, 2]. PS I converts light energy into chemical energy by transferring electrons across the thylakoid membrane from plastocyanine or cytochrome c_6 to ferredoxin. Structures of PS I from the cyanobacterium *Thermosynechococcus elongatus* [2] (formerly *Synechococcus elongatus;* we will use *Synechococcu*s as a shorthand in the following discussion) and higher plant *Pisum sativum* [3] were recently determined at 2.5 and 4.4 Å resolution by X-ray crystallography. A recent computational study provided an atomic model of plant PS I [4]. While cyanobacterial PS I is trimeric, [2] that of higher plants is monomeric with the core surrounded by peripheral antenna complexes [3,4]. (PS I of the deep-water, low illumination strains of cyanobacterium *Prochlorococcus marinus* [5] as well as some other cyanobacteria grown under iron stress conditions [6, 7] also contains peripheral light-harvesting complexes, the *IsiA* and *PcB* proteins that form a ring surrounding the trimeric PS I core.) The similarity of the core structures of PS I from cyanobacteria and plants indicates that evolution caused only minor variations in the core organization and function, and also provides a legitimate reason to believe that the structure and function of PS I cores from other organisms are also similar. Each core monomer is a complex network of chlorophyll *a* (Chl *a*) molecules embedded in protein with ~ 90 antenna Chls *a* surrounding the "reaction center" (containing the electron transfer chain which consists of primary electron donor P700, accessory Chls *a,* phylloquinone and 3 4Fe4S clusters) and funneling sunlight energy into it. While the majority of antenna Chls *a* absorb at

670-690 nm, some absorb at even longer wavelengths than the strongly coupled reaction center dimer, P700 [8, 9]. It has been shown that these "red antenna states" are localized on multimers of Chls *a* (closely spaced and strongly coupled), rather than on single Chl *a* molecules that interact peculiarly with their protein environment. Three red antenna states (C710, C715, C719) were resolved in PS I of *Synechococcus* [10] and two (C706 and C714) in PS I of *Synechocystis* PCC 6803 [9, 11]. Spectral hole burning (SHB) experiments [9, 10, 12] showed that several properties of the lowest energy antenna states of *Synechococcus* (C719) and *Synechocystis* (C714) PS I are nearly identical, suggesting that very similar aggregates are responsible for those red antenna states, with the small difference in their energy most likely due to small differences in protein environment. Both states revealed strong electron-phonon coupling, large permanent dipole moment change, and large rates of pressure-induced shift of spectral holes (lines) indicating that electron exchange interaction contributes significantly to the excitonic coupling of the lowest-energy C714 and C719 ensembles. The relations between structural and spectral features in cyanobacterial PS I remain undetermined. Originally, based on the strength of the dipole-dipole coupling between the chlorophyll molecules, B31-B32-B33, A38-A39, B37-B38 and B7-A32 were identified as the most probable origins of the red antenna states in *Thermosynechococcus elongatus* [13] (Figure 1A). The structure of PS I from *Synechocystis* was not measured; however, taking into account the similarity between the structures of *Synechococcus* [2] and plant [3] PS I, one might expect that the PS I structure for *Synechocystis* is quite similar to that for *Synechococcus*. For inter-pigment distances smaller than 10 Å the use of dipole-dipole approximation is questionable. Based on the results of Full Coulomb [14] and INDO/S calculations [15], respectively,

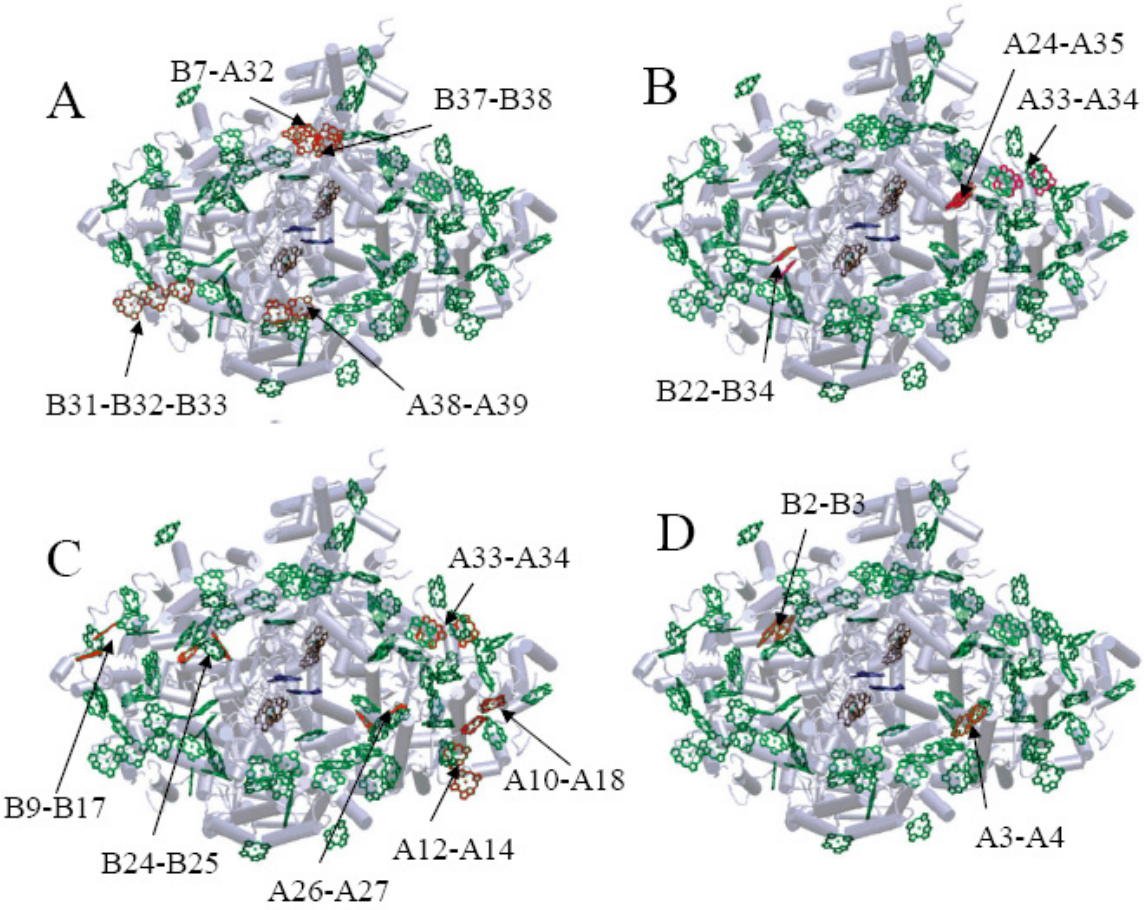

Figure 1. Chlorophyll ensembles proposed to be the origin of the red antenna states in PS I of *Synechococcus*. (Figure 1 from ref. 14 was used as a template.) A: From ref. [13]. B: From ref. [14]. C: From ref. [15]. D: From refs. [16, 17]. Note that the ensembles presented in A were considered in refs. [14] and [15] as well; they are not highlighted in B and C in order to preserve clarity. Direction towards trimer symmetry axis is upward.

several other chlorophyll dimers were identified which could contribute to the PS I absorption at $\lambda > 700$ nm, namely A33-A34, A24-A35 and B22-B34 [14] (Figure 1B), or A33-A34, A26-A27, A10-A18, A12-A14, B09-B17 and B24-B25 [15] (Figure 1C). Note that both refs. [14] and [15] still predict strong coupling between chlorophylls involved in the B07-A32 dimer (or B06-B07-A31-A32 tetramer) as well as for the A38-A39 and B37-B38 dimers, but not for the B31-B32-B33 trimer. Balaban suggested that the *syn*-ligated chlorophyll dimers B02-B03 and A03-A04 are responsible for the red antenna states in cyanobacterial PS I [16, 17] (Figure 1D). Gobets et al. concluded from fluorescence kinetics data that the lowest-energy red antenna state is localized on the B31-B32-B33 trimer in the PS I of *Synechococcus* [18]. This assignment, however, contradicts the spectral hole burning results demonstrating the similarity between the C714 state of *Synechocystis* and the C719 state of *Synechococcus* [9, 10, 12]; (Note that the B31-B32-B33 trimer most probably is absent or at least rearranged/disrupted in *Synechocystis* due to the lack of the histidine residue coordinating the respective chlorophylls of *Synechcoccus* [14, 18]). In addition, assignment of the *Synechococcus* red antenna states to the B31-B32-B33 trimer is inconsistent with data [8, 9] indicating that the lowest-energy red states of both *Synechococcus* (C719) and *Synechocystis* (C714) are localized close to the trimerization domain of PS I.

SHB is a powerful frequency domain technique for studying the $S_1(Q_y)$ excited state electronic structure, excitation energy transfer (EET), and electron transfer (ET) dynamics of protein-chlorophyll complexes at low temperatures. Despite its frequency selectivity, SHB still probes inhomogeneous ensembles of complexes, meaning that certain properties may be subject to distribution for chlorophylls absorbing at the same

wavelength. This is manifested, for example, by broadening of the spectral holes in external pressure and electric fields [19]. Single photosynthetic complex spectroscopy allows the properties of the complexes to be individually investigated, thereby removing effects due to inhomogeneity. While significant progress has been achieved in the spectroscopic studies of single LH2 complexes [20-26] as well as LH1 [27, 28] and LHCII [29] complexes, there is very little single complex data available for PS I. Until recently, there has been only one paper published on single PS I from *Thermosynechococcus elongatus* [30] (the data from this paper was later included in several reviews). The main feature of the individual PS I spectra in [30] was a broad structureless band peaked at about 725-730 nm. This band was accompanied by several narrow lines at 710-712 nm. The former broad band has been assigned to the same state, which exhibited very strong electron-phonon coupling in SHB experiments [10]. The same group published another paper on single PS I earlier this year [31]. It was demonstrated that the emission of pre-reduced PS I is multi-component, since after intensive (~ 600 μW) illumination resulting in bleaching of the main fluorescence band peaked at ~ 730 nm, a second emission component, peaked at 745 nm became observable. It was not determined, though, which absorption band correspond to the emission band at ~ 745 nm. Undoubtedly, the lack of published results is due to the complexity of PS I. As mentioned above, there are 288 Chls *a* per PS I trimer, i.e. almost 300 spectral lines/bands in a relatively narrow wavelength range. Furthermore, PS I does not possess the high symmetry of the light harvesting complexes from purple bacteria [20-28] which reduces the number of observable lines in the spectra of those complexes. Jelezko et al. focused exclusively on the red antenna state region of PS I

from *Synechococcus*. As mentioned above, their results confirmed that the lowest-energy state (C719) is characterized by very strong electron-phonon coupling [30]. On the other hand, their observation of narrow zero-phonon lines near 711-712 nm, most likely belonging to the higher-energy red state(s) of *Synechococcus*, present in both emission and fluorescence excitation spectra, suggested that different red antenna states (i.e. C710 and C719) are not connected by efficient energy transfer at low temperatures. This suggestion, however, contradicts the fluorescence anisotropy data [8], which indicates that C710→C719 energy transfer in *Synechococcus* does occur. To address the nature of the red antenna absorption bands, energy transfer and the low-energy emitting states, we describe below SHB results obtained for bulk PS I samples and the single complex emission spectra of PS I from both *Thermosynechococcus elongatus* and *Synechocystis* PCC 6803 obtained under identical experimental conditions. We will also demonstrate the importance of comparing the results of conventional absorption and emission spectroscopy (ensemble, low resolution), spectral hole burning (ensemble, high resolution), and single complex spectroscopy, which has rarely been done in the same manuscript.

Experimental

Wild-type trimeric PS I complexes from *Synechocystis* PCC 6803 were extracted as described in ref. [9]. The concentrated samples (stored at -70^0 C) were from the same batch as those used in our earlier hole burning experiments [9, 12]. Wild-type trimeric PS I complexes from *Thermosynechococcus elongatus* were prepared by dissolving high quality crystals similar to those used in X-ray diffraction experiments [2] in buffer containing 5 mM Mes, pH 6.4, 50 mM $MgSO_4$, 0.02 % dodecylmaltoside.

For bulk experiments, the above solution was mixed with buffer (10 mM MOPS, 0.02% β-dodecylmaltoside, pH = 7) and then mixed with glycerol (1:2) so that the final Chl *a* concentration was ~ $2 \cdot 10^{-5}$ M. The buffer-glycerol matrix provides good quality glass upon cooling to liquid helium temperatures. Absorption spectra and hole-burning spectra were measured with a Bruker IFS 120HR Fourier-transform spectrometer at 2 cm^{-1} resolution. Spectral holes were burned with a Coherent CR-699 laser with Exciton LD-688 dye (650-720 nm). Bulk emission spectra were measured with ~ 1 nm resolution using a McPherson 2061 1-m focal length monochromator with a Princeton Instruments diode array as a detector. These spectra were obtained with an excitation wavelength of 308 and/or 514 nm.

For experiments involving single complexes, concentrated PS I samples were first diluted with a suitable buffer (*vide supra*) to achieve the $OD_{680} \approx 0.4$ per 1 cm thickness, which corresponds to a Chl *a* concentration of approximately 10^{-5} M, i.e. to a concentration of trimeric PS I complexes of less than 10^{-7} M, taking into account 96 Chl *a* per P700. This solution was diluted again in a buffer/glycerol mixture (3:1) by a factor of ~ 1000, and then spin-coated on a plasma-cleaned sapphire plate yielding a film thickness of less than 1 μm. The use of glycerol here was not meant to facilitate formation of a transparent glass, but to adjust the viscosity of the solution for better thin film formation. Polymers were not used for sample preparation because, based on our experience (unpublished results), the photosynthetic complexes embedded in dry polymer films are disrupted compared to those studied in typical bulk experiments. The sample was placed in a cold (< 0º C), dark, oxygen-free cryostat and temperature was lowered to liquid helium temperature in about 20 minutes. Experiments were performed at 10 K in

helium gas or at 2 K in superfluid helium. To avoid sample degradation, all room-temperature sample-handling procedures were performed in dim light as quickly as possible.

The optical setup was based on a home-built confocal microscope with a Newport 60x 0.85 NA achromatic objective attached to the sample holder inside the cryostat (Janis). In order to reduce sample movements due to temperature expansion, the rod of the sample holder was made from fused quartz. The sample was moved in relation to the objective along the objective axis using an electromagnet with two parallel coils, one superconducting (for $T < 7$ K) and the other made from copper wire. A computer-controlled scanning mirror was used to move the focal spot across the sample plane. Excitation was performed with a Coherent CR-699 laser with Exciton LD-688 dye (650-720 nm), and with intra-cavity etalons removed, providing a linewidth of several GHz. After adjustment to ensure that the PS I-containing film was indeed in the focal plane of the objective, the scanning mirror was moved while the fluorescence (excited at 675-680 nm) was collected (at $\lambda > 700$ nm) by the avalanche photodiode (Perkin-Elmer, dark count < 25 s^{-1}). The experimental setup is schematically depicted in Figure 2A. An example of the resulting 10 K "raster-scan" image is presented in Figure 2B. The fluorescence peaks (red) correspond to individual PS I complexes from *Synechocystis* PCC 6803. In order to focus on individual complexes, the mirror was then moved to positions determined from the raster-scan image and spectroscopic measurements were performed. Emission spectra were collected with either a Princeton Instruments PI-MAX intensified CCD camera or a liquid nitrogen-cooled, back–illuminated CCD camera through Omega AELP 700 long-pass filter (and DRLP 710 dichroic mirror) and a Jobin-

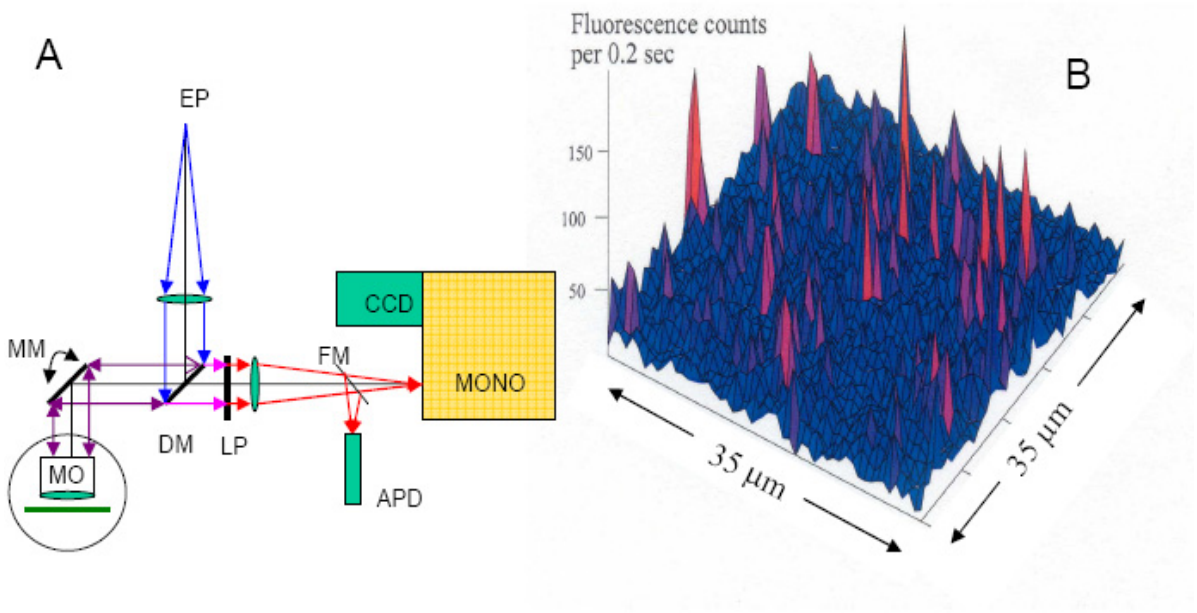

Figure 2. Frame A: Scheme of the confocal microscope used for individual complex spectroscopy. EP is excitation pinhole, DM is dichroic mirror, MM is motorized mirror, MO is microscope objective, LP is long-pass filter, and FM is flipping mirror. APD itself and the monochromator's slit were used as detection pinholes. Frame B: Raster-scan image of the thin film containing single PS I complexes from *Synechocystis* PCC 6803 (red peaks) obtained by varying the orientation of the scanning mirror. Fluorescence was collected with a 180 μm-diameter avalanche photodiode used as a pinhole. Complexes were excited with 250 nW / μm^2 (25W/cm^2) at 680 nm and fluorescence was collected at $\lambda > 700$ nm. T = 10 K.

Yvon Triax 320 spectrometer with a resolution of 0.4 nm. Excitation was at 675-680 nm. Excitation intensities (adjusted using neutral filters, LOMO) are given in the figure captions. In calculating these intensities, it was assumed that the laser was focused at a 1 μm^2 spot. In order to reduce background (mainly broadband dye fluorescence) an Omega 3rd Millennium SP700 short-pass filter was placed after the laser power stabilizer (BEOC).

Results and Discussion

***Synechocystis* PCC 6803.** The bulk 5 K emission spectrum of trimeric PS I from *Synechocystis* PCC 6803 showed a single fluorescence origin band with a maximum near 720 nm (see below), in agreement with emission spectra reported in [9, 33]. The shapes of the absorption spectrum, and of the satellite hole structure resulting from downhill excitation energy transfer following high-energy excitation, were also in agreement with earlier results [9, 12]. Therefore, it is assumed in the following discussion that the spectra described reflect the properties of the intact trimeric *Synechocystis* PS I complexes.

The noisy spectrum in Figure 3A is a typical low-temperature emission spectrum of a single PS I complex from *Synechocystis* PCC 6803. The spectrum peaks at 720 nm and is quite broad (FWHM = 12 nm) and structureless. This result is in agreement with the spectral hole burning data [9, 37] and supports the assignment of [9] where it was demonstrated that electron-phonon coupling for the emitting (C714) state is very strong, with a total Huang-Rhys factor S of about 2. The strong electron-phonon coupling, along with possible light-induced spectral diffusion, is the reason why ZPLs belonging to the C714 state were not observed. Similar strong electron-phonon coupling for the lowest-

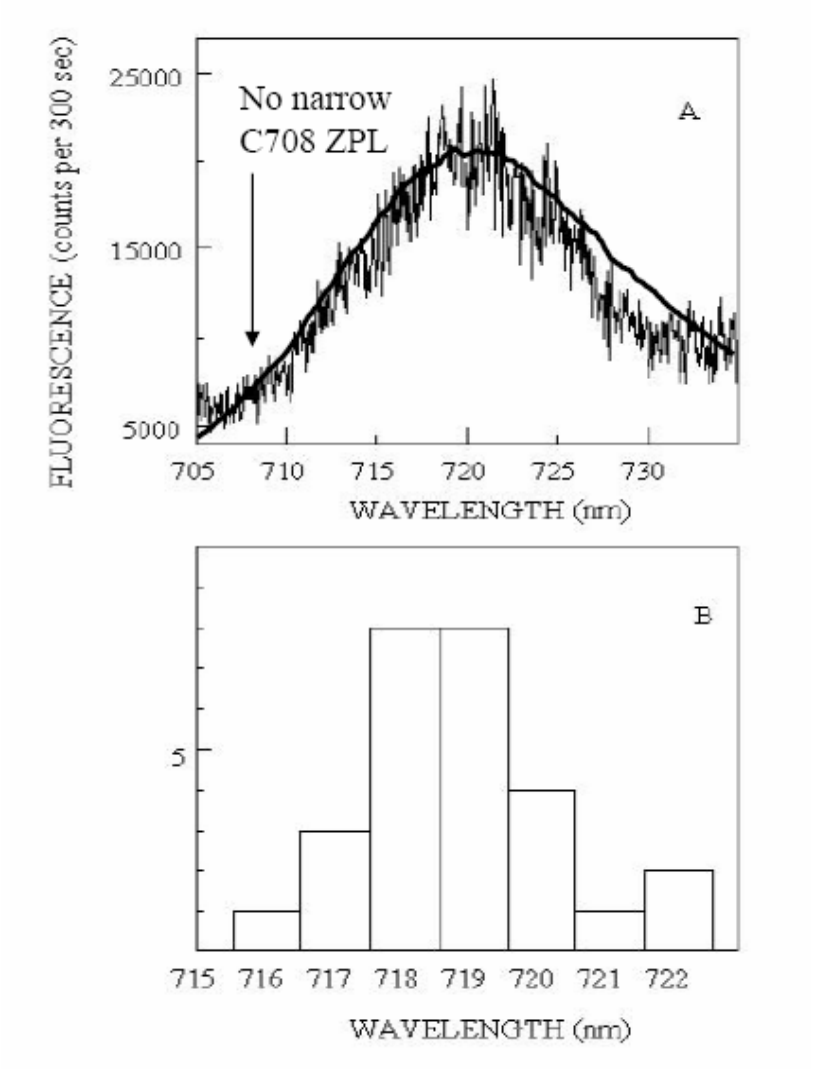

Figure 3. Frame A: Typical emission spectrum of a single PS I complex from *Synechocystis* PCC 6803 excited at 675 nm. Approximately 1.5 μW was focused on the single complex (i.e. the excitation intensity was ~150 W / cm^2 assuming 1 μm^2 focal area) and the collection time was 300 seconds. T = 10K. Bulk emission spectrum (thick solid curve; excitation at 308 nm) is superimposed on the single complex emission spectrum. Frame B: Histogram of the emission band maximum wavelengths based on the data from 27 single PS I complexes. Excitation was at 675 nm.

energy red antenna state of single PS I complexes from *Synechococcus* (C719) was demonstrated in ref. [30]. No sharp zero-phonon lines were observed near 706-708 nm, where direct emission from the C706 state might be expected. At this point, it may be asked if this finding actually suggests that there is only one red antenna state in *Synechocystis* PCC 6803, as proposed in ref. [18]. However, as demonstrated in refs. [9] and [34], electron-phonon coupling changes across the red antenna absorption band, becoming significantly weaker at 706-710 nm ($S \leq 1.2$) than at 714-718 nm ($S \approx 2$). Furthermore, significant differences were also observed for the permanent dipole moment change between excited and ground state $\Delta\mu$ [9], again supporting the presence of more than one red antenna state. We are unaware of a theoretical model that could explain the variation of S and $\Delta\mu$ by a factor of two within a single inhomogeneously broadened band. However, let us assume for a moment that just one red antenna state with such correlation is present in PS I and consider its possible manifestations on a single complex level. The emission from the PS I complexes with the one and only lowest state absorption at longer wavelengths (for example at ~ 715 nm) is expected at ~ 720 nm and should be broad and structureless due to strong electron-phonon coupling, $S \approx 2$ (as observed). The emission from PS I complexes with the lowest state absorbing at shorter wavelength (for example at ~ 708 nm) is expected to contain a well-defined ZPL at about the same wavelength (due to weaker electron-phonon coupling, $S \leq 1.2$). The single complex spectroscopy results in Figure 3B definitely do not fit this line of reasoning. Figure 3B contains the diagram of the emission band maxima of 27 single complexes. All measured single complex emission spectra contained only a broad band peaked at 716-722 nm; none exhibited narrow zero-phonon lines at ~ 708 nm. Also, the bulk

emission spectra in this work and in refs. [9] and [33] did not exhibit any shoulders at 706-710 nm. (For easy comparison, the bulk emission spectrum of *Synechocystis* PS I is superimposed on the single complex spectrum in Figure 3A.) This is a good illustration of the importance of comparing the results of single complex spectroscopy with those of ensemble techniques, such as SHB whenever possible. The results of single complex spectroscopy **alone** do not prove that there are two red antenna states in PS I of *Synechocystis* PCC 6803. Likewise the SHB results **alone** do not allow distinguishing between the cases of two red antenna states and of one state with a correlation between the wavelength and the electron-phonon coupling. Only when the two techniques are combined do the results prove the presence of the two states.

The absence of narrow lines in the spectra of single PS I from *Synechocystis* PCC 6803 may indicate that the red antenna states in *Synechocystis* are connected by fast and efficient energy transfer, in agreement with spectral hole burning results [12] which yield 5-6 ps for the C706 state lifetime. (Obviously, a 5-6 ps energy transfer time corresponds to a quite narrow, ~ 1 cm^{-1}, ZPL. Since the fluorescence lifetime of the C706 state is in the nanosecond range, the fluorescence yield must be smaller than 0.005, which makes ZPL unobservable in single complex experiments at 0.4 nm resolution, especially if spectral diffusion is present.) However, to prove that we were capable to observe narrow ZPLs using our experimental setup, single PS I complexes from *Thermosynechococcus elongatus* were also studied and results were compared to those described in refs. [30] and [31].

Thermosynechococcus elongatus. Unlike in previous spectroscopic studies, here the *Thermosynechococcus elongatus* PS I samples were prepared by dissolving high-

quality PS I crystals. Absorption and hole-burning spectra of trimeric PS I from *Synechococcus* are presented in Figure 4 along with the absorption spectrum obtained earlier for conventionally prepared sample under similar conditions [10]. The absorption spectra are normalized for equal bulk antenna absorption at ~ 680 nm. The absorption spectrum (thick solid curve in Frame A) is similar to that reported in [8, 10, 32], except for the red-antenna state region (~ 700 - 740 nm), which appears to have significantly greater oscillator strength. In addition, a comparison of the shapes of the absorption spectra in the 700 -740 nm region suggests that the relative intensity of the band peaking at 710 nm is approximately the same for both samples while the intensities of the lower-energy (C715 and C719) bands are greater for the sample studied in this work. To test this suggestion, we explored the shape of the hole spectra (and its time evolution during the hole-burning process) resulting from non-resonant excitation at 670 nm (Figure 4B). Formation of satellite holes at lower energies is due to downhill energy transfer followed by spectral hole burning. At low burn fluences ($\leq$ 10 J / cm^2) the only low-energy satellite hole observed is peaked at 719 nm (dotted curve in Frame B of Figure 4). In our experiment, the hole at 719 nm was observable directly, in contrast to the spectra presented in ref. [10], where the C719 state was only detectable in the difference (curve c in the insert in Figure 4B) of satellite hole spectra obtained with different burn fluences (curves a and b in the insert in Figure 4B). With the increase of the burning dose, the 719 nm hole became obscured by the much stronger hole peaked at 715 nm. Thick solid and dashed curves in Frame B of Figure 4 are hole spectra resulting from irradiation with 500 J /cm^2 at 670 nm for samples studied in this work and in ref. [10], respectively. In the earlier work the third satellite hole, at 710 nm, was as strong as the 715 nm hole [10].

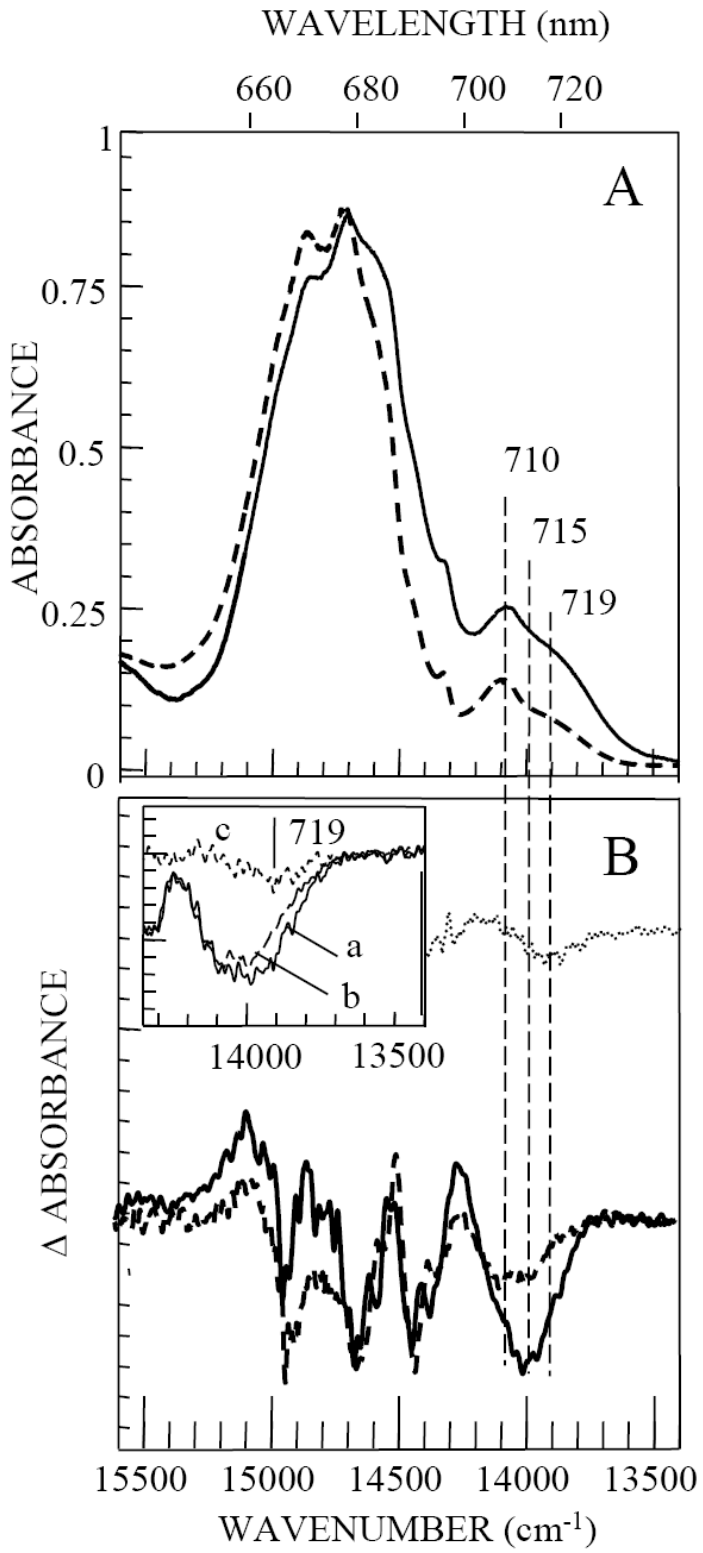

Figure 4. 5 K bulk spectra of PS I of *Thermosynechococcus elongatus.* Frame A: Bulk absorption spectra. Thick solid curve: trimeric PS I sample used in this work. Thick dashed curve: trimeric PS I sample used in [10]**.** Spectra are normalized to approximately equal absorbance in the bulk antenna region, ~ 680 nm. Frame B: Satellite hole spectra resulting from illumination at 670 nm of the trimeric PS I sample used in this work with about 10 J / cm^2 (25 mW/cm^2 for 420 sec; dotted curve) and about 500 J / cm^2 (several burns with intensity of up to 300 mW/cm^2; solid curve). Thick dashed curve: hole spectrum resulting from illumination at 670 nm with about 500 J / cm^2 for the sample explored in [10]. Insert: the evolution of the hole spectrum shape for the sample described in [10]. Solid curve *a* corresponds to a burning fluence of about 3 J / cm^2 and long-dashed curve *b* – to about 100 J / cm^2. Curve *a* was multiplied by a factor of ~ 2 to normalize it to curve b at 700 nm (14285 cm^{-1}). Short-dashed curve (c**)** is the difference of curves *a* and *b*.

But in this work (solid curve in Figure 4B), the 710 nm hole is just a shoulder compared to the 715 nm hole. Thus, we conclude that C715 and C719 bands in our samples have higher oscillator strength than in other *Thermosynechococcus elongatus* PS I samples explored thus far. Note that the integral intensity and shape of the red antenna region are sensitive to the monomeric / trimeric state of PS I. Such a tendency was observed for both *Synechococcus* [8] and *Synechocystis* [9]. Therefore, one might conclude that the supposedly trimeric *Synechococcus* samples in the previous studies by us and other groups could, in fact, contain a certain fraction of monomeric PS I. The emission spectrum (Figure 5, solid curve) is peaked at 732 nm, at approximately the same wavelength as in the previously described samples (dashed curve in Figure 5; from ref. [10]). This emission band is assigned to the same chlorophylls which have their absorption maximum at 719 nm (C719), in agreement with the data on electron-phonon coupling [10]. In this work, no weak shoulders near 710 nm (indicated by the solid arrow) were observed. Also, the band at ~ 685-690 nm (indicated by the dashed arrow) was significantly weaker than in the earlier works. No contribution from disconnected chlorophylls, which might be expected at ~ 670 nm, could be detected. Resonant hole-burning experiments (results not shown) confirmed that the electron-phonon coupling is very strong ($S \geq 2$) for the C719 state and relatively weak ($S \sim 1$) for the C710 state, in agreement with earlier work [10]. Thus, we concluded that the *Synechococcus* samples appear to be the most intact trimeric PS I samples studied thus far.

The emission spectra of individual PS I complexes from *Thermosynechococcus elongatus* are shown in Figure 6. The main feature of the individual PS I spectra is a broad band peaked at about 725-727 nm, in good agreement with [30]. This band closely

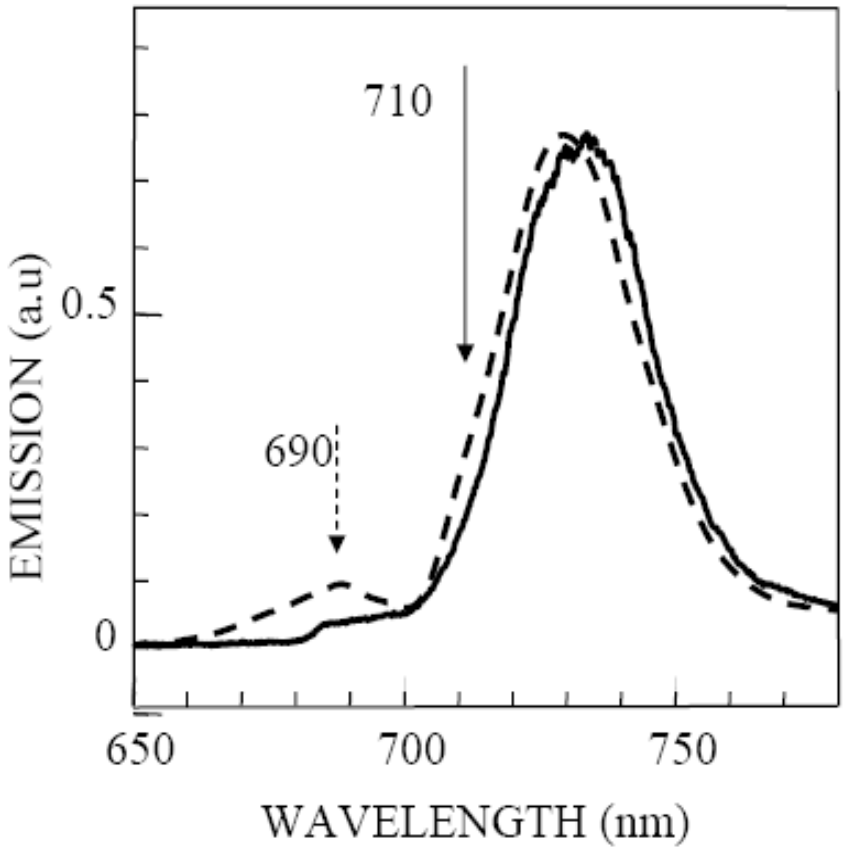

Figure 5. 5 K emission spectra (excited at 308 nm) of the *Synechococcus* PS I samples used in this work (solid curve) and in [10] (dashed curve). Spectra are normalized to equal intensity at 730-732 nm. Solid arrow indicates the shoulder at 710 nm in the spectrum from ref. [10]. Dashed arrow indicates a feature at ~ 690 nm.

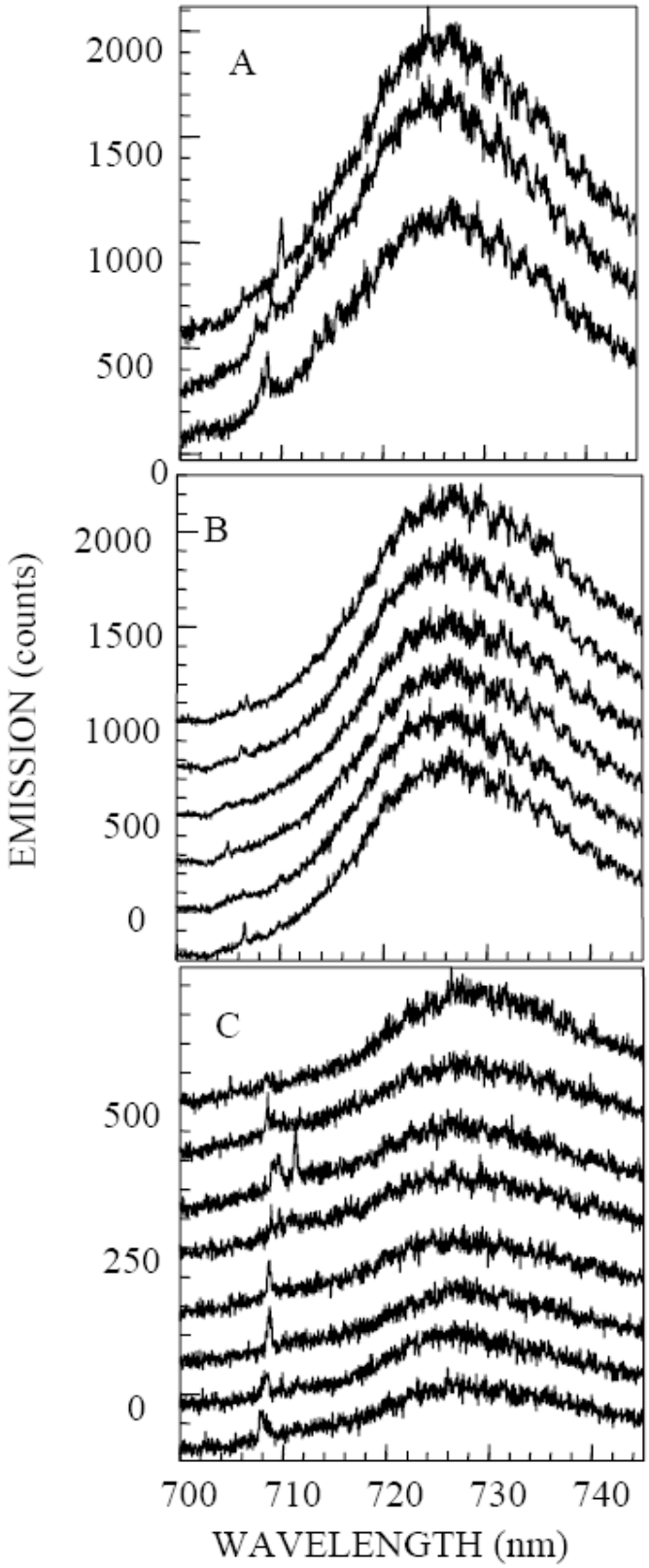

Figure 6. Single complex emission spectra of PS I of *Thermosynechococcus elongatus*. About 5 μW at 680 nm were focused to a spot of about 1 μm^2 (i.e. the excitation intensity was 500W/cm^2) and collection times were 300 seconds (Frame A) and 60 seconds (Frames B and C). Frames A-C contain spectra of three different complexes. Consecutively taken spectra of the same complex are depicted in each frame. T = 9 K. Spectra are shifted along the vertical axis for clarity.

resembles the bulk emission spectrum and most likely originates from the C719 state, characterized by strong electron-phonon coupling [10]. This broad band was sometimes accompanied by narrow lines at 706-713 nm. Assuming weak to moderate electron-phonon coupling observed with SHB at ~ 710 nm [10], the absorption maximum of the state from which the narrow ZPLs originate should be 709-710 nm in the bulk spectra, i.e. the lines most likely belong to the C710 state. Narrow zero-phonon lines (ZPL) in the 706-713 nm region were at least occasionally observed in 80% of the single complexes. The relative intensities of these narrow ZPL and of the main emission band at ~ 725-727 nm varied from one complex to another. The number of lines also varied from one complex to another and from spectrum to spectrum for the same complex, so that no lines were observed in about 50% of the spectra Frames A-C of Figure 6 show consecutively collected emission spectra of three different complexes. (Periodic features at $\lambda > 730$ nm most probably originate from the etaloning effect of the back-illuminated CCD, i.e. the interference between reflections from the front and back surfaces of a thinned back-illuminated CCD chip.) It is evident that the positions of the sharp lines varied with time, and sometimes the lines disappeared entirely only to reappear later (on the time scale of tens of seconds). This is an indication of relatively slow spectral diffusion. For fixed laser excitation intensity, we did not notice any significant statistical difference between either the probability of observing narrow lines or their spectral diffusion behavior at 10 K and at 2 K. (Unfortunately, we were unable to follow the same single complex from 10 K to 2 K.) Thus, we conclude that the observed spectral diffusion is predominantly light- and not thermally induced. In other words, we observed a process analogous to

non-resonant spectral hole burning in the bulk experiments (frame B of Figure 4). The relative insignificance of thermally induced spectral diffusion is consistent with the slow filling of spectral holes below 20 K in the dark.

Single complex emission spectra obtained for PS I in this work as well as in work previously published by Jelezko et al. [30] indicate that the emission from the C719 state (peaked at 730 nm) is significantly more intense than the emission from the C710 state, although the bulk absorption of the two states is comparable. No significant shoulder near 710 nm was observed in the bulk emission spectra (Figure 5, solid curve). These data suggest that emission from the C710 state upon high-energy (indirect) excitation is relatively weak (if present at all). On the other hand, upon direct excitation, sharp lines belonging to the C710 state were detected by Jelezko et al. in fluorescence excitation spectra even though their experimental setup, including a filter transmitting at $\lambda > 725$ nm, did not favor the detection of the ~ 710-712 nm emission [30]. The most probable explanation for these observations involves relatively efficient energy transfer from the C710 state to the C719 state. It is noteworthy that we never observed more than two lines in a single spectrum (perhaps the result of a spectral diffusion event occurring during the collection time), while Jelezko et al. [30] reported up to four lines in a single spectrum for the same collection time, 60 sec. It was recently demonstrated that the red state emission is polarized [31], and the differences in the number of observed lines from complex to complex in the same experiment could be explained by orientation effects. However, both in this work and in [30] the samples were produced in a similar manner, and it is unclear why the average orientation of the complexes should be different in this work and in ref. [30]. The possibility of rapid spectral diffusion (which could average away the

narrow lines at long collection times) was investigated by reducing the spectrum collection time from 60 sec to 10, 5 and 1 sec, respectively, for some of the complexes that did not reveal any narrow lines. Since no narrow lines were observed even for the shortest collection times, we believe that narrow lines were truly absent in the emission spectra of some *Synechococcus* PS I complexes. It is tempting to suggest that the differences between our observations and those by Jelezko et al. are due to higher intactness of the samples used in this work, which results in a higher probability of C710 $\rightarrow$ C719 energy transfer.

The energy transfer processes occurring in PS I of *Synechococcus* are summarized in Figure 7. The energy absorbed by the bulk antenna (650-700 nm) is transferred to the reaction center (P700) or to the red antenna states C710, C715 and C719. The differences from complex to complex in the relative intensities of the fluorescence originating from the C710 and C719 states may be due to orientation effects or to varying probability of EET from the higher-energy core states to the C710 state or to varying probability of C710 $\rightarrow$ C719 energy transfer. Unfortunately, polarization measurements employing conventional setups such as those used in this work and in [30, 31] do not allow one to determine whether or not the effects related to variations in the EET probabilities are present in addition to the orientation effects. One can suggest, however, that the very fact that narrow C710 lines were observed for *Synechococcus* PS I indicates that the C710 $\rightarrow$ C719 energy transfer times are, at least in some PS I complexes, significantly longer than 5-6 ps observed for the C706 state of *Synechocystis* by means of spectral hole burning [12].

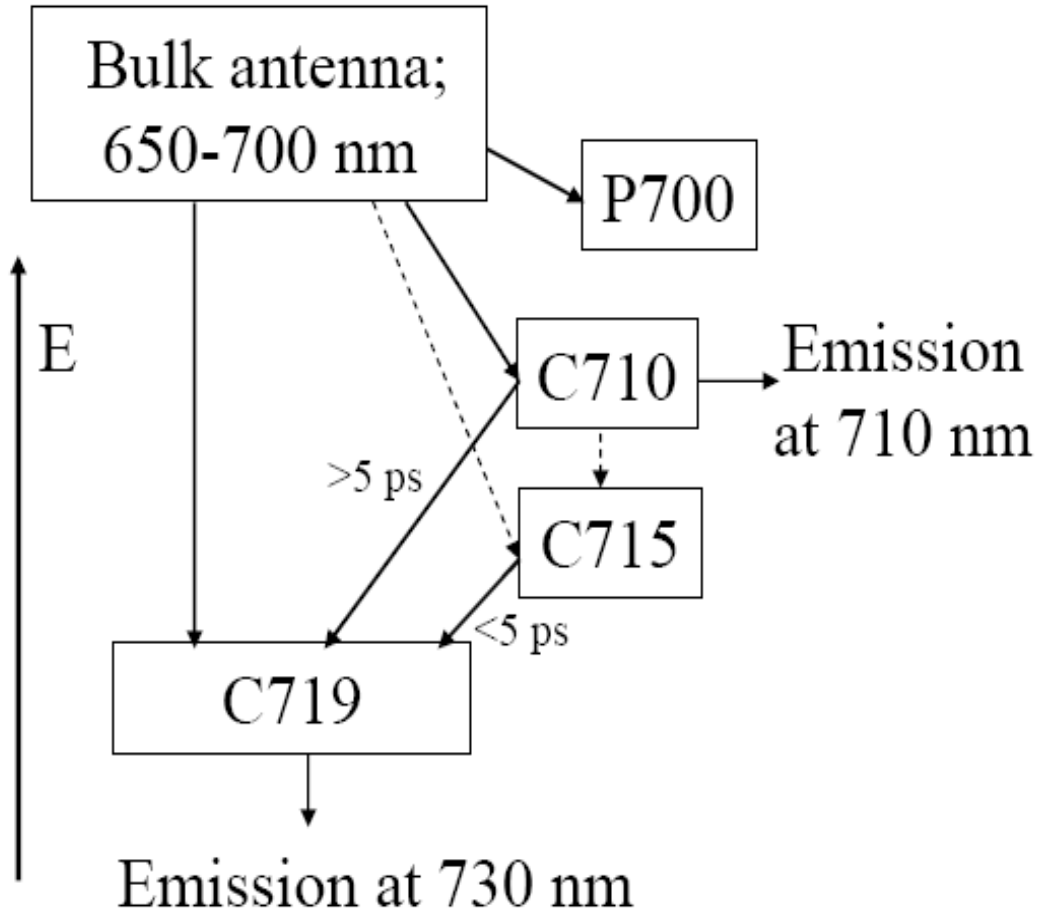

Figure 7. Diagram of energy transfer processes in PS I of *Thermosynechococcus elongatus*.

We hasten to remind the reader that while the C714 band of *Synechocystis* PCC 6803 and the C719 band of *Thermosynechococcus elongatus* very likely belong to the same chlorophyll multimer [10, 12], the C706 band of *Synechocystis* and the C710 band of *Synechococcus* most probably do not. It is quite possible that the C706 band of *Synechocystis* corresponds to the C715 band of *Synechococcus* since both are sensitive to the trimeric / monomeric state of the PS I complexes [8, 9], and since no features attributable to the C715 state were observed in the single PS I spectra of *Synechococcus* as well as for the C706 state in *Synechocyctis*. The latter observation suggests that the C715 $\rightarrow$ C719 energy transfer in *Synechococcus* occurs on a timescale of $\leq$ 5 ps (as for C706 $\rightarrow$ C714 energy transfer in *Synechocyctis*), in agreement with assignment of the C715 and C719 (or C706 and C714) states to two chlorophyll multimers located close to each other in the trimerization domain, i.e. B37-B38 and B7-A32. (In SHB experiments [12] zero-phonon holes could be observed even if energy transfer is very fast, because the spectra are accumulated.) However, it cannot be excluded that fast spectral diffusion, in addition to fast energy transfer, contributes to our inability to observe narrow lines originating from the C706 state of *Synechocystis* and the C715 state of *Thermosynechococcus elongatus*.

Conclusions

It has been demonstrated that combining spectral hole burning and single complex spectroscopies (using the same PS I preparations) provides unique insights into the excitonic structure and excitation energy transfer processes in these complex biological systems. Application of both bulk and single-entity techniques is especially informative when the spectroscopic properties of the systems under study are dependent

on sample preparation. We have used highly purified PS I crystals from *Thermosynechococcus elongatus* similar to those used in X-ray diffraction experiments; dissolved crystals yielded samples whose absorption spectra revealed significantly stronger "red" antenna bands. These samples have also provided more convincing data that PS I from *Thermosynechococcus elongatus* indeed possesses three "red" antenna states, i.e. C710, C715, C719, in agreement with our earlier assignment [10]. In addition, the presence of the narrow ZPLs in the vicinity of 710 nm in the emission spectra of single PS I complexes from *Thermosynechococcus elongatus* has been confirmed. Their weakness suggests that the energy transfer from the C710 to the C719 state is relatively efficient. The absence of narrow lines near 706-708 nm in the emission spectra of single PS I complexes from *Synechocystis* PCC 6803 indicates that energy transfer from the C706 state to the C714 state is fast (~ 5 ps) and efficient. Finally, our results provide additional proof of the similarity of the lowest-energy states of PS I from *Synechococcus* and *Synechocystis* (C719 and C714, respectively) as well as of the presence of two different red antenna bands (C706 and C714) in PS I of *Synechocystis* PCC 6803.

Acknowledgements

In memory of Professor Gerald J. Small. We acknowledge Dr. John M. Hayes (Ames Laboratory USDOE) and Mr. Tse-Ming Hsin (ISU) for their involvement in the early stages of the project, and Drs. Ingo Grotjohann and Hongqi Yu (ASU) for their participation in preparation of *Thermosynechococcus elongatus* PS I crystals. We thank Dr. Fedor Jelezko (University of Stuttgart) for sharing unpublished details of his experiments on *Thermosynechococcus elongatus*.

References

1. Fromme, P., Mathis, P., *Photosynth. Res*. **2004**, 80, p. 109.
2. Jordan. P., Fromme, P., Witt, H. T., Klukas, O., Saenger, W., Krauβ, N., *Nature* **2001**, 411, p. 909.
3. Ben-Shem, A., Frolow, F., Nelson, N., *Nature* **2003**, 426, p. 630.
4. Jolley, C., Ben-Shem, A., Nelson, N., Fromme, P., *J. Biol. Chem.* **2005**, 280, p. 33627.
5. Bibby, T. S., Nield, J., Partensky, F., Barber, J. *Nature* **2001**, 413, p. 590.
6. Bibby T. S., Nield, J., Barber, J., *Nature* **2001**, 412, p. 743.
7. Boekma, E. J., Hifney, A., Yakushevska, A. E., Piotrowsky, M., Keegstra, W., Berry, S., Michel, K.-P., Pistorius, E. K., Kruip, J., *Nature* **2001**, 412, p. 745.
8. Pålsson, L.-O., Dekker, J. P., Schlodder, E., Monshouwer, R. van Grondelle, R., *Photosynth. Res.* **1996**, 48, p. 239.
9. Rätsep, M., Johnson, T. W., Chitnis, P. R., Small, G. J., *J. Phys. Chem. B* **2000**, 104, p. 836.
10. Zazubovich, V., Matsuzaki, S., Johnson, T. W., Hayes, J. M., Chitnis, P. R., Small, G. J. *Chem. Phys.* **2002**, 275, p. 47.
11. Melkozernov, A. N., Lin, S., Blankenship, R. E., Valkunas, L., *Biophys. J.* **2001**, 81, p. 1144.
12. Hsin, T.-M., Zazubovich, V., Hayes, J. M., Small, G. J., *J. Phys. Chem. B* **2004**, 108, p. 10515.
13. Byrdin, M., Jordan, P., Krauβ, N., Fromme, P., Stehlik, D., Schlodder, E., *Biophys. J*. **2002**, 83, p. 433.

14. Sener, M. K., Lu, D., Ritz, T., Park, S., Fromme, P., Schulten, K., *J. Phys. Chem. B* **2002**, 106, p. 7948.

15. Damjanovic, A., Vaswani, H. M., Fromme, P., Fleming, G. R., *J. Phys. Chem. B* **2002**, 106, p. 10251.

16. Balaban, T. S. *FEBS Letters* **2003**, 545, p. 235.

17. Balaban, T. S., private communication.

18. Gobets, B., van Stokkum, I. H. M., van Mourik, F., Dekker, J. P., van Grondelle, R. *Biophys. J.* **2003**, 85, p. 3883.

19. Köhler, M., Friedrich, J., Fidy, J., *Biochem. Biophys. Acta* **1998**, 1386, p. 255.

20. Hofman, C., Ketelaars, M., Matsushita, M., Michel, H., Aartsma, T., Köhler, J., *Phys. Rev. Lett*. **2003**, 90, p. 13004.

21. Hofman, C., Aartsma, T., Michel, H., Köhler, J., *Proc. Natl. Acad. Sci. USA* **2003**, 100, p. 15534.

22. Ketelaars, M., Matsushita, M., van Oijen, A. M., Köhler, J., Aartsma, T. J., Schmidt, J., *Biophys. J.* **2001,** 80, p. 1591.

23. Matsushita, M., Ketelaars, M., van Oijen, A. M., Köhler, J., Aartsma, T. J., Schmidt, J., *Biophys. J.* **2001**, 80, p. 1604.

24. Tietz, C., Chekhlov, O., Dräbenstedt, A., Schuster, J. Wrachtrup, J., *J. Phys. Chem. B* **1999**, 103, p. 6328.

25. van Oijen, A. M., Ketelaars, M., Köhler, J., Aartsma, T. J., Schmidt, J., *Chem. Phys*. **1999**, 247, p. 53.

26. van Oijen, A. M., Ketelaars, M., Köhler, J., Aartsma, T. J., Schmidt, J., *Biophys. J.* **2000**, 78, p. 1570.

27. Gerken, U., Jelezko, F., Götze, B., Branschädel, M., Tietz, C., Ghosh, R., Wrachtrup, J., *J. Phys. Chem. B* **2003**, 107, p. 338.

28. Ketelaars, M., Hoffman, C., Köhler, J., Howard, T. D., Cogdell, R. J., Schmidt, J., Aartsma, T. J., *Biophys. J.* **2002**, 83, p. 1701.

29. Tietz, C., Jelezko, F., Gerken, U., Schuler, S., Schubert, A., Rogl, H., Wrachtrup, J., *Biophys. J.* **2001**, 81, p. 556.

30. Jelezko, F., Tietz, C., Gerken, U., Wrachtrup, J., Bittl, R, *J. Phys. Chem. B* **2000**, 104, p. 8093.

31. Elli, A. F., Jelezko, F., Tietz, C., Studier, H., Brecht, M., Bittl, R., Wrachtrup, J., *Biochemisty* **2006**, 45, p. 1454.

32. Pålsson, L.-O., Fleming, C., Gobets, B., van Grondelle, R., Dekker, J., Schlodder, E., *Biophys J.* **1998**, 74, p. 2611.

33. Gobets, B., van Amerongen, H., Monshouwer, R., Kruip, J., Rögner, M., van Grondelle, R., Dekker, J. P., *Biochem. Biophys. Acta* **1994**, 1188, p. 75.

34. Hayes, J. M., Matsuzaki, S., Rätsep, M., Small, G. J., *J. Phys. Chem. B* **2000**, 104, p. 5625.

CHAPTER 7 – PHOTOSYNTHETIC COMPLEXES: A MODEL FOR THE DESIGN AND CONSTRUCTION OF MOLECULAR ELECTRONICS

Currently there is a wealth of information concerning the energy and electron transfer properties in photosynthetic complexes. The physical properties of light harvesting and RC complexes that constitute the PSUs of anoxygenic and oxygenic organisms have been extensively studied with high-resolution time domain (e.g. ultrafast) [1-3] and frequency domain (e.g. hole-burning, photon-echo, single-molecule) spectroscopies [4-6]. This along with X-ray structural information [7-10] provides a well-established paradigm for describing these biological electron transfer processes. Thus, this extensive knowledge database offers an excellent model for the further development of "third generation" photovoltaics [11], solar cell devices with efficiencies that are higher than current solar technology limits (~ 25-30 %), and that even approach Carnot efficiency limits (~ 85-90 %). However, the development of these third-generation devices will require much more sophisticated cell architectures than current thin-film semiconductor technologies employ. These devices will most likely have to incorporate tandem and multi-band cell designs [11] that can be selective for different photon wavelengths, and thus different energy band gaps, to provide the highest efficiency for utilizing solar light.

PSUs, which have internal quantum EET and electron transfer (ET) efficiencies ranging from 70-99%, along with spectral selectivities across nearly the entire visible wavelength range (~ 400-800 nm) [12-13], function as an ideal model for these more advanced photovoltaic technologies. Studying the architecture and functioning of PSUs

can address features such as optimal engineering efficiency for light absorption and solar energy conversion, energetic tolerance against onset of failure, and construction and assembly of solar cells on nanoscale dimensions [14]. One unique feature in photosynthetic systems is the functional specialization for different Chl pigments, i.e. some Chl molecules function as light harvesting antenna Chls for primary EET while RC Chls are responsible for electron transfer and charge separation. Light absorption and solar energy conversion in PSUs is maximized through the optimization of the photon absorption rate and Chl-Chl distances for EET and ET. Light harvesting is optimal with a PSU size ranging from 30-330 Chl molecules (considering that the absorption cross-section for a Chl molecule is ~ 0.30^2 A) to yield typical biological catalysis rates of 10^2-10^4 s^{-1} [13, 14]. Maximal excitation energy and electron transfer is achieved when Chl-Chl distances are ≤ 10-20 nm and ≥ 1.4 nm, respectively [14]. It has also been found that the distributions of Chl-Chl distances in PSUs do not need to be uniform for a high EET probability. For example, Chl-Chl distances that range from a minimum of 1 nm and a maximum of 4-8 nm still result in energy transfer quantum efficiencies of more than 98% according to Förster energy transfer theory [14]. In fact, most Chl-Chl distances are ~ 4 nm. However, the lower bound for the PSU Chl-Chl distances is much less variable. This is because Chl-Chl distances shorter than this can result in the formation of excitonic dimers (see Chapter 2.4.2), which can quench excited states [14-17]. Lastly, Chl-Chl dipoles are oriented non-randomly in the antenna system so that EET is favored over non-radiative decay channels [18, 19].

PSUs are also engineered to efficiently dissipate excess light energy and to prevent the formation of damaging cation or anion radicals. Other pigment molecules,

such as carotenoids, act as photoprotective excitation quenchers due to their fast non-radiative decay rates [14, 20]. These pigment molecules complement the absorption spectrum of the Chl antenna molecules, thereby increasing the absorption cross-section of the PSU. Cation and anion radicals can also be formed during electron transfer steps, which can oxidize or reduce the Chl pigment molecules and thereby damage the PSU [21]. RC pigments avoid this through multiple electron steps along energetically similar pigments that do not have large separation distances (< 6 nm) so that electron transfer and charge recombination is fast enough to avoid the formation of these radicals [14, 22]. However, ET between LH and RC pigments can generate long-lived radicals that can damage the antenna complexes. Photosynthetic systems counteract this by having light harvesting pigment molecules that are energetically higher than the primary electron donor radical, and through LH-RC pigments distances (~ 2-3 nm) that minimize oxidation or reduction reactions but that still allow for almost unity EET probability [14]. Thus, it is evident that the molecular architecture of PSUs offers important engineering and design blueprints for developing highly efficient nanoscale molecular photovoltaic electronics.

Currently, research efforts have progressed to synthesizing biomemetic systems that attempt to simulate the design of PSUs for use as molecular electronics. For example, Moore et al. [23] have recently developed an artificial RC complex where a purpurin macrocycle is linked to a C_{60} fullerene and to a carotenoid polyene. In this moiety, the purpurin is the primary electron donor, with the carotenoid functioning as an antenna and secondary electron donor, while the fullerene acts as the primary electron acceptor. After excitation a charge separated state forms in ~ 10 ps time scale with a

quantum efficiency of ~ 32%. Developments such as this, where the architecture of the PSU is used as a design blueprint, may have important implications for the development of future nanoscale molecular electronics. There has also been research progress made in directly coupling biological photosynthetic systems (e.g. RCs) to solid-state materials to fabricate biomolecular electronic and photovoltaic devices. One of the first successful attempts in this area was obtained by Greenbaum et al., [24] in which they fabricated a biophotovoltaic device by orienting monomeric photosystem I (PS I) RC complexes from green plants on 2-mercaptoethanol functionalized gold surfaces. Additional work by Greenbaum et al. [25] has involved the immobilization of monomeric PS I RC complexes in solid-state sol-gel glasses, in which the biological functioning of the complexes were retained in order to catalyze H_2 generation. Baldo et al. [26] have demonstrated the integration of electrically active purple bacterial and monomeric PS I RC complexes in solid-state devices, realizing photodetectors and photovoltaic cells with short circuit densities of ~ 0.10 mA/cm^2. The electronic integration of the devices was accomplished by self-assembling an oriented monolayer of mutated bacterial reaction centers from *Rb. Sphaeroides*. The complexes were stabilized with surfactant peptides [27-30] and then coated with a protective organic semiconductor. Most recently, Carmeli et al. have reported the ordering of monomeric and trimeric PS I mutant complexes on atomically flat gold surfaces through covalent cysteine bonding [31]. Through Kelvin probe force microscopy, photovoltage measurements were obtained which indicated that these oriented RCs were functional and able to generate a light-induced electric potential of ~ 0.5 V. In addition, we have recently finished experiments where trimeric PS I complexes are oriented on 2-mercaptoethanol functionalized gold surfaces, to form functional

photovoltaic devices that can be measured through wet cell photoelectric measurements (see Chapter 8).

It is apparent, then, that the next phase of photosynthesis research is going beyond studying the physics the energy and electron transfer properties of PSUs and their corresponding photosynthetic complexes, to actually using the information gained from these studies to either design next generation molecular electronic and photovoltaic devices or to use these photosynthetic complexes as a basis for biomolecular electronics. This is especially promising as further developments in biochemistry and site-directed mutagenesis may allow the fabrication of tailored PCs that can be coupled to solid-state materials to form advanced architectures, such as tandem and multi-band photovoltaic cells, for the development of third generation photovoltaics. Considering the limited resources of non-renewable energy sources, the considerable impact that this avenue of research could have would be well worth the investment.

References

1. van Amerongen, H. and van Grondelle, R., *J. Phys. Chem. B* **2001**, 105, p. 604.
2. Groot, M. L., Pawlowicz, N. P., van Wilderen, L. J. G. W., Breton, J.; van Stokkum, I. H. M., van Grondelle, R., *Proc. Natl. Acad. Sci. U.S.A*. **2005**, 102, p. 13087.
3. Brixner, T., Stenger, J., Vaswani, H. M., Cho, M., Blankenship, R. E., Fleming, G. R., *Nature* **2005**, 434, p. 625.
4. Riley, K., Jankowiak, R., Ratsep, M., Small, G.J., *J. Phys. Chem. B* **2004**, 108, p. 10346.
5. Prokhorenko, V. I. and Holzwarth, A. R., *J. Phys. Chem. B* **2000**, 104, p. 11563.
6. van Oijen, A. B., Ketelaars, M., Kohler, J. Aartsma, T. J., Schmidt, J., *Science* **1999**, 285, p. 400.
7. Loll, B., Kern, J., Saenger, W., Zouni, A., Biesiadka, J., *Nature* **2005**, 438, p. 1040.
8. Jordan, P., Fromme, P., Witt, H.T., Klukas, O., Saenger, W., Krauss. N., *Nature* **2001**, 411, p. 909.
9. McDermott, G., Prince, S.M., Freer, A.A., Hawthornthwaite-Lawless, A.M., Papiz, M.Z., Cogdell, R.J., Isaacs, N.W., *Nature* **1995**, 374, p. 517.
10. Koepke, J., Hu, X., Muenke, C., Schulten, K., Michel, H., *Structure* **1996**, 4, p. 581.
11. Green, M.A., *Third Generation Photovoltaics: Advanced Solar Energy Conversion*; Springer-Verlag: New York, 2003; Chapter 1, p. 1.

12. Blankenship, R. *Molecular Mechanisms of Photosynthesis*; Blackwell Science: Oxford, England, 2002.

13. Kamen, M.D., *Primary Processes in Photosynthesis*; Academic: New York, 1963.

14. Noy, D., Moser, C.C., Dutton, L*, Biochim. Biophys. Acta* **2006**, 1757, p. 90.

15. van Amerongen, H., Valkunas, L., van Grondelle, R., *Photosynthetic Excitons*; World Scientific: Singapore, New York, 2000; p. 50-71.

16. Knox, R.S., *J. Phys. Chem.* **1994**, 98, p. 7270.

17. Beddard, G.S., *Philos. Trans. R. Soc.* **1998**, 356, p. 421.

18. Sener, M.K., Lu, D.Y., Ritz, T., Park, S., Fromme, P., Schulten, K., *J. Phys. Chem. B* **2002**, 106, p. 7948.

19. Yang, M., Damjanovic, A., Vaswani, H.M., Fleming, G.R., *Biophys. J.* **2003**, 85, p. 140.

20. Hu, X.C., Ritz, T., Damjanovic, A., Autenrieth, F., Schulten, K., *Q. Rev. Biophys*. **2002**, 35, p. 1.

21. Law, C.J., and Cogdell, R.J., *FEBS Lett.* **1998**, 432, p. 27.

22. Moser, C.C., Page, C.C., Cogdell, R.J., Barber, J., Wraight, C.A., Dutton, P.L., *Adv. Prot. Chem.* **2003**, 63, p. 71.

23. Gould, S.L., Kodis, G., Liddell, P.A., Palacios, R.E., Brune, A., Gust, D., Moore, T.A., Moore, A.L., *Tetrahedron* **2006**, 62, p. 2074.

24. Lee, I., Lee, J.W., Greenbaum E., *Phys. Rev. Lett*. **1997**, 79, p. 3294.

25. O'Neill, H. and Greenbaum, E., *Chem. Mater.* **2005**, 17, p. 2654.

26. Das, R., Kiley, P.J., Segal, M., Norville, J., Yu, A.A., Wang, L, Trammell, S.A., Reddick, L.E., Kumar, R., Stellacci, F., Lebedev, N., Schnur, J., Bruce, B.D., Zhang, S., Baldo, M., *Nano Lett.* **2004**, **4**, p. 1079.

27. Vauthey, S., Santoso, S., Gong, H., Watson, N., Zhang, S., *PNAS* **2003**, 8, p. 5355.

28. Von Maltzahn, G., Vauthey, S., Santoso, S., Zhang, S., *Langmuir* **2003**, 19, p. 4332.

29. Kiley, P., Zhao, X., Vaughn, Baldo, M.A., Bruce, D., Zhang, S., *PloS Biology* **2005**, 7, p. e230.

30. Zhang, S., *Biotech. Ad*. **2002**, 20, p. 321.

31. Frovlov, L., Rosenwaks, Y., Carmeli, C., Carmeli, I., *Adv. Mat.* **2005**, 17, p. 2434.

CHAPTER 8 – TRIMERIC PS I COMPLEXES: A ROBUST BASIS FOR NANOSCALE CIRCUIT ARCHITECTURE IN MOLECULAR ELECTRONIC DEVICES

Preliminary data - to be submitted for publication.

Kerry J. Riley, Valter Zazubovich, Yuri Markushin, and Ryszard Jankowiak

Introduction

Renewable solar energy technology goals currently include the development of "third generation" photovoltaics; high efficiency, thin film cells having energy conversion values double or triple the current limits of 25-30% [1]. Photosynthetic pigment reaction center (RC) complexes utilize solar energy for electron transfer which results in a charge separated state across the complex. This energy conversion process has a quantum efficiency approaching that of unity with redox potentials ranging from 0.4 – 1.2 V [2], making RC complexes ideal for use as individual nanoscale (~ 100 nm size range) solar cells in third generation technology. For example, a 1 cm^2 chip of oriented photosynthetic complexes could have a minimum theoretical power output of ≥ 10 W [5]. It can be argued then, that the most powerful application of current photosynthesis research would be to develop solar cell technology that either mimics these biological photosynthetic systems or actually uses these highly evolved and efficient organisms as circuit architecture for energy transduction.

During the last few years, research groups have made significant advances developing this promising area of research. Greenbaum et al. have reported a

biophotovoltaic device in which photosynthetic RC complexes were used to generate a photovoltage [3,4]. Specifically, they showed that monomeric photosystem I (PS I) RC complexes from green plants could be selectively oriented by chemical modification of the substrate surface [4]. Additional work by Greenbaum et al. involved the immobilization of monomeric PS I RC complexes in solid-state sol-gel glasses, in which the biological functioning of the complexes was retained [5]. Also, Baldo et al. [6] demonstrated the integration of electrically active purple bacterial and monomeric PS I RC complexes in solid-state devices, realizing photodetectors and photovoltaic cells with short circuit densities of ~ 0.10 mA/cm^2 and reported internal quantum efficiencies (QE) of ~ 12% (however, recent discussions with the authors indicate that there was as error in this estimation by two orders of magnitude). The electronic integration of these devices was accomplished by self-assembling an oriented monolayer of mutated bacterial reaction centers from *Rb. Sphaeroides*. The complexes were stabilized with surfactant peptides [7-9, 11] and then coated with a protective organic semiconductor. Most recently, Carmeli et al. have reported the ordering of monomeric and trimeric PS I mutant complexes on atomically flat gold surfaces through covalent cysteine bonding [12]. The construction of these functionalized substrates using photosynthetic complexes has also attracted a growing interest for their possible applications in various chemo - and biosensor devices, along with their important implications to renewable solar energy technology [14-17].

Along with the work presented in refs [3-6], recent findings in this area clearly suggest that the most important step in the nanofabrication of biomolecular devices is the controlled functional orientation of proteins on a two-dimensional surface [10-15].

Photosynthetic protein complexes (PC) function in lipid bilayer membranes, and, consequently, these protein structures have developed a delicate balance of hydrophilic and hydrophobic interactions, such that their native conformation and functional integrity will not be retained outside this environment [18, 19]. Thus, the coupling of photosynthetic complexes to inorganic substrates, which necessitates a stabilizing interface, is indeed a challenging task. Ideally, a large, rugged photosynthetic RC complex where the RC cofactors are well shielded by the surrounding protein matrix, and has a large number of redundant antenna pigments, should be used for fabrication of photosynthetic RC-biomolecular devices. The trimeric cyanobacterial photosystem I (PS I) with 270 antenna chlorophylls (Chls) and 3 RCs possesses all these attributes and is therefore ideal. Presented here, for the first time, are atomic force microscopy (AFM) images of ordered *trimeric* PS I complexes on gold surfaces along with preliminary data for using these ordered PS I surfaces as photovoltaic devices. Functionalization of gold surfaces with the isolated photosystem II (PS II) RC complex from green plants was attempted and confirmed by AFM measurements as well.

The cyanobacterial PS I complex exists *in vivo* most exclusively as a trimer. The trimer has a molecular weight of 1068 kDa, forming a cloverleaf structure with a diameter of 22 nm and height of 9 nm [22]. Each monomer contains 90 light harvesting Chls and 22 carotenoids which transfer energy down to the electron transport chain which consist of six Chls, two phylloquinones, and three 4Fe4S clusters. Charge separation initiates at P700, a heterodimer of chlorophyll *a* and chlorophyll *a´*, with electron transfer proceeding along a branch of the symmetrically arranged Chl and phylloquinone subunits to the three 4Fe4S clusters. The oxidation potential of P700+ is only +0.4 V, but the

reduction potential of the 4Fe4S cluster is –0.7 V, giving an overall redox potential of 1.1 V. We have used trimeric PS I complexes obtained from high quality crystals of cyanobacterial *Thermosynnechococcus elongatus*. This is to ensure high sample purity and structural integrity for the PS I complexes. The use of trimeric PS I complexes immediately offers two important advantages in surface functionalization when compared to monomeric P SI RC complexes. First, trimeric cyanobacterial PS I complexes are more disk-like than isolated plant PS I complexes and should provide a better orientation uniformity and packing density, which are essential requirements for maximal current generation. Second, its larger and more intact antenna system compared to monomeric PS I RC complexes (~ 40 Chl molecules per RC [4]) used by Greenbaum et al. [4] and Baldo et al. [6] should provide higher efficiency light harvesting and energy funneling to the RC.

Experimental

PC solar cell devices were fabricated as described by Greenbaum et al [3]. Gold surfaces were prepared by evaporating gold (~ 200 nm) onto atomically flat silicon wafers (P100) at a temperature of 300-400 °C at high vacuum (~ 10^{-8} torr). Cut glass slides were then glued to the gold surface in a clean room environment and allowed to dry. The glass slides could then be removed from the wafer, possessing a surface that was the mirror image of the silicon wafer. The gold surfaces were then functionalized by immersion in a solution of 2-mercaptoethanol for ~ 10 minutes, resulting in a low energy hydrophilic surface. After this, the substrates were rinsed with nanopure distilled water, dried under ultrapure nitrogen (99.995%), and then incubated in a buffered PS I solution (~ 10^{-3} M conc.) overnight for ~ 12 hrs at 5º C, resulting in a surface derivatized with PS

I trimers. The majority of these RC complexes orient perpendicular, with the P700 Chls closest to the to the substrate, so that electron transport is vectorial and normal (i.e. downward) to the surface [3]. After PS I incubation, the devices were then stored in a buffered solution (pH = 6.4) if they were not to be immediately tested, but not for a period of time longer than 1 week (usually 24-72 hrs). Before testing the devices, the surfaces were again rinsed with nanopure water and dried under ultrapure nitrogen. AFM images were then acquired for the functionalized gold surfaces. Randomly selected 1000 nm X 1000 nm areas were imaged for bare gold surfaces, 2- mercaptoethanol derivatized surfaces, and PS I derivatized surfaces. AFM surface roughness and grain analysis comparisons were performed for bare gold, 2-mercaptoethanol functionalized, and PS I functionalized surfaces to verify that the PS I functionalized gold surfaces were not experimental artifacts. AFM images were acquired with a Nanoscope IIIa in multimode at room temperature and room atmosphere. All AFM images were analyzed with Scanning Probe Image (SPI) Processor v. 4.3.1.0.

Simplified schematics of the working photovoltaic devices are shown in Figure 3A-B. A wet electrochemical device (Figure 3A) and solid state electronic device (Figure 3B), were tested. Preliminary photoinduced short circuit current measurements of these devices were made by first soldering a shielded cable to the gold surface of the device to be tested (~ 1 cm^2), for use as an electrode contact. Then the devices were placed in a shielded container and the electrode contacts connected to a Keithley picoammeter to measure the photocurrent. For the wet cell devices, a Pt reference electrode was used where PBS buffer (pH = 7.2) was the electrolyte. For the solid state devices, a conductive rubber (ZOFLEX®CD45.1) was used as the reference electrode,

and the device was illuminated from the transparent bottom of the substrate. The wet cell and solid state devices were illuminated with a 75 W Hg arc lamp, and the current change with light on-off was recorded. The photocharacteristic spectrum (see Figure 3E) was also acquired by illuminating with an excitation intensity of ~ 1.5 W/cm^2 from a 75 W Xe arc lamp and using bandpass filters (~ 10 nm bandwidth) that spanned the PS I spectrum from 620-700 nm, and recording the current change with light on-off. For the photocharacteristic spectrum measurements, a wet piece of buffered gel (~ 1mm thick) was placed on the substrate surface of the wet electrochemical device so that there would be rugged and durable contact between the surface and the Pt reference electrode. The buffered gel electrode contact was prepared by mixing SIGMA Agarose Type I-A: Low EEO gel powder with nanopure PBS buffer (pH = 7.2) under heat until boiling, then refrigerating at 5º C for at least 4-6 hours. For all the devices tested, when the light was switched on the signal always reappeared at the same value. Lastly, control experiments of bare gold surfaces and 2-mercaptoethanol derivatized surfaces did not reveal any photoinduced current generation during illumination, confirming that the electrical activity was due to the presence of photosynthetic complexes.

Results and Discussion

A. Trimeric PS I RC Functionalized Surfaces. Cyanobacterial PS I complexes self-orient to readily form ordered monolayers on hydrophilic –OH terminated surfaces as suggested by refs. [4, 12]. As determined by AFM grain analysis (Figure1A-C), the mean particle size diameter and surface height for the PS I functionalized surfaces were ~ 30 nm and ~ 9 nm, respectively (as shown in Figure 1D-E), with a surface coverage > 85% for three randomly selected PS I derivatized areas. This corresponds well to the

dimensions of the trimeric PS I complex (20 nm x 20 nm x 9 nm), and indicates successful, regular orientation of the complex on the 2-mercaptoethanol treated surface, as the ethanol groups hydrogen bond to and orient the PS I trimer complexes. While the surface height of the functionalized surface almost corresponds exactly to the z-axis dimension of the PS I complex (9 nm), the diameter according to the grain analysis does not (30 nm vs. 20 nm). This is likely due to fact that the AFM tip size (~ 10 nm) is larger than the distance between some of the adjacent complexes, which results in a blurring of the surface image and undercounting of individual complexes. This also results in the asymmetric grain diameter distribution as shown in Figure 1D. The integrity and robustness of the oriented trimeric PS I complexes were then demonstrated by photocurrent measurements (see below), showing that these derivatized surfaces can act as nanoscale photovoltaic devices.

It is interesting to compare our PS I surface coverage (< 85%) with the result published by Greenbaum et al. (~ 70%). However, they used "isolated" monomeric PS I complexes from spinach which contain only ~ 40 Chl molecules out of the 167 Chl molecules per RC in the native monomeric form [3, 4]. Consequently, these complexes have lower surface area (6 nm x 5nm) compared to cyanobacterial trimeric PS I, and therefore should have lower probability of stable binding to the mercaptoethanol derivatized gold surface. Additionally, since these monomeric PS I complexes are altered from their native configuration during the purification process; their positively charged ends, which bind ferredoxin and plastocyanin, may be disrupted. Therefore, some of these complexes may not be able to effectively H-bond to the –OH groups on the

functionalized gold surface, or remain bound to the surface after multiple washing and drying steps [4].

The short circuit current density of the wet electrochemical devices was ~ 25 $\mu A/cm^2$, under white light illumination with an excitation intensity of ~ 1 W/cm^2, and ~ 2 nA/cm^2 (with the gel electrode contact), under illumination at λ = 680 nm with an excitation intensity of ~ 1.5 W/cm^2. We note that assuming a surface coverage density of 85% this corresponds to an estimated internal QE of < 0.01% for the wet device with excitation at 680 nm when assuming no reflection from the Au surface (see Appendix A). While this value is much lower than the QE value presented by Baldo et al. for their fabricated devices (0.12% when accounting for overestimation), it is reminded that no stabilizing layer was used for the photosynthetic complexes in our devices. It is possible that without using a stabilizing medium such as surfactant peptides, the native conformation of the PS I complex changes enough so that some of the Chl-Chl distances are shortened appreciably. If this happens, then quenching, and thus effects such as triplet bleaching, becomes significant [19, 25]. It is also possible that without the stabilizing peptide layer, the quenching of Chl excited states by the Au surface could be a factor as well [14]. Since there is no direct coupling between the oriented RC complexes and the cathode, an intermediary electron acceptor/donor might be needed to facilitate conduction. For example, recent work by Trammell et al. [14], reported wet cell measurements of ordered bacterial RC monolayers on Ni-NTA terminated Au surfaces that required the presence of ubiquinone-10 in the buffered solution to maximize the current output (500 nA for 1 W/cm^{-2} excitation at > 700 nm). Regardless, our QE result is important in that it illustrates the robust nature of trimeric cyanobacterial PS I

complexes, i.e. they can be directly coupled to a metallic surface and result in a working molecular electronic device.

As shown in Figure 2E, the action spectrum of the photocurrent is in agreement with the red absorption spectrum of PS I, indicating that the current originates from charge separation within the PS I complexes (see below). The corresponding time scan of the current generated by a wet chemical PS I functionalized device with the light on-off is shown in Figure 2C. Reversible and repeatable changes were clearly observed, with the current only generated when the light is on, suggesting that PS I retains its activity. We also confirmed that the electron transfer direction is toward the liquid electrode, suggesting that most of the complexes are indeed oriented perpendicular, with P700 closest to the Au surface (data not shown), in agreement with ref. [4]. These devices were operational for several days (~ 1-7 days). We note that stable currents were observed when the light was switched on for several hours. Experiments with the solid state devices, using the conductive rubber (ZOFLEX®CD45.1) as an electrode, showed a short circuit current density of ~ 5 $\mu A/cm^2$, under an illumination intensity of ~ 1 W/cm^2, which is about five times smaller than the current observed with the device shown in Figure 2A. This is most likely due to the less effective coupling of the rubber electrode to the surface compared to the wet device. A typical current as a function of time for this device with the light on-off is shown in Figure 3D. Overall, these experiments, while not definitive, offer further evidence for the robust structural integrity of trimeric PS I complexes that can be directly bound to metal surfaces, without any stabilizing interface, for use as nanoscale photovoltaic devices, as indicated in ref. [12].

B. Isolated PS II RC Functionalized Surfaces. Surface functionalization of 2-mercaptoethanol derivatized gold surfaces was also attempted with isolated PS II RC complexes. PS II is the other photosynthetic reaction center in cyanobacteria and green plants, and is responsible for the splitting of water due its to extremely high redox potential (~ 1.2 eV). PS II RC complexes can be prepared in "isolated" form, which consist of only the reaction center chlorin pigment molecules (6 chlorophyll and 2 pheophytin molecules) that are bound by the D_1/D_2 proteins and the cytochrome b_{559} complex [24]. Since the isolated PS II RC is only a part of the native PS II complex, they should not orient as preferentially to the hydrophilic –OH surface as the trimeric PS I complex. However, it should give an indication of whether smaller photosynthetic pigment complexes (e.g. light harvesting complexes such as bacterial LH1 and LH2) and cofactors (e.g. beta carotene molecules and other carotenoids) might bind to selectively functionalized surfaces.

Functionalized PS II gold surfaces were prepared via the procedure described earlier, except that the gold surfaces were immersed in a buffered solution (pH = 7.0) of isolated PS II RC complexes (~ 10^{-4} M conc.) for 10 minutes at room temperature [26]. AFM images of the gold surfaces incubated with PS II RC complexes indicated high-density functionalization, as shown in Figure 3. Grain analysis of the PS II surfaces indicated that the average z-axis dimension of the functionalized surface was ~ 5 nm (Figure 3C), which corresponds well to the dimensions of the isolated PS II RC complex (5 nm x 5nm x 5nm) used in our study [27]. Since the PS II RC is smaller than the AFM tip, the individual complexes could not be resolved; however, the surface coverage could and was estimated to be ~ 70%. This shows that the isolated PS II RC complex also

binds extremely well to the mercaptoethanol treated gold surfaces to form ordered monolayers. Since the isolated PS II RC complex is square in its dimensions, determining the functionalized orientation of these bound complexes was not feasible. Regardless, these experiments indicate that other photosynthetic complexes may orient on functionalized surfaces.

Conclusions

With these experiments we reaffirm that photosynthetic complexes may be successfully used as an interfacial material in photovoltaic devices as indicated in previous results. It is feasible that more elaborate designs (e.g. layered structures, tandem cell designs) with a controlled orientation could achieve significantly higher quantum efficiencies. With better nanoscale architectures that more efficiently promote electron transport and prevent energy-wasting recombination, significant improvements are anticipated. More specifically, architectures could be designed to mimic the efficient photon absorption and charge separation properties characteristic of *in vivo* biological photosynthetic units (light harvesting complexes + RC complexes) [25]. For example, the use of intact PS I complexes with peripheral light harvesting antenna complexes (e.g. LHCI) may lead to improved power conversion efficiency, as light harvesting antennas could increase the absorption cross-section. The use of additional electron transporting materials in fabrication could also increase quantum efficiency; for example, polyelectrolyte gels [17] that have charged moieties could help stabilize the orientation and the structural integrity of other less robust protein complexes (such as the PS II RC complex). Moreover, a number of systems have been identified which polymerize into hydrogels, such as alginate and hyaloronan polysaccharides [28], poly (ethylene oxide)

dimethacrylates [29] and poly (ethylene glycol) diacrylate [30]. Methods of protecting sensitive molecules from light-induced polymerization have also been developed recently [31]. This is achieved by incorporating sensitive molecules into gelatin-based wet granules. We also note that cells (chondrocytes) [29] and proteins (bovine serum albumin) [31] survived photo-polymerization even without gelatine protection. Finally, successful development of surface oriented (and stable) single PCs and/or protein arrays, which would reduce or eliminate the inhomogeneous spectral broadening, is also of interest for spectroscopic studies (polarization-sensitive measurements), as it could lead to profound and new insights that are unobtainable through studying bulky samples (e.g. energy transfer time determination via zero-phonon linewidths, excitonic band structure, transition dipole moment vector directions).

Appendix A. Quantum Efficiency Calculation

The QE of our fabricated photovoltaic devices can be approximated as

$$QE = \frac{\text{electron output of device}}{\text{photons absorbed by device}} \quad (1)$$

For an excitation intensity of 1.5 W/cm^2 at 680 nm, this yields ~ 5.1 x 10^{19} photons. Assuming the extinction coefficient for trimeric PS I complexes at 680 nm is 11.4 x 10^5 (M^{-1}) (cm^{-1}) [32] and that the PS I concentration is ~ 1.8 x 10^{-10} M (surface coverage where each PS I complex is separated by 10 nm), then ~ 2.0 x 10^{16} photons/cm^2 can be absorbed by the device. With a maximal current output of 2.0 nA/cm^2 this corresponds to a QE = 0.0001 or < 0.01 for the fabricated devices.

A

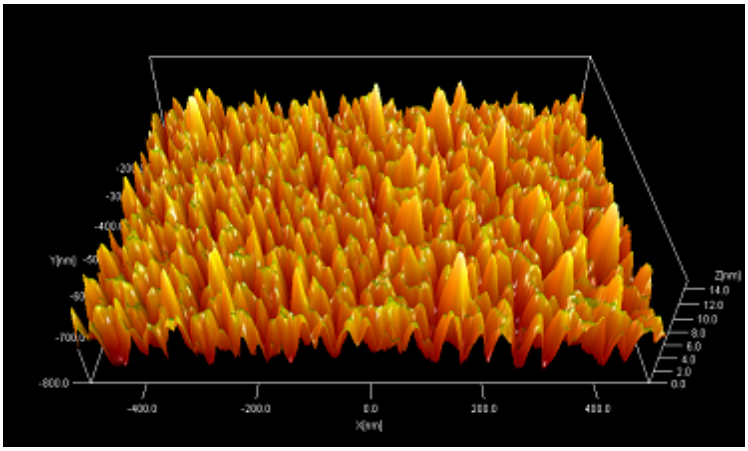

B

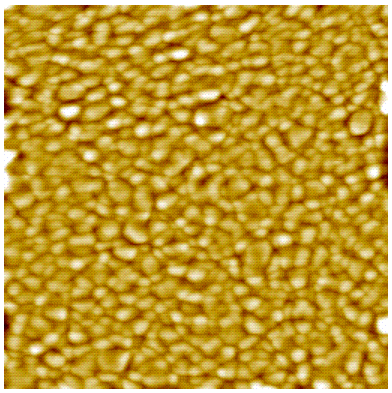

C

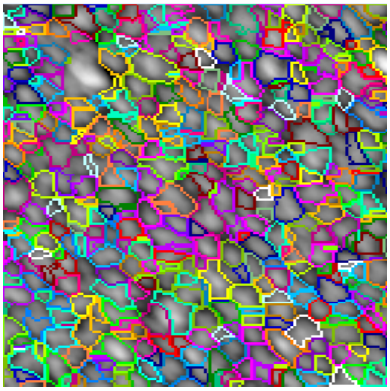

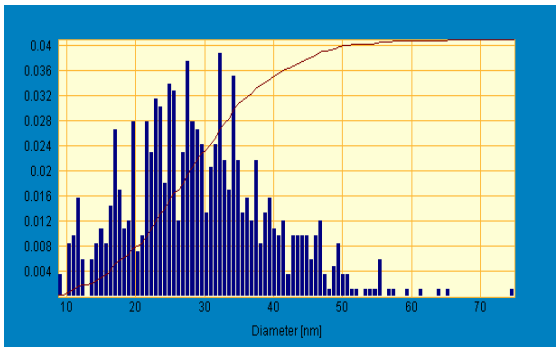

D

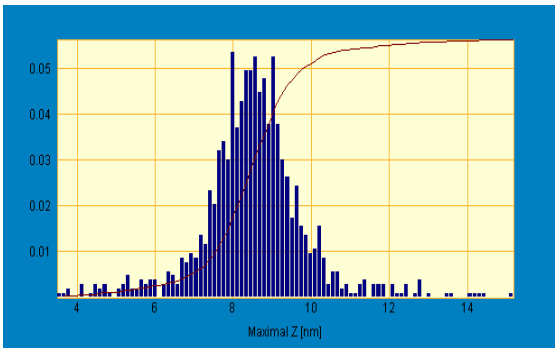

E

Figure 1. Surface and particle analysis of PS I derivatized gold surfaces. (A) A 1000 nm x 1000 nm 3D AFM surface profile image of the functionalized gold surface, which shows the highly dense and regularly ordered network of oriented PS I RC complexes. (B). A 1000 x1000 nm AFM surface image and a corresponding grain analysis image (C), with the corresponding grain height (Maximal Z) and size distributions (Diameter) shown in (D) and (E). (see text for more details).

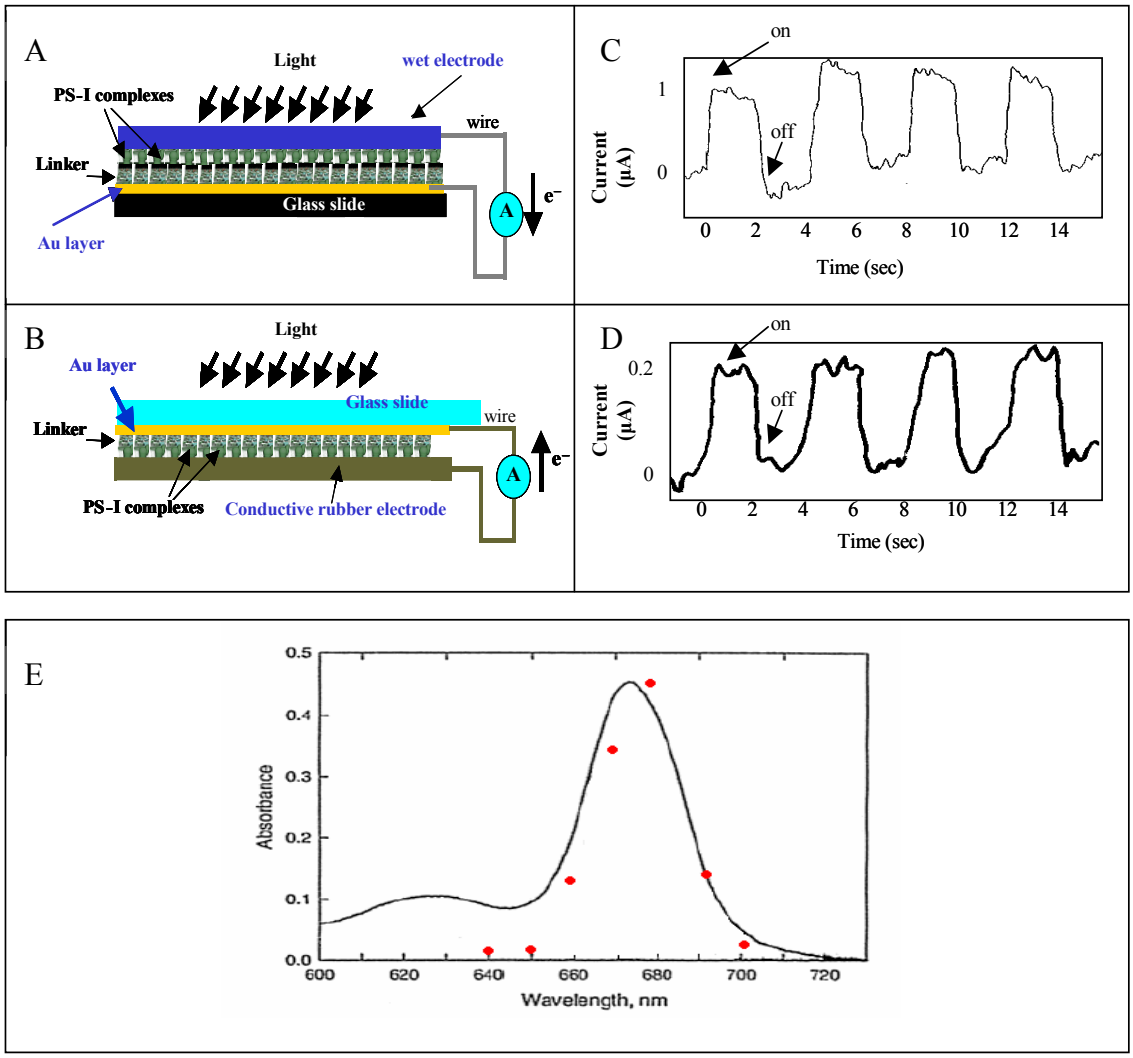

Figure 2. Schematics of working photovoltaic devices with immobilized PS I RC complexes and their corresponding photocurrent characteristics. (A) The photovoltaic device uses a gel electrode contact; the corresponding photocurrent with light modulated on-off in 2 sec intervals is shown in (C). (B) The photovoltaic device uses a rubber electrode; the corresponding photocurrent with light modulated on-off in 2 sec intervals is shown in (D). (see text for details). In (E) preliminary photocharacteristic absorption spectrum of a working photovoltaic device (red dots) that corresponds to the red edged PS I absorption spectrum (solid line) [2] is shown.

A

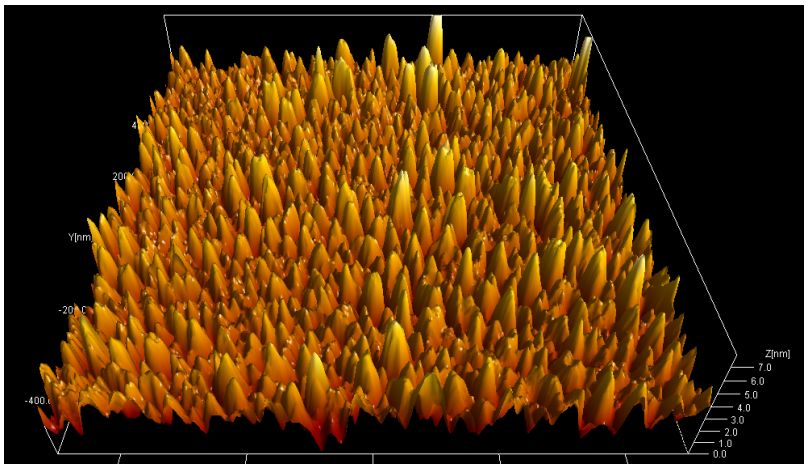

B

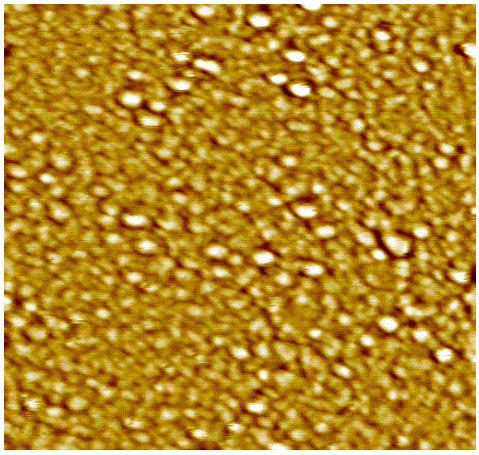

C

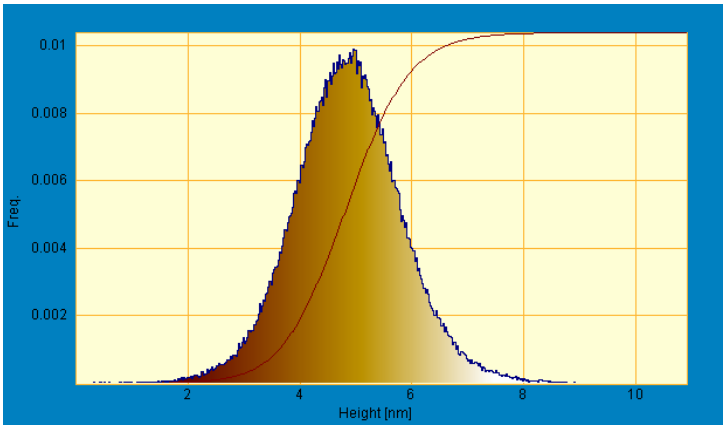

Figure 3. Surface and particle analysis of PS II derivatized gold surfaces. (A) A 1000 nm x 1000 nm, 3D AFM surface profile image of the PS II functionalized gold surface, which shows the dense surface coverage. (B) The AFM surface image and (C) its corresponding grain height distribution. (see text for more details)

References

1. Green, M.A., *Third Generation Photovoltaics: Advanced Solar Energy Conversion*; Springer-Verlag: New York, 2003; Chapter 1, p. 1.
2. Blakenship, R.E., *Molecular Mechanisms of Photosynthesis*; Blackwell Science: Oxford, England, 2002; Chapter 6, p. 95.
3. Greenbaum, E., Blankinship, S.L., Lee, J.W., Ford, R.M., *J. Phys. Chem. B* **2001**, 105, p. 3605.
4. Lee, I., Lee, J.W., Greenbaum, E., *Phys. Rev. Lett.* **1997**, 79, p. 3294.
5. O'Neill, H. and Greenbaum, E., *Chem. Mater.* **2005**, 17, p. 2654.
6. Das, R., Kiley, P.J., Segal, M., Norville, J., Yu, A.A., Wang, L, Trammell, S.A., Reddick, L.E., Kumar, R., Stellacci, F., Lebedev, N., Schnur, J., Bruce, B.D., Zhang, S., Baldo, M., *Nano Lett.* **2004**, 4, p. 1079.
7. Vauthey, S., Santoso, S., Gong, H., Watson, N., Zhang, S., *PNAS* **2003**, 8, p. 5355.
8. Von Maltzahn, G., Vauthey, S., Santoso, S., Zhang, S., *Langmuir* **2003**, 19, p. 4332.
9. Kiley, P., Zhao, X., Vaughn, M., Baldo, M.A., Bruce, B.D., Zhang, S., *PloS Biology* **2005**, 7, p. e230.
10. Lee, I., Lee, J.W., Stubna, A., Greenbaum, E., *J. Phys. Chem. B* **2000**, *104*, 2439.
11. Zhang, S., *Biotech. Adv.* **2002**, 20, p. 321.
12. Frovlov, L., Rosenwaks, Y., Carmeli, C., Carmeli, I., *Adv. Mat.* **2005**, 17, p. 2434.
13. Zhang, S., *Nature Mat.* **2004**, 3, p. 7.

14. Trammell, S.A, Wang, L., Zullo, J.M., Shashidhar, R., Lebeder, N., *Biosen. Bioelect.* **2004**, 19, p. 1649.

15. Zhang, S., Marini, D.M., Hwang, W., Santoso, S., *Curr. Op. Chem. Biol.* **2002**, 6, p. 865.

16. Minai, L, Fish, A., Anczykowski, B., Schidt, A.E., Elings, V.B., *Appl. Phys. Lett.* **1998**, 72, p. 2613.

17. Zhang, S., Yan, L., Altman, M., Lässle, M., Nugent, H., Frankel, F., Lauffenburger, D.A., Whitesides, G.M., Rich, A., *Biomaterials* **1999**, 20, p. 1213.

18. Iida, K., Kiriyama, H., Fukai, A., Konings, W.N., Nango, M., *Langmuir* **2001**, 17, p. 2821.

19. Dashdorj, N., Zhang, H., Kim, H., Yan, J., Cramer, W.A., Savikhin, S., *Biophys. J.* **2005**, 88, p. 4178.

20. Stamouli, A., Frenken, J.W.M., Oosterkamp, T.H., Cogdell, R.J., Aartsma, T.J., *FEBS Lett.* **2004**, 560, p. 109.

21. Bopp, M.A., Sytnik, A., Howard, T.D., Cogdell, R.J., Hochstrasser, R.M., *Proc. Natl. Acad. Sci. USA* **1999**, 96, p. 11271.

22. Grotjohn, I. and Fromme, P., *Photosynth. Res.* **2005**, 85, p. 51.

23. Personal Communication, P. Fromme.

24. Barber, J. and Archer, M.D., *J. of Photochem. Photobiol. A* **2001**, 142, p. 97.

25. Noy, D., Moser, C.C., Dutton, L., *Biochim. Biophys. Acta.* **2006**, 1757, p. 90.

26. Personal communication, M. Seibert.

27. Tsiotis, G., Psylinakis, M., Woplensinger, B., Lustig, A., Engel, A., Ghanotakis, D., *Eur J. Biochem.* **1999**, 259, p. 320.

28. Smeeds, K. A. and Grinstaff, M. W., *J. Biomed. Mat. Res*. **2001**, 54, p. 115.

29. Eliseeff, J., Anseth, K., Sims, D., McIntosh, W., Randolph, M., Langer, R., *PNAS* **1999**, 96, p. 3104.

30. Mellott, M. B., Searcy, K., Pishko, M. V., *Biomaterials* **2001**, 22, p. 929.

31. Baroli, V., Shastri, P., Langer, R., *J. Pharmaceutical Sci.* **2003**, 92, p. 1186.

32. Muh, F. and Zouni, A., *Biochim. Biophys. Acta.* **2005**, 1708, p. 19.

CHAPTER 9 – CONCLUSIONS

This dissertation presents the results of recent hole-burning and single-complex spectroscopy experiments on photosynthetic RC complexes. In addition, preliminary results are also presented on the fabrication of biomolecular electronic devices through orienting photosynthetic RC complexes on solid-state materials,

Using a combination of hole-burning spectroscopy measurements on the low energy donor state (P680) of the PS II RC and theoretical modeling, the nature of the primary charge separation dynamics in PS II was investigated. Previously, it has been suggested by Prokohorenko and Holzwarth that the charge separation kinetics in the PS II RC are highly dispersive, based upon low temperature (5 K) photon echo experiments (*J. Phys. Chem. B* **2000**, 104, 11563). Assuming that the PS II charge separation kinetics are indeed highly dispersive, a distribution of charge separation times was used in theoretical simulations of NPHB and TBHB experiments to better explain hole-profiles burned into the low energy region (680-684 nm) of isolated PS II RC complexes. The theoretical simulations showed increased correlation to experimental results and indicated that the primary charge separation rate in the PS II RC may indeed be highly dispersive due to intrinsic structural heterogeneity resulting from the protein matrix. In light of this, the nature of the weakly absorbing band at 684 nm (P684), which is a shoulder of the intense primary electron donor band (P680), was argued to result from a subset of more intact isolated PS II RC complexes. This conclusion was supported by other HB experimental data and theoretical calculations. Specifically, Stark and high-pressure HB experiments showed similar hole-burning experimental results (e.g. $f\Delta\mu$ values and linear-pressure

rates, respectively) for both P680 and P684 bands, electron-phonon coupling parameters and NPHB profiles were also very similar for holes burned from 680-684 nm. Excitonic calculations of the isolated PS II RC, according to the "pentamer" model by Jankowiak et al. (*J. Phys. Chem. B* **2002**, 106, 8803), provide additional evidence by asserting that two populations of isolated PS II RC complexes, one with the primary donor band at 680 nm and the other at 684 nm, could result in the observed isolated PS II Q_y absorption spectrum.

PS I - CP43′ supercomplexes of cyanobacterial *Synechocystis* PCC 6803, which form under iron stress conditions, were studied and new insights into the energy transfer dynamics of PS I were gained. Absorption, fluorescence excitation, emission, and HB spectra were measured at liquid helium temperatures for *Synechocystis* PCC 6803 PS I - CP43′ supercomplexes and for trimeric PS I core complexes, respectively. The results were then compared to room temperature, time-domain experiments (Melkozernov et al, *Biochemistry* **2003**, 42, 3893), as well as with low-temperature, steady-state experiments on PS I - CP43′ supercomplexes of *Synechococcus* PCC 7942 (Andrizhiyevskaya et al, *BBA* **2002**, 1556, 265). It was found that in contrast to CP43′ complexes of *Synechococcus* PCC 7942, CP43′ complexes of *Synechocystis* PCC 6803 possess two low-energy states that are analogous to the quasi-degenerate states A and B of CP43 PS II (Jankowiak et al, *J. Phys. Chem. B* **2000**, 104, 11805). It was determined that energy transfer between CP43′ and the PS I core occurs significantly through state A. Through interpretation of absorption and fluorescence excitation spectra along with NPHB results it was demonstrated that the low temperature (5K) EET time between state A of CP43′

and the PS I core in PS I - CP43′ supercomplexes from *Synechocystis* PCC 6803 is ~ 60 ps, which is significantly slower than EET observed at room temperature. Experimental NPHB results are also consistent with fast (≤ 10 ps) energy transfer from state B to state A. It was concluded that energy absorbed by the CP43′ manifold has, *on average,* a greater chance of being transferred to the RC and utilized for charge separation than for energy to be absorbed by the PS I core antenna. Thus, at low temperatures, the energy transfer from CP43′ to the RC occurs along a relatively well-defined path, avoiding the "red antenna state" Chl pigments. This indicates that the "red states" of the PS I core are most likely localized on the B7-A32 and B37-B38 Chl dimers located close to the PS I trimerization domain (PsaL subunit). It is also suggested that the A38-A39 dimer does not contribute to the red antenna Chl pool, as this dimer is located along the CP43′-PS I energy transfer path.

Low temperature (2–10 K) NPHB and single photosynthetic complex spectroscopy experiments were used to probe the excitonic structure and EET processes of "red state" Chl pigments in trimeric cyanobacterial PS I complexes from *Synechocystis* PCC 6803 and *Thermosynechococcus elongatus*. It was shown that individual PS I complexes of *Synechocystis* PCC 6803 (which have two red antenna states, i.e. C706 and C714) reveal only a broad structureless fluorescence band with a maximum near 720 nm, indicating strong electron-phonon coupling for the lowest-energy C714 red-state. The absence of zero-phonon lines (ZPLs) belonging to the C706 red- state in the emission spectra of individual PS I complexes from *Synechocystis* PCC 6803 suggests that the C706 and C714 red antenna states of *Synechocystis* PCC 6803 are connected by efficient energy transfer with a characteristic transfer time of ~ 5 ps. This finding is in agreement

with previous spectral hole burning data obtained for bulk samples of *Synechocystis* PCC 6803 (Hsin et al., *J. Phys. Chem. B* **2004**, 108, 10515). Samples prepared from dissolved *Thermosynechococcus elongatus* PS I crystals showed the presence of narrow ZPLs near 710 nm in addition to the broad fluorescence band at ~ 730 nm, as previously reported by Jelezko et al. (*J. Phys. Chem. B* **2000**, 104, 8093), for both NPHB and single-complex spectroscopy measurements; however, the origin of these narrow ZPLs is still undetermined. These experiments demonstrate the importance of comparing the results of ensemble (spectral hole burning) and single complex measurements, as both techniques were required to determine the presence of two red state pools (C706 and C714) in *Synechocystis* PCC 6803 and to confirm the narrow ZPL features at ~ 710 nm in *Thermosynechococcus elongatus*.

Finally, preliminary experiments with molecular electronic devices fabricated from trimeric PS I photosynthetic complexes were presented. It was found that trimeric PS I complexes form self-assembled monolayers on 2-mercaptoethanol derivatized surfaces as suggested by Greenbaum et al. (*Phys. Rev. Lett.* **1997**, 79, 3294). This was confirmed by surface characterization with AFM, as the mean particle size (20 x 20 nm) and height (9 nm) of derivatized surfaces correlated to the dimensions of the PS I complex. The PS I surface coverage was estimated to be ~ 85%. Current generation was possible with these devices after photoexcitation over the PS I absorption wavelength range (~ 400-700 nm). This indicates that the trimeric PS I complexes remain functional after orientation and immobilization on the gold surface even though there is no stabilizing interfacial medium. It is possible then that photosynthetic complexes could be used in future photovoltaic cells.

ACKNOWLEDGEMENTS

First and foremost, I would like to thank all the former teachers and mentors during my life, whether at school, college, or work, that have inspired me along the way.

I am very thankful, though, to the sincere guidance from my advisor, Professor Ryszard Jankowiak, for all his thorough input on my research and support that he has given. Also to Professor Yeung, who was willing to serve as my co-major professor. Along with this, I am indebted to the faculty and staff at the Department of Chemistry at Iowa State for all their support during my recent illness.

I also cannot forget to mention the "Small-Jankowiak" group for all their advice and assistance: To Valter Zazubovich, who was a trusted reference for photosynthesis research and superb mentor in the lab, and to Tõnu Reinot, for all the spectroscopy and solid-state physics expertise that he has shared with me. Also to John Hayes, who helped with all my questions ranging from hole-burning to safety training. To the former Small group graduate students (Abdulilah Dawoud, Nhan Dang, Nenad Grubor, Tse-Ming "Bob" Hsin, Satoshi Matsuzaki) and post-docs (Yuri Markushin, Marzena Banasiewicz), thank you for your fellowship and I wish you all continued success and happiness in life. In addition, I would also like to mention my former advisor – the late Professor Gerald J. Small, an outstanding scientist and teacher, whose enthusiasm and passion for fundamental research remain an inspiration.

Lastly, I am grateful to my family (especially Mom and Dad), for all their encouragement in all my endeavors.

This work was performed at Ames Laboratory* under Contract No. DE-AC02-07CH11358 with the US Department of Energy. The United States government has assigned the DOE report number IS-T 2396 to this thesis.

*Ames Laboratory - 2002-4 William E. Catron Fellowship – awarded for promising research relating to the development of solar cell science and technology